

# **Liquid cooled micro-scale gradient system for magnetic resonance**

Zur Erlangung des akademischen Grades eines  
DOKTORS DER INGENIEURWISSENSCHAFTEN  
(Dr.-Ing.)

von der KIT-Fakultät für Maschinenbau des  
Karlsruher Instituts für Technologie (KIT)

genehmigte

## **DISSERTATION**

von

M.Sc. Markus Valentin Meissner

Tag der mündlichen Prüfung:	29.11.2022
Referent:	Prof. Dr. Jan G. Korvink
Korreferent:	Prof. Dr. Dr. hc Jürgen Hennig

This work is licensed under a Creative Commons "Attribution-ShareAlike 4.0 International" license.



# Abstract

Switchable magnetic field gradient coils are a viable tool to modulate the nuclear spin precession in pulsed nuclear magnetic resonance (NMR) spectroscopy and imaging. Magnetic resonance imaging (MRI) of microscopic samples requires strong, rapidly-switchable magnetic field gradients to suppress diffusion related artefacts, to mitigate susceptibility effects, and to decrease the acquisition time. Several techniques can be used to achieve a high gradient strength, such as increasing the current strength or making the coil windings denser. Bringing the gradient coils physically closer to the specimen is another practical approach. As a consequence, heat dissipation caused by Joule heating becomes then a critical issue.

In this work, a novel design of a magnetic field gradient chip is introduced, and a micro fabrication process and a NMR based evaluation are proposed. The gradient coils were developed at a high level of miniaturisation by applying enhanced and newly-established micro structuring technologies. First, a fabrication technique to establish a micro radio frequency (RF) NMR coil was proposed, which reduces the processing complexity by employing mask-less lithography from the rear. This method was driven by nano-particle ink-jet printing, where the printed tracks themselves act as the mask to define an electroplating mould. Thus, the resulting sidewalls of the mould become self-aligned by the printed seed layer. Anisotropic electroplating was then possible to increase the electrical conductivity of the printed tracks.

The insights gained from the derived manufacturing techniques were applied to develop an optimised coil design for a uni-axial and a tri-axial linear-gradient

chip. The uni-axial linear z-gradient coil design was computed by a stream-function method with the optimisation to exhibit minimum power dissipation. The gradient coils were implemented on two bi-planes which were built-up with Cu electroplating in combination with photo definable dry-film laminates. In the presented fabrication process, the initial plating seed served for implementing resistive temperature detectors. The coil design and the electroplating process were tailored to enhance the electroplated height to construct low-resistive coils. The consolidated chip structure incorporated an active cooling system to equalise the heat-up of the coils for increased efficiency.

The heat-up was monitored through the combination of thermographic imaging and integrated temperature sensors, in order to analyse the current rating of the coil dual stack. The gradient coil was assembled with a RF micro coil in a flip-chip configuration and the assembly was subjected to a one-dimensional (1D) NMR experiment. Line-image profiles from a micro-engineered phantom were recorded to examine the linearity of the resultant gradient field. A gradient efficiency of  $3.15 \text{ T m}^{-1} \text{ A}^{-1}$  was achieved for a profiled length of 1.2 mm.

# Zusammenfassung

Schaltbare magnetische Feldgradientenspulen sind ein geeignetes Werkzeug für die Modulation der Kernspinpräzession in der gepulsten Kernspinresonanzspektroskopie und Bildgebung. Die Magnetresonanztomographie von mikroskopischen Proben benötigt starke, schnell schaltbare Magnetfeldgradienten, um diffusionsbedingte Artefakte zu unterdrücken, Suszeptibilitätseffekte abzuschwächen und um die Messzeit zu verkürzen. Verschiedene Techniken können eingesetzt werden, um eine hohe Gradientenintensität zu erreichen, wie zum Beispiel die Erhöhung der Stromstärke oder die Steigerung der Windungsdichte der Feldspule. Ein weiterer, geeigneter technischer Ansatz besteht darin, die Gradientenspulen näher an der Probe zu platzieren. Als Konsequenz wird aber die durch die Joule-Erwärmung verursachte Wärmeentwicklung zu einem zentralen Problem.

In dieser Arbeit wird ein neuartiges Design, ein Mikroherstellungsprozess und eine Kernspin-Evaluierung eines Feldgradientenchips präsentiert. Die Gradientenspulen wurden besonders hoch miniaturisiert und durch den Einsatz von verbesserten und neuartigen Strukturierungsverfahren entwickelt. Zuerst wird ein Fertigungsverfahren zur Herstellung einer kompakten Hochfrequenzspule vorgestellt. Durch den Einsatz einer maskenlosen Rückseitenlithographie konnte die Prozesskomplexität reduziert werden. Dieses Verfahren wurde durch Tintenstrahldruck mit Nanopartikeln realisiert, wobei die gedruckten Strukturen selbst als lithographische Maske für die Herstellung einer galvanischen Form dienen. Somit werden die Seitenwände der galvanischen Form durch die gedruckte Seed-Schicht optimal selbst ausgerichtet. Dies ermöglichte eine an-

isotrope Galvanisierung, um eine höhere elektrische Leitfähigkeit der gedruckten Leiterbahnen zu erzielen.

Aus den Erkenntnissen der ausgearbeiteten Herstellungsprozesse wurde ein optimiertes Spulendesign für ein-axiale sowie drei-axiale linearen Gradientenchips entwickelt. Die einachsige lineare z-Gradientenspule wurde mit der *Stream-Function-Methode* berechnet, wobei die Optimierung darauf abgestimmt wurde, eine minimale Verlustleistung zu erzielen. Die Gradientenspulen wurden auf zwei Doppellagen implementiert, die mittels Cu-Galvanik in Kombination mit fotodefinitiven Trockenfilm-Laminaten aufgebracht wurden. Bei dem hier vorgestellten Herstellungsverfahren diente die erste Metallisierungsschicht gleichzeitig dazu, Widerstands-Temperaturdetektoren zu integrieren. Um niederohmige Spulen zu realisieren wurde der Galvanisierungsprozess soweit angepasst, um eine hohe Schichtdicke zu erzielen. Die Chipstruktur beinhaltet ein aktives Kühlsystem, um dem Aufheizen der Spulen entgegenzuwirken.

Thermographische Aufnahmen in Kombination mit den eingebetteten Temperatursensoren ermöglichen es, die Erhitzung der Spule zu analysieren, um die Strombelastbarkeit zu ermitteln. Die Gradientenspule wurde mit einer Hochfrequenz-Mikrospule in einer Flip-Chip-Konfiguration zusammengebaut, und mit diesem Aufbau wurde ein eindimensionales Kernspinexperiment durchgeführt. Es wurde eine Gradienteneffizienz von  $3.15 \text{ T m}^{-1} \text{ A}^{-1}$  bei einer Profillänge von 1.2 mm erreicht.

# Contents

<b>Abstract</b> . . . . .	<b>i</b>
<b>Zusammenfassung</b> . . . . .	<b>iii</b>
<b>1 Introduction</b> . . . . .	<b>1</b>
1.1 Nuclear magnetism and spin interactions . . . . .	2
1.2 Diffusion . . . . .	7
1.3 Magnetic resonance imaging . . . . .	11
1.4 Hardware . . . . .	15
1.4.1 Miniaturised RF coils . . . . .	16
1.4.2 Field gradients for magnetic resonance microscopy . . . . .	20
1.5 Thesis objectives . . . . .	32
1.6 Thesis outline . . . . .	35
<b>2 Microfabrication</b> . . . . .	<b>37</b>
2.1 Materials . . . . .	38
2.2 Conductive ink-jet printing on permanent resist . . . . .	56
2.3 Copper electroplating . . . . .	59
<b>3 Process evaluation</b> . . . . .	<b>67</b>
3.1 Wire bonded magnetic resonance gradient coils . . . . .	67
3.2 Mask-less micro coil fabrication using ink-jet printing . . . . .	70
3.2.1 Plating mould fabrication by back-side lithography . . . . .	72

3.2.2	Copper electroplating of the micro coil . . . . .	76
3.2.3	Electrical passivation and interconnect fabrication . . . . .	77
3.2.4	RF characterisation . . . . .	81
<b>4</b>	<b>Micro gradient design . . . . .</b>	<b>83</b>
4.1	Uni-axial z-gradient . . . . .	86
4.2	Coil generation from nested contours . . . . .	93
4.3	Tri-axial gradient design . . . . .	96
4.4	Supplemental components . . . . .	104
<b>5</b>	<b>Gradient chip fabrication . . . . .</b>	<b>109</b>
5.1	Plating seed and electroplating mould . . . . .	113
5.2	Micro electroplating of the first gradient coil layer . . . . .	118
5.3	Fluidic cooling channels and first encapsulation . . . . .	125
5.4	VIA top-up by copper electroplating . . . . .	126
5.5	Formation of the second coil layer . . . . .	131
5.6	Encapsulation of the second coil layer . . . . .	137
5.7	Back-end processing . . . . .	140
<b>6</b>	<b>Characterisation . . . . .</b>	<b>143</b>
6.1	Physical characteristics . . . . .	143
6.2	Electrical characteristics . . . . .	144
6.3	Thermal characterisation . . . . .	147
6.3.1	Thermal characteristics of the Topcool design . . . . .	152
6.3.2	Thermal characteristics of the Midcool design . . . . .	157
<b>7</b>	<b>NMR experiments . . . . .</b>	<b>163</b>
7.1	MRI experiments with the printed micro coil . . . . .	164
7.2	Evaluation of the uni-axial z-gradient . . . . .	169
7.2.1	PaperClip micro coil . . . . .	169

7.2.2	Micro engineered phantom . . . . .	172
7.2.3	1D-imaging using the miniaturised uni-axial z-gradient . . . . .	176
<b>8</b>	<b>Conclusion and outlook . . . . .</b>	<b>185</b>
<b>A</b>	<b>Process description . . . . .</b>	<b>195</b>
A.1	Gradient chip fabrication . . . . .	195
A.2	Tx/Rx micro coil fabrication . . . . .	220
	<b>Bibliography . . . . .</b>	<b>229</b>
	<b>Acronyms . . . . .</b>	<b>253</b>
	<b>List of publications . . . . .</b>	<b>259</b>
	<b>Acknowledgement . . . . .</b>	<b>265</b>



# 1 Introduction

Over the last 60 years of scientific advancement,<sup>[1]</sup> nuclear magnetic resonance (NMR) spectroscopy has become an indispensable tool in analytical chemistry. NMR makes it possible to study the magnetic properties of atoms, up to complex molecules, which are inaccessible by any other current method.<sup>[2]</sup> Magnetic resonance spectroscopy uses NMR as a quantitative measurement tool to gain detailed molecular information and to examine dynamic processes. The noninvasive measurement approach employs radio frequency (RF) waves to excite internal magnetic fields around atomic nuclei, leading to chemical shifts and a change in its resonance frequency.

Section 1.1 briefly explains the concept of magnetic resonance (MR) spectroscopy, a measurement tool to identify the composition of chemical compounds. In Section 1.2, the principle of investigating the molecular diffusion using NMR techniques is briefly described. By adding precise field gradients to an NMR setup, the technique extends to the unique, non-invasive imaging modality, magnetic resonance imaging (MRI) which is further described in Section 1.3. The state-of-the-art of various compact NMR probes with the integration of imaging hardware is described in Section 1.4. The detection hardware in MRI is subject to continuous improvement and this chapter concludes the technical limitations that arise in the context of micro imaging hardware.

Comprehensive explanations on the physical conditions are described within the relevant literature for NMR spectroscopy<sup>[3–6]</sup> and MRI.<sup>[7–9]</sup> The publication by Lacey *et al*<sup>[10]</sup> addresses the fundamentals of NMR spectroscopy of very small sample volumes ( $\approx 1$  nL) including the advancement of micro fabricated

NMR hardware. In the field of MR micro imaging, Glover and Mansfield summarised the major limitations of the magnetic resonance microscopy (MRM) technology.<sup>[11]</sup>

## 1.1 Nuclear magnetism and spin interactions

An integral part of atomic nucleons with an odd number of protons, neutrons or both is the existence of a nuclear spin. Some frequently used NMR isotopes such as  $^1\text{H}$ ,  $^{13}\text{C}$ ,  $^{19}\text{F}$  or  $^2\text{H}$  show an outward directed magnetic spin and permit for a detailed investigation. In brief, the nuclear spin is an abstract property of the particle and specifies a quantum property. It is a form of angular momentum which is an intrinsic property, that is not generated by the self-rotation of the particle itself.

The principle of NMR spectroscopy is related to the *Zeeman effect*, which describes an energy splitting on the magnetic moment of the atomic nucleus by the influence of an external magnetic field. The first investigation of a spin state was performed in the famous *Stern-Gerlach* experiment,<sup>[12]</sup> where the direction of the electron spin of silver atoms was quantised. In short, the intrinsic angular momentum shows an observable, directed interaction along an inhomogeneous magnetic field. There are two energy states  $E$  or levels of a spin  $s$ , in the case of a spin-half *spin-up* and *spin-down*, generally expressed as  $E_\alpha = -1/2 \hbar \gamma \mathbf{B}_0$  and  $E_\beta = +1/2 \hbar \gamma \mathbf{B}_0$ , where  $\gamma$  is the gyromagnetic ratio,  $\hbar$  is Planck's constant and  $\mathbf{B}_0$  is the main magnetic field.

The tendency for spins to be in a state of lower energy is neutralised by thermal collisions that tend to counterbalance the two spin states. In the equilibrium state in absence of a static, homogeneous magnetic field, the magnetic moments are oriented in random directions. In the presence of an external magnetic field  $\mathbf{B}_0$ , when considering a bulk sample of nucleons, there are parallel and anti-parallel energy states which line-up in direction with  $\mathbf{B}_0$ . In a three-dimensional representation, we consider  $\mathbf{B}_0$  to be aligned in z-direction. The number of

spins which align to  $\mathbf{B}_0$  generally depends on the magnetic field strength of  $\mathbf{B}_0$  and the temperature. For the collective interaction of many spins, one speaks of an isochromat<sup>[3]</sup> or the bulk magnetisation, which converts to a net magnetisation vector  $\mathbf{M}_0$ . Boltzmann equilibrium law provides an estimate of the net magnetisation which can be estimated by,

$$\mathbf{M}_0 \approx N \frac{\gamma^2 s(s+1)\hbar}{3 k_B T} \mathbf{B}_0, \quad (1.1)$$

where  $N$  is the number of spins,  $k$  is the Boltzmann constant,  $T$  is the absolute temperature and  $\mathbf{B}_0$  represents the statically applied main magnetic field.

The nuclear spin angular momentum of a particle results in a magnetic dipole momentum and this precession is formed respectively to  $\mathbf{B}_0$ , which can be expressed by the proportional relationship, the so-called *Larmor precession*,

$$\omega_0 = \gamma \cdot |\mathbf{B}_0| \quad (1.2)$$

where  $\omega$  is the *Larmor frequency* and  $\gamma$  is the gyromagnetic ratio of the nucleus. One example is  $^1\text{H}$  with a constant gyromagnetic ratio  $\gamma_{^1\text{H}}$  of  $42.58 \text{ MHz T}^{-1}$ .

The NMR signal is obtained by the interaction between an external applied, alternating high frequency field and the intrinsic magnetic moments of the bulk sample. Such RF radiation is necessary to generate a flip of the nuclei spin state. The contributing electromagnetic energy causes the nuclei to change their energy levels and is equivalent to energy difference between the two spin states. The energy necessary to transform from  $E_\alpha$  to state  $E_\beta$  consequently results in  $\hbar\gamma\mathbf{B}_0$ .

In every kind of physical examination, a suitable sensor is essential to obtain, monitor and retrieve quantitative information regarding a specific physical phenomenon. Much similar to radar technology, the hardware necessary for the transmission of the RF excitation is a solenoid coil with a magnetic field  $\mathbf{B}_1$  in the x-y plane, with its direction perpendicular to  $\mathbf{B}_0$  as shown in Figure 1.1(a).

By modifying the RF pulse width and amplitude, it is possible to flip the intrinsic spin angular momentum towards or against  $\mathbf{B}_0$ . With the z-directed bulk magnetisation flipped towards the x-y plane, it can be detected by the same coil or by employing a dedicated receive coil. The net magnetisation  $\mathbf{M}$  is observable as long as the individual nuclear spins precess collectively, in coherence with one another. To prevail spin coherence over the entire sample, it is obligatory that all spins experience an equal interaction with the transmitted RF field.

After applying the  $\mathbf{B}_1$  pulse, the nuclear spins re-align in the direction of  $\mathbf{B}_0$ , which results in a decaying magnetic dipole precession around the z-axis. The processes that take place after diverting the nuclear spin magnetisation back to its state of equilibrium is called *relaxation*, as illustrated in Figure 1.1(b). The decaying signal oscillation is known as the free induction decay (FID) which is recorded by a pick-up coil according to Faraday's law of induction. The extremely weak NMR signal is further amplified in time-domain, sampled by its quadrature using an analog-to-digital converter (ADC), and  $\mathcal{F}$ ourier transformed to obtain the NMR frequency spectrum.

A distinction is made between the two relaxation times  $T_1$  and  $T_2^*$ , which are of particular interest.<sup>[6]</sup> The return of the excited nuclear spin system to its equilibrium state is known as the longitudinal or *spin-lattice* relaxation or  $T_1$ -relaxation, see Figure 1.1(c). Besides, the *spin-spin* relaxation or transversal relaxation time  $T_2^*$  describes the time constant of the exponential decay, which is observed after the RF excitation.

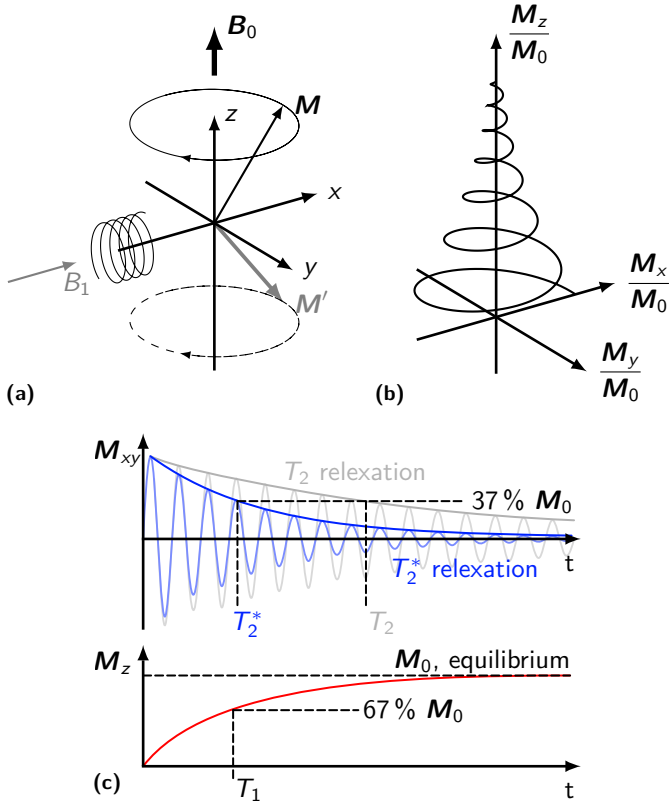


**Figure 1.1:** (a) the net magnetisation  $M$  in the equilibrium state is rotated to  $M'$  by an applied RF magnetic field  $B_1$  in  $x$ -direction. (b) FID in the laboratory frame, governed by the Bloch equations in Equation (1.3). (c) the decay of the magnetisation after a  $90^\circ$  pulse starting at  $t = 0$ s. (Figure inspired by [4, 6, 7])

The electrodynamic behaviour of the decaying magnetisation vector is described in terms of its precessional motion by the *Bloch equations*,<sup>[13]</sup>

$$\frac{d\mathbf{M}}{dt} = \gamma \mathbf{M} \times \mathbf{B}_0 - \begin{pmatrix} \frac{M_x}{T_2^*} \\ \frac{M_y}{T_2^*} \\ \frac{M_z - M_0}{T_1} \end{pmatrix}. \quad (1.3)$$

The *Bloch equations* provide the classical description for the dynamic behaviour of the magnetisation vector and present the equations of motion of the NMR signal. For a precise model of the behaviour of a nuclear spin, a quantum description offers a more complete and detailed explanation.

In a practical observation of the relaxation, magnetic field inhomogeneities, and to a minor extent, susceptibility discontinuities lead to a dispersion of the FID with respect to an ideal relaxation.  $T_2^*$  is considered as the *observed* time constant and is always less or equal than the *true*  $T_2$ . A lower  $T_2^*$  indicates a more rapid signal drop.  $T_2'$  contributes reversibly to  $T_2^*$  and is stochastically independent from the *natural* or *true*  $T_2$ ,

$$\frac{1}{T_2^*} = \frac{1}{T_2} + \frac{1}{T_2'}, \quad \text{with } T_2' \sim \frac{1}{\gamma \Delta \mathbf{B}_0}. \quad (1.4)$$

In molecular compounds, a shift in the resonant frequency of the nucleus can be observed, which is influenced by the magnetic susceptibility change of the orbital electrons. In terms of  $^1\text{H}$  spectroscopy, individual substituents or functional groups can therefore be identified in the NMR spectrum. The result is a shift in the spectral lines which is called the *chemical shift*. In spectroscopy, the chemical shift refers to the displacement of the resonant frequency with respect to the standard in the magnetic field. The chemical shift scale is established by referencing on a calibration compound from which

a spectral peak defines the zero point on the chemical shift scale. For  $^1\text{H}$  and  $^{13}\text{C}$  the standard reference compound tetramethylsilane (TMS) is widely used. Although, the chemical shift  $\delta_{(\text{ppm})}$  is an independent measure with respect to the main magnetic field strength computed by

$$\delta_{(\text{ppm})} = 10^6 \times \frac{\nu - \nu_{\text{ref}}}{\nu_{\text{ref}}}, \quad (1.5)$$

with  $\nu$  being the resonance frequency in Hz of the observed sample and  $\nu_{\text{ref}}$  being the frequency in Hz of the spectral line from the reference compound.

It is worth mentioning that within a molecular system, hyper-fine spin interactions between chemical bonds produce a splitting of resonance lines within the observed spectra. The effect is called *J-coupling*, which is also known as *indirect spin-spin coupling* and provides a direct spectral description of a chemical bond. The unit of *J-coupling* is specified in hertz and the observed quantity is the separation of frequencies between the multiplet peaks.

## 1.2 Diffusion

In liquids, molecules translate relative to their molecular mass centre throughout space. Diffusion is the *Brownian motion* of molecules or ions caused by their internal thermal energy. Quantifying the effects of molecular diffusion or flow movements by means of magnetic gradient encoding is a major topic and NMR provides a very elegant measurement approach.<sup>[14]</sup> Molecular motion by diffusion has an indirect or direct effect on the contrast of MR images.<sup>[15,16]</sup>

The mean squared displacement of a molecule  $\langle r_{(t)}^2 \rangle$  in the  $n$ -dimensional case that diffuses in a time period  $t$  is given by

$$\langle r_{(t)}^2 \rangle = 2 \cdot n D t, \quad (1.6)$$

with  $D$  being the diffusion constant. The distribution of squared displacement can be treated as a statistical process and is characterised by a Gaussian distribution with its peak representing zero displacement. The self-diffusion coefficient can be estimated by the Stokes-Einstein relation, which shows a linear temperature dependency.<sup>[17]</sup> Accordingly, stable temperature conditions must be maintained during a diffusion measurement.

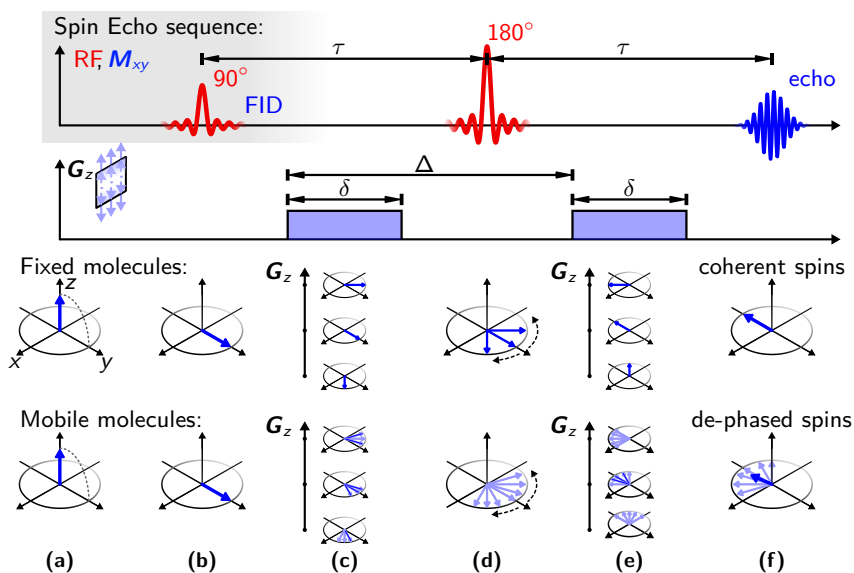


**Figure 1.2:** Pulsed field gradient (PFG) spin-echo (SE) sequence for measuring molecular diffusion. (a) initial state. (b)  $90^\circ$  pulse to flip the spins. (c) PFG SE: the phase distributes along the gradient axis. (d) the  $180^\circ$  pulse causes the phase to invert. (e) PFG SE: phase refocusing. (f) the resulting echo signal. (Figure inspired by [4, 5, 18, 19])

For the description of the pulse sequence for NMR based diffusion measurement, the SE must be presented first. The SE sequence is mainly used to measure the  $T_2$  process, but also for  $T_1$ -weighting. However, diffusion weighted imaging is associated with  $T_2$ -weighting due to the longer minimum echo time (TE) imposed by the diffusion module. Based on *Bloch's* theory, Hahn<sup>[19]</sup> derived

the SE pulse sequence, that utilises two excitation pulses (Figure 1.2). In the beginning, the net-magnetisation aligns with  $\mathbf{B}_0$ , Figure 1.2(a). The first  $90^\circ$  pulse (Figure 1.2(b)) flips the net-magnetisation towards the  $x, y$ -plane. The removal of the  $\mathbf{B}_1$  pulse results in *de-phasing* of the spins caused by spatial  $\mathbf{B}_0$  variations and  $T_2$  spin-spin interactions, which is related to Equation (1.4). The *De-phasing* of the spins predominantly arises from the translational diffusion within an inhomogeneous magnetic field. The important property of the spin-echo sequence is the *re-phasing* by a further  $180^\circ$  pulse that re-clusters the spins and reverses the aforementioned *de-phasing*, Figure 1.2(d).

In the beginning of the NMR diffusion measurements, static magnetic field gradients have been used to measure self-diffusion coefficients. Nuclear spins, which are located at various positions along the gradient, precess at different angular frequencies.<sup>[20]</sup> However, from the arising inhomogeneities throughout the gradient, the transverse relaxation time  $T_2$  in Equation (1.4) shortens even further.<sup>[21]</sup>

As a variation of Hahn's spin-echo sequence,<sup>[19]</sup> switched gradient pulses before and after the  $180^\circ$  pulse allow the measurement of diffusion coefficients of small molecules in a more flexible way, as shown in Figure 1.2.<sup>[22]</sup> By adding two gradient pulses of length  $\delta$  and strength  $\mathbf{G}$ , the conventional spin-echo sequence extends to the pulsed field gradient (PFG) spin-echo (SE) technique, which allows for the measurement the self-diffusion coefficient. With the first gradient pulse in Figure 1.2(c), the phase of the spins unravels over the spatial direction of the gradient field, along the gradient axis. The second gradient pulse has the same shape of the first gradient pulse and refocuses the phase as shown in Figure 1.2(e). The phase change  $\Phi_2 - \Phi_1$  that remains for a particle for a displacement  $x_2 - x_1$  after the  $180^\circ$  pulse is given by,

$$\Phi_2 - \Phi_1 = -\gamma \delta \mathbf{G} (x_2 - x_1). \quad (1.7)$$

The resultant signal of all spins in total is then attenuated due to the incoherence of multiple spins of the bulk sample. The relevant literature usually deals with the relationship between the diffusion-attenuated signal  $S_{(2\tau, G)}$  and the signal without the influence of a gradient  $S_{(2\tau, G=0)}$  as described by the *Stejskal–Tanner* equation for an echo time of  $2\tau$ ,

$$\frac{S_{(2\tau, G)}}{S_{(2\tau, G=0)}} = \exp\left(-\gamma^2 \delta^2 \mathbf{G}^2 D \left(\Delta - \frac{\delta}{3}\right)\right). \quad (1.8)$$

The diffusion constant is typically determined by solving Equation (1.8) for a set of spectra, which are recorded using multiple distinct gradient amplitudes. The diffusion is then encoded as a spatial displacement with regard to the elapsed time between the two gradient pulses.<sup>[23]</sup> The measurement results in a progressive, exponential decay of the signal amplitude.<sup>[24]</sup> The exponential signal decay affected by diffusion may also be expressed by the relaxation time  $T_2^*$  as described by the *Torrey equation*,

$$\frac{1}{T_2^*} = \frac{1}{T_2} + \frac{1}{3} D \gamma^2 \mathbf{G}^2 \delta^2. \quad (1.9)$$

More generally,  $T_2^*$  is dominated by field inhomogeneity, which warrants an extra term in equation (1.9), i.e. see equation (1.4). The described formalism also allows to utilise an NMR diffusion experiment for benchmarking the one-dimensional (1D)-gradient homogeneity.

Another application of diffusion pulse sequences is the selective suppression of resonances within the spectrum.<sup>[25]</sup> In general, the excitation band-width (BW) of the RF pulse is generally much greater than the sweep-width (SW) of the entire spectra ( $\text{BW} \gg \text{SW}$ ). The  $180^\circ$  re-phasing *hard* pulse is then replaced by a selective pulse with an adjusted BW. It is then possible in combination with the gradient pulses to *re-phase* only a certain part of the spectra. The areas of the spectra which are suppressed by the filter remain out-of-phase, and therefore do not show up in the spectra.

## 1.3 Magnetic resonance imaging

MRI is a noninvasive tomographic imaging technique, generally used for medical diagnostics. The spatial imaging modality gives information about the abundance of a specific nuclei at specific locations in the sample, independent of their chemical configuration. One particular advantage of MRI is the possibility to observe the structure of biological tissue non-destructively. In human body MRI scanners, the imaging resolution is currently limited to the order of a millimetre. When downsizing the equipment to a small-animal imaging unit, the smallest detail or voxel is typically 75  $\mu\text{m}$  to 50  $\mu\text{m}$ .

The imaging technique was first discovered by Mansfield and Lauterbur in 1972 by utilising dynamically switched magnetic field inhomogeneities with the objective of encoding spatial information into the received NMR signal.<sup>[26,27]</sup> Therefore, external magnetic fields are overlaid in a defined manner over the sample space, thereby creating a location specific magnetic configuration that leads to a location-specific RF response. In practice, such linear field inhomogeneities are added to the static magnetic field  $\mathbf{B}_0$ , and those are generated by a gradient coil setup. In the early years, the technical challenges were the demanding requirements on the signal processing and maintaining the magnetic flux of the gradient over the confined sample space, without degrading the superconducting magnet. To capture high resolution images, the gradient field strength  $\mathbf{G}$  ( $\text{T m}^{-1}$ ) is the key feature. It is common that the gradient efficiency scales by square while the inner diameter or conductor separation is reduced. In this context it is preferable to position the gradient conductors as close as possible to the specimen.

An imaging gradient setup consists of three gradient coils in  $x$ -,  $y$ - and  $z$ -direction, which collectively generate an arbitrary gradient vector  $\mathbf{G}$ .<sup>[7]</sup> For a

linear, spatial variation of the magnetic field, the gradient vector is composed of the three orthogonal components  $\mathbf{G}_x$ ,  $\mathbf{G}_y$  and  $\mathbf{G}_z$ ,

$$\begin{aligned}\mathbf{G} &= \frac{\partial \mathbf{B}_z}{\partial x} \cdot \hat{x} + \frac{\partial \mathbf{B}_z}{\partial y} \cdot \hat{y} + \frac{\partial \mathbf{B}_z}{\partial z} \cdot \hat{z} \\ &\equiv \mathbf{G}_x \cdot \hat{x} + \mathbf{G}_y \cdot \hat{y} + \mathbf{G}_z \cdot \hat{z}.\end{aligned}\tag{1.10}$$

The use of defined, linear field gradients is the way of choice in healthcare applications, since the linear field distribution also results in a constant voxel size. Also the signal intensities over the entire image can be compared directly. This makes the linearity an important design parameter for targeting the imaging field-of-view (FOV). Consequently, only a constant correction factor is sufficient to adjust for a variation in the gradient efficiency among the three gradient coils.

During an MRI experiment, a specially designed pulse sequence is executed, in which the gradients are switched to perform frequency and phase encoding of the respective voxels. Throughout Figure 1.3, the three gradient directions vary linearly in the illustrated representation. The imaging plane may also be selected arbitrary independent of Cartesian axis directions, as shown in the figure.

Spatial encoding in magnetic resonance can be performed by the here illustrated two-dimensional (2D) GRE sequence, that can be subdivided into three sections, within the order of the applied gradient types:

**slice selection:** The first gradient pulse is imposed during RF excitation and defines the imaging slice. The shape of the RF is for example a windowed sinc pulse that mathematically performs an ideal excitation. Both, the RF band-width (BW)  $\Delta f$  and the gradient  $\mathbf{G}_z$  correspond to the frequency

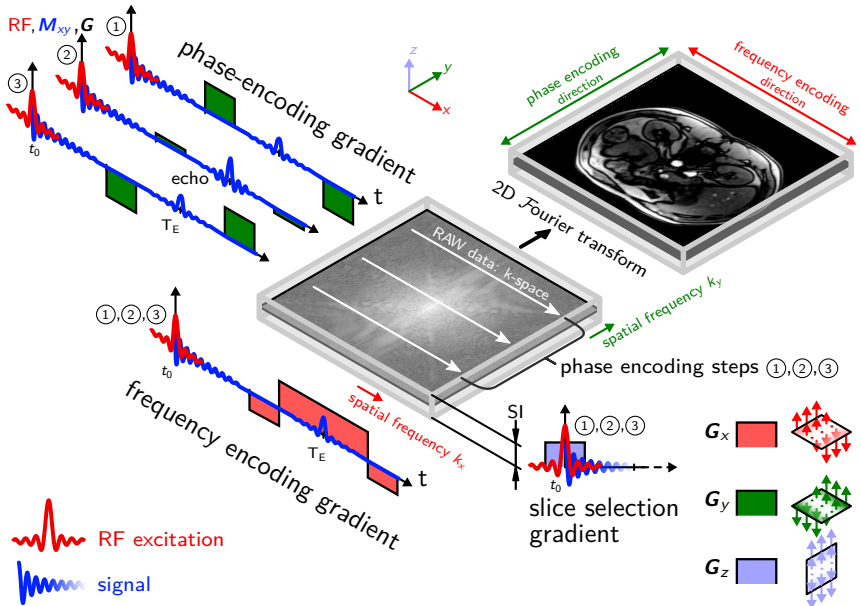


**Figure 1.3:** The gradient echo (GRE) pulse sequence with the gradient coil axis selected to fit the Cartesian grid. (Figure inspired by [7, 28], MRI slice of my abdomen recorded 2018 at Shenzhen People's Hospital, China)

range where the *Larmor equation* applies. Hence, the excited area or slice thickness (SI) is defined by,

$$SI = \frac{2\pi \cdot \Delta f}{\gamma \mathbf{G}_z}. \quad (1.11)$$

If the selected slice is located in the isocenter of the gradient, the RF carrier frequency is equal to the reference *Larmor frequency* of the magnet,  $\mathbf{B}_0$ . In the GRE sequence, there is no  $180^\circ$  excitation pulse and flip angles below  $90^\circ$  are generally used. A shorter flip angle has the advantage of lower RF power which reduces the specific absorption in the sample, when compared to a spin-echo sequence.

**phase encoding:** The principle which lies behind the phase encoding is to induce a spatial phase shift into the magnetisation. A gradient lobe is applied while the magnetisation is in the transverse plane, after the excitation and before the readout. By varying the amplitude of the phase coding gradient for the line-readout, different amounts of linear phase variation are introduced. The phase encoding gradient  $\mathbf{G}_y$  is predominantly orthogonal to the frequency encoding direction, while exposing an angular frequency of precession  $\omega = \gamma \mathbf{G}_y y$ . Although, the gradient lobe  $\mathbf{G}_y$  is switched on for a duration  $T$ , and the particular position of the encoded phase  $\Phi$  is determined by,

$$\Phi(y) = y \gamma \int_0^T \mathbf{G}_y t' dt'. \quad (1.12)$$

**frequency encoding:** To generate the echo, first, a gradient pulse with a negative polarity is switched to add a phase to the spins. The bulk magnetisation is then re-phased by the readout gradient pulse, that possesses a positive polarity. The MR signal further becomes a measure of the position along the gradient. The echo time  $T_E$  is the duration from the centre of the RF excitation pulse to the middle of the echo. The gradient lobe  $\mathbf{G}_x$  during echo readout causes a variation in the *Larmor precession*  $\omega \equiv \omega_0 + \omega_{x_j}$ , which distributes linearly across the object, according to

$$\omega_{x_j} = \gamma \mathbf{G}_x x_j. \quad (1.13)$$

The received angular frequencies map directly to the locations of the spin isochromats. The GRE sequence produces susceptibility weighted images since there is no refocusing during the acquisition of the echo. The extracted images are contrast weighted by the factor  $\exp(-T_E/T_2^*)$ .

## ***k*-space sampling**

The *k*-space sampling concept facilitates the understanding of the pulse sequence. The domain was called *k*-space since the *F*ourier transform variables are given the symbol *k*. The time-varying signals are organised as trajectories as shown in Figure 1.3 and each phase encoding gradient pulse begins with a new line in *k*-space. For the visual interpretation of the data, the sampled *k*-space data is reconstructed into the imaging domain by a 2D *F*ourier transformation. The *F*ourier conjugate of the *k*-space trajectory correspond to the coherent net magnetisation in the 2D space.<sup>[7]</sup>

## **1.4 Hardware**

NMR magnets with field strengths of more than 36.1 T can be constructed on the basis of using modern superconductor materials.<sup>[29–31]</sup> Such a high field strength is obtained in the centre region of the space-constrained magnet bore, which further requires a compact assembly and integration of the NMR detector. NMR systems made from compact permanent magnets (up to 1 T to 3 T) are becoming even more popular and can benefit from a compact transmit and receive (Tx/Rx) and gradient coil assembly. One example of such a magnet was constructed by Moresi *et al*,<sup>[32]</sup> where metal plates with high permeability were inserted into a permanent *Halbach magnet* configuration to further homogenise and accumulate the field in the centre. When combining such a magnet with a microfluidic sample delivery system, compact electronics, and a microfabricated detector – that sort of MR spectrometer facilitates its fully portable operation at the point-of-care.<sup>[33,34]</sup> In the confined space between the gradient and the sample, it is also necessary to implement a compact Tx/Rx coil topology. Two of the biggest hardware challenges in NMR spectroscopy and micro imaging are the sensitivity of the RF Tx/Rx coil and the field strength of the gradient system.

The applied field variation of a gradient coil is generally independent from the primary magnetic field strength  $B_0$ . Both, high and low field systems can therefore benefit from a space-saving miniaturised gradient system and would also allow for smaller bore sizes of the magnets. When scaling down the measurement equipment, the ratio between the magnet size and the size of the sensitive volume is fairly constant. Although, if one reduces the size of the magnet, a smaller homogeneous volume is obtained, which compromises the sensitivity.<sup>[35]</sup> However, the accuracy and linearity of  $B_0$  limits the resolution. Consequently not many publications reported an isotropic resolution of less than 10  $\mu\text{m}$ . The wide application of high-resolution NMR equipment is not only limited by its price, but also by its size and continuous maintenance.

### 1.4.1 Miniaturised RF coils

The measured NMR signal is extremely weak and requires a well engineered detector.<sup>[36,37]</sup> The fraction  $V_{\text{total}}/V_S$  of the *total* volume involved in the NMR experiment and the *effective* sample volume  $V_S$  covered by the RF micro detector should ideally become equal to one. The RF detector must record a considerable amount of the FID amplitudes with a minimum of randomly added noise. A weak signal-to-noise ratio (SNR) results in a small number of received spins  $N$  and consequently longer measurement times are required.<sup>[38]</sup> Therefore, a high SNR of the NMR detector is an essential prerequisite.

Hoult and Richards<sup>[39]</sup> investigated the influencing factors on the SNR, which give a general design description to levitate the amplitude of the signal and to reduce the level of the noise. The significant factors which are contributing to the SNR are the temperature of the probe and the sample, the  $B_1$  homogeneity of the coil, the coil sensitivity, the probe's efficiency and filling factor  $\alpha_F$  and geometry of the coil. Also, the noise figure of the RF pre-amplifier and the amount of polarised spins due to the  $B_0$  field strength degrade the SNR. Most of the electronic noise in the RF detector is generated by the thermal motion of

the electrons, which is known as the thermal noise voltage or *Johnson–Nyquist* noise,

$$v_n = \sqrt{4 k_B T R \Delta f}. \quad (1.14)$$

Where  $k_B$  is the Boltzmann's constant,  $T$  is the absolute temperature,  $R$  is the coil resistivity and  $\Delta f$  is the bandwidth in Hz over which the noise was measured. The SNR is defined as the height of the signal, is generally divided by the the root-mean-square (RMS) noise,<sup>[10]</sup> which is given for an MR coil by,<sup>[40]</sup>

$$\text{SNR} = \frac{k_0 \left( \frac{\mathbf{B}_1}{i} \right) V_S N \gamma \frac{\hbar^2}{4\pi^2} I(I+1) \frac{\omega_0^2}{k_B T 3\sqrt{2}}}{v_n}. \quad (1.15)$$

$k_0$  includes the contribution of  $\mathbf{B}_1$  field inhomogeneities,  $I$  is the quantum number of the angular momentum and  $N$  is the amount of contributing spins. Equation (1.15) of the SNR is often found in a simpler form,<sup>[41,42]</sup>

$$\text{SNR} \propto \frac{\mathbf{B}_1}{i} \frac{V_S \omega_0^2}{\sqrt{R_n}}. \quad (1.16)$$

Hoult and Richards have established the *principle of reciprocity* for NMR detectors, which states that the induced signal into a coil is directly proportional to a generated  $\mathbf{B}_1$  field of the coil per unit current. In this context, the coil sensitivity can be described as  $\mathbf{B}_1 \cdot i^{-1}$ , the magnetic flux density per unit current.

In high frequency applications, the skin effect dominates the direct current (DC) resistance of the coil conductor and degrades the achievable SNR. Through the skin effect, the resistance of the conductor is proportional to the square-root of the frequency and the current density decreases exponentially from the surface of the conductor to the centre.

A miniaturised NMR coil enhances the sensitivity of the magnetic field by increasing the induced voltage per mass unit when compared to a larger

coil.<sup>[43,44]</sup> Over the past decades, the methods have been optimised to achieve higher resolutions and to extract localised chemical information.<sup>[45–47]</sup> With micro coils, elementary studies can be performed on samples as small as individual cells.<sup>[48]</sup> For the first time, Aguayo *et al*<sup>[49]</sup> recorded images of a toad ova that had a diameter of approximately 1 mm at an imaging resolution of  $10 \times 13 \times 250 \mu\text{m}$ .

Different micro coil configurations applicable for studies in the field of magnetic resonance microscopy (MRM) are outlined in the following.

**Solenoids:** Solenoid micro detectors are one of the most popular geometries and can achieve a high filling factor, ideal for volume-limited samples. The limit of detection can be reduced to  $10^{15}$  nuclear spins.<sup>[40]</sup> Micro solenoids can be wound around a glass capillary tube, while providing an excellent signal to noise ratio for detecting sample volumes below  $1 \cdot 10^{-4} \mu\text{L}$ .<sup>[50,51]</sup> A solenoid has to be oriented perpendicular to the  $\mathbf{B}_0$  field, which causes a field distortion in the intrinsic RF centre. Solenoid micro coils have been immersed into susceptibility matching liquid, that significantly improved the spectral line-width resulting in a central peak to a full width at half maximum (FWHM) of 0.6 Hz.<sup>[52]</sup> A limiting factor of hand wound solenoids is the elaborate craftsmanship and therefore automated manufacturing processes were introduced to enhance the reproducibility using an automated wire bonder.<sup>[53]</sup> Another significant limitation of a micro solenoids with sub-millimetre dimensions appear to be the inherent difficulties associated with accurate sample positioning. Consequently, previous research focused on the development of micro coil with an integrated fluidic sample delivery system.<sup>[54]</sup> McDonnell *et al*<sup>[55]</sup> combined in his measurement setup a larger, commercial RF coil and a detection only micro coil. Such methods retain the  $\mathbf{B}_1$  homogeneity of a larger RF coil with the added sensitivity of a micro solenoid.

**Helmholtz coils:** In contrast, miniaturised *Helmholtz* detectors were developed that offer superior  $\mathbf{B}_1$  field homogeneity and allows a more

flexible specimen positioning. More recently, a miniaturised *Helmholtz coil* was reported by Spengler *et al.*,<sup>[56]</sup> which showed a high spectral sensitivity, as there were fewer jumps in magnetic susceptibility near the site of detection. However, the outlined design made use of two glass substrates bi-plates to build up the coils onto, and consequently, substrates required extensively more volume than the sample itself.

**Saddle coils:** Similar to a *Helmholtz coil* design, the saddle coil topology allows an alignment parallel to the  $B_0$  direction. The saddle geometry moreover fits ideally into a vertical bore magnet system and does not cause unlike the solenoid large susceptibility jumps. One particular advantage of a saddle coil is the relatively large sample space and the homogeneous RF centre that yields in a high spectral resolution. Wang *et al.*<sup>[57]</sup> fabricated a saddle-geometry micro detector on a flexible substrate, which was rolled around a 620  $\mu\text{m}$  glass capillary. The utilised polyimide substrate had a thickness of 25  $\mu\text{m}$ , and consumed considerably less space than micro detectors based on glass or silicon wafers. Wang utilised his rolled-up micro coil in NMR spectroscopy and imaging experiments. Wang's detector is well suited for combining it with the micro gradient design of this work.

**Planar coils:** A fourth type of micro coil topology that can be manufactured with the aid of photo lithography is the planar coil geometry.<sup>[41,58,59]</sup> Watzlaw *et al.*<sup>[60]</sup> presented a planar micro coil composed of four stacked single layers based on a polyimide substrate with a total DC resistance of  $9.5\ \Omega$  with a homogeneous region of  $2\ \text{mm} \times 2\ \text{mm}$ . Massin *et al.*<sup>[61]</sup> presented a planar NMR micro coil with an inner diameter of 500  $\mu\text{m}$  based on an electroplating process. Leidich *et al.*<sup>[62]</sup> stacked two planar type coils similar to a *Helmholtz* arrangement. A glass capillary served as a sample container which was inserted through a deep reactive-ion etched bore through the centre of the detector coils. More recently, rectangular planar micro coils have been co-integrated with the low-noise amplifier

(LNA) on-chip using the same complementary metal oxide semiconductor (CMOS) fabrication for the entire detector.<sup>[63]</sup>

In certain applications, RF coil designs, which are arranged orthogonal to  $\mathbf{B}_0$ , allow an easier integration into the range of magnets or gradient coil arrangements. Alfonsetti *et al*,<sup>[64]</sup> constructed a butterfly coil, which is particularly suitable when installation restrictions occur mainly in the  $\mathbf{B}_0$  or z-direction due to a compact permanent magnet configuration.<sup>[65]</sup> The butterfly is also of significant relevance for implementing it into the subjected gradient systems of this thesis. Much similar in geometry, the volume microstrip RF coil by Jasiński *et al*<sup>[42]</sup> has a similar bi-planar geometry and used in MRI microscopy to investigation flat samples at a high SNR.

Much similar to phased arrays in radar technology, multiple NMR micro coils can be arranged in an array to increase the FOV<sup>[66]</sup> or to enhance sample throughput. A miniaturised phased array consisting of seven micro coils was presented, providing a flat sensitive area applicable for spectroscopy and MRI.<sup>[67]</sup>

### 1.4.2 Field gradients for magnetic resonance microscopy

The term nuclear magnetic resonance microscopy (MRM) can be distinguished from the conventional MRI in having pixel resolutions smaller than  $100\ \mu\text{m}$ .<sup>[11]</sup> Especially the resolution of MRM experiments take particular advantage when stronger magnetic field gradients are available and when gradients can be switched rapidly at a high slew-rate, the rate of change of the gradient amplitude ( $\text{T m}^{-1} \text{s}^{-1}$ ).<sup>[68]</sup> To compensate for magnetic susceptibility effects, it is possible to use magnetic field gradients that are strong enough to dominate susceptibility-induced field variations.<sup>[69]</sup>

The *Biot-Savart law* is the primary tool for designing magnetic gradient coils. The magnetic field for a given conductor with volume  $V$ , generated by a constant electric current is calculated by,

$$\mathbf{B}(\mathbf{r}) = \frac{\mu_0}{4\pi} \int_V \frac{(\mathbf{r} - \mathbf{r}') \times \mathbf{J}(\mathbf{r}')}{\|\mathbf{r} - \mathbf{r}'\|^3} dV' \quad (1.17)$$

where  $\mathbf{B}(\mathbf{r})$  is the magnetic induction vector at point  $\mathbf{r}$ ,  $\mathbf{J}(\mathbf{r}')$  is the current density at the source point  $\mathbf{r}'$  and  $\mu_0$  is the magnetic permeability of free space. In the design process, only the z-component of the magnetic field vector is considered. The resulting x- and y-components do not bias the main magnetic field  $\mathbf{B}_0$  and can therefore be neglected.

Gradient coils aligned on a cylinder have proven themselves in MRI to effectively utilise the available space in a circular magnet bore. Especially for high-field human-body systems with a field strength  $\mathbf{B}_0 \geq 3$  T, the available space needs to be preserved for the patient. Doty<sup>[70]</sup> had addressed the major design challenges and constraints for small-animal cylindrical gradient systems. Gradient coil optimisations are generally performed on the aspects of linearity, resistance/power, the maximum achievable gradient gain and the inductance. The self-inductance of a conductor is generally given by,

$$L = \frac{\mu_0}{4\pi I^2} \int_V \int_V \frac{\mathbf{J}(\mathbf{r}) \cdot \mathbf{J}(\mathbf{r}')}{\|\mathbf{r} - \mathbf{r}'\|} dV' dV, \quad (1.18)$$

where  $V$  is the volume of the conductor and  $I$  is the total current with respect to the volumetric current density  $\mathbf{J}(\mathbf{r})$ .

The field homogeneity  $\delta_V$  of a field gradient is of concern and is often calculated for the respective volume of interest  $V_{VOI}$ ,<sup>[71]</sup>

$$\sqrt{\delta_V} = \sqrt{\frac{1}{V_{VOI}} \int_V \left( \frac{\mathbf{B}_{\text{achieved}}}{\mathbf{B}_{\text{desired}}} - 1 \right)^2 dV_{VOI}}. \quad (1.19)$$

When comparing the induced  $\mathbf{B}_{\text{achieved}}$  with an ideal, linear field variation  $\mathbf{B}_{\text{desired}}$ , one can consider the terms homogeneity and linearity as equivalent, which is often found in the literature.

When gradients are switched rapidly, eddy currents are induced in the surrounding conducting materials and produce time-dependent fields or added field variations, lowering the gradient amplitude.<sup>[72]</sup> Shielding is another requirement to minimise external interactions, especially with the superconducting magnet.<sup>[73,74]</sup> Active shield coils are designed complementary with the gradient coil, in order to cancel the field outside the gradient coil.<sup>[75]</sup> However, shielding is typically not required if the distance of the magnet bore diameter to the gradient coil is twice as large.<sup>[70,76]</sup>

Even before the actual MRI technique was explored, the beginning in the gradient development was established by Weston Anderson<sup>[77]</sup> and much similar by Zupancic *et al.*<sup>[78,79]</sup> Both research groups introduced field correcting coils, that are also called *shim coils*, to adjust inhomogeneities in the main magnetic field. For NMR spectroscopy, it is a prerequisite to apply an almost homogeneous  $\mathbf{B}_0$  field and, consequently, field inhomogeneities of higher orders must be corrected. An inhomogeneous  $\mathbf{B}_0$  causes spectral broadening, and without field correcting coils, it is highly difficult and even not possible to produce an almost homogeneous  $\mathbf{B}_0$  field. Anderson reported a variety of field coils for different orders, on the basis of long straight tracks or circular conductors. The significant innovations of Anderson's *shim coils* were the simple coil topologies, which are straightforward for realisation.

Table 1.1 illustrates the Anderson quadrupole z-gradient, and next to it the y-gradient composed out of four conductors. For the same  $z_0$  separation, the y-gradient is more effective than the z-variant. The conductor positions are arranged symmetrically with respect to the illustrated plane, such that higher-order field derivatives cancel out in the centre. Wire configurations with a current direction in symmetry with respect to origin ( $I_x [y, \pm z] = -I_x [-y, \mp z]$ ) lead to a linear z-gradient, since all terms  $\partial^n \mathbf{B}_z / \partial y^n$  and also terms  $\partial^m \mathbf{B}_z / \partial z^m$

	linear z-gradient (longitudinal)	linear y-gradient (transversal)
coil model		
gradient efficiency	$\mathbf{G}_{z,\max} = \frac{\mu_0 I_x}{\pi z_0^2}$ $\approx 0.318 \frac{\mu_0 I_x}{z_0^2}. \quad (1.20)$	$\mathbf{G}_{y,\max} = \frac{-2 \cdot \left( (\sqrt{2} - 1)^2 - 1 \right)}{\pi \left( (\sqrt{2} - 1)^2 + 1 \right)^2} \frac{\mu_0 I_x}{z_0^2}$ $\approx 0.384 \frac{\mu_0 I_x}{z_0^2}. \quad (1.21)$
gradient homogeneity		

**Table 1.1:** Anderson’s electrical current shims in a linear y and z configuration based on indefinitely long conductors.<sup>[77]</sup> The gradient efficiency scale the maximum achievable gradient strength with respect to  $z_0$  separation.

with an even value of  $m$  vanish in the centre. If the current is of equal direction by symmetry, ( $I_x[y, \pm z] = I_x[-y, \pm z]$ ) a linear y-gradient is produced. In this configuration,  $\partial^m \mathbf{B}_z / \partial z^m$  derivatives vanish by symmetry and derivatives  $\partial^n \mathbf{B}_z / \partial y^n$  with an odd  $n$  have to be considered.<sup>[77]</sup>

According to Equation (1.19), contour plots of the gradient homogeneity are one way to represent the local gradient field error with respect to the available sample volume.<sup>[80]</sup> The plots in Table 1.1 provide an intuitive visualisation of the achieved field accuracy.

A wide range of tri-axial gradient systems found in the literature were composed out of a combination of different coil topologies. Table 1.2 gives a summary on the performance parameters for a selection of MRM gradient systems.

For cylindrical gradient assemblies, it can be shown in Figure 1.4(a) that the gradient efficiency scales by square while the inner diameter reduces. Larger coils or coils with many windings possess a higher inductance, but low inductance gradients consequently allow for faster switching. The gradient efficiency scales linearly with the number of coil windings  $n$ , but also the inductance scales by  $n^2$ . For the coils surveyed in here, there is no clear relationship in terms of the coil inductance with respect to the gradient strength per unit current.

Field gradients are not constantly switched on as the on-time is limited by the repetition rate  $T_R$ . The repetition rate is also governed by the  $T_1$  time as the longitudinal magnetisation needs to recover before repeating the pulse sequence. The achievable gradient amplitude is not mainly limited by the size or number of wire turns but by the acceptable temperature rise. The fraction of the period during which the gradient is active is often referred as the duty cycle. In practice, the duty cycle of each gradient is therefore much less than 2% of each acquisition cycle. For a selection of gradient coils Figure 1.5 illustrates the specified duty cycle.

	Model	Ref.	Gradient type	Grad. efficiency [T/(mA)]	linearity [%]	$\approx$ FOV [mm <sup>3</sup> ]	$L$ [ $\mu$ H]	$R$ [ $\Omega$ ]
(g)	Shtirberg <i>et al</i>	[81]	Cylindrical assembly, Golay.	1.75–4.66	(—)	(—)	1.75	0.55
(h)	Weiger <i>et al</i>	[82]	Anderson design, vertical orientation, multiple windings.	1.083	(—)	1	(—)	0.98
(i)	Seeber <i>et al</i>	[50]	$G_{x,y}$ Anderson design, $G_z$ Maxwell pair, horizontal orientation.	0.255	5	0.5	0.1	0.3
(j)	20-42T Doty	[70]	Cylindrical assembly.	0.125	5	6300	70	0.8
(k)	Tsuchiya <i>et al</i>	[83]	$G_{x,y}$ Anderson design, $G_z$ Maxwell pair, horizontal orientation.	0.063	(—)	1.5	1.5	0.52
(l)	Micro5 Bruker	[84]	Cylindrical assembly.	0.05	1.3	3050	18	0.18
(m)	26-40 Doty	[85]	Cylindrical assembly, wire wound Golay embedded into ceramic forms.	0.048	5	5600	37	1.4
(n)	Demyanenko <i>et al</i>	[86]	Stream-function coil design, vertical orientation, uni-planar.	0.037–0.041	5	4	(—)	0.15–0.6
(o)	24-40 Doty	[70]	Cylindrical assembly.	0.038	5	6900	21	0.8
(p)	50-72S Doty	[70]	Cylindrical assembly.	0.008	5	40 800	35	0.6
(q)	50-72W Doty	[70]	Cylindrical assembly.	0.007	5	56 700	42	0.6
(r)	66-98T Doty	[70]	Cylindrical assembly.	0.007	5	123 000	65	0.7
(s)	85-120W Doty	[70]	Cylindrical assembly.	0.004	5	287 000	130	0.6

(—) information not available.

**Table 1.2:** Operational parameters for a selection of tri-axial gradient setups that are sorted by the gradient efficiency. The listed data for reference [70] refers to the high-performance axis.

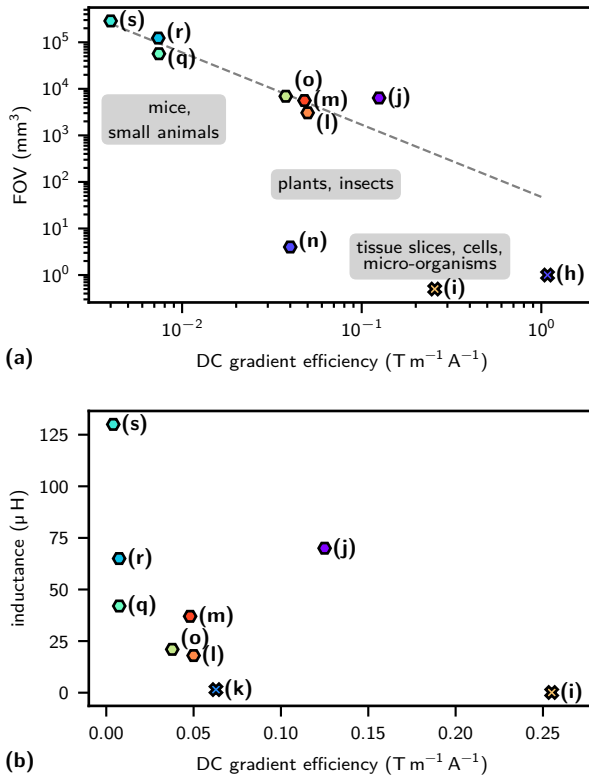


**Figure 1.4:** Field-of-view (a) and inductance (b) with respect to the achieved gradient efficiency from the selection in Table 1.2.

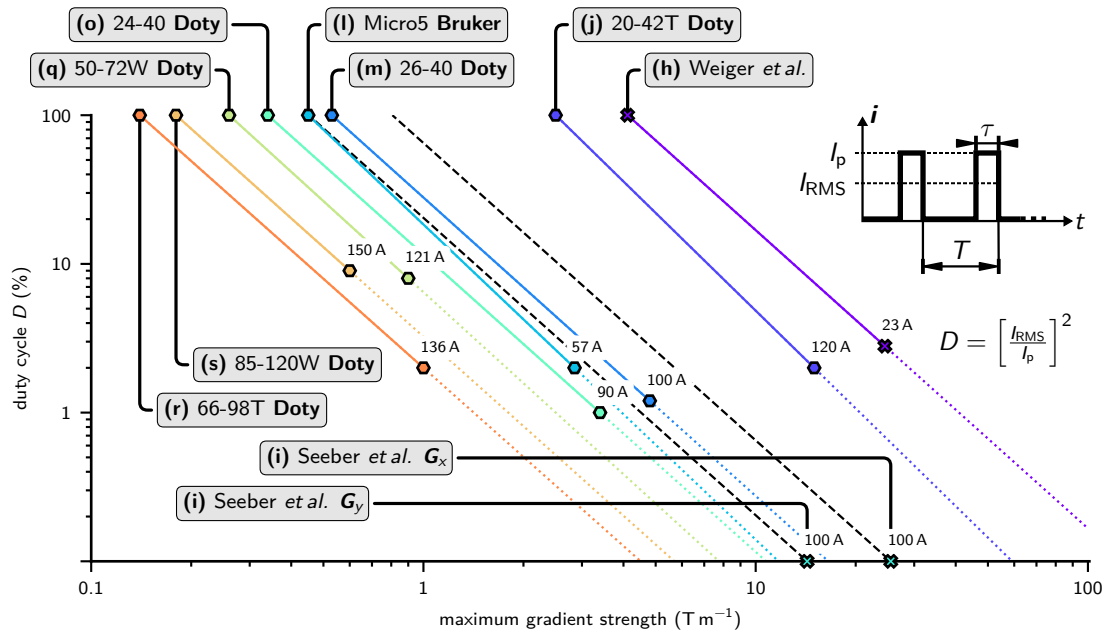


Figure 1.5: Comparison of the rated gradient strength for different gradient coils, used in MRM.

The following hardware review discusses the state-of-the-art progress, categorised with respect to the different gradient coil design topologies:

**Straight conductors:** Gradient coils based on straight conductors have been widely used for an imaging FOV of a few centimetres.<sup>[87]</sup> Such gradients were typically used to produce a linear field in the transversal direction and remain technologically relevant.<sup>[83,88]</sup> One of the first notable implementations was presented by Seeber *et al.*<sup>[50]</sup> He defined a support structure to wind 650  $\mu\text{m}$  thick copper strands for the  $x$ - and  $y$ -gradient coils according to the *Anderson* design (see Table 1.1). Seeber *et al* used a conventional, multi-winding anti-Helmholtz (*Maxwell*) coil pair for the  $z$ -gradient. Frollo *et al*<sup>[89]</sup> published a four wire extended version of an Anderson  $z$ -gradient, in which additional conductors were added to allow for a higher gradient strength and homogeneity.

Much similar to the Seeber design, Dodd *et al*<sup>[90]</sup> optimised a co-planar arranged gradient coil, by adding concentric return paths at calculated positions. The coil design also added shielding to minimise the exposed field. Such an approach allows for instance an installation into a smaller magnet bore.

Goloshevsky *et al*<sup>[91]</sup> structured a bi-axial Anderson design on a planar printed circuit board (PCB) substrate. The combined linear  $y$ - and  $z$ -gradient on both sides of a two layer PCB allowed to perform MR flow imaging. However, the relatively large distance of the PCB tracks to the sample and the weak current carrying capacity limited the achievable gradient strength.

Ellersiek *et al*<sup>[92]</sup> implemented an uni-planar bi-axial planar gradient system which was aligned in the same direction as  $\mathbf{B}_0$ . The two coils were defined on a 5  $\mu\text{m}$  thick polyimide substrate to minimise the thickness of the gradient set to be intentionally used with a permanent magnet. The  $x$ -gradient consisted of four rectangular loops made-up of 100  $\mu\text{m}$  wide and 25  $\mu\text{m}$  thick tracks.

Weiger *et al*<sup>[82]</sup> presented one of the strongest tri-axial imaging gradients which became commercially available. The high gradient field strength was achieved by multiple coil winding in combination with an active cooling system. Figure 1.5 illustrates the outstanding gradient efficiency compared to other gradient coil. However, no further information was provided about the fabrication principles of the active cooling system. Even though possible sample heat-up not be excluded at very high duty-cycles.

More recently, Sahebjavaher *et al*<sup>[93]</sup> presented another implementation much similar to the Seeber design. The authors focused on a micro manufacturing approach to define the conductors by using lithography and copper etching. The height of the bi-planar gradient system assembly was about 16 mm and allowed for the integration into a permanent magnet.

**Circular loops:** Uni-axial gradient coils have also been implemented by a set of axial aligned circular loops. Zhang *et al*<sup>[25]</sup> presented a circular z-gradient coil geometry with a gradient efficiency of more than  $4 \text{ T m}^{-1} \text{ A}^{-1}$ . The coil design was derived from a standard *Maxwell* coil pair. The publication presented one of the strongest uni-axial gradient configuration and proposed a gradient strength up to  $600 \text{ T m}^{-1}$ .

Much similar to Zhangs work, Bowtell *et al*<sup>[94]</sup> analysed the influence of the coil inductance and resistance with respect to the number of turns and fabricated a  $1.65 \text{ T m}^{-1} \text{ A}^{-1}$  strong uni-axial z-gradient coil, composed of 120 windings around a cylindrical substrate. For his linearity investigation, he used a phantom with alternating structures, inserted into a 5 mm NMR tube and recorded an one-dimensional profile.

Wright *et al*<sup>[95]</sup> constructed a linear z-gradient coil ( $1.3 \text{ T m}^{-1} \text{ A}^{-1}$ ) and combined it with commercial available x- and y-gradients. Tri-axial imaging was performed and an axial resolution of  $1 \mu\text{m}$  was achieved with the z-gradient utilised for phase encoding.

**Golay:** The *Golay* field coil design produces a transverse gradient, and it is similar in the geometry to a stack of two saddle coils. Much comparable to Anderson's approach, the *Golay* coil was also originally defined for homogenising the main magnetic field  $B_0$ .<sup>[96]</sup>

Bowtell *et al*.<sup>[69]</sup> constructed a MR microscope for a 11.7 T magnet, which achieved a resolution of  $4.5 \mu\text{m}^3 \times 4.5 \mu\text{m}^3 \times 100 \mu\text{m}^3$ . This high resolution was achieved by implementing modified, shielded *Golay* coils for transverse encoding at  $20 \text{ mT m}^{-1} \text{ A}^{-1}$  to  $23 \text{ mT m}^{-1} \text{ A}^{-1}$ . Besides NMR applications, gradients in the form of multi-turn *Golay* coils ( $1.75 \text{ T m}^{-1}$  to  $2.7 \text{ T m}^{-1}$ ) and a *Maxwell* coil pair ( $4.66 \text{ T m}^{-1}$ ) were employed in electron spin resonance (ESR) microscopy.<sup>[81,97]</sup> To maintain mechanical and thermal stability, the gradient coils were embedded in a thermally conductive adhesive with a thermal conductivity better than  $4 \text{ W m}^{-1} \text{ K}^{-1}$ . ESR benefits from very rapidly switchable gradients with relatively short on-times of  $0.2 \mu\text{s}$  to  $2 \mu\text{s}$  offering resolutions much below  $1 \mu\text{m}$ .<sup>[98]</sup>

**Target field:** One of the most successful gradient coil design techniques is probably Turner's *target field approach*.<sup>[99,100]</sup> The technique assumes a magnetic field on a defined geometry. With the approach the current densities  $J$  on a cylindrical surface with respect to a desired target field are computed. The method synthesises a field coil geometry by optimising for a minimum resulting field error. In fact, the symmetry conditions as derived by Anderson<sup>[77]</sup> also applies to numerically optimised gradient coils. Various research implemented further optimisations by addressing for instance a minimisation of the coil inductance,<sup>[101]</sup> a reduction of hot-spot temperatures<sup>[102]</sup> or an improved power dissipation.<sup>[103]</sup>

Beside Turner's approach, other methods facilitate the creation of coil patterns on arbitrary surfaces.<sup>[104,105]</sup> Demyanenko *et al*.<sup>[86]</sup> developed a new type of gradient probe based on the stream function method with an embedded RF coil and an uni-planar gradient coil. With the presented liquid cooled gradient set, it was possible to encode tomographic images

of 2 mm tissue slices. In contrast to a symmetric bi-planar design, the uni-planar probe suffers from weaker gradient strengths. However, such an open design with easy access to the sample is characterised by its high flexibility in terms of sample access and positioning.

Besides linear gradient encoding, non-linear concepts such as non-Cartesian curvilinear gradients (e.g., Patloc) are also worth mentioning.<sup>[106–108]</sup> Non-Cartesian gradient field arrangements require adapted encoding strategies. Since the FOV for miniaturised gradient setup only consists of just a few voxels, it is straight forward to use linear gradient encoding. In this work, linearity was a primary focus, since isotropic parameters using constant gradients can be mapped more intuitively.

Compact gradient coils have also been applied in tomographic magnetic particle imaging,<sup>[109,110]</sup> or to build up a magnetic navigation system to guide magnetic particles<sup>[111]</sup> or micro-robots.<sup>[112]</sup>

## 1.5 Thesis objectives

As an introduction to the subject matter of this thesis, an imaging unit with a hand-wound three-dimensional (3D) gradient system based on the Anderson design was constructed.<sup>[113]</sup> Figure 1.6 shows the opened probe with the two gradient half-plates and the electrical connectors to the probe base. When

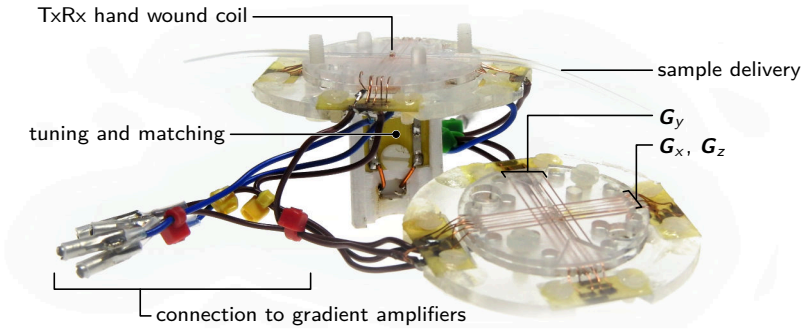


**Figure 1.6:** Openable macroscopic MR gradient probe. (Figure reproduced from [113])

compared to Seeber's implementation, it was possible to omit the  $\mathbf{G}_z$  Maxwell coil pair, by combining the x- and z-gradients onto the same bi-plane to conserve space. As a result, the number of gradient coil layers reduces to  $2 \times 2$  stacked layers to build up gradient system in all three axes. The alignment of the gradient conductors was achieved by laser cutting V-groves into the poly(methyl methacrylate) (PMMA) substrate. Further, the conductors were soldered individually to small PCBs attached at the edges of the PMMA. The rigid PMMA plates were interconnected and screwed to a 3D printed acrylonitrile butadiene styrene (ABS) part (MakerBot Replicator 2x), as shown in Figure 1.7(a).

For spin excitation and readout a solenoid micro-coil was wound around a 1.6 mm thick glass capillary (inner diameter (ID) of  $800 \mu\text{m}$ ). Figure 1.7(b) presents a microscope image of the top view of the gradient system with the

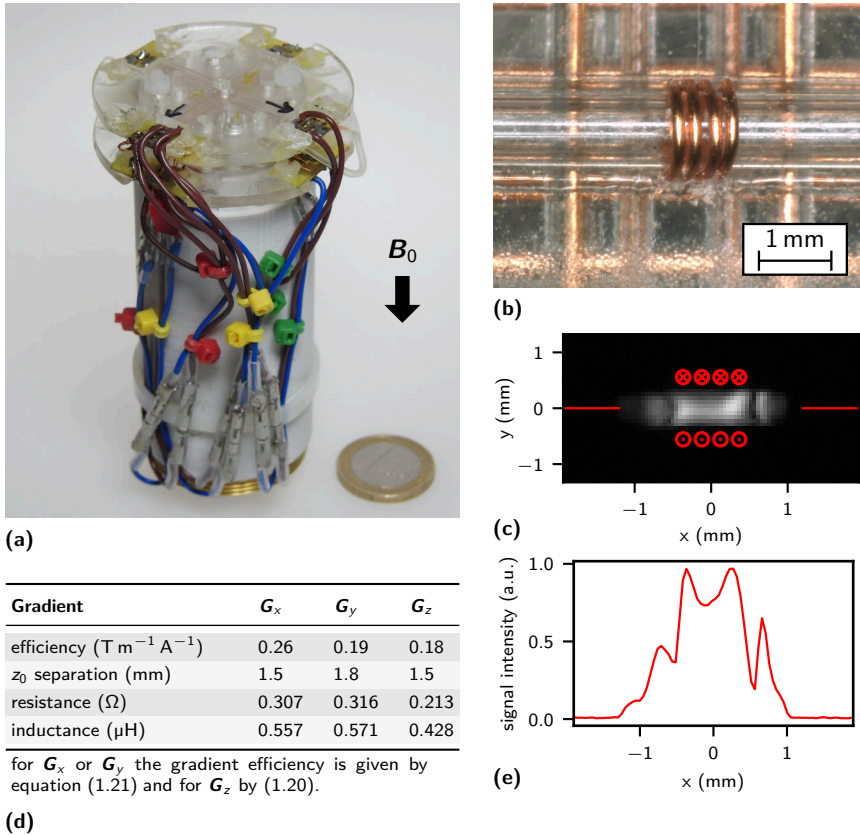


**Figure 1.7:** (a) the assembled probe. (b) close-up of the gradient conductors. (c) recorded MR image. (d) gradient coil parameters with the impedance measurement performed at 1 MHz (E4991A RF Impedance Analyzer, Agilent Technologies). (e) intensity profile extracted from the MR image in (c) at  $y = 0$ .

hand-wound receive coil. An MRI experiment in the transversal plane was performed, as illustrated in Figure 1.7(c). The reconstructed image shows a water sample inside the capillary. The image was acquired using a fast low angle shot (FLASH) sequence at an echo time ( $T_E$ ) of 2.5 ms, a repetition

time ( $T_R$ ) of 800 ms and a flip-angle ( $FA$ ) of  $40^\circ$ . Power adjustments were done by the spectrometer's software and the reference power adjustments were acquired automatically to raise the spin excitation. The gradient efficiencies, as summarised in Figure 1.7(d), were compared against the MRI image and match with the mathematical model, which is further described in Table 1.1.

Much similar as the Seeber design, the imaging device operated without a cooling system. Hence, the imaging was performed at short duty cycles to avoid excessive thermal load on the un-cooled gradient system. At higher duty cycles, the material failure occurred at the solder joints that possessed a significant higher electrical resistance than the copper conductors.

The purpose of the aforementioned experiment was to identify expectable limitations and to gain better insight into the topic. The following operational objectives are formulated for a micro-integrated gradient system:

**Gradient coil design.** Long, straight coil tracks can be easily defined on planar substrates. However, single layer coil designs based on the *target-field approach*<sup>[114]</sup> allow for a higher gradient efficiency. Such coils can be realised using flexible deposition techniques such as electroplating and can be easily replicated. With a suitable combination of different gradient design methods, a high-performance planar gradient system can be designed for a very confined microchip.

**Current load capacity.** With coil conductors being manufactured with an adequate electrical conductivity and thermal capacity, the gradient system remains stable even at elevated currents. The integration of an active cooling system allows long-term measurements to be carried out with short repetitions times, avoiding overheating of the gradient system and excessive heat transfer to the sample. The gradient chip is enhanced by a custom packaging concept to ensure that the electrical resistance of the connecting leads is as low as possible.

**Target FOV.** The range of the field-of-view (FOV) as a design parameter for the gradient system depends mainly on the dedicated sample object. The capability to study the well-known model organism *caenorhabditis elegans* (*c. elegans*)<sup>[115]</sup> spatially resolved with MR is a decisive aspect for the design of the gradient system. By a suitable coil design and manufacturing concept, the aim is to achieve an elongated FOV, suitable for such specimens. Thus, the gradient system provides a sufficient field accuracy and linearity to image an object like the *c. elegans* nematode. By the use of a micro fabricated phantom with suitable test structures, the field accuracy can be validated.

**RF coil integration.** To perform the NMR experiment, an RF coil with its resonance tuned to the *Larmor frequency* of the respective isotope is required. The Tx/Rx coil generates the spin-flip of the  $^1\text{H}$  isotopes and records the spin relaxation of the decaying signal, the so called FID. In a human MRI scanner, the gradient and the RF coils are tailored in such a way that they allow for the most compact magnetic bore possible, but also to provide sufficient room for the patient. A similar arrangement of the components is pursued here. This requires the RF coil design and stack-up to be as large as the sample itself.

## 1.6 Thesis outline

The work is structured according to the following systematic approach:

**This chapter** introduces the fundamentals and applications of NMR and MRI. Then, the state-of-the-art NMR detection hardware and different field gradient setups are described and put into comparison.

**Chapter 2** shows the evaluation of the patterning techniques with a focus on the implementation of the micro gradient. Different resist materials, and in particular dry film resists (DFRs) are discussed. An electrodeposition

setup for the copper deposition to form the gradient conductors is described.

**In Chapter 3**, the manufacturing techniques were applied to implement a rectangular microcoil using a maskless lithography process. Presenting a self-aligned, mask-free micro-fabrication technique for creating thick-layered conductive metal micro-structures within electroplating moulds.

**Chapter 4** describes the chip and coil design of the uni-axial and the tri-axial field gradients. A liquid cooling network and a compact RF detection coil were incorporated into the design.

**In Chapter 5**, the manufacturing process of the bi-planar arranged gradient chips is outlined.

**Chapter 6** discusses the physical characteristics, electrical performance, and thermal properties of the fabricated micro gradient coils.

**In Chapter 7**, several NMR spectroscopy and imaging experiments are presented, showcasing the potential applications of the fabricated microcoils, and an investigation of the linearity of the uni-axial micro gradient is presented.

## 2 Microfabrication

To further reduce the overall dimensions of a gradient system, new manufacturing techniques were derived to achieve a higher degree of miniaturisation and integration. Within the past decades, the fabrication of micro electro mechanical systems (MEMS) devices has evolved, especially by the use of photo lithography to accurately define micro features. MEMS fabrication and replication techniques opened up several possibilities to integrate microelectronic, micromechanic and microfluidic components on a single microchip. Such integrated devices are generally built-up on planar substrates by applying multi-layer structuring. The fabrication techniques underlie a procedural layout description and demand a reliable, repeatable and precise process control.

With the introduction of the LIGA process (lithography, electroplating, and moulding *German acronym for: Lithographie Galvanoformung, Abformung*) in the early 1980s, it was first possible to pattern micro structures with an aspect ratio of up to 50.<sup>[116,117]</sup> However, LIGA relies on expensive synchrotron radiation, which materially restricts its general use. In applications with lower requirements on the aspect ratio and height, LIGA has been replaced by the more cost-effective “UV-LIGA”. The structuring techniques presented here were predominantly based on such UV-lithography. Section 2.1 of this chapter discusses a selection of UV photo-polymers and their process specific and mutual compatibility when targeting multi-layer buildups.

Lift-off has become the primary technique to structure metallic thin films at a sub-micron precision.<sup>[118]</sup> The gold standard for depositing thin, planar metal layers is physical vapour deposition (PVD). However, PVD relies on

time-consuming, high-vacuum processing, that requires pressures below of  $10^{-5}$  mbar. If the PVD is performed on existing polymer structures, thermal stability becomes an important issue, especially when the PVD is repeated on multiple layers. In contrary to PVD, metal nano-particle ink-jet printing has become an alternative patterning technique to define electrically conductive micro structures without the need of vacuum processing. [119,120] Nano-particle ink-jet printing on pre-cured ORDYL<sup>®</sup> SY or SU-8 polymers is presented in Section 2.2.

Electroplating was employed to structure metals into a mould master. In many applications, a PVD thin films act as the plating base to start the electroplating. In here, Cu electroplating was used to increase the electrical conductivity of ink-jet printed silver tracks. A self-constructed setup was prepared for parallel electroplating [121] that is further described in Section 2.3.

## 2.1 Materials

With respect to the coil structuring of the micro gradient, it was focused on negative tone photoresists. Negative resists are typically developed in organic solvents, by solving the unexposed, not cross-linked resist. [122] Accordingly, cross-linked negative type resists possess a high chemical stability towards a variety of organic solvents. Since only negative tone resists were employed, it was not necessary to create inverted lithographic masks, which also facilitated testing of different processing techniques.

### SU-8

Epoxy-based SU-8 resin offers a high transmission in the near UV range. [123] The excellent low optical loss of SU-8 EPON epoxy allows for an exposure, even through thick layers, thus creating almost vertical sidewall profiles. The outstanding properties of the SU-8 resist ranges down to nano patterning. [124]

SU-8 shows strong adhesion on various metallic surfaces and substrates.<sup>[125]</sup> Enhanced adhesion is promoted by a dry, dehydrated, plasma-cleaned substrate. The adhesion of SU-8 towards glass can be generally improved by using adhesion promoters such as Omnicoat (MicroChem, USA) or Ti-prime (MicroChemicals GmbH).<sup>[126,127]</sup>

The removal of highly cross-linked SU-8 epoxy using physical and chemical methods is difficult and mainly requires temperatures above 200 °C.<sup>[128]</sup> Wet chemical stripping of the SU-8 without harming, e.g., electroplated metal micro-features is almost impossible.

When processing SU-8, especially after the post exposure bake (PEB), mechanical stress may occur between the substrate and the resist layer.<sup>[129]</sup> Such stress effects inevitably increase with the thickness of the resist, and become more dramatic for film thicknesses larger than 100 µm. Due to the coefficient of thermal expansion (CTE) mismatch between the substrate and resist, rapid temperature changes may induce a curvature into the substrate.<sup>[130]</sup> Specifically, rapid temperature gradients while lowering from the PEB to room temperature cause such a substrate bow to evolve. Limiting the PEB temperature is another effective countermeasure to reduce substrate bending.<sup>[131]</sup> In various observations, substrate deflections were also effectively reduced by minimising the cross-linked SU-8 surface area on the wafer.

There are a number of different SU-8 compounds containing different solvents used in adjusted concentrations.<sup>[132]</sup> The SU-8 product, that was used throughout this thesis was SU-8 3000 series (MicroChem, Westborough, MA). Its solvent concentration exhibits lower film stress, while providing enhanced adhesion on borosilicate glass such as Borofloat 33 (SCHOTT Malaysia). Multi-layer processing of SU-8 allows to define micro-fluidic channel networks.<sup>[133,134]</sup> SU-8 films can be successively stacked to structure several layers by applying the SU-8 resist only temporarily on a support polyimide film.<sup>[135]</sup>

In a cross-disciplinary side-project within the scope of this thesis, a SU-8 film was used to measure the near-field light perturbation of *Synechocystis cells*.<sup>[136]</sup> A high resolution imprint of the light pattern adjacent to a single cell was replicated into the resist. Figure 2.1(a) shows a schematic illustration of the executed photolithography.

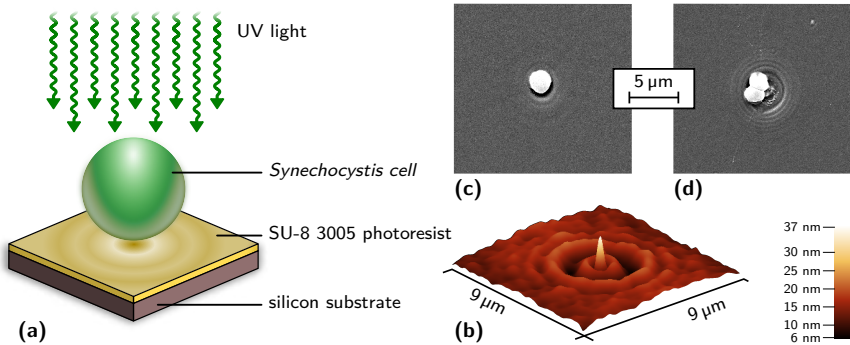


**Figure 2.1:** (a) photolithography to imprint the light pattern of a *Synechocystis cell*. (b) height profile reconstructed from an AFM image. (c),(d) scanning electron microscope (SEM) images of cells which remained attached after development. (Figure adapted from [136])

Therefore, SU-8 3005 was coated at a final rotation speed of 4000 rpm on a pre-cleaned silicon wafer. The photosensitive film was subjected to a soft bake at 95 °C for 5 h. Droplets (4 mL) of an exponentially growing *Synechocystis* culture in BG11 medium were dispensed on top of the 5 μm thick photo resist.<sup>[136]</sup> After letting the buffer medium evaporate, the *Synechocystis cells* remained separated, but also in cell clusters on top of the wafer. Sharp rendering of the scattering patterns into the SU-8 film was achieved by performing a lithographic series at the characteristic wavelength of 356 nm using *i-line* filtering. The optimal dose for the flood exposure was 85 mJ cm<sup>-2</sup>.

Although during the wet development, the cells were mostly flushed away using the standard propylene glycol methyl ether acetate, 1-methoxy-2-propanol

acetate (PGMEA) SU-8 developer. Figure 2.1(c) and Figure 2.1(d) illustrates cells that were still attached to the wafer after SU-8 development. The reflective surface of the silicon wafer was crucial to achieve the sufficient adhesion of the resist at such a moderately low exposure dose. It was not feasible to select a transparent glass substrate for this experiment.

After post-lithography processing, height profiles of the scattering pattern were obtained by an atomic/scanning force microscope (AFM) measurement in tapping-mode (Dimension Icon, Bruker, CA, USA). The exposed SU-8 had a median surface roughness  $R_a$  of 3.2 nm which is consistent with values found in the literature.<sup>[137,138]</sup> The SU-8 layer rendered a height-dependent cross-linked structure similar to grayscale lithography.<sup>[139]</sup> The *Synechocystis cells* produced distinctive near-field optical scattering patterns on the polymer surface, as shown in Figure 2.1(b).<sup>[136]</sup> Dominant is a remarkably sharp and intense peak or nano-jet beneath the centre of each cell. From the scattering pattern in Figure 2.1(b), the mean of six axially-symmetric profiles was computed in order to average out the noise of the surface roughness. A FWHM of  $281 \pm 33$  nm (mean and standard deviation) was calculated from these profiles at different angles. The width of the peak indicates that the near-UV light is focused to a spot with a diameter less than the wavelength.<sup>[136]</sup>

The here performed experiment demonstrated the more than sufficient, high sensitivity nano-structuring possibilities of the SU-8, capable to precisely define MR field coils at a micro precision.

## **SUEX and ADEX**

SUEX/ADEX are thick epoxy DFR sheets for the fabrication of MEMS components. These DFRs were purchased in pre-cut sheets with the exact size of the wafer, and thus offer a more resource saving alternative to the wet applied resists. The resist consumption of wet applied SU-8 resist is almost 10 times

higher. SUEX is manufactured by a solvent-free process to maintain uniformity during resist processing.<sup>[140,141]</sup>

SUEX and ADEX are applied by hot-roll or vacuum lamination. The experiments performed in this thesis showed process compatibility between SU-8 and SUEX/ADEX with strong inter-layer adhesion, much comparable to the fabrication performed by Meier *et al*.<sup>[142]</sup> who successfully applied a combination of SU-8 and PerMX 3050<sup>[143]</sup> resists.

When sputtering a combination of metal layers on-top of each another, the substrate and an underlying lift-off resist layer can reach temperatures above 180 °C.<sup>[144]</sup> To validate the stability of the SUEX fabric under thermal load, a combined differential scanning calorimetry (DSC) and thermogravimetry (TG) measurement was performed as shown in Figure 2.2. The temperature

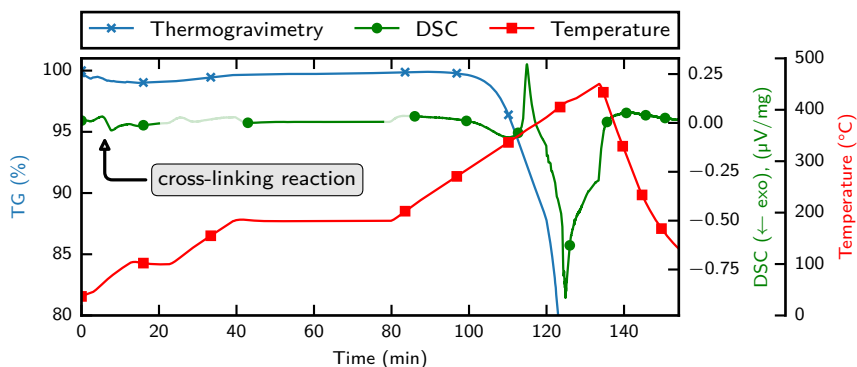


**Figure 2.2:** DSC and TG scans from a 2 mm thick SUEX DFR. The measurement was carried out using a NETZSCH STA 449 C (Netzsch-Gerätebau GmbH) with respect to an  $\text{Al}_2\text{O}_3$  reference crucible under ambient atmosphere. Data with measurement uncertainty were masked out.

ramp in the diagram was chosen to closely match a real temperature cycle during an excessive PVD step. The DSC shows an exothermic peak at around 55 °C to 65 °C which indicates the cross-linking reaction. The necessary resist

crosslinking temperature after UV-exposure is much comparable to the wet applied SU-8.<sup>[145,146]</sup>

After the resist was baked at 95 °C for 10 min to perform the recommended PEB, the temperature was increased to 180 °C and kept for 40 min. The DSC remained unchanged during this isothermal period.

In terms of the thermal stability, the TG measurement is of greater interest. No significant weight loss was measured by the TG at temperatures between 100 °C to 300 °C. This makes SUEX a suitable candidate to be coated with a conductive metal layer by PVD in order to further build up electroplated structures.

### **ORDYL® SY series**

Another popular negative-tone dry film resist (DFR) is ORDYL® SY, which was mainly used in the field of micro fluidics,<sup>[147,148]</sup> to perform adhesive wafer bonding.<sup>[56,148,149]</sup> Vulto *et al*<sup>[150]</sup> examined the chemical stability of the ORDYL® SY on a fluidic chip. Although, the exact composition of ORDYL® SY was not published, it consists of a major amount of acrylic polymer of approximately 40 % to 60 %. With the applied ORDYL® SY on a glass substrate, Vulto performed Ag electroplating for layering up pre-structured electrodes.

Huesgen *et al*<sup>[151]</sup> optimised the processing conditions of the acrylic laminate and performed multi-wafer adhesive bonding to define 3D MEMS. A substrate bond of *glass—ORDYL® SY—glass* can be carried out in the range of 80 °C to 120 °C. Huesgen performed a subsequent post-bake at 150 °C for 2 h, to ensure curing and thus, to achieve an enhanced bond strength. In terms of substrate adhesion, ORDYL® SY is more robust towards rapid temperature changes than the SU-8 or the SUEX.

Within the scope of this thesis, processing possibilities were investigated to deposit a conductive electroplating seed on top of pre-cured ORDYL® SY. Since

there was no literature available that described the details of the cross-linking process and stability of ORDYL<sup>®</sup> SY, first, a combined DSC-TG analysis was performed, as shown in Figure 2.3.

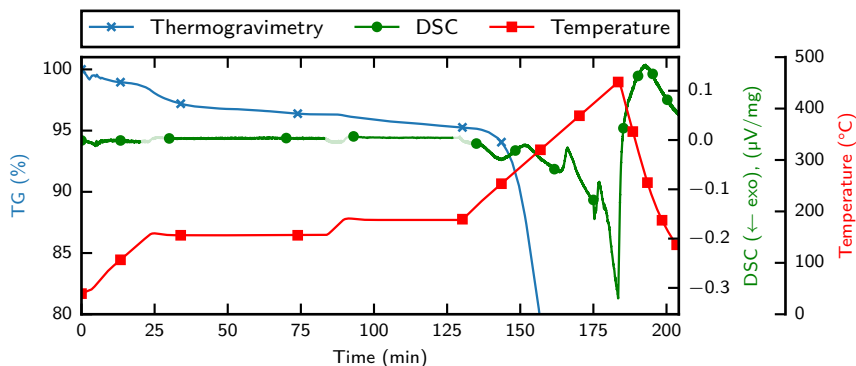


**Figure 2.3:** Combined TG and DSC of flood exposed ORDYL<sup>®</sup> SY with thermal ramps to investigate the thermal behaviour for evaluating PVD compatibility. The conditions were similar to those in the experiment in Figure 2.2.

Polymer cross-linkage would appear as a variation of the heat flux. Within the respective temperature range, no indication of cross-linking appeared in the DSC curve. With the utilised instrument, it was not possible to prove the results of Huesgen *et al.* [151] Although, one can see the significant exothermic reaction for the SUEX as shown in Figure 2.2 on page 42. In fact, the dynamic resolution of the available instrument was also limited. During the decomposition of the ORDYL<sup>®</sup> SY, the multiple peaks in the DSC curve indicate a higher diversity of compounds when compared to the SUEX experiment.

After a conventional resist application, the DFR exhibited extended vapour evolution when baking it at elevated temperatures above 140 °C. The mass change through out-gassing was also observed by the DSC-TG measurement. The progressive loss of material for temperatures above 120 °C indicates the out-gassing of the volatile components. Considering the time-resolved TG curve, one can detect a mass loss of 3% to 5% after 2 h of heat-up. The observed

characteristics also revealed the incompatibility with other DFR coatings such as SUEX and SU-8, e.g., in terms of long-term bonding stability between different resist layers. The proposed compatibility as published by Paul *et al*<sup>[152]</sup> could not be endorsed.

Nevertheless, the metal deposition of WTi/Pt (10 nm / 80 nm) and also of Cr/Cu (5 nm / 100 nm) was carried out on top of a ORDYL<sup>®</sup> SY 355 layer. Prior to the deposition, the wafers were flood exposed and baked for 5 h at 150 °C. Figure 2.4 illustrates the metallisation attempts of the final formation of both deposited films. For both of the two experiments, no adequate conductivity

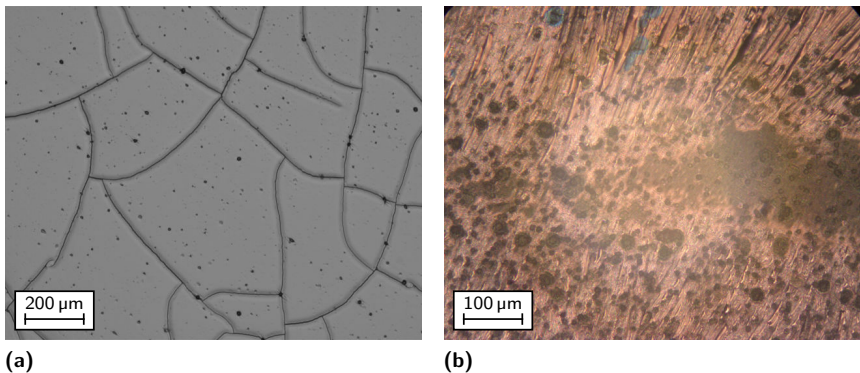


**Figure 2.4:** (a) sputtering of WTi/Pt caused the formation of islands that were not interconnected. (b) metal evaporation of Cr/Cu resulted in an unstable metallic film that peeled off.

over the entire film was measured. In spite of the high temperature during PVD processing, it was feasible to apply conductive metal tracks by ink-jet printing, which is further described in Section 2.2.

To determine the appropriate lithography parameters for the ORDYL<sup>®</sup> SY, exposure tests were carried out, as shown in Figure 2.5. For testing the patterning, the ORDYL<sup>®</sup> SY was hot-roll laminated on a glass substrate and exposed at a peak wave length of 365 nm with an exposure energy of 9 mW cm<sup>-2</sup> using

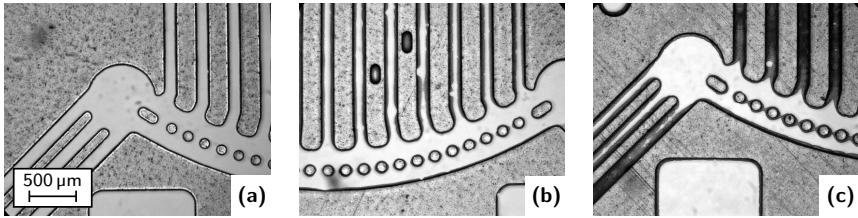


**Figure 2.5:** Exposure tests with the respective exposure times using a foil lithographic mask. (a) 16 s for ORDYL<sup>®</sup> SY 355. (b) 18 s for ORDYL<sup>®</sup> SY 355. (c) 18 s for ORDYL<sup>®</sup> SY 390.

standard front-side (FS) lithography. Even a slight over-exposure lead to the formation of a fine resist-skin within fluidic channels. In particular for the 90 μm thick ORDYL<sup>®</sup> SY 390, such an over-exposure cannot be avoided since adequate adhesion had to be maintained towards the glass. In terms of the achievable structuring resolution, ORDYL<sup>®</sup> SY is clearly inferior to SU-8. This is due to photo diffusion and the opacity of the ORDYL<sup>®</sup> SY material. However, the described effects were successfully avoided by a back-side (BS) lithography, which is further described in Section 3.2.1.

### ma-N 1400 series

The novolac based non-permanent photosensitive ma-N 1400 resin (micro resist technology, Berlin) is applied by spin-coating on hexamethyldisilazane (HMDS) primed silicon or glass substrates. Prior to the HMDS treatment, it is important to turn the glass substrate hydrophilic by an oxygen plasma activation, to enhance the density of hydroxyl binding sites.<sup>[153]</sup> The resin shows high sensitivity towards *i-line* (356 nm) exposure. During wet development, an undercut profile can be achieved that allows for lift-off processing. Cross-linking of the resin and especially the resulting undercut depends on the photo speed, the intensity of the exposure, and development time.<sup>[154]</sup> ma-N 1400 is suitable for a variety of PVD depositions, especially within the W/Ti/Pt system.<sup>[144]</sup>

The resist can be stripped by organic solvents (isopropyl alcohol (IPA), acetone) or alkaline solutions.

During excessive thermal penetration within certain PVD processes, the temperature can reach up to 160 °C to 190 °C. In such scenarios, the resin can be thermally stabilised by a hard-bake to facilitate a clean lift-off. Such a hard-bake was omitted to avoid additional cross-linking. However, lower PVD temperatures were achieved by dividing the deposition into several steps with additional waiting times.

If the resin got extensively cross-linked, it was still possible to remove it by a dedicated stripper (mr-Rem 400 or mr-Rem 700, micro resist technology, Berlin). During stripping using the mr-Rem 700, the vapour deposited Cu seed layer was penetrated. The Cu layer solved more rapidly than the actual resin.

Within the scope of a multi-layer metal deposition process, it was tested to apply the ma-N 1400 on top of freestanding 250 µm high and 6 mm × 6 mm wide SU-8 plateaus. Therefore, a spin-coater with a bell-shaped cover was used (GYRSET®, SÜSS MicroTec, Germany). Such a processing tool reduces the air turbulence by the co-rotating cover. Spin coating with the cover keeps a solvent atmosphere that enhances the uniformity of the resist layer, and corner effects and comets are minimised. It was possible to apply ma-N 1420 on top of the SU-8 plateaus without a previous HMDS treatment.

After WTi/Pt sputtering, the lift-off in acetone and IPA was carried out and the result is shown in Figure 2.6(a). The resulting WTi/Pt track width was 40 µm, and small metal flakes remained attached to the track. During acetone stripping, the SU-8 layer and the edges of the sputtered track got slightly penetrated<sup>[155]</sup> and the resulting lift-off time was much greater than the standard of 50 s.

In contrast to the application by the GYRSET® based spin-coating, the ma-N 1410 resist was successfully ink-jet printed using a Dimatix material printer (DMP-2831, Dimatix-Fujifilm). For the very first attempt, a test patterns was printed by using a 1 pL cartridge which got accurately resolved as shown in

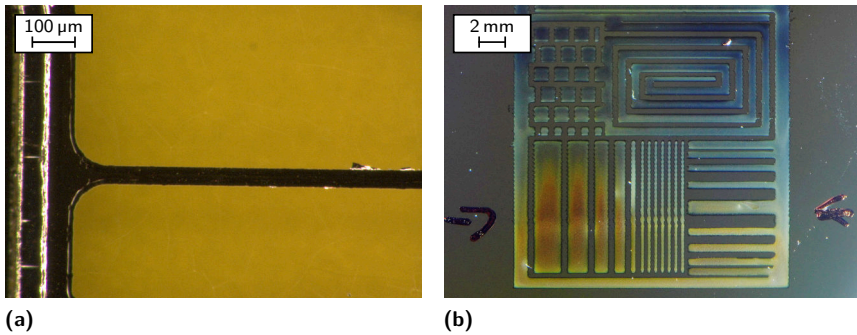


**Figure 2.6:** (a) lift-off on a cured SU-8 plateau. (b) ink-jet printed ma-N 1410 structures after soft-baking and flood exposure.

Figure 2.6(b). The pattern was printed on top of a Si wafer with minor adjustments to the standard jetting sequence. An acceptable height homogeneity of the printed plateaus was achieved, which ranged from 4.6 μm to 5.1 μm. Ink-jet printing of such lift-off resist is independent of the height of the predefined structures.

Due to the availability of the aforementioned equipment, it was focused on a whole-surface seed instead of lift-off based structuring for building up the multi-layer micro gradient. The ma-N 1400 was exclusively used for structuring the first metalised layer.

### **ORDYL® FP 450**

ORDYL® FP 450 is a non-permanent DFR dedicated for the production of printed circuit boards. It is similar in the resist application as the ORDYL® SY. The resist is available in a maximum thickness of 55 μm and does not require a PEB after lithographic structuring. Its chemical stability towards sulfuric acid allows it to define an electroplating mould for the deposition of Cu. For the development and stripping, only mild chemicals are needed, which extends its

compatibility towards other photo resist. The shape of the side walls show a tapered profile after the patterning, that also facilitates stripping of the resist. Multiple layers of ORDYL<sup>®</sup> FP 450 can be laminated on top of each other. The constraining factor is the loss of light transmission with respect to the thickness of the resist layer. Figure 2.7(a) shows the optical transmission for a variety of resist heights by successive lamination.

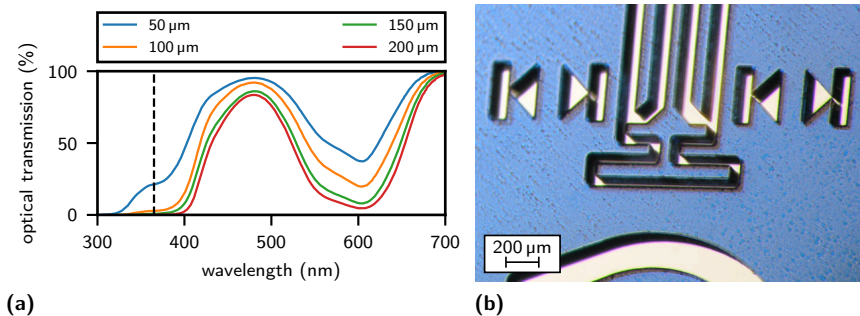


**Figure 2.7:** (a) ORDYL<sup>®</sup> FP 450 transmission behaviour for successive laminated resist layers. (b) test pattern of a double layer of ORDYL<sup>®</sup> FP 450 on a silicon substrate.

The transmission spectra was recorded for the ORDYL<sup>®</sup> FP 450 after flood exposure, measured using a Varian UV-VIS-NIR spectrophotometer. It was experimentally found that only a double resist layer with a thickness of approximately 100 μm could be exposed that finally provided sufficient adhesion to the substrate. As shown in Figure 2.7(b), structures of 85 μm in width were reliably resolved using inexpensive lithographic foil masks.

In a preliminary investigation, a Cr/Cu PVD layer was applied by vacuum evaporation on top of an exposed ORDYL<sup>®</sup> FP 450 layer. The resist showed compatibility towards its use as a sacrificial layer. It showed adequate adhesion and thermal stability to deposit a novel seed layers such as Cu or Au and in principle allowed for electrodeposition. It was possible to build-up a bridge structure above the first ORDYL<sup>®</sup> FP 450 layer by Cu electroplating. When it

came to resist removal, the ORDYL<sup>®</sup> FP 450 could not be stripped below the electroplated bridge structure using the conventional 3% NaOH. Wet stripping combined with plasma ashing could be feasible but was not tested.

## AZ 125 nXT

AZ 125 nXT serves for patterning a non-permanent electroplating template. Electroplated structures of up to 400  $\mu\text{m}$  can be achieved with this negative tone resist.<sup>[156,157]</sup> A precisely defined resist height is not decisive when applying the AZ 125 nXT, but it must be at least 10% higher than the targeted electroplating height. The AZ 125 nXT in combination with ORDYL<sup>®</sup> SY 390 was used for identifying a processing method to encapsulate electroplated micro coil structures as shown in Figure 2.8. In order to pattern cooling channels or structures in close proximity to a Cu micro-coil, resist bonding in combination with lithographic structuring was performed. The result of the process is shown in Figure 2.10.

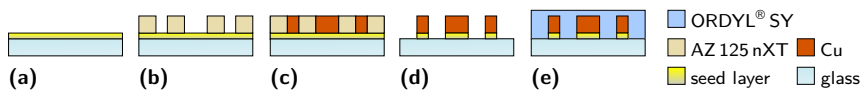


**Figure 2.8:** Embossing process for defining initial cooling structures into electroplated patterns. (a) seed layer deposition on a glass wafer. (b) AZ 125 nXT application. (c) Cu electroplating. (d) AZ 125 nXT and seed layer stripping. (e) DFR bonding and lithography.

First, the Cr/Au seed layer was deposited as shown in Figure 2.8(a). Approximately 6 mL of AZ 125 nXT resist was pipetted on the 4" wafer and the resist was spin coated dynamically. To achieve a target height of approximately 120  $\mu\text{m}$  to 150  $\mu\text{m}$ , spin coating was performed for 1 s at 1600 rpm followed by spinning for 8 s at 800 rpm. The soft baking step was conducted at 140  $^{\circ}\text{C}$  for 180 s, which enhanced the flatness but did not solidify the resist. For this reason, a proximity contact exposure was conducted to avoid contamination of the utilised foil

mask. Resist cross-linking emerges during the exposure at a relatively high dose of  $3 \text{ J cm}^{-2}$ . With the absence of a PEB, the resist was developed in 3 × baths using the aqueous AZ® 726 MIF developer (Figure 2.8(b)).

Cu was electroplated up to a height of  $80 \mu\text{m}$  to remain right below the ORDYL® SY 390. Stripping of the resist was possible using the N-Methyl-2-pyrrolidone (NMP) free mr-Rem 700 remover. The complete removal of the Cr/Au seed layer between the coil windings was critical. Figure 2.10 shows visible residues after seed layer etching. Noble material combinations such as Cr/Au below electroplated Cu are generally removed by selective etching solutions. Seed layer removal by selective etching was not subject of the current process evaluation, and is further discussed in Section 5.5 on page 135.

The Cu structures were wet chemically cleaned and activated by an oxygen-plasma. An alternative to hot-roll lamination is vacuum lamination. Air inclusions were eliminated by applying the DFR within a high-vacuum chamber. This processing step was performed inside a substrate bonder (SB6 Wafer Bonder 1<sup>st</sup> gen., SÜSS MicroTec, Germany) which acted much similar as a hot-embossing tool (see the sketch in Figure 2.9(a)). It was more practical to insert the DFR with the protection foil on a support wafer which was placed onto the bottom chuck. In the beginning, spacers separated the wafer from attaching to the DFR layer. At a temperature of around  $75 \text{ }^\circ\text{C}$ , the spacers slipped out and the two chucks moved together under minimum available force. Figure 2.9(b) illustrates the processing parameters for bonding a ORDYL® SY 390 layer. Subsequently, the lithography was performed and the wafer was subjected to a PEB.

ORDYL® SY was chosen for this experiment, since it gives a much better leak-tight substrate adhesion than the SUEX. The resist was about  $15 \mu\text{m}$  higher than the  $80 \mu\text{m}$  Cu plating. It would have been possible to plate even higher, but however the electroplated height is limited to the subsequently bonded DFR. Since the alignment marks were removed through the seed layer stripping, the foil mask was aligned manually under a microscope and the wafer

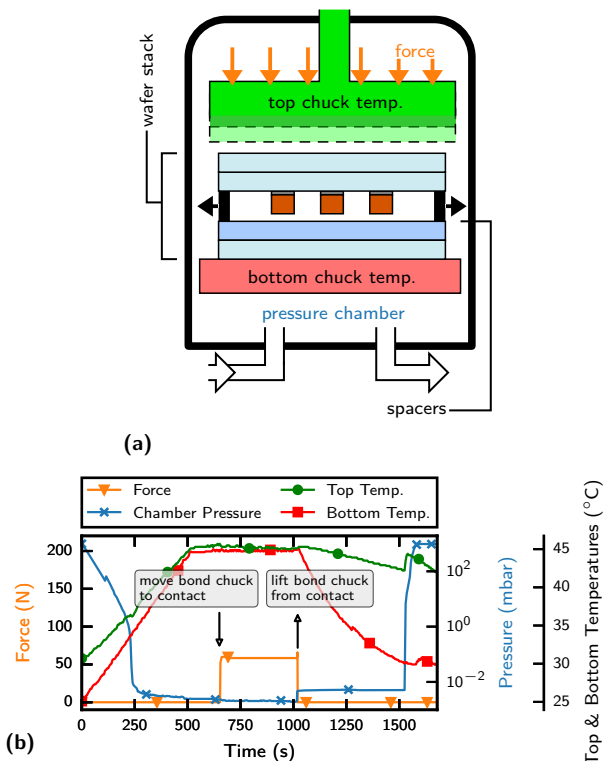


**Figure 2.9:** (a) schematic sketch of the bonding tool to apply the DFR on the substrate. Wafer stack from bottom to top: 500  $\mu\text{m}$  support wafer, polyethylene terephthalate (PET) film, ORDYL<sup>®</sup> SY 390, (spacers), Cu structures & seed layer, 500  $\mu\text{m}$  glass substrate, 500  $\mu\text{m}$  support wafer. (b) characteristic parameters of the bonding process.

was flood exposed. An excellent surface homogeneity of the ORDYL<sup>®</sup> SY layer was achieved, which also enables an additional multi-layer application of DFR by hot-roll lamination.

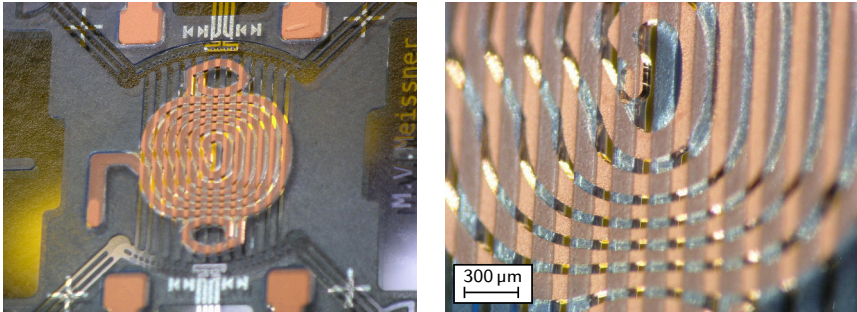


**Figure 2.10:** Patterned ORDYL® SY 390 DFR that was bonded on top of electroplated structures.

## Summary

SU-8, and the ADEX/SUEX and ORDYL® SY photo definable DFRs were selected to remain permanently on the substrate. With the absence of a soft bake for the ADEX/SUEX, also the maximum process temperature reduced and it was possible to initiate the cross-linking at temperatures in the range of 50 °C to 90 °C. The SU-8, ADEX and SUEX photo polymers maintain static stability of the MR gradient coil assembly and showed limited out-gassing. They either served as an electrical isolation layer, for fluidics channel routing, alignment structures or to define the electroplating mould. The use of uncross-linked DFRs for the fabrication of fluidic networks allowed for a significant reduction in the process complexity.<sup>[142,158,159]</sup>

For structuring the electroplating mould, photo resists that can be applied with a resist height of 100 µm or even higher were chosen. ORDYL® SY showed considerably fewer possibilities than SU-8 based resins and is not available in the required thickness. Optical transparency of these resists was another important property, to easily monitor the manufacturing process towards multiple layers. Wapler *et al.*<sup>[160]</sup> assessed the magnetic susceptibility for the listed polymers by MRI-driven experiments. He identified those materials to closely match the magnetic susceptibility of water, making them suitable for MR detectors.

Also non-permanent photo resists were required and for different purposes, ma-N 1400 (micro resist technology GmbH), AZ 125 nXT (MicroChemicals GmbH) and ORDYL<sup>®</sup> FP 450 (Elga Europe) were evaluated. These photo resists require to be completely removable without residues, by the aid of organic solvents or alkaline strippers. However, the aforementioned permanent resists had to withstand these stripping agents. AZ 125 nXT could only be processed on the substrate directly, rather it could not be selectively removed from the ORDYL<sup>®</sup> SY or the SU-8. All of the listed photo polymers remained their stability when immersed into acidic chemistry during copper electroplating.

The processing parameters and compatibility of the evaluated resins are listed in Table 2.1 on the facing page.

	ORDYL® SY	ORDYL® FP 450	AZ 125 nXT	SU-8 3000	SUEX / ADEX
<b>Type:</b>	negative DFR, permanent	negative DFR, non-permanent	negative spin-on, non-permanent	negative spin-on, permanent	negative DFR, permanent
<b>Adhesion:</b>	👍👍👍 soda-lime glass 👍 borosilicate glass	👍 Au/Cu seed layer	👍👍 Au/Cu seed layer	👎 soda-lime glass 👍👍 borosilicate glass	👎 soda-lime glass 👍 borosilicate glass
<b>Thickness:</b>	50–95 µm	50–100 µm			
<b>Exposure:</b> *	135–145 mJ cm <sup>-2</sup>	650–850 mJ cm <sup>-2</sup>			
<b>Soft bake:</b>	👍 not required	👍 not required	125 °C	95 °C	👍 not required
<b>PEB:</b>	85 °C for 1 min, with the PET foil on top	👍 not required	👍 not required	50–90 °C	50–90 °C
<b>Development:</b>	2×ORDYL Dev/IPA 3 min/3 min/3 min	0.8–1.2% Na <sub>2</sub> CO <sub>3</sub> , 21 °C	3 × AZ Dev 700	PGMEA (mr-Dev 600)	PGMEA (mr-Dev 600)
<b>Removal:</b>	not tested	1% to 3% NaOH, 55 °C, resolves and swells, removal is compatible with resist: SU-8/SUEX/ADEX	1 h to 2 h mr-Rem 700 resolves and swells	not tested	not tested
<b>PVD seed layer:</b>	👎👎 out-gassing in vacuum	👍 vacuum evaporation	not tested	👍👍 vacuum evaporation	👍👍 vacuum evaporation
<b>Applications:</b> **	<ul style="list-style-type: none"> <li>▪ Wafer level bonding</li> <li>▪ Ink-jet printing</li> </ul>	<ul style="list-style-type: none"> <li>▪ Electroplating mould on subsequent layers.</li> <li>▪ Encapsulation of SU-8 fluidic layers during processing.</li> <li>▪ Protection of Cu electroplated structures.</li> </ul>	<ul style="list-style-type: none"> <li>▪ First electroplating mould.</li> </ul>	<ul style="list-style-type: none"> <li>▪ First electroplating mould.</li> <li>▪ Microfluidics.</li> <li>▪ Ink-jet printing.</li> </ul>	<ul style="list-style-type: none"> <li>▪ Encapsulation.</li> <li>▪ Microfluidics.</li> <li>▪ Electrical isolation.</li> </ul>

\* The lithography dose was extended by a factor of 1.5 to compensate the absorption of the polymer mask (included in the exposure dose value).

\*\* Only the intrinsic use cases, identified for the fabrication steps in this thesis were listed.

**Table 2.1:** Summary of the most important photo resist systems, identified for the manufacture of miniaturised magnetic field coils.

## 2.2 Conductive ink-jet printing on permanent resist

In the following, a metallisation process is shown, which makes it possible to define highly conductive, interconnected Ag structures on ORDYL<sup>®</sup> SY without the need of PVD.<sup>[127]</sup> In previous to this research, ink-jet printing of metals has been driven towards a low-cost ( $\approx$  £300 setup-costs) structuring technique for the rapid manufacture of functional electronic devices.<sup>[161]</sup> Particularly in a laboratory environment, material printers with exchangeable print heads are used to evaluate the printing behaviour of different inks.

Conductive silver nano particle ink-jet printing was performed using a Dimatix materials printer (DMP-2831, Dimatix-Fujifilm) with a 10 pL cartridge.<sup>[127]</sup> The ink ejection waveform was similar as reported by Meier *et al.*,<sup>[120]</sup> but the nozzle temperature was limited to a maximum of 30 °C. Meier has demonstrated printing of 25  $\mu$ m wide silver track onto a polyimide substrate.

Wang *et al.*<sup>[57]</sup> ink-jet printed and cured silver nano particle ink on a polyimide foil to define flexible, rolled-up micro coils. However, the 50  $\mu$ m thick polyimide foil blocks *i-line* exposure and is not suitable as substrate material when performing the purposed backside lithography (see Section 3.2.1). The curing of a spin-on polyimide layer in a convection oven requires high temperatures of 350 °C to 400 °C.

In here, printing was performed on polymer films, that formed excellent adhesion towards the printed tracks after sintering. For a photo-structured multi-layer process using a homogeneous resist combination, SU-8 and ORDYL<sup>®</sup> SY were identified to serve as the printing base.<sup>[127]</sup> The printing resolution depended on the surface energy which was precisely adjusted to render sharp edges of the printed tracks.

An optimised protocol for ink-jet printing of the Suntronic U5603 ink (SunChemicals) on SU-8 is given here. Adhesion of SU-8 towards float glass is optionally promoted by spin-coating Ti-prime (MicroChemicals GmbH) according to the

standard recipe. Either a  $10\ \mu\text{m}$  layer of SU-8 (SU-8 3010, MicroChem, spin rate 3000 rpm) or  $50\ \mu\text{m}$  (SU-8 3010, MicroChem, spin rate 3000 rpm) thick layer was applied by spin coating and subjected to a soft-bake for approximately 5 h at  $95\ ^\circ\text{C}$ . After the substrate cool-down (about  $2\ ^\circ\text{C}\ \text{min}^{-1}$  to  $7\ ^\circ\text{C}\ \text{min}^{-1}$ ), the SU-8 was flood exposed with an energy of  $200\ \text{J}\ \text{cm}^{-2}$  and subjected to a PEB.

Accurate ink-jet printing on pre-cured SU-8 coated substrates required a surface modification step. Oxygen plasma activation was one method to achieve a temporal change of the SU-8 surface energy. Conventionally processed SU-8 possessed a contact angle  $\theta$  larger than  $75^\circ$ .<sup>[127]</sup>

After a moderate oxygen plasma activation at 50 W for 2 min, the contact angle dropped significantly. Walther *et al*.<sup>[137]</sup> observed a recovery of the SU-8 surface energy after an oxygen plasma flash. After several weeks, the contact angle  $\theta$  reverted back to  $25^\circ$  to  $45^\circ$ . The approach in here was to accelerate this recovery by a controlled post baking step. Beginning with a moderate plasma activation, a hard bake was carried out at different temperatures as shown in Figure 2.11. The hard bake duration was 10 min and the samples were dried after each measurement and reused.<sup>[127]</sup>

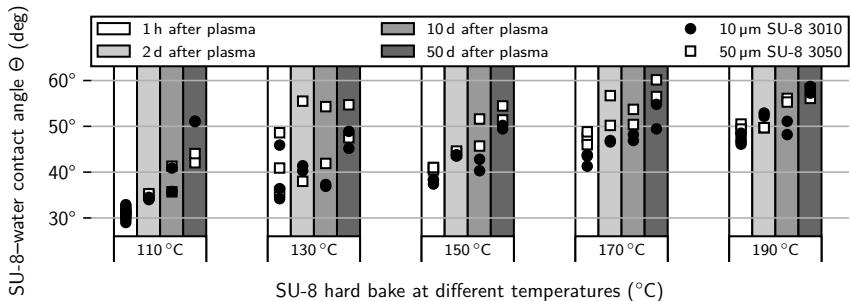


**Figure 2.11:** Measured surface contact angle of de-ionised water droplets on SU-8 for different hard bake temperatures. (Figure reproduced from [127])

A number of SU-8 samples were investigated and the projected surface area of a series of printed silver ink droplets was measured as shown in Figure 2.12. The surface area that was covered by the droplets within the  $10 \times 7$  grid was statistically analysed. The droplet spacing for the grid was  $88 \mu\text{m}$  and for the printed lines, it was set to  $22 \mu\text{m}$ . The lines were spaced centre-by-centre by  $88 \mu\text{m}$ . [127]

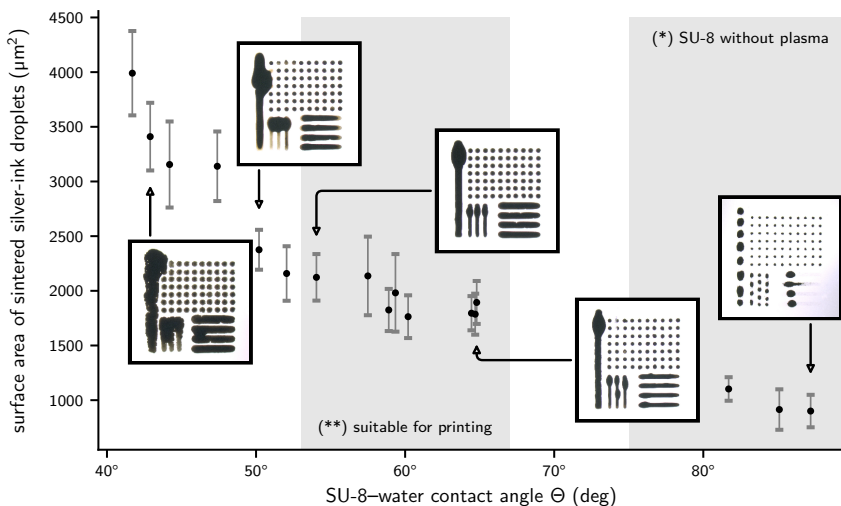


**Figure 2.12:** Silver ink droplet spread versus water contact angle for a pre-treated and (\*) untreated SU-8 surface. Indicated is the range of (\*\*) suitable substrate contact angles, for which vertical and horizontal lines did not coalesce after printing. (Figure reproduced from [127])

According to Figure 2.12 and Figure 2.11, the SU-8 surface was adjusted to water contact angles between  $54^\circ$  to  $66^\circ$  by a plasma activation and subsequent hard baking step at  $160^\circ\text{C}$  to  $180^\circ\text{C}$  for 10 min.

Nano-particle ink-jet printing on ORDYL<sup>®</sup> SY required less complex pre-treatment compared to SU-8. [127] Clean glass substrates were activated by a oxygen plasma flash at 80 W for 2 min (TePla, Technics Plasma GmbH, oxygen flow 500 sccm at 1 mbar). ORDYL<sup>®</sup> SY 317 dry film was applied by hot-roll

lamination (Polamat UVL 600, Polatek, lamination pressure 2.5 bar, speed  $1 \text{ m min}^{-1}$ ).<sup>[147]</sup> After flood exposure with a dose of  $200 \text{ mJ cm}^{-2}$  a PEB was carried out on a vacuum hotplate at  $70^\circ\text{C}$  for 2 min while leaving the PET cover film on top of the ORDYL<sup>®</sup> SY. The protective foil was statically charged after the removal.<sup>[127]</sup> Table 2.2 lists the observed contact angles and the measurements of transparency for different thermal treatments.

Ordyl SY post exposure bake (PEB) parameters				transmission at 360 nm to 380 nm	
temperature ( $^\circ\text{C}$ )	duration (min)	with/without PET foil	contact angle** ( $^\circ$ )	ORDYL <sup>®</sup> SY 317 (%)	ORDYL <sup>®</sup> SY 355 (%)
$70^\circ\text{C}$	2 min	with*	$55^\circ$ to $57^\circ$	80 % to 89 %	59 % to 78 %
$70^\circ\text{C}$	2 min	without	$58^\circ$ to $61^\circ$		
$100^\circ\text{C}$	5 min	without	$64^\circ$ to $68^\circ$	81 % to 89 %	66 % to 83 %
$180^\circ\text{C}$	20 min	without	$66^\circ$ to $68^\circ$	89 % to 92 %	76 % to 85 %

\* The PET film was removed shortly before measuring the contact angles.

\*\* Measured contact angles of Ordyl SY317 and SY355 were similar.

**Table 2.2:** ORDYL<sup>®</sup> SY PEB parameters with respect to the measured water contact angle and optical transmission at the indicated wavelength.  
(Table reproduced from [127])

The PET protection foil on the ORDYL<sup>®</sup> SY was peeled off just before printing. However, it was advantageous to keep the PET protection foil on top of the ORDYL<sup>®</sup> SY, to preserve the surface from contamination. After the ink-jet printing process, the silver structures were sintered at  $180^\circ\text{C}$  for around 20 min.<sup>[127]</sup>

## 2.3 Copper electroplating

Electrodeposition is one of the most widely used deposition techniques to produce low-expense, high purity, non-porous metal layers. The amount of deposited material can be estimated precisely. However, numerous process variables are based on empirical findings.

Faraday's scientific findings suggest that, the amount of electrochemical reactions in a electrochemical cell are proportional to the quantity of electric charge  $Q$  through the substance.<sup>[162]</sup> For the deposited weight  $w$  at the electrode in electrolysis, Faraday's law states the relationship,

$$w = Z \cdot Q, \quad \text{with} \quad Q = \int i dt. \quad (2.1)$$

The constant of proportionality is  $Z$  which is known as the electrochemical equivalent and is calculated from the molar mass of the substance, divided by the number of valency ions and the Faraday constant,

$$Z = \frac{M}{z_i \cdot F}. \quad (2.2)$$

$M$  is the molar mass of the substance,  $z_i$  the valency of the ion and  $F$  the Faraday constant of  $96.485 \cdot 10^3 \text{ C mol}^{-1}$ . If a  $\text{Cu}^{2+}$  salt is involved in the deposition, the valency number of the ion  $z_i$  is 2. From Equation (2.2),  $Z_{\text{Cu}^{2+}}$  follows a value of  $3.293 \cdot 10^{-4} \text{ g mol}^{-1}$  for the copper molar mass  $M_{\text{Cu}}$  of  $63.546 \text{ g mol}^{-1}$ .

The deposit thickness in an anisotropic plating process can be predicted, if the area  $A$  of the plating seed is know. From Equation (2.1), Equation (2.2) and the volumetric mass density relationship, the deposit thickness  $h$  follows,

$$h = \frac{M}{z_i \cdot F \cdot \rho \cdot A} \int i dt. \quad (2.3)$$

The composition and monitoring of the electrolyte is critical in the electroplating process. In other publications electrolytes without commercially available additives were used.<sup>[163]</sup> The characteristic copper plating is affected by the concentrations of copper salts, additives, free acid, temperature, current density and electrolyte movement.<sup>[164]</sup> Electrolyte additives affect the surface quality and performance at levitated current densities. Various publications<sup>[165–167]</sup> suggest for instance the use of polyethylene glycol (PEG).The PEG inhibits

the deposition with respect to an overpotential at which the current density rises rapidly.

In here, the electroplating bath was based on the Cuprostar LP-1 electrolyte system (Enthone-OMI GmbH) which is generally used for PCB fabrication. Figure 2.13(a) illustrates the surface quality with the Cuprostar LP-1 electrolyte, and a plating test before adding the Cuprostar LP-1. The plating area was  $\approx 25 \text{ cm}^2$  and the current density was  $2 \text{ A dm}^{-2}$  with the magnetic stirrer set to 500 rpm.

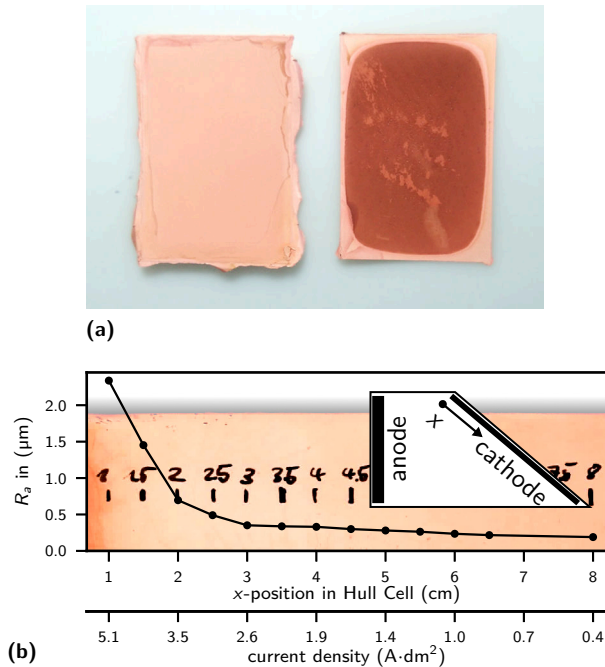


**Figure 2.13:** (a) difference of the surface quality of the electrolyte with (left, measured weight 1.04 g) and without (right, measured weight 1.12 g) the addition of Cuprostar LP-1. (b) 250 mL Hull-Cell experiment of the electrolyte including the Cuprostar LP-1, at ambient temperature, displaying the roughness of the deposited layer.

A batch of 5 L aqueous electrolyte was composed of 393 g Copper(II) sulfate pentahydrate, 550 mL  $\text{H}_2\text{SO}_4$ , 0.4 g NaCl and 12 mL Cuprostar LP-1. The electrolyte allows plating at room-temperature at current densities up to  $3 \text{ A dm}^{-2}$ .<sup>[121]</sup> At too high current densities, the roughness of the plating increases as observed in a Hull-Cell experiment, shown in Figure 2.13(b).<sup>[168]</sup> With the Hull-Cell, the cathode is arranged at an angle which provokes a variation in the current density in order to determine the efficiency of the electrolyte. The plated film gives information about the working range of the electrolyte.

Heating of the electrolyte to  $40^\circ\text{C}$  allowed plating at current densities of  $40 \text{ mA cm}^{-2}$ . It is possible to achieve a electrical conductivity of  $57.4 \cdot 10^6 \text{ S m}^{-1}$  of the plated structures.<sup>[169]</sup> The following parameters of the Cuprostar LP-1 plating bathe was determined. The Cu content of  $24.94 \text{ g L}^{-1}$  was determined by titration and a sulfuric acid content of  $192.815 \text{ g L}^{-1}$  was examined. The electrolyte had a density  $\rho$  of  $1.196 \text{ kg dm}^{-3}$ , measured by a hydrometer at a temperature of  $23^\circ\text{C}$ .

The Cu was electroplated with DC-current by using a self-constructed bath and a custom-made 8-channel bipolar current sink as shown in Figure 2.14. Multiple current outputs allows to electroplate in batch, to increase the production volume within the framework of the self-built laboratory-type electroplating setup. The electrolyte was immersed into standard beaker glassware,<sup>[170]</sup> and placed on a magnetic-stirred hot-plate. Sacrificial copper anodes per purchased (phosphorus content of 0.04 % to 0.06 %, Galva-Metall GmbH, Rödermark) that were cut in shapes of  $150 \text{ mm} \times 120 \text{ mm} \times 10 \text{ mm}$ . The anodes were scrubbed to remove oxidisation and were wrapped into polypropylene filter bags (PP8935, Winkler Filtration Technology GmbH). The filter retained copper particles larger than  $20 \mu\text{m}$  and prevented those from plating. The immersed anode area was adjusted to fit 4" substrates. Since the copper anode did slowly dissolve in the absence of an applied plating current, it was removed from the bath when no plating was performed and stored in a 10 %  $\text{H}_2\text{SO}_4$  solution.<sup>[121]</sup>



**Figure 2.14:** Cu electroplating setup to perform the copper deposition on 6 substrates in parallel. (Figure reproduced from [121])

The holders to keep the anode and the substrate accurately in place were fabricated out of PMMA. The PMMA parts were fabricated via laser-cutting (VLS2.30, Universal Laser Systems Inc.). The chemical and mechanical stability of the holder was improved by a post annealing process after laser cutting.<sup>[171]</sup>

For accurate control of the plating current and timing a digital adjustable bipolar precision current sink was developed. Figure 2.15 illustrates the concept and electrical setup of the galvanic cell. With a single anode connected to common ground potential, the two subjected cathodes were coated at the same time. In the present configuration, both cathodes were tied to a negative potential by the bipolar current sink.

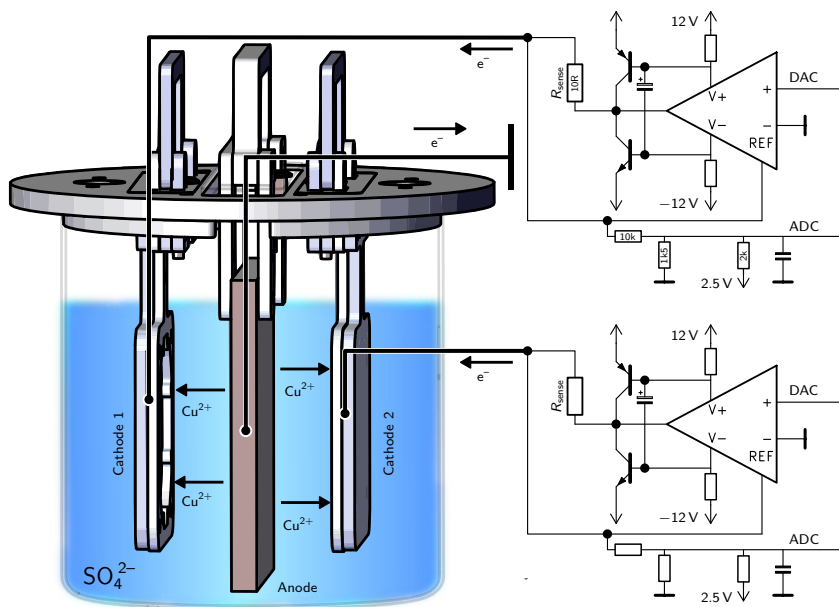


**Figure 2.15:** Concept of the electroplating system.

The output current was regulated by the LT1990 operational amplifier (OP-AMP) which acts much similar as a Howland current source.<sup>[172]</sup> Since conventional OP-AMP are limited in their output current, additional components were added to boost the output current of the LT1990.<sup>[173]</sup> Primarily, two bipolar junction transistors (BJTs) were necessary to build up a push-pull class-B common-emitter follower.<sup>[174]</sup> The circuit was used for constant currents with the electrical resistance through the galvanic cell, smaller than a few  $\Omega$ . However, the slew rate is additionally reduced by the boosting BJTs. The two isolated DC/DC converters supply the  $\pm 12\text{V}$  supply for the individual sinks (see Figure 2.16). Heat sinks and a fan were added to maintain thermal stability during long term electroplating.

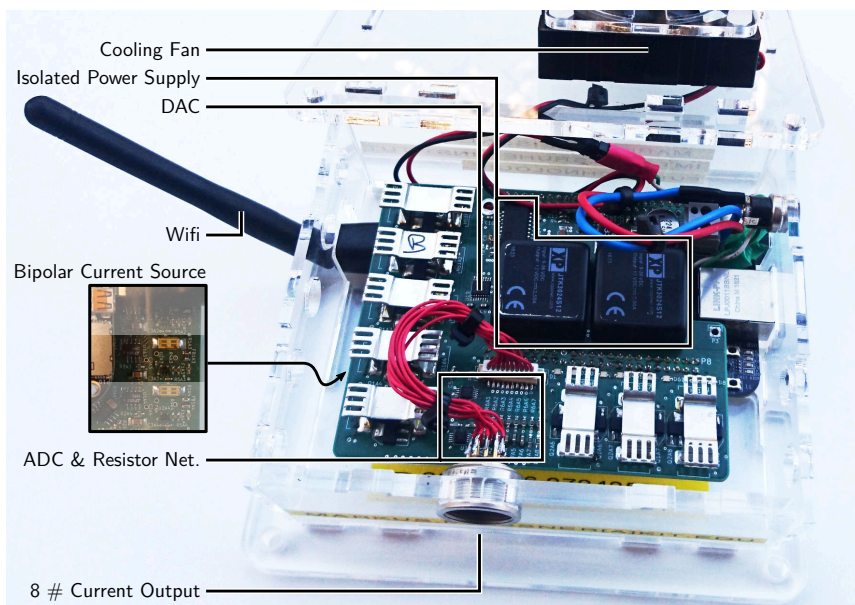


**Figure 2.16:** Multi-channel BeagleBoneBlack (BBB) electroplating current source cape.

As shown in Figure 2.15, the voltage drop across  $R_{\text{sense}}$  is proportional to the cathode current and regulates according to the input voltage set by an external digital-to-analog converter (DAC) that was controlled over serial peripheral interface (SPI) (DAC8568, Texas Instruments, USA) [175]. The current through the galvanic cell is sensed by  $R_{\text{sense}}$  and the OP-AMP adjusts the current such that the output current is always  $V_{\text{DAC}}/R_{\text{sense}}$ . The digital control was carried out by a BBB based on a python script with online web-based monitoring. [176,177]

The zero point of the current source was adjusted manually in the BBB. With respect to the resolution of the DAC, a quiescent current smaller than  $\pm 48 \mu\text{A}$  remained after calibrating against a  $2.5 \Omega$  resistor. However, within the actual application, currents in the mA range were used, such that this quiescent current was neglected and not further optimised. The output current was linearly adjusted by factors of 1.0072 to 1.0028 with respect to the DAC input

voltage, to achieve an accuracy much better than 1%. The current output precision completely fulfilled the requirements for the electroplating. However, the output current was limited to 250 mA. Since each current sink was operated independently, multiple of the current outputs could be connected in parallel and thus the total output current added up.

The plating voltage drop through the galvanic cell was monitored indirectly by three 3-channel ADC (ADS1112, Texas Instruments, interfaced over Inter-Integrated Circuit (I<sup>2</sup>C)).<sup>[178]</sup> As illustrated in Figure 2.15, the voltage divider was biased using the internal 2.5 V reference voltage of the DAC. In such a way, the bipolar voltage span through the galvanic cell was linearly adjusted to adapt with the positive input voltage range of the ADC. This was adapted to the unipolar output range of an ADC by means of the available internal reference voltage of the DAC.

The output of the current sink is fully galvanic isolated, and may also be applicable for controlling the shim current in the NMR experiment.

## 3 Process evaluation

In here, two application specific examples are outlined to identify and foster the processing steps for the fabrication of the micro gradient. Preliminary to this thesis, a field gradient coil was constructed that was composed out of wire bonded conductors.<sup>[179,180]</sup> The thermal stability of this field coil was examined within the context of this work.

Section 3.2 discusses an application to define rectangular micro coils based on an ink-jet printing process.<sup>[181]</sup> In MEMS technology, high-aspect conductive micro structures are generally patterned by electroplating. For the presented Tx/Rx micro coil, electroplating was used to increase the electrical conductivity of the printed silver tracks. To allow for anisotropic Cu plating, an electroplating mould was formed by backside lithography into a permanent negative resist.<sup>[182]</sup> With the printed tracks acting as the mask, lithographic shadow masks were therefore not required in this rapid manufacturing process.

### 3.1 Wire bonded magnetic resonance gradient coils

Within the past years, automated wire bonding had been further developed to a key technology for the rapid fabrication of solenoid micro-coils. Automated wire bonding is characterised by its high reproducibility and manufacturing efficiency to define miniature MR field coils.<sup>[44,54,183]</sup> One of the first wire-bond (WB) gradient systems was reported by Fischer *et al.*<sup>[184]</sup> However, Fischer did not highlight the operational parameters, field orientation and fabrication

precision of the illustrated on-chip gradient coil. In order to verify the feasibility, a WB gradient coil was built using refined methods.

The WB process was previously used for applications in NMR, to fabricate perfect solenoid micro-coils. More complex coil designs can only be constructed by a set of sophisticatedly placed alignment structures. The bond wire is generally wound around a polymer support structure. With a precisely adjusted bond head trajectory, also air-coils with freestanding conductors have been fabricated.<sup>[184]</sup>

A micro manufactured  $x$ -,  $y$ -gradient system can be realised by several straight aligned, WB conductors, embedded into photo-definable permanent dry film resist (DFR) as shown in Figure 3.1. The Anderson<sup>[77]</sup>  $y$ -axial linear shim

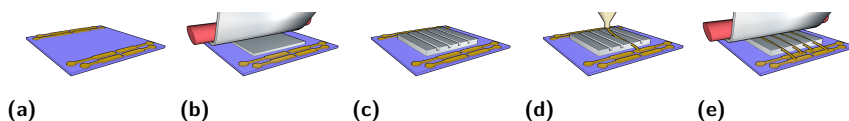


**Figure 3.1:** WB gradient coil fabrication process. **(a)** structuring of Au bond pads by electroplating. **(b)** lamination and lithographic structuring of a bond plateau and alignment channels. **(c)** finished alignment channels. **(d)** automated Au wire bonding. **(e)** encapsulation of the wire bonded conductors.

coil design turned out as a suitable model to implement the gradient coils on bi-planar substrates (see also Section 1.4.2 on page 22).

The clean-room based fabrication started on a bare Borofloat 33 wafer. The substrate was metallised by a seed layer based gold-electroplating using the standard AZ9260 resist (Microchemicals GmbH, Ulm), to pattern the WB pads and electrical supply tracks. A 250  $\mu\text{m}$  thick SU-8 layer (SU-8 2150, Microchem, USA) was spin-coated and photo-structured to add an offset that facilitated the bond wire alignment. Within the same lithography step, cooling channels were patterned into the SU-8 resist. A photo-definable 50  $\mu\text{m}$  PerMX 3050 DFR (DuPont) was added to define WB alignment channels. Insulated, 25  $\mu\text{m}$

thick gold-wires were routed inside the alignment channels and bonded to the opposing pads by utilising an automatic WB machine. During the entire bonding process, it was required to keep the wire under tension while keeping the bond tool in close proximity above the channel.

To fix the WB conductors entirely, another dry film resist layer was laminated on top. As shown in Figure 3.2(a), perpendicular alignment channels for the  $x$ -gradient were already defined into the top encapsulation layer. After the encapsulation step in Figure 3.1(e), the process was repeated to position the  $90^\circ$  rotated  $x$ -gradient conductors. To complete the miniaturised gradient system, two chips were assembled in a flip-chip configuration as shown in Figure 3.2(b). The manufacturing process was verified optically and a variation of the conductor positions of  $17\ \mu\text{m}$  to  $36\ \mu\text{m}$  was determined.

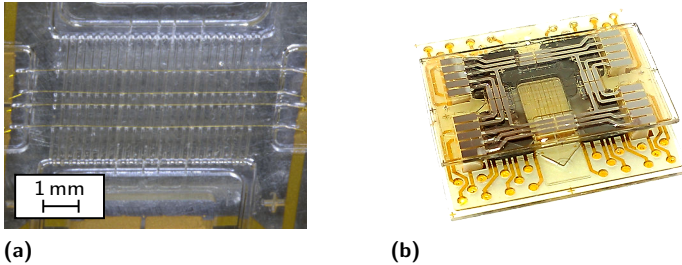


**Figure 3.2:** (a) bond wires aligned into micro-channels with top encapsulation. (b) flip-chip of the WB gradient system using a two component epoxy resin. (Figure reproduced from [179])

The resistivity of the approximately 8 mm long bond wires measured  $0.398\ \Omega$  to  $0.421\ \Omega$ . The thermal stability was examined with a thermal camera as shown in Figure 3.3. There was significant lower heating in proximity the bond pads, especially when no liquid cooling was in progress. During active liquid cooling, the bond pads did heat-up, since no cooling channels were routed within that area.

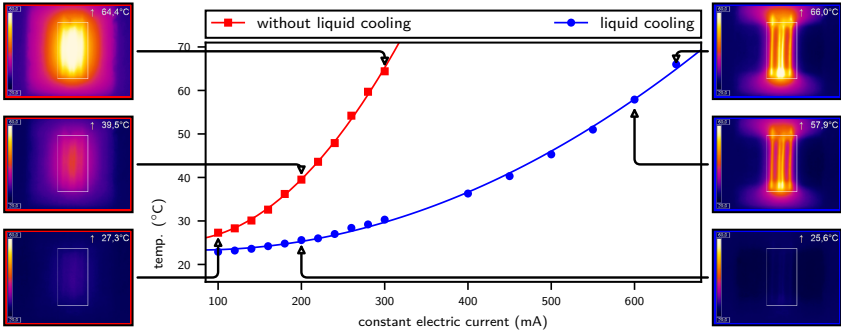


**Figure 3.3:** Thermal analysis of the WB single layer gradient system, with and without active liquid cooling.

The bond wire can be driven by a static current of 400 mA which respectively results in a gradient strength of approximately  $0.8 \text{ T m}^{-1}$ , causing moderate heat-up to the package. Furthermore, the individual conductors can be driven independently to provide fine-tuning of the induced field, as well as field focusing.

Given the limitations of the bond wire thickness and the resulting current carrying capacity, it was focused on an electroplating process to implement field coils with a higher electrical conductivity. Wire bonding is a rapid manufacturing technique, but it is limited in defining round traces or arbitrarily curved patterns. Patterning of curved tracks was essential for the 2D bi-planar target field design of the here proposed micro gradient.

### 3.2 Mask-less micro coil fabrication using ink-jet printing

In this section, a mask-less fabrication technique to manufacture rectangular micro coils is described. This technique combines printing of metal ink with UV-LIGA patterning.<sup>[181]</sup> Such a mask-free patterning method allowed for direct

structuring of coils on a transparent substrate without the need of additional lithographic shadow masks. However, the fabrication technique had a strong influence and induced possible design limitations for the realisation of some specific MR microcoils.

Therefore, the coil design needs to be specially tailored to the manufacturing tolerances for ink-jet printing. A planar single loop coil shape is the simplest for ink-jet printing a coil. They can be either screen or ink-jet printed, with the benefit of directly obtaining a fairly thick and conductive track through screen printing or having the option of easily changing the shape, but getting thin conductive layers using ink-jet printing.

The here described process involved silver nano-particle printing and sintering, electroplating mould structuring and micro-electroplating.<sup>[127]</sup> An overview of the individual processing steps is illustrated in Figure 3.4. Direct printing of silver nano particle on bare soda-lime float glass (AGC Glass EUROPE, thickness 550  $\mu\text{m}$ ) or boro-silicate glass did not exhibit sufficient adhesion when subjected to wet processing.

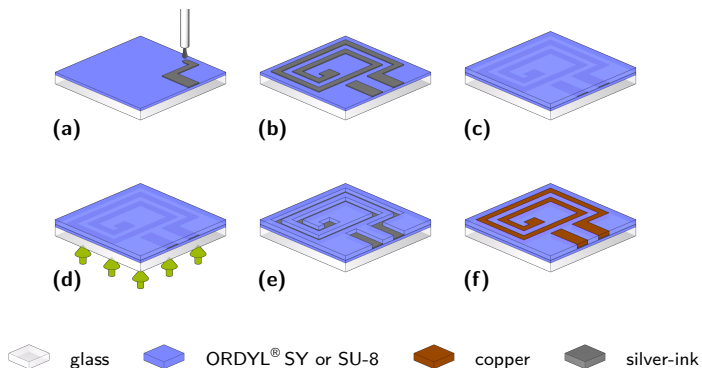


**Figure 3.4:** (a) direct, drop-on-demand silver nano-particle printing. (b) sintered, conductive silver tracks. (c) thick-film permanent photoresist deposition. (d) backside exposure and resist development. (e) fabricated electroplating moulds. (f) copper electroplating. (Figure reproduced from [127])

As a printing base, substrates were pre-coated with SU-8 or ORDYL<sup>®</sup> SY DFR. The adhesion of the two polymers on the glass substrates was enhanced by a wet-chemical cleaning process using piranha etch solution. Residues and particles were removed by quick-dump-rinsing (QDR), which followed spin drying and dehydration in an oven at 200 °C for 2 h. These polymer films act as adhesion promoters and were applied respectively throughout the electroplating mould structuring and encapsulation (Figure 3.4(d) and Figure 3.4(e)). The preparation of the two photo polymers for ink-jet printing was already described in Section 2.2 on page 56.

The silver nano particle ink (Suntronic U5603, SunChemicals) was printed with the Dimatix materials printer onto the negative photoresists, defining the shape of the conductive tracks. After printing, the ink was sintered and thereby formed up a solid, electrically conductive and optically opaque tracks. SU-8 as a printing base required a higher sintering temperature at around 230 °C for 25 min, such that the tracks did properly adhere to the polymer. In fact, this temperature was above the glass transition temperature  $T_{g,SU-8} > 200$  °C. [123]

Sintering the metal ink on the ORDYL<sup>®</sup> SY printing base was performed at a lower temperature of 180 °C. An increase in optical transmission [148] and extended out-gassing of ORDYL<sup>®</sup> SY was observed during the sintering. However, such a thermal penetration resulted in a weight loss of around 4 % to 5 % (compare with Figure 2.3). Wet development was not required for both the polymers, since the entire resist layer was exposed and cross-linked.

#### **3.2.1 Plating mould fabrication by back-side lithography**

The printed tracks were sufficiently dense and resolved to be used as a shadow lithographic mask. Therefore, another resist layer of SU-8 or ORDYL<sup>®</sup> SY was applied on top of the silver tracks to structure the electroplating mould. Dehydration and oxygen plasma activation were performed to enhance the

resist wetting. It was possible to spin-coat or laminate above the approximately 500 nm thick silver printed tracks without the risk of getting air-bubbles trapped.

To achieve a higher SU-8 layer thicknesses than with the aid of spin-coating, SU-8 can also be dispensed statically while the substrate is heated to 65 °C to 70 °C. However, thicker SU-8 layers require a longer soft-bake duration and slower hot-plate ramping. Rapid heat-up to 95 °C for the soft bake caused the solvents to evaporate quicker which resulted in dents similar to an orange peel, distributed all over the whole resist layer.

Fabricating the electroplating mould into an ORDYL<sup>®</sup> SY layer was more practical and was achieved by hot-roll lamination. Successive lamination of two layers of ORDYL<sup>®</sup> SY 355 resulted in a total resist height of 100 µm. For a successful lithography, the transmission behaviour of the ORDYL<sup>®</sup> SY 355 printing-base must be adequate enough and the exposure dose had to be adjusted accordingly. Recorded transmission spectra are illustrated in Figure 3.5 with the respective wavelength indicated at 365 nm. A 180 °C cured ORDYL<sup>®</sup> SY 355 on the substrate resulted in a reduced transmission of 70 %.

As shown in Figure 3.4(d), the lithography was performed through the rear, through the substrate. The printed tracks cast a shadow onto the top resist layer that prevented the resist to cross-link there. Exposure with an i-line filter was done using a mask aligner (MA6, SÜSS MicroTec, Germany). Since no predefined mask was used, exposure was possible with any collimated light source. No mask-holder was installed within the exposure system, and consequently no wedge error compensation (WEC) was performed. Thus, no pressure was applied to the delicate glass wafer during exposure, which also allowed the use of thin glass substrates with thicknesses below 100 µm.

An anti-reflection foil (Spectral Black, Aektar Ltd.) was placed below the resist to decrease UV-light back-reflection from the wafer chuck. With no anti-reflection foil, the photoresist did cross-link directly above the reflective silver tracks, and the result was a thin electrically isolated resist layer above

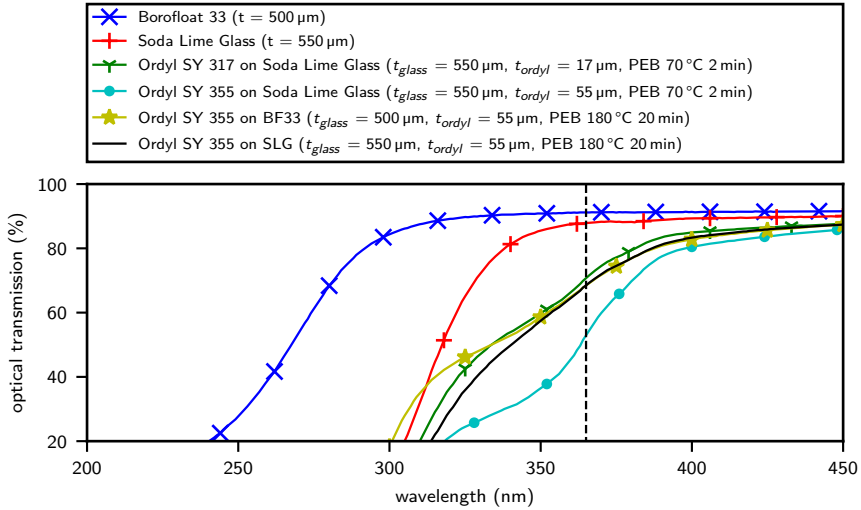


**Figure 3.5:** Transmission spectra recorded for different ORDYL<sup>®</sup> SY 355 printing base materials (Varian UV-VIS-NIR spectrophotometer).

the silver tracks that prevented the electrodeposition. An exposure series was performed to adjust the required exposure energy.

An approximately 200  $\mu\text{m}$  thick SU-8 layer was exposed with a dose 250  $\text{mJ cm}^{-2}$ . After the PEB, the structures were development in PGMEA for 15 min to 20 min in a mega-sonic bath. One example of a fabricated SU-8 electroplating mould is illustrated in Figure 3.6.

As the interface to the cured resist (previously called printing base) was exposed with the incident energy by means of using the back-side (BS) exposure, enhanced adhesion of the electroplating mould was thereby achieved. In contrast, for the purpose of sufficient resist adhesion on borosilicate glass substrates, an extended exposure dose by a factor of 1.2 to 1.5 was required when processing SU-8 with conventional front-side (FS) lithography.

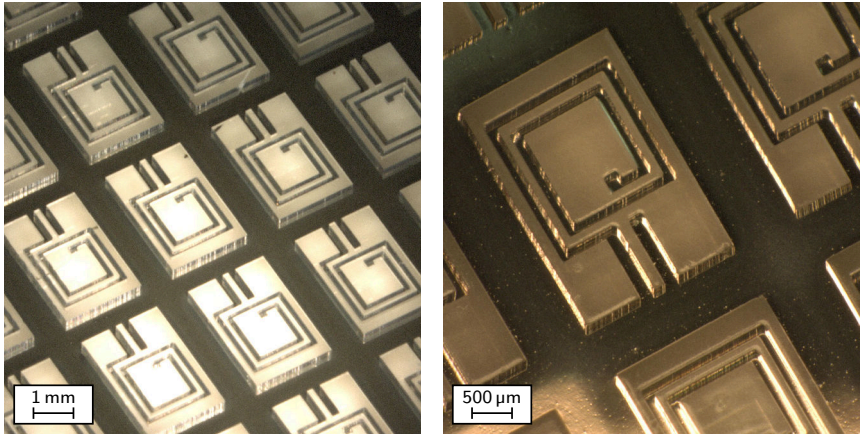


**Figure 3.6:** Electroplating mould fabrication by back-side (BS) exposure into SU-8 with a targeted thickness of 190  $\mu\text{m}$  to 210  $\mu\text{m}$ . (Figure reproduced from [127])

The double laminated ORDYL<sup>®</sup> SY 355 (100  $\mu\text{m}$ ) resist was exposed with an exposure energy of 95  $\text{mJ cm}^{-2}$  to 105  $\text{mJ cm}^{-2}$ . Figure 3.7 illustrates the electroplating mould from an ORDYL<sup>®</sup> SY DFR. The mould structures (gray/black)

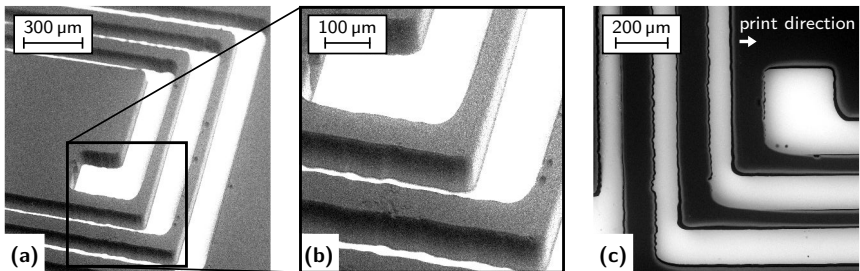


**Figure 3.7:** 100  $\mu\text{m}$  high ORDYL<sup>®</sup> SY plating moulds. (Figure reproduced from [127])

were not metallised for the SEM and therefore appear in visual contrast to the printed silver tracks (white).<sup>[127]</sup> Trenches of 80  $\mu\text{m}$  and freestanding resist structures were accurately resolved.

The printed tracks were in direct contact with the photoresist and so the quality of the pattern did not degrade by diffraction or Fresnel-reflection. The silver tracks fulfilled a twofold function without demanding separate masks including alignment steps, thus cutting down processing complexity. The principle of the backside exposure was comparable to the self-aligned doping process in joint-gate CMOS technology, where the gate-structure masks the depletion region. As reported by Robinson *et al.*,<sup>[185]</sup> the edges of the source and drain region were rendered consistently with the overlap of the gate. In this way, only a single mask defined the channel length. Much similar as the gate electrode remained as a functional element, also the printed tracks remained permanent on the substrate and supplementary served as the plating seed for the Cu electroplating.

#### **3.2.2 Copper electroplating of the micro coil**

The achievable layer thicknesses by the ink-jet printed layer was in the range of a few hundred nm which was far too thin to compensate for the skin-effect in RF applications. Now the electroplating step, therefore, created an extruded version of the planar printed tracks out of solid copper. Electroplating was carried out using the electrolyte Cuprostar LP-1 as described in the previous Section 2.3.

The pre-diced substrate with the coil structures had a size of  $2\text{ cm}^2 \times 2\text{ cm}^2$  with an effective plating area of  $2\text{ cm}^2$ . Similar to the wetting problems during ink-jet printing (Section 2.2), insufficient electrolyte wetting led to trapped air bubbles within the electroplating mould. If air bubbles were trapped, local inhomogeneities of the thickness or voids occurred in the deposited layer.

To reduce the surface energy, an oxygen plasma activation was not carried out. Experiments have shown that even a week plasma activation at 80 W oxidised and physically etched the printed silver tracks. As a countermeasure, air-bubbles were removed in a vacuum chamber with the substrate immersed

in the electrolyte or by releasing the air bubbles manually with the aid of a microfiber swab.

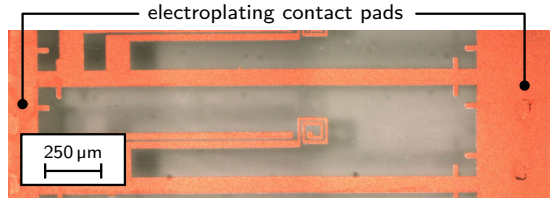


**Figure 3.8:** An undiced glass substrate with an electroplated coil structure including feed tracks. (Figure reproduced from [127])

For the deposition of a  $100\ \mu\text{m}$  thick copper layer, electroplating was carried out at a current density of  $4\ \text{A dm}^{-2}$  for 110 min. The electrolyte was heated to a temperature of  $40\ ^\circ\text{C}$  and the printed silver seed tracks retained their strong adhesion to the substrate, see Figure 3.8. [127] The height of the plated tracks was defined by the resist thickness and rendered the shape of the underlying silver tracks.

### 3.2.3 Electrical passivation and interconnect fabrication

Multi-turn planar coils require an inside-to-outside interconnection, in order to electrically connect the inner winding to the feed tracks. [182] Such structuring was done on an additional layer. On the subject of an entirely mask-free process, again ink-jet printing was employed to structure vertical interconnect access (VIA) openings, and to print and electroplate a bridge structure. The interconnection required adequate conductivity to build up a high quality RF resonator.

Figure 3.9 illustrates the process flow and extends the single layer electroplated coil from Figure 3.4.

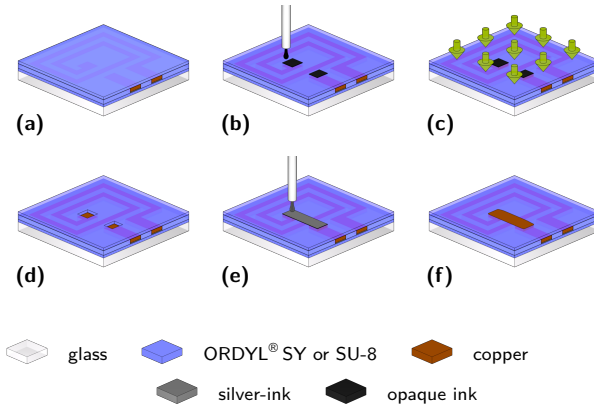


**Figure 3.9:** (a) passivation of the electroplated structures via lamination of photo-definable dry resist. (b) ink-jet printing of a wet removable optically opaque mask. (c) front-side (FS), flood exposure. (d) developed passivation layer, showing the VIAs. (e) silver ink-jet printing of the interconnect seed layer. (f) Cu electroplating to reduce the electrical resistance of the printed interconnect. (Figure reproduced from [127])

The existing ORDYL<sup>®</sup> SY layer was first cleaned by an oxygen plasma (approximately 80 W for 10 min) and a 50 μm ORDYL<sup>®</sup> SY 355 layer was applied by lamination. Thinner ORDYL<sup>®</sup> SY laminates with a thickness of 17 μm were also tested but did not fulfil the requirements to compensate inhomogeneities or accumulated copper-spikes from the previous electroplating. After the lamination the substrate was soft-baked for 2 min at 75 °C.

The PET cover film was not removed and served as a removable base to print an opaque mask, in order to define the VIA openings. Black Lumocolor<sup>®</sup> marker ink (type 48523, Staedtler) was filled into a 1 pL Dimatix cartridge. The waveform used to print the Lumocolor<sup>®</sup> ink is shown in Figure 3.10. Four jets were used for the printing and the print-head was positioned at a height of 0.8 mm above the substrate. After several days of inactivity, the nozzles of the Lumocolor<sup>®</sup> filled cartridge dried-up but it was possible to clean them using acetone for repeated use.

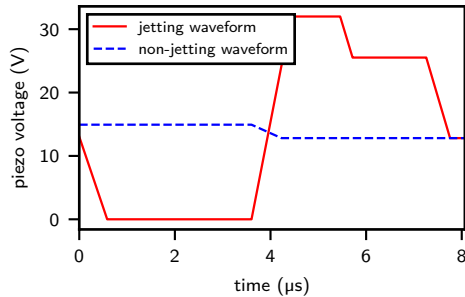


**Figure 3.10:** Dimatix printing waveform for printing the Lumocolor<sup>®</sup> ink.

The location where the opaque marker ink was printed was precisely adjusted by the stage of the printer, as shown in Figure 3.11(a). The marker ink dried instantly and the substrate was flood exposed with an exposure energy of  $150 \text{ mJ cm}^{-2}$ . The PET foil was removed, and a PEB was performed.

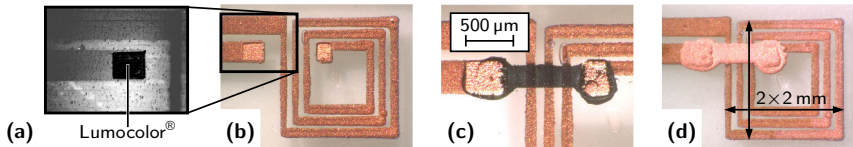


**Figure 3.11:** Structuring of the VIA openings within the passivation layer. (a) camera view of the Dimatix Printer showing the deposited, black Lumocolor permanent marker ink. (b) exposed and wet developed VIA openings. (c) ink-jet printed and sintered interconnect at  $180^\circ\text{C}$  between the two VIA openings. (d) further electroplating of the VIA openings and printed interconnection. (Figure reproduced from [127])

By peeling the PET cover film after the lithography, the ink removal by using solvents was superfluous. The un-crosslinked resist, which was masked by the deposited ink was removed in ORDYL<sup>®</sup> SY developer (see Figure 3.11(b)). The bare VIA openings were further topped-up with Cu in order to adjust the height of the plated copper to the ORDYL<sup>®</sup> SY.

In a subsequent step, the two VIA plateaus were interconnected by printing a track of silver nano particles. Since the electroplating of the VIAs was performed at 40 °C, a narrow gap opens between the ORDYL® SY resist and the Cu plateau, after cooling down to room temperature. A small amount of silver ink seeped into the gap and resulted in an increase of the resistance of the printed track as shown in Figure 3.11(c). The resistance of the track reached a few hundred  $\Omega$ .

It was still possible to further electroplate the partially transparent track as shown in Figure 3.11(d). The resistance of the interconnection was reduced to 10 m $\Omega$  by electroplating to a height of approximately 50  $\mu\text{m}$ .

Due to the line-by-line based printing process, high resolution printing and structuring was restricted to rectangular patterns. Path-based movement of the print head could have enabled curved patterning, which is mostly common in fused deposition modeling (FDM) 3D printing. In the laboratory setup, the yield was reduced by nozzle blocking which resulted in unpredictable printing defect (Figure 3.12(a) and (b)). Nozzle blocking was caused by the accumulation of silver nano particles and can be decreased by occasional nozzle cleaning during printing. However, each cleaning cycle resulted in a loss of ink.

The reliability of the ink-jetting nano particles was critical and also influenced the subsequent processing steps. For instance changes in the effective silver printed area also altered the parameters for the electroplating and lead to a mushroom shaped overplating. Some other processing circumstances are presented in Figure 3.12.

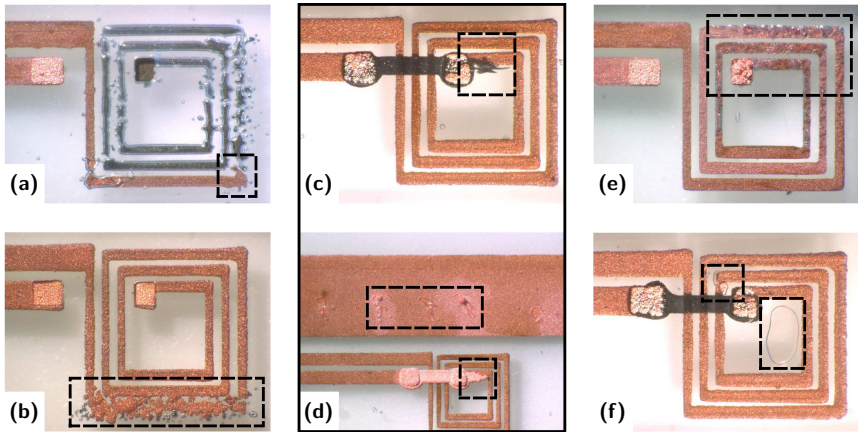


**Figure 3.12:** Common failures during processing by ink-jet printing of silver nano particles, which resulted in unpredictable defects. **(a)** nozzle blocking. **(b)** electroplated ink blots, but the VIA opening were successfully structured. **(c)** ink blur in the ORDYL® SY surface. **(d)** electroplated ink blur and vacancies in the ORDYL® SY laminate. **(e)** & **(f)** air bubbles that were trapped during the lamination.

### 3.2.4 RF characterisation

Eleven micro-coils from three different fabrication batches were electrically characterised. The DC resistance was measured by four-terminal sensing and values in the range of  $35\text{ m}\Omega$  to  $45\text{ m}\Omega$  with a mean value  $\mu$  of  $38\text{ m}\Omega$  and standard deviation  $\sigma$  of  $3.7\text{ m}\Omega$  were obtained.<sup>[127]</sup> The influence of the solder connection from the test-board to the printed micro-coils was included in the measured DC resistance.

To evaluate the reproducibility of the process, eleven coils from three different fabrication batches were characterised by measuring the 1-port, S11 return loss (E5071C ENA Series network analyser (NWA), Agilent). For all the coils, a self-resonance frequency in the region of  $955\text{ MHz} \pm 15\text{ MHz}$  was measured.<sup>[127]</sup>

For the acquired frequency range, up to the self-resonance frequency of the coil, the quality factor  $Q_L$  of the coil was calculated by the following equation,

$$Q_L = \frac{2\pi f \cdot L}{R} = \frac{|X_L|}{R}. \quad (3.1)$$

The calculation of the impedance from the S1P scattering parameters<sup>[186]</sup> was post-processed using scikit-rf, an open-source Python package for RF & Microwave applications. Figure 3.13 shows a plot of the frequency dependent quality factor. For targeting its application in MRI, the fabricated coils measured a quality factor of 28 to 31 at 500 MHz.

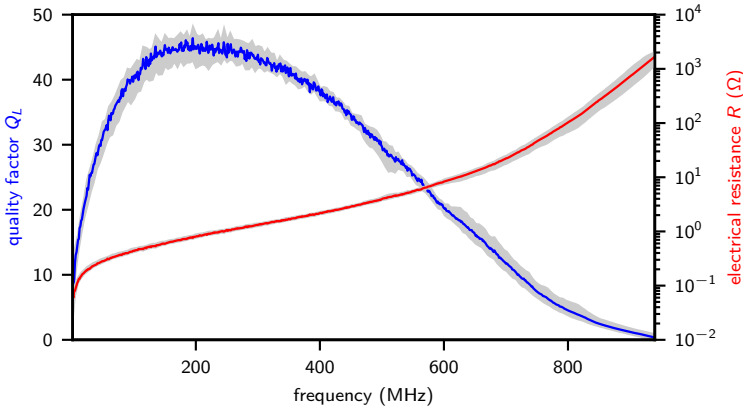


**Figure 3.13:** Frequency dependent quality factor and frequency dependent resistance. Displayed is the mean value from a measurement of eleven coils.

The printed micro coil was subjected to an MR imaging study which is further discussed in Section 7.1 on page 164.

## 4 Micro gradient design

This chapter describes the design process of the miniaturised gradient chip. Two different gradient configurations were considered, a uni-axial and a tri-axial gradient coil design. The explosion view in Figure 4.1 shows the design concept of the tri-axial gradient assembly with integrated micro fluidic cooling channels that were placed between the gradient coil layers. The flip-chip design was extended with a Tx/Rx micro coil to compose the MR imaging unit.<sup>[187]</sup>

The chip stack-up can be categorised into three different structural sections. Much similar to the printed circuit board (PCB) technology, there were conductive and electrically isolating layers. In addition, the chip's sandwich-structure embodied hollow features that were separated from the conductive elements, to route micro fluidic cooling channels. Throughout the entire layer stack, VIAs were necessary to built up electrically connected coil loops.<sup>[187]</sup>

As illustrated in Figure 4.1, the entire assembly was composed of two individual chips, where each single chip embedded two, bi-planar copper layers to define the gradient coils. In general, more than two coil layers or additional coil windings could provide a higher gradient efficiency or an improved field homogeneity.<sup>[25]</sup> On the contrary, supplemental coil layers, e.g., shielding coils, would consequently increase the thermal dissipation of the entire assembly, and would also constrain the capacity of the cooling system.

The gold standard in human body MRI scanners is active liquid cooling. However, a liquid cooling system implies the risk of leakage with related reliability issues. To reduce the processing complexity, only one layer within the layer-stack was subjected for placing the cooling channels. For circulating a

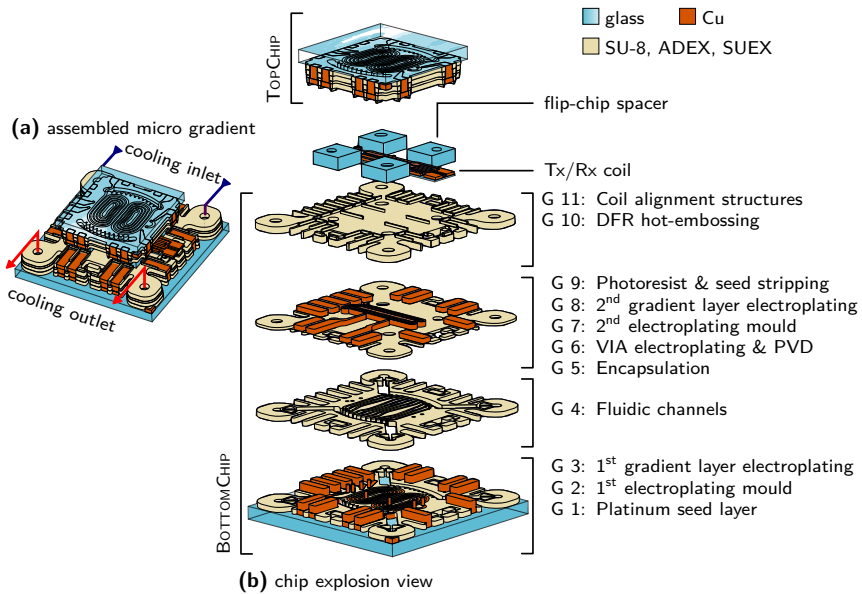


**Figure 4.1:** Design concept of the gradient flip-chip. **(a)** flip-chip assembly of the micro gradient with the highlighted cooling connections. **(b)** explosion view of the major chip components.

coolant in proximity to the gradient coils, two different variants for routing the liquid cooling channels were considered. With the MIDCOOL design, the cooling channels were placed between the two gradient coil layers. The TOPCOOL design variant added the cooling above the gradient coils, and this concept was later derived. For the two different cooling variants, separate mask sets were defined. It was focused on de-ionised water (DIW) as coolant, which has a sufficiently high dielectric strength. The fluidic delivery should not be located above the sample in the  $B_0$  direction to limit susceptibility mismatch, which could not be avoided completely for the tri-axial design.

The BOTTOMCHIP, on which the assembly was based on, included the primary current connections to drive the gradient coils and contained the fluidic in- and

outlets. Hence, these external connections consumed most of the chip space and consequently the lateral length of the quadratic BOTTOMCHIP reached  $14.6 \text{ mm} \times 14.6 \text{ mm}$  in size.

The TOPCHIP was designed with a smaller footprint, with a side length of  $8.8 \text{ mm}$ .<sup>[187]</sup> It was finally attached above the BOTTOMCHIP by the use of glass spacers. The purpose of the glass spacers was to maintain an accurate separation gap between the gradient bi-plates. Such a flip-chip underlies a similar assembly concept as implemented in previous research involving comparable glass based MEMS build-ups.<sup>[148,183]</sup>

Obviously, the size of the gradient pattern was the crucial design parameter since the coil pattern consumed most of the chip area. For mechanical stability, the coils were embedded into SUEX epoxy DFR. Another objective was to decrease the effective chip area, to further minimise mechanical stress between the resist layers and the substrate.<sup>[131]</sup> Based on the processing experience of previous research, the entire chip outline, including the fluidic and electrical connectors, should be smaller or similar to the size of the *micro-fluidic NMR probe*, presented by Meier *et al.*<sup>[54]</sup> In here, it was focused on a gradient pattern of a maximum size of  $5.6 \text{ mm} \times 5.6 \text{ mm}$ .

The spatial dimension of the imaging region or region-of-interest (ROI), also referred in here as the target field region of the gradient, was chosen to accommodate the size of an elongated nematode. One target specimen was the *caenorhabditis elegans* (*c. elegans*) which measures in the adult state a maximum length of  $1 \text{ mm}$  and a diameter of  $50 \mu\text{m}$  to  $80 \mu\text{m}$ .<sup>[188]</sup> The intended use-case for such a small sample promoted the construction of the here presented, very compact NMR imaging probe.

One principal design objective was to allow the positioning of the gradient flip-chip in an orthogonal, and likewise in a parallel orientation with respect to the direction of the main magnetic field  $B_0$ . Since it was unclear where the development would lead to, a symmetrical chip design was considered that

permitted the positioning in both directions. The electrical connections were also designed in such a way to be compatible for both the chip orientations. For the two different orientations and for changes in the bi-plate separation, it was required to adjust the gradient design, and therefore two different mask sets were developed simultaneously.

To minimise design errors while handling the extensive layout complexity, the major design elements, such as the gradient coils and fluidic channels, were drawn by parametric scripts. The layout was created in Klayout (<http://www.klayout.de>, a layout editor maintained by Matthias Köfferlein) and was structured by a hierarchical set of individual parametric design cells. The Python-based scripting environment in Klayout and the very popular SciPy<sup>[189]</sup> toolbox were used to facilitate spline interpolation and geometric calculations.

### 4.1 Uni-axial z-gradient

Regarding the magnetic susceptibility, the alignment of the chip with the main magnetic field is favourable.<sup>[187]</sup> Previously, Ryan *et al*<sup>[190]</sup> investigated different shapes of vertical aligned sample containers using NMR techniques. In addition, Ryan modified the cross-section and implemented passive shimming structures to enhance the magnetic field homogeneity further. The findings confirmed that a vertically positioned sample container is preferable.

Figure 4.2 illustrates the assembly concept and the coil patterns that were used for the first fabrication prototype. It was focused on an uni-axial z-gradient design where both of the coil bi-layers contributed to the gradient field. The pattern of the uni-axial gradient was designed in collaboration with Peter While,<sup>[187]</sup> and the design routines were based on the *minimum power stream-function design method* derived from Forbes *et al*.<sup>[191]</sup> The design method was further refined and extended by While *et al*<sup>[103,192]</sup> by applying his optimised *genuine-minimum-power* design method.

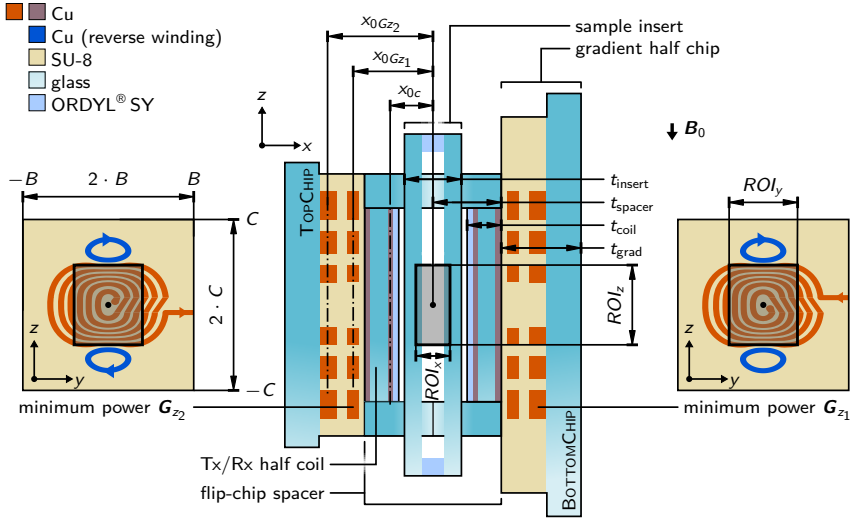


**Figure 4.2:** Orientation and dimensions of the z-gradient chip assembly. The figure presents the major components with the bi-plates oriented in parallel with  $B_0$ . (Figure adapted from [187])

The two coil layers were parameterised in terms of the current density distribution on the planar chip surface ( $B = C = 2.8 \text{ mm}$ ), in order to achieve an extra strong gradient field. The computed coil patterns are illustrated on the left and right side of the sectional view in Figure 4.2. The current density distribution was optimised to exhibit minimum power dissipation while producing a gradient field within the ROI with an average error of 1%. [187] These field errors correspond to the fields generated by continuous current densities, which was before the discrete coil windings were extracted.

It was inevitable, that the process of discretisation of the gradient contours resulted in a higher field error when compared to the continuous case. When discretised into contours that represent the coil windings, this average field error increased to 3% for a single plate. Furthermore, the nested contours had to be connected in series, which introduced a degree of asymmetry to the

final winding patterns (see the gradient patterns in Figure 4.2). Hence, the gradient efficiency and average field error of the fabricated coil was expected to be inferior to the theoretical design.<sup>[187]</sup>

For the *genuine-minimum-power* method, the choice of the number of coil windings was made prior to the optimisation and therefore resulted in different coil winding patterns. Considering the number of windings and based on the previous investigations of the photoresist materials, the minimum conductor spacing was set to 85  $\mu\text{m}$ , to be compatible with the selected ORDYL<sup>®</sup> FP 450 DFR. It was enforced that no windings were produced that cross the boundaries of the plates, in order to create closed contour loops.

In the first design approach, the single-axis micro-gradient was specified for a target field in  $x$ - and  $y$ -direction of 200  $\mu\text{m}$  ( $\text{ROI}_{x,y}$ ), that extended along the  $z$ -axis by 2 mm ( $\text{ROI}_z$ ). A picture of a fabricated prototype wafer is also shown in Figure 5.1 on page 109. The coil windings on each bi-plate were defined, such that each plate occupied nearly identical coil patterns, for the four coils in the entire stack. On one coil, the current spirals inwards and was then connected to the second coil in the centre, where it spirals in reverse, back out again. The coil pattern creation process is further described in Section 4.2 on page 93.

Within the first prototype as shown in Figure 4.2, there was very little space around the central streamline to fit the interconnecting VIA. As a result, the central VIA was designed too small and it was not possible to establish a sufficient electrical contact between the two coil layers. Consequently, the constrained VIA position would have also added additional field distortion.

Since the gradient coils are switched at high currents that cause power losses, effective cooling becomes a challenge. As previously mentioned, two different liquid cooling concepts were considered. For the first fabrication prototype, it was focused on the MIDCOOL design and Figure 4.3 illustrates a preliminary evaluation.

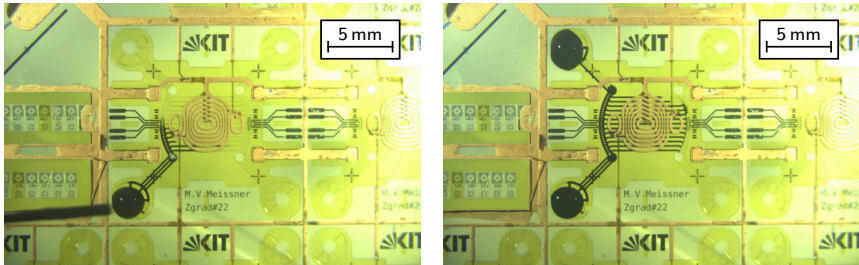


**Figure 4.3:** Selected pictures from a video recording showing the self-filling of the fluidic micro channels.

Self-filling of the rectangular micro-channels was tested by pipetting ink droplets at the subjected inlets. The MIDCOOL design routed the channels between the two field coils and allowed for an improved, liquid tight encapsulation with a lower tendency to leak. There were no trapped air bubbles within the centre channels. The channel depth was  $100\ \mu\text{m}$  which was defined by the utilised SUEX laminate and the channel width was  $128\ \mu\text{m}$ . The channel dimensions were chosen on the basis of previous research. <sup>[142,193,194]</sup> In general, a constrained depth and width of the channel in combination with the large contact angle alter the capillary pressure and prevent self-filling.

Based on the findings of the first prototype, a second design was purposed, with an extended target region in  $y$ -direction ( $\text{ROI}_y$ ) of  $800\ \mu\text{m}$  to keep the inner VIA further apart from the centre. The central VIA and the VIAs at the interconnect were designed with a diameter of  $300\ \mu\text{m}$  and larger and the fluidic channels had additional clearance to these interconnects. The number of contours was reduced from six to five and it became feasible to eliminate the reverse winding at the edges of the main coil. These windings are also highlighted in blue in Figure 4.2 were further substituted within the reworked layout.

An illustration of the mask layout of the second design is shown in Figure 4.4(a). Figure 4.4(b) illustrates the 3D current path, as a line current for the gradient

coil with the supply tracks. The contour plots in the box at the axes edges of the 3D representation refer to the origin but were placed outside for visibility reasons. The field was calculated for the  $B_z$  component using the Biot-Savart law. When routing the feed tracks in the z-direction no field error is produced since those conductors do not exhibit field variations in z-direction. A more

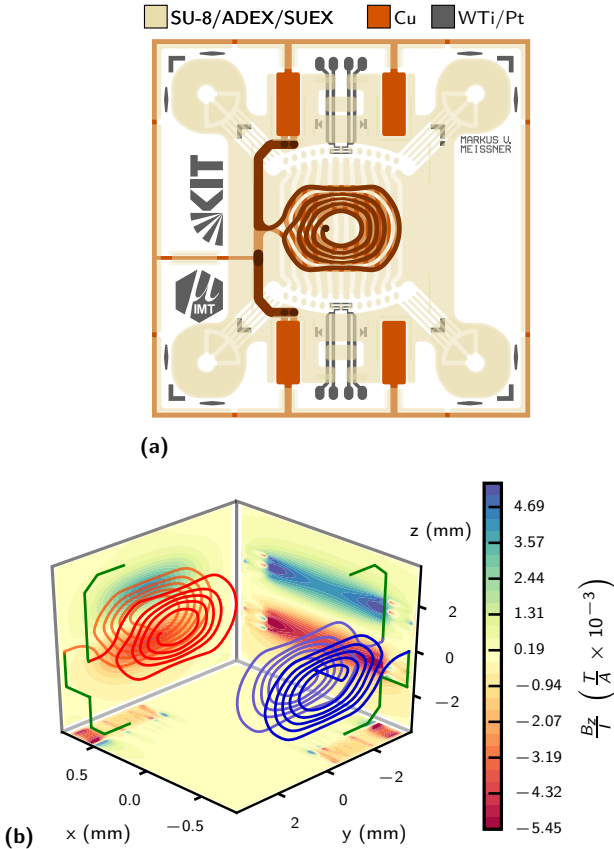


**Figure 4.4:** (a) illustration of the layer structure of the revised uni-axial z-gradient. (b) current path of the uni-axial z-gradient coil.

accurate calculation considering the volumetric current density distribution would have required a more intensive model generation.

Figure 4.5 shows the contour plots of the computed field including the supply tracks for the two central planes. The corresponding ROI is highlighted in grey. On the basis of the MIDCOOL variant, coil patterns were calculated for  $x_0$

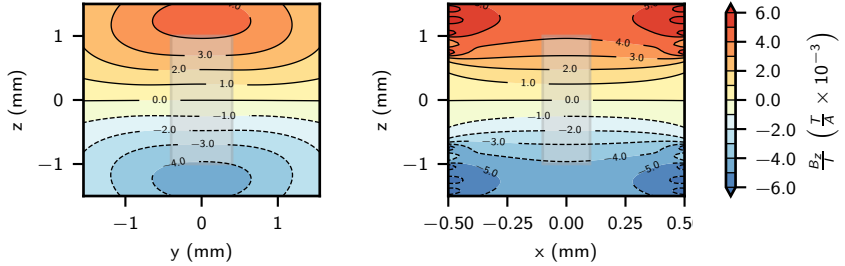
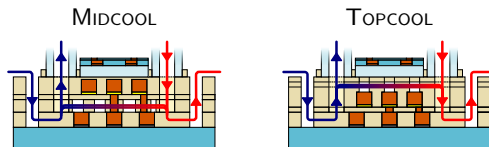


**Figure 4.5:** Field plots of the  $z$  component of the magnetic flux density, computed from the line-current, with  $x_{0Gz_2}$  of  $778 \mu\text{m}$  and  $x_{0Gz_1}$  of  $553 \mu\text{m}$  with the coil patterns as illustrated in Figure 4.4(a).

of  $553 \mu\text{m}$ ,  $678 \mu\text{m}$  and  $778 \mu\text{m}$ . The average error for the single coils of the continuous contours was approximately 1%, and for the discretised contours 3.17%, 2.55% and 1.9% with respect to  $x_0$ . Maximum field errors of 6.27%, 5.03% and 3.84% resulted for the coils respectively.

Table 4.1 lists the design parameters from the theoretical design consideration. At first, the focus was on the MIDCOOL cooling method and the added separation gap for the intermediate cooling layer resulted in a minor decrease in the total gradient strength, with respect to the coil layer that was placed close to the substrate ( $x_{0Gz_2}$ ). The gradient coil distances in the table were based on preliminary estimations, which are not representative to the layer stack of the actual manufacturing process. Both designs were based on a glass spacer thickness  $t_{\text{spacer}}$  of around  $500 \mu\text{m}$ . The coil patterns calculated for the MIDCOOL variant were later used analogously for the TOPCOOL variants, even though they did not match the exact bi-plate separation. Later, the TOPCOOL was



<b>gradient coil separation</b> ( $\mu\text{m}$ ):	$x_{0Gz1}$ :	553	$x_{0Gz1}$ :	553
	$x_{0Gz2}$ :	778	$x_{0Gz2}$ :	678
<b>grad. efficiency</b> ( $\text{T m}^{-1} \text{A}^{-1}$ ):	$\mathbf{G}_{z1} \cdot I^{-1}$ :	2.22	$\mathbf{G}_{z1} \cdot I^{-1}$ :	2.22
	$\mathbf{G}_{z2} \cdot I^{-1}$ :	1.67	$\mathbf{G}_{z2} \cdot I^{-1}$ :	1.85
	$\Sigma \mathbf{G}_z \cdot I^{-1}$ :	3.89	$\Sigma \mathbf{G}_z \cdot I^{-1}$ :	4.07

**Table 4.1:** Theoretical considered parameters of the uni-axial z-gradient consisting of  $2 \times 2$  coil layers according to Figure 4.2.

dimensioned and was introduced to reduce the processing complexity. However, in an ideal scenario, the micro fluidic cooling channels would be routed above each gradient coil layer in a design that would combine the MIDCOOL and TOPCOOL variants. In fact, also a thermal gradient was expected, with respect to the illustrated channel routing in Figure 4.4(a).

Due to some modifications to the fabrication process, the resulting gradient layer stack could not be fabricated according to the theoretically specified coil separations,  $x_{0Gz1}$  and  $x_{0Gz2}$ .<sup>[187]</sup> The manufacturing process and layer build-up of the second iteration is further discussed in Chapter 5 on page 109 and the subjected NMR evaluation in Section 7.2 on page 169. A comparison of the field variation for the design model and the actual manufactured gradient is further shown in Figure 7.12(b) on page 178.

## 4.2 Coil generation from nested contours

To allow the operation of the gradient coil from a single electrical connection, the individual contours from the stream-function contour plot must be interconnected. Figure 4.6 gives an illustrative overview of the interconnection method to define practically realisable coil windings from the nested contours.<sup>[103]</sup>

Figure 4.6(a) shows the individual contours which were separated by additional gap contours. These separating gap contours will, later on, define the electroplating mould throughout fabrication.

First, the coil contours and gaps contours were split at positions where the contours were close to each other. The *split-path* as shown in Figure 4.6(b) was manually placed to intersect through all windings, from the right innermost winding to the left innermost winding. Since the interconnection method contributes an additional field error, the *split-path* was chosen to be far apart from the ROI, at conductor parts with a low  $B_z$  contribution. Here in the illustrated example, the *split-path* bends far apart around the centre of the coil to minimise the field error.<sup>[103]</sup>

A defined distance  $d_{sp}$  was removed from the coil and gap contours. If a significantly large distance was chosen to be removed from the contours, the interconnection bends smoother but may contribute additional field error. The individual contours were then interconnected by approximating a spline in between. To produce the interpolated interconnections, a B-spline representation<sup>[195]</sup> provided by the function `splprep` in the `scipy.interpolate` python module was employed. Five control points were used to define the B-spline. Two control points from the end and start of the gaps/coil contours were used to preserve the first derivative, to achieve a smooth transition between the contour and B-spline. The centre control point was selected on the *split-path*, between the coil contours to be connected. The final interconnected coil and gap curves are illustrated in Figure 4.6(c).

In the next step, the specified maximum track width for the coil and minimum gap width were applied. Throughout the thesis, a minimum gap width of  $85\ \mu\text{m}$  was set to fulfil the requirements for the fabrication. Precisely, the minimum separation gap corresponded to the resolution limit of lithographic mask and minimum feature size of the resist. The coil with a variable track width is illustrated in Figure 4.6(d). To make the designs fabrication-ready, the gap contours were removed. The overlay of the gap track was then subtracted from the coil track which resulted in a variable width of the coil track, with a defined minimum separation gap. This method allowed to approximate the current density much better than by defining a fixed width of the conductors without subtracting the loop separating gap curve.<sup>[103]</sup>

To get the current in and out of the coil, the innermost loop had to be connected back to the outer edge somehow. This step was achieved by using a VIA to connect to a separate layer, on which either a straight thick conductor aligned with the z-axis was used (to minimise heating and unwanted field contributions), or the symmetrically identical winding pattern was used to spiral the current back out to the edge (Figure 4.6(e)).<sup>[187]</sup> By this method, it was also possible to get the current out of the coil without requiring an interconnecting track to be placed on an additional layer. The coil track was then split at an external loop to finally connect it to an amplifier to drive the coil current.

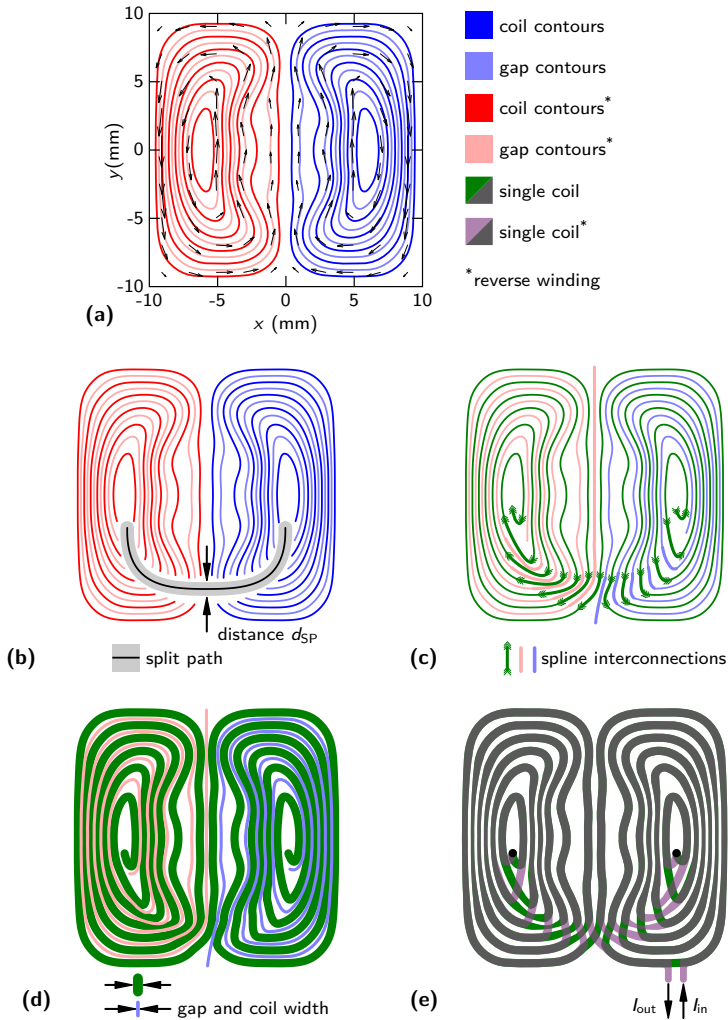


**Figure 4.6:** An illustrative example of how to define an interconnected gradient coil on a single plane. (a) stream function contour plot and associated current density (arrows) for a genuine minimum power x-gradient coil. (b) coil and gap contours split by a manually added path. (c) interconnection of the split contours by a b-spline approximation to create a single coil loop and two gap loops. (d) assigned coil and gap width to define the tracks. (e) dual layered x-gradient with the gap curve subtracted from the coil track. (Figure reproduced from [103])

### 4.3 Tri-axial gradient design

When performing MRI tomography, a tri-axial gradient is generally employed. In addition to the previously presented uni-axial z-gradient, a *tri-axial* gradient design is presented, where the chip is positioned horizontally with respect to the magnet bore. The coil configuration was based on the concept in the introduction, which had been further refined with a streamline-based x-gradient coil (compare with Figure 1.6 on page 32). The tri-axial design is discussed in the following, but within the context of this thesis it was not further experimentally verified.

To build up a tri-axial gradient setup, generally  $2 \times 6$  bi-planar coil layers would be required as shown in Figure 4.7(a). The gradient patterns included a return path and were aligned normal to the main magnetic field direction. As shown in Figure 4.7(b), it was possible to reduce the number of coil layers by combining the y- and z-gradient on the same bi-layer. The y- and z-gradients were based on the Anderson shim coil design,<sup>[77]</sup> and the x-gradient was computed by the aid of the *genuine-minimum-power* design method.<sup>[103]</sup>

Figure 4.8 illustrates the dimensioning and the assembly concept of the tri-axial gradient design. Since the Anderson model was based on a lower number of loops, it resulted in a weaker gradient efficiency, which was about half of the x-gradient efficiency. For the Anderson shim coils, the usable volume resulted from the  $z_{0G_{y,z}}$  distance and also from the length of the straight conductors which was 5.2 mm. The y-gradient generated a stronger gradient field than the corresponding z-gradient coil. The conductor positions of the y-gradient were adjusted with respect to the wire spacing and track width, so that the gradient conductor could be positioned next to the  $G_z$  conductors (see also Table 1.1 on page 23). Since the x-gradient essentially occupied most of the pre-defined gradient space, the straight  $G_y$  and  $G_z$  traces were stretched, to allow for placing the interconnecting VIAs outside. The target field for the x-gradient streamlines and the applied length of the straight y- and z-gradient

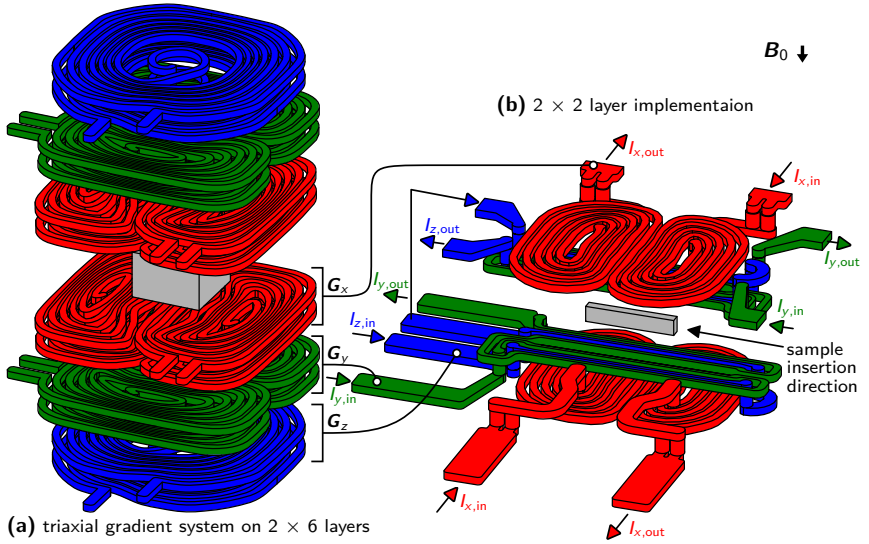


**Figure 4.7:** (a) tri-axial gradient coil composed of  $2 \times 6$  coil layers. (b) simplified tri-axial gradient coil design with the  $x$ -gradient coil based on the stream function method and the  $y$ - and  $z$ -gradient based on the Anderson design, embedded on  $2 \times 2$  coil layers. (Figure adapted from [103])

conductors produced an elongated imaging region, suitable for imaging a single *c. elegans* nematode.

In addition to the gradient homogeneity plots, the gradient strengths for the centre-lines, with respect to the unit-current were plotted as shown in Figure 4.9. Consequently, the sensitive region of the Tx/Rx coil must be limited within the range where the gradient stays positive.

The target region or ROI for the  $x$ -gradient was first set to 2 mm for the  $ROI_x$ , to 800  $\mu\text{m}$  for the  $ROI_y$  and to 300  $\mu\text{m}$  for the  $ROI_z$ . Much comparable to the design process of the uni-axial  $z$ -gradient, the  $x$ -gradient pattern was first calculated for a too small target field in the  $y$ -direction and the central VIAs crossed the straight conductors of the Anderson gradients. By extending the

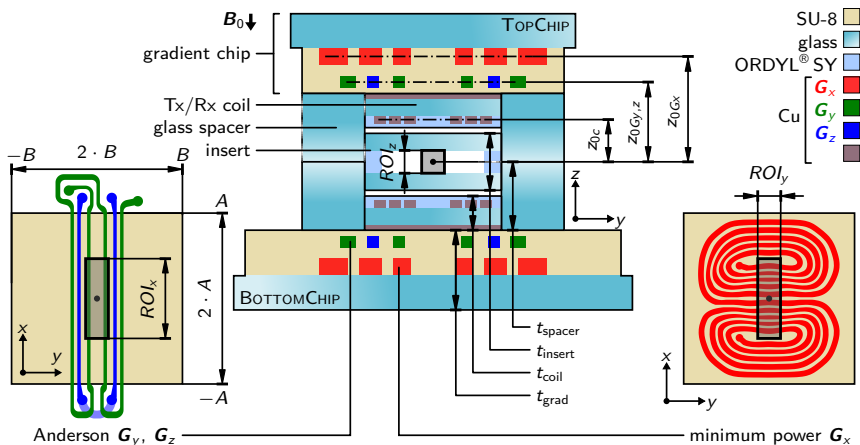


**Figure 4.8:** Cross sectional view of the tri-axial gradient chip, with the gradient coil bi-planes oriented perpendicular to the  $B_0$  field.

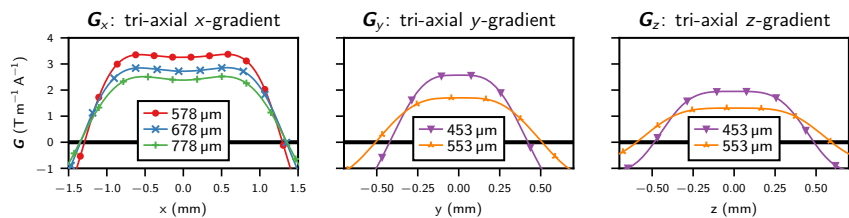


**Figure 4.9:** The gradient strength calculated for the centre line for the tri-axial design with respect to the  $z_0$  bi-plate separation.

target region  $ROI_y$  for the x-gradient to 2 mm, a conformal VIA placement was achieved.

The field linearity must consistently match for all the three gradient axis within the specific ROI and was graphically addressed. The ROI was also defined in accordance with the Anderson gradients, where the size of ROI was smaller and had to be adjusted to confirm with the bi-plate separation and conductor length. When reconstructing an MR image, nonuniformities in the gradient field can

result in voxel shifts or intensity variations. To a certain extent, non-uniformities can be corrected by the post-processing.<sup>[196]</sup>

The  $x$ -gradient was based on a single bi-layer with no reverse winding on an additional layer. Therefore a higher field inhomogeneity due to the asymmetry had to be tolerated. The  $x$ -gradient patterns were calculated for a  $z_0$  displacement of 778  $\mu\text{m}$ , 678  $\mu\text{m}$  and 578  $\mu\text{m}$  which resulted in an average field error for the discretised contours of 7.92 %, 7.24 % and 7.83 %, respectively. Figure 4.10 shows the homogeneity contour plots for a  $z_0$  separation of 678  $\mu\text{m}$ . The homogeneity plots included the tracks for driving the coil as illustrated in Figure 4.7(b).

Figure 4.11 and Figure 4.12 illustrate the gradient homogeneity for the combined Anderson gradients  $\mathbf{G}_y$  and also  $\mathbf{G}_z$ , calculated for a bi-plane separation  $z_{0G_y,z}$  of 553  $\mu\text{m}$ . The field of the Anderson gradients was spatially more confined and the thick, black contours illustrate the positions where the gradient field inverted. The imaging region for the sample must not cross that region to avoid fold-back problems and to maintain a correct encoding.

The achievable gradient efficiencies from the theoretical design process are listed in Table 4.2. To obtain the desired gradient efficiency, also a bi-plate separation using a glass spacer with a thickness  $2 \times 400 \mu\text{m}$  was considered.

For such an arrangement, magnetic susceptibility discontinuities would inevitably occur from the different materials of the stacked layers, which can be further compensated by encoding at a high gradient field strength. The presented gradient setup is particularly suitable for magnets offering very strong  $\mathbf{B}_0$  fields<sup>[29]</sup> that have a compact imaging region, and also for permanent Halbach magnets with a constrained  $z$ -space.

Much comparable to the uni-axial  $z$ -gradient, it would also be feasible to define the coils in a vertical orientation. However then, the Anderson  $y$ - and  $z$ -gradients can not be combined on the same layer, and the  $y$ -gradient efficiency in the vertical orientation would be at least 10 times weaker. A comparative

study on a vertical aligned  $y$ -gradient design was previously discussed by White *et al.* [103]

		MIDCOOL		TOPCOOL	
<b>glass spacer</b> ( $\mu\text{m}$ ):	$t_{\text{spacer}}$ :	500	400	500	400
<b>gradient coil separation</b> ( $\mu\text{m}$ ):	$z_0 G_{y,z}$ :	553	453	553	453
	$z_0 G_x$ :	778	678	678	578
<b>gradient efficiency</b> ( $\text{T m}^{-1} \text{A}^{-1}$ ):	*) $\mathbf{G}_x \cdot I^{-1}$ :	2.36	2.71	2.71	3.20
	***) $\mathbf{G}_x \cdot I^{-1}$ :	2.44	2.78	2.78	3.33
	*) $\mathbf{G}_y \cdot I^{-1}$ :	1.68	2.50	1.67	2.50
	*) $\mathbf{G}_z \cdot I^{-1}$ :	1.31	1.94	1.31	1.94

**Table 4.2:** Theoretical considered parameters for the tri-axial gradient setup. \*) calculated by the Biot-Savart line integral in the centre region. \*\*) calculated from the surface current density, during the coil design process.

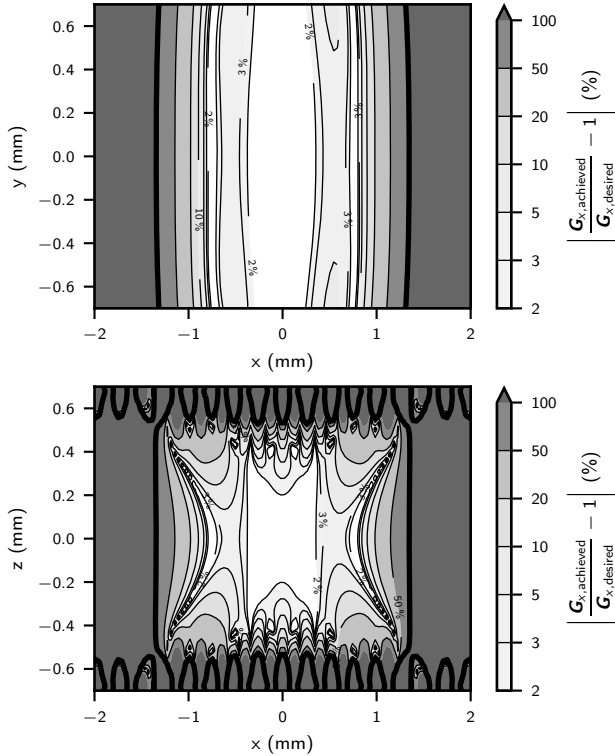


**Figure 4.10:** The homogeneity plot for the *genue-minimum-power* x-gradient with the plotted planes subjected to the centre for a  $z_{0G_x}$  separation of  $678 \mu\text{m}$ .

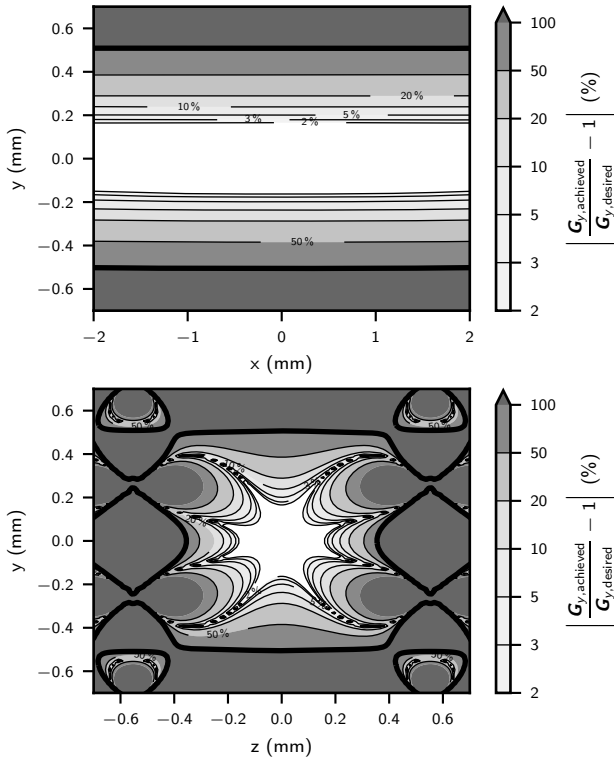


**Figure 4.11:** The homogeneity plots with the plotted planes subjected to the centre for a  $z_{0G_{y,z}}$  separation of  $553 \mu\text{m}$  for the Anderson  $y$ -gradient.

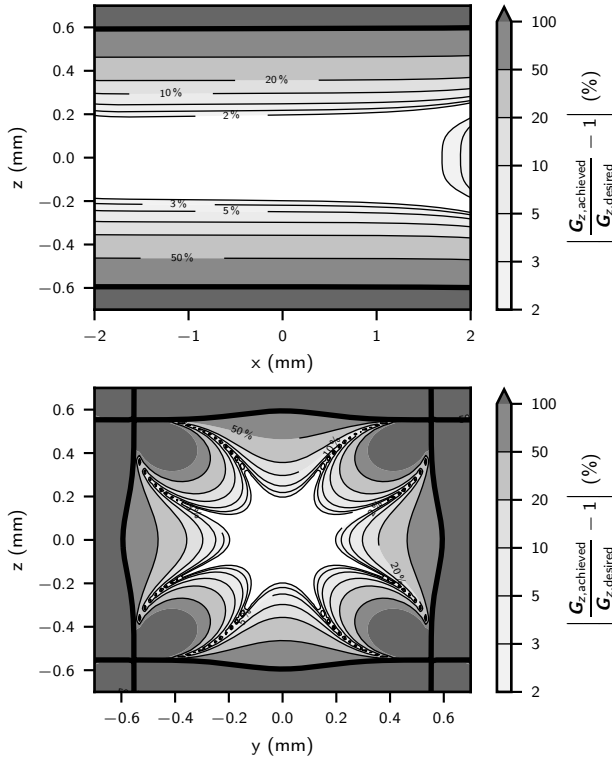


**Figure 4.12:** The homogeneity plots with the plotted planes subjected to the centre for a  $z_0 G_{y,z}$  separation of  $553 \mu\text{m}$  for the Anderson z-gradient.

## 4.4 Supplemental components

The gradient coil separation for the bi-planes,  $x_{0G_{z1}}$  and  $x_{0G_{z2}}$  for the uni-axial z-gradient and similarly  $z_{0G_{y,z}}$  and  $z_{0G_x}$  for the tri-axial gradient, had a substantial influence on the efficiency and the design of the interior. The composition of the sample insert and the Tx/Rx coil with the corresponding glass spacer are listed in Table 4.3.

**Flip-chip spacer.** Similar to the work of Spengler,<sup>[56]</sup> the flip-chip spacers were machined out of glass wafers, which possess a uniform thickness. In the theoretical design process, two different gradient bi-plate separations of  $2 \times 500 \mu\text{m}$  (*option 1*) and  $2 \times 400 \mu\text{m}$  (*option 2*) were considered and a stack of two wafers was used for this purpose. It would have been possible to make these spacers from a single wafer, but for the total thicknesses required, there was no suitable wafer available and it would have also been difficult to perform accurate dicing. A monolithic, one-piece coil and spacer assembly was not pursued, since it was focused on a modular, open-able assembly for easier adjustment of the individual components. The modular concept mitigated installation risks, but consequently caused higher tolerances in the final assembly.

**Sample insert.** The concept of the sample holder is comparable to a micro flow and culture cuvette,<sup>[197]</sup> used in micro biology, that was further refined for NMR applications.<sup>[198]</sup> The fabrication of such a sample insert can be executed by substrate bonding. The total sample holder thickness would measure less than  $300 \mu\text{m}$  by using  $100 \mu\text{m}$  glass substrates and in between ORDYL<sup>®</sup> SY 390. Despite allowing an insert positioning tolerance of approximately  $50 \mu\text{m}$ , the sample is always within the imaging range, with respect to the subjected ROI of the presented gradient coils. However, the dimensions of the sample insert would also permit to use a commercially available rectangular capillary tube instead (Product 5012, sample space

depth 100  $\mu\text{m}$ , width 2 mm, glass thickness 100  $\mu\text{m}$  and capillary length 5 cm, VitroCom, USA).

	<i>option 1</i>	<i>t</i> ( $\mu\text{m}$ )	<i>option 2</i>	<i>t</i> ( $\mu\text{m}$ )
glass spacer ( $t_{\text{spacer}}$ ):		500		400
sample insert:	D 263 <sup>®</sup> T ECO	100	D 263 <sup>®</sup> T ECO	100
	ORDYL <sup>®</sup> SY 390	90	ORDYL <sup>®</sup> SY 390	90
	D 263 <sup>®</sup> T ECO	100	D 263 <sup>®</sup> T ECO	100
	$t_{\text{insert}}/2$ :	$\Sigma$ 145		$\Sigma$ 145
Tx/Rx coil:	ORDYL <sup>®</sup> SY 330	30	ORDYL <sup>®</sup> SY 317	17
	ORDYL <sup>®</sup> SY 355	55	ORDYL <sup>®</sup> SY 320	20
	MEMpax <sup>®</sup>	200	MEMpax <sup>®</sup>	150
	Cu	20	Cu	20
	$t_{\text{coil}}$ :	$\Sigma$ 305		$\Sigma$ 207
$t_{\text{insert}}/2 + t_{\text{coil}} \approx$		450		350

**Table 4.3:** The two coil and sample insert options to match with the two glass spacer thicknesses. MEMpax<sup>®</sup> and D 263<sup>®</sup> T ECO are borosilicate glass-ware that were purchased from SCHOTT Malaysia.

With respect to the NMR measurement principle, a suitable Tx/Rx coil design must be chosen to exhibit its  $\mathbf{B}_1$  field orthogonal to the direction of  $\mathbf{B}_0$ . In principal, the magnetic dipole of the RF coil generates in the near field a high magnetic field strength and this effect is used to achieve the high sensitivity of the microcoil.

Meier *et al*<sup>[54]</sup> designed a solenoid micro coil with a sample capillary tube diameter of 150  $\mu\text{m}$ . The solenoid had a distance of 100  $\mu\text{m}$  to the sample, whereas the  $\mathbf{B}_1$  homogeneity becomes somehow inferior close to the windings. A higher filling factor was achieved by Kamberger *et al*<sup>[199]</sup> who applied the solenoid support structure from the outside. Solenoids achieve the highest sensitivity, but they require an appropriate assembly concept, since the aforementioned coils use most of the space for the interconnections and support structures. Massin *et al*<sup>[61]</sup> placed the sample capillary glass tube directly towards a copper

planar micro coil, and the sample was only separated by the tube wall that had a thickness of 190  $\mu\text{m}$ .

However, in the aforementioned articles, the employed substrate materials were too thick to be incorporated into the demonstrated micro gradient. Because of the limited space, an adjusted coil assembly concept was considered.

Figure 4.13 illustrates the purposed bi-planar micro coils. In order to minimise the entire complexity, the Tx/Rx micro coil was fabricated in a separate batch. To avoid wrap around artefacts of long samples, it must be insured that the RF sensitivity from the body coil is low enough outside of the ROI. Another possibility would be to restrict the sample container to the ROI. To attenuate the  $^1\text{H}$  signal from the liquid cooling of the micro gradient, a Cu layer of 20  $\mu\text{m}$  was considered, that can be structured on the rear of the substrate of the receive coil. The focus on the layer stack-up was *option 1* in Table 4.3, by defining the RF coil using electroplated tracks into the ORDYL<sup>®</sup> SY, in a much comparable way as described in Section 3.2. With minor adjustments to the dual-stack of the ORDYL<sup>®</sup> SY, *option 1* would also allow the integration of Spengler's wire-bonded *Helmholtz* coil.<sup>[56]</sup>

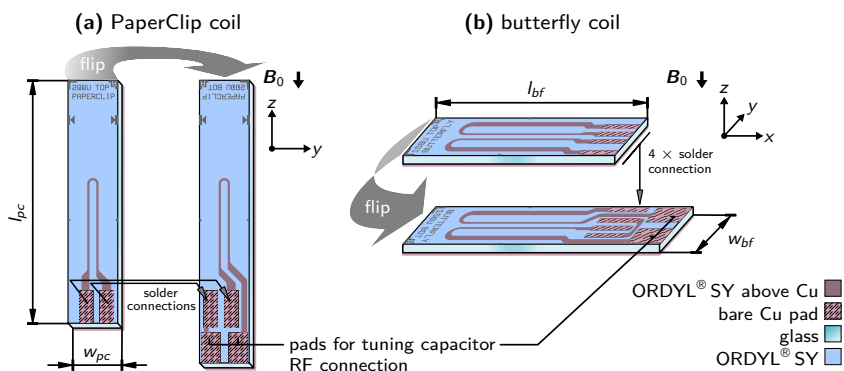


**Figure 4.13:** The design concept of (a) the PAPERCLIP micro coil, and (b) the bi-layer butterfly coil.

**Tx/Rx coil (PAPERCLIP) for the uni-axial gradient.** For the uni-axial gradient, a bi-layer planar-shaped surface coil was designed, which consisted of a single loop on each layer as shown in Figure 4.13(a). The coil shape had a close similarity to a saddle coil<sup>[39,200]</sup> and was stretched to capture the spins within the elongated ROI of the z-gradient. As illustrated in the Figure, the top glass slide on the *left hand side* was flipped above the glass slide on the *right hand side*. The RF interconnection of the coil and the connection between the bi-plates were realised by solder connections and the two glass-slides were displaced by the thickness of the sample insert. The simplistic coil shape allowed for an implementation on a glass slide with a width  $w_{pc}$  of 2 mm and a length  $l_{pc}$  of 10 mm. The distance between the coil traces was 400  $\mu\text{m}$  and the trace width was 100  $\mu\text{m}$ .

**Tx/Rx coil for the tri-axial gradient.** For the tri-axial gradient, a suitable Tx/Rx coil would be a solenoid or the so called *butterfly* coil.<sup>[64]</sup> An adjusted *butterfly* coil design is shown in Figure 4.13(b) and allows for an implementation on a bi-plane, aligned in the same orientation as the respective gradient bi-plates. The top glass slide was considered with a dimension of  $w_{bf}$  of 2.2 mm and  $l_{bf}$  of 8 mm.

The u-shaped bi-layer coil is further called the PAPERCLIP micro coil, which was investigated experimentally in Section 7.2 on page 169. The fabrication steps to define the PAPERCLIP micro coil are listed in Section A.2 on page 220 and a detailed description regarding the fabrication process of the gradient system is provided in the next chapter.



## 5 Gradient chip fabrication

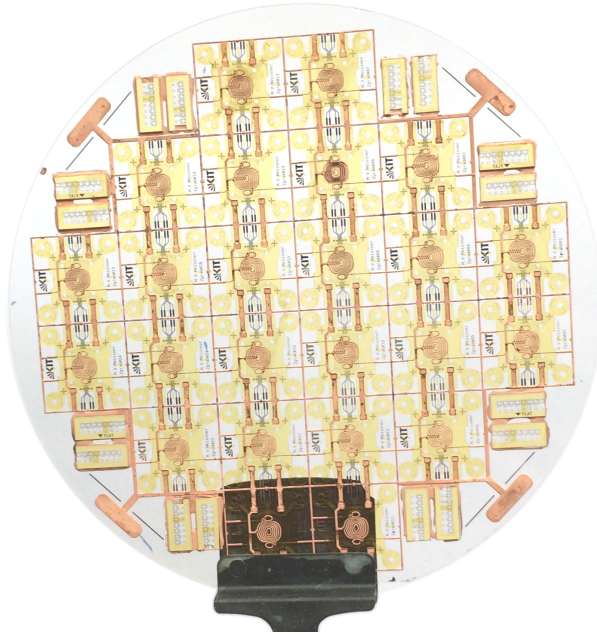


**Figure 5.1:** The first manufactured processing prototype of a micro z-gradient based on a 4" glass substrate.

This chapter discusses the manufacturing process to define bi-planar arranged miniaturised gradient chips.<sup>[187]</sup> Figure 5.1 shows the first prototype of a wafer containing z-gradient coils. The following description covers the second iteration of the manufacturing process, that was based on the methods discussed in Chapter 2 on page 37. Figure 5.2 and in addition Figure 5.3 on page 111

illustrate the significant processing steps to define the gradient coil metallisation and the fluidic cooling network. A detailed processing recipe is provided in the appendix, in Section A.1 on page 195.

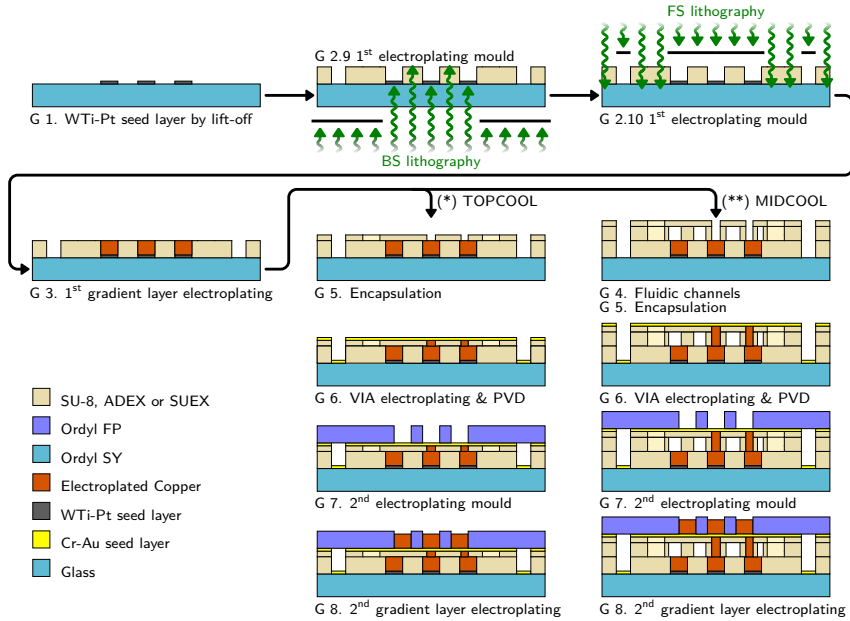


**Figure 5.2:** The first part of the fabrication process. The process flow is completed in Figure 5.3 on the facing page. (\*) TOPCOOL and (\*\*) MIDCOOL indicate the two process variations. (Figure adapted from [187])

After patterning the first coil layer, two processing variants for the liquid cooling were pursued. The TOPCOOL variant implemented the cooling channels above the second coil layer as shown in the latter sketch of Figure 5.3. In the MIDCOOL process variation, the cooling channels were embedded in between the two coil layers. The intermediate resist layers had a different thicknesses because of the added cooling channels.

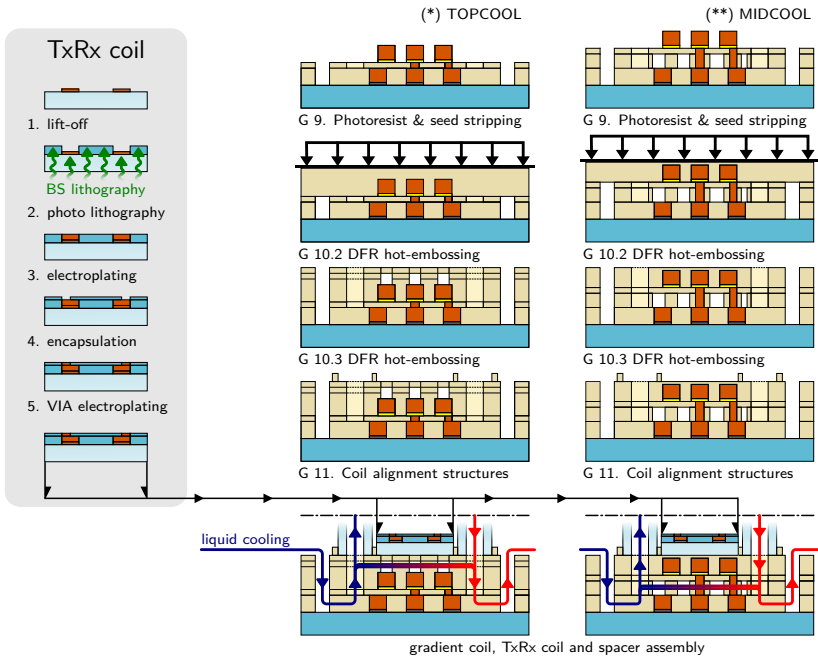


**Figure 5.3:** The second part of the fabrication process. (Figure adapted from [187])

Processing of the Tx/Rx coil, as shown in Figure 5.3 was done in a separate batch. Within the final assembly, the Tx/Rx coil was then manually placed on top of the gradient chip. To enhance visual inspection and to facilitate the chip assembly, mainly transparent photo-polymers and substrate materials were employed.

For the photo lithography, polymer film masks ( $\approx 12$  € per mask) were used, which were a more cost-saving alternative to e-beam written chromium masks on a glass master. The resolution of the polymer-film masks was 25.000 dpi and offered a minimum line width of  $10\ \mu\text{m}$  to  $20\ \mu\text{m}$  (Fotoplot, KOENEN GmbH). However, the polymer master absorbed approximately 30 % of the

incident UV-light at a wavelength  $\lambda$  of 365 nm and consequently required an increase of the lithography dose.

Due to adaptations within the production process, there were also changes in the gradient coil bi-plate separation. Table 4.3 describes the essential stack of permanent resist layers with respect to the bi-plate separation, as they were applied within the fabrication. More details are provided in following sections. The coils with the adjusted separations were not recalculated at this point. The resulting gradient field for the uni-axial gradient is further investigated in Section 7.2.3 on page 176.

TOPCOOL				MIDCOOL			
layer:	$t$	<i>opt. 1</i>	<i>opt. 2</i>	layer:	$t$	<i>opt. 1</i>	<i>opt. 2</i>
	( $\mu\text{m}$ )	( $\mu\text{m}$ )	( $\mu\text{m}$ )		( $\mu\text{m}$ )	( $\mu\text{m}$ )	( $\mu\text{m}$ )
glass spacer:		500	400	glass spacer:		500	400
ADEX	50			SUEX (*)	90	$\times_0G_{z2}, z_0G_{y,z}$ : 555	455
ADEX	50			ADEX	50		
SUEX (*)	90	$\times_0G_{z2}, z_0G_{y,z}$ : 655	555	SUEX (*)	90	$\times_0G_{z1}, z_0G_x$ : 780	680
ADEX	50			SU-8	100		
SU-8	100	$\times_0G_{z1}, z_0G_x$ : 790	690	Borofloat 33	500		
Borofloat 33	500						
$\Sigma$	840			$\Sigma$	830		

**Table 5.1:** Description of the layer stack-up as it was applied within the manufacturing process. (\*) The thickness of the SUEX layer got reduced by approximately 10  $\mu\text{m}$  to 15  $\mu\text{m}$  within the vacuum lamination process. The ADEX layer that was applied for the coil and spacer alignment was omitted from the list.

## 5.1 Plating seed and electroplating mould

Processing started on bare 4" Borofloat 33 (Schott Glass Malaysia) substrates, that were wet-chemically cleaned by piranha etch solution, rinsed in DIW and spin dried (see Section A.1 on page 195, G 1.1).<sup>[187]</sup> As a preparation for the ma-N 1440 lift-off resist (Micro Resist Technology GmbH), that required HMDS surface functionalisation, O<sub>2</sub> plasma was performed to saturate an oxide layer on the glass surface. The plasma power was between 200 W to 300 W using a 13.56 MHz RF source. The substrates followed a HMDS treatment to make the hydrophilic surfaces more hydrophobic, which was an important precondition to enhance the resist adhesion.

The initial plating seed was patterned by lift-off processing and the ma-N 1440 negative tone lift-off resist was applied by spin coating. Subsequently, substrates were pre-baked and exposed by lithography (see G 1.8). The thickest resist variant from the ma-N 1400 series was chosen to facilitate the lift-off after sputtering. In fact, the targeted patterning required a minimum resolution of at least 20 µm which was fulfilled by the chosen 4 µm thick resist. To resolve a strong undercut, the development time was increased to 155 s using the ma-D 533s developer (Micro Resist Technology GmbH). Even when developing an undercut of 1 µm to 2 µm, the ma-N resist remained in strong adhesion towards the substrate. If the same alkaline development bath of 0.5 L was used for more than 6 substrates, the development time was generally increased by 5 s to 10 s as the solubility decreased, and consequently, unexposed residues remained on the substrate.

The manufacturer of the ma-N 1400 reported an additional thermal post-baking step combined with deep UV flood exposure to endure elevated temperatures (above 120 °C) during the physical vapour deposition (PVD).<sup>[144]</sup> Such a thermal post-treatment was not considered in order to limit cross-linking and to preserve the solubility of the resin in acetone or dimethyl sulfoxide (DMSO) after the PVD.

The PVD was started at a vacuum pressure between  $4.0 \cdot 10^{-6}$  mbar to  $8.0 \cdot 10^{-7}$  mbar. Ar gas was introduced and the 9 nm thick W/Ti adhesion layer was sputtered at 100 W. After a waiting time of at least 10 min, the 80 nm thick Pt layer was deposited at 300 W RF power. Lower sputtering peak temperatures were achieved by adding additional waiting times. The lift-off was conducted in DMSO and three alternating acetone bathes, followed by an IPA rinse and a final quick-dump-rinsing (QDR).<sup>[187]</sup>

If the ma-N resist was extensively cross-linked, lift-off release was still possible using the mr-Rem 700 stripper (Micro Resist Technology GmbH) or mechanically with the aid of a microfiber swab. After the lift-off, organic contaminants and potential residues of the ma-N 1400 lift-off resist were removed by a supplemental standard wet cleaning procedure (type (III), see A.1, page 198, G 2.1).

A freshly deposited Pt thin film exhibits a water contact angle between  $25^\circ$  to  $40^\circ$ . However, Pt is a catalytic material and a variety of chemical contaminants like CO, hydrocarbons and other organic compounds can absorb on the Pt surface and result in a different wetting behaviour. The Pt thin film can again be changed more hydrophilic by an oxygen plasma flash, similar as the Borofloat 33 surface can be activated.<sup>[201]</sup> Pt as the initial layer was selected because its suitable wettability of the electrolyte and Cu electroplating compatibility. Pt has almost the same temperature coefficient as the Cu but shows a more linear behaviour. Its excellent chemical stability made it suitable for the first permanent metallisation, since it was not further etched by the utilised Au, Cr and Cu etchants. This property made it possible to permanently retain the Pt patterns on the substrate to structure the alignment marks for the lithography and lately wafer dicing.

Within the application, the applied WTi/Pt metallisation not only served as the seed layer for the electroplating, it was also used to implement resistance temperature detectors (RTDs) to detect heat-up of the gradient coils.<sup>[187]</sup> Much similar as described in Section 3.2.1 on page 72, the WTi/Pt plating

seed was used to perform the back-side (BS) lithography to structure the SU-8 based electroplating mould.

Before applying the SU-8 3050 resist, a plasma activation was again performed. To reduce the surface tension and to additionally clean the glass substrate, an oxygen plasma flash was performed for 10 min at 80 W. A stronger plasma of more than 120 W altered the Pt film.

SU-8 3050 with a targeted thickness of 100  $\mu\text{m}$  was applied by spin coating (G 2.7). For an improved SU-8 adhesion, the substrates were baked at 200  $^{\circ}\text{C}$  for around 30 min, to dehydrate the glass surface. Optionally, TI Prime (Micro-Chemicals GmbH) can be applied beforehand, to promote the SU-8 adhesion (G 2.5). Strong SU-8 adhesion is imperative for all further processing steps, especially for the implementation of liquid-tight, micro-fluidic cooling channels. The wafers did not cool down completely and had an approximate temperature between 70  $^{\circ}\text{C}$  to 40  $^{\circ}\text{C}$  while pipetting 3 mL to 4 mL of the SU-8 resist. Besides, the grid-structured Pt tracks simplified the manual deposition of the SU-8 resist to the rotational centre of the glass substrate. In comparison to the SU-8 processing recommendations, the spin-coating parameters were adjusted to the local cleanroom conditions. The final rotational speed was increased from the given value in the datasheet<sup>[202]</sup> of 1000 rpm to 1250 rpm and the final spin duration was extended to 35 s.

The soft-bake of a SU-8 layer thicker than 100  $\mu\text{m}$  required a special procedure. Lee *et al*<sup>[203]</sup> achieved a more uniform surface quality of the film by performing the soft-bake while keeping an atmosphere of edge bead removal (EBR) solvent above the substrate.

In here, the substrates were covered by petri dishes and soft-baking was performed on a levelled hotplate for 1 h and 30 min at 95  $^{\circ}\text{C}$ . The hotplate was heated up slowly during 3 min to 5 min to decrease the rate at which the solvents evaporated. For the first 45 min, the bake was carried out with the wafers covered by petri-dishes to keep an atmosphere of the evaporating cyclopentanone

solvent. This method lead to a more planar resist surface without wrinkles in the resist film. During the remaining soft-bake, the petri-dishes were removed to condense most of the solvent.

After the cool-down, the lithography was performed subsequently from both sides of the wafer. Therefore two shadow masks were employed. The required doses for the back-side (BS) and front-side (FS) lithography were determined by an exposure series. An anti-reflection foil (Spectral Black, Acktar Ltd.) was placed between the lithography chuck and the wafer, to suppress back-reflections through the transparent glass substrate.<sup>[187]</sup>

**Exposure from the rear.** (G 2.9) During the first exposure step, the electroplating mould was structured by illuminating through the BS of the transparent wafer. This method resulted in high-aspect-ratio electroplating moulds. The photo mask as shown in G 2.9 on page 200 was only used to spare out the chip regions in which the fluidic structures were structured by the FS lithography in the second step. Technically, the first mask only contained openings to expose through the already structured Pt plating seed to define the moulds for the gradient coils. The vapour deposited Pt structures were subject of the BS lithography step and masked the mould for the electroplating. A polymer-mask was completely sufficient for this purpose, that was placed towards the BS on the bare glass of the wafer. It was not intended to achieve high resolution structuring by this foil mask, since it also was positioned at a distance of 500  $\mu\text{m}$  above the SU-8, separated by the glass substrate.

Adding an anti-reflection foil below the substrate was nevertheless necessary to suppresses imprints from the vacuum chuck. Otherwise the SU-8 coated wafer would be pulled directly by the vacuum towards the chuck. In addition, the exposure from the rear had to be performed before the exposure of the topside, since the partially exposed SU-8 got deformed during the WEC when loaded into the mask-aligner. The spin-coated SU-8 remained thicker at the edge of the wafer and consequently only

the edges were pressed gently and showed rough imprints from the anti-reflection foil. Anyway, these edge regions were spared out by the first mask and were not subjected to the BS lithography step. An exposure dose without *i-line* filtering of  $550 \text{ mJ cm}^{-2}$  was sufficient.

**Exposure from the front.** (G 2.10) To allow structuring of the fluidic supply channels and edges structures of each chip, a second mask got involved, which inversely blocked the light from exposing the electroplating moulds for the gradient coils. In fact, the gradient coil electroplating moulds were already defined by the previous lithography step (see Figure 5.2, compare step G 2.9 with G 2.10).

A significantly higher exposure dose of  $740 \text{ mJ cm}^{-2}$  was experimentally found to achieve sufficient cross-linking and adhesion between the SU-8 and the glass substrate. An important aspect of the conventional FS lithography was light absorption within the SU-8 resist. For a different, but comparable type of SU-8, Ling *et al*.<sup>[204]</sup> determined the optical absorption in dependence to the SU-8 thickness. From the incident UV light, approximately 70 % reached the interface between a  $100 \mu\text{m}$  thick SU-8 epoxy and the glass wafer. The required FS exposure dose was about 30 % higher, when compared to the BS exposure. In terms of the achievable aspect ratio, Kang *et al*.<sup>[205]</sup> investigated the sidewall profiles of SU-8 when exposing it at different doses. A higher exposure dose caused an enlarged resist width in proximity to the substrate. In contrast, the lower exposure energy during the BS lithography exhibited nearly vertical sidewalls.

It was necessary to design the edges of the mask with an offset of at least  $50 \mu\text{m}$  to  $80 \mu\text{m}$  from the Pt structures to suppress light reflections from the Pt tracks, while maintaining the required exposure dose. Designing any mask edge too close to the Pt tracks caused cross-linking of a thin SU-8 layer above the tracks, which further prevented any electro-deposition.

It should be mentioned that the BS exposure produced an excellent resist adhesion compared to the FS exposure, since the incident light exposed the interface between the glass and the SU-8 with highest exposure energy. To maintain a consistent exposure of the SU-8 film, an overlapping area around the gradient structures of approximately 50  $\mu\text{m}$  was exposed from the front as well as from the rear.

The substrates were subjected to a PEB at a maximum temperature of 75  $^{\circ}\text{C}$ , to reduce stress within the SU-8 film.<sup>[131]</sup> After the development, profiles of the SU-8 film thickness were measured. The SU-8 thickness of a batch of four wafers at four different positions is listed in Table A.1 on page 202. The entire batch measured a mean layer thickness of 99.7  $\mu\text{m}$  with a standard deviation of 3.0  $\mu\text{m}$ . Depending on the age of the SU-8 resist and storage condition, the solvent level may decrease and will result in even higher film heights of up to 130  $\mu\text{m}$ .

## 5.2 Micro electroplating of the first gradient coil layer

Filling up the SU-8 moulds with copper by means of electroplating required a precise control of the electroplating process.<sup>[187]</sup> Prior the electroplating, an oxygen plasma flash was performed. Oxygen plasma activation of the SU-8 surface was indispensable to achieve improved wetting of the electrolyte. The power of the RF plasma source was kept low, such that the energised oxygen ions did not immobilise the Pt atoms of the seed layer.

In a preliminary investigation, the oxygen plasma power was raised to 200 W for around 15 min. Such an elevated plasma penetrated the Pt thin film and nearby SU-8 sidewalls got covered with the ejected, re-sputtered Pt atoms. Consequently, the sidewalls possessed sufficient electrical conductivity and eventually, copper was deposited (see Figure A.3 on page 204).

A plasma power as low as 80 W was appropriate. The substrates were immersed into the electroplating bath without wait time, since the plasma surface activation of the mould and seed layer degraded over time.<sup>[137,201]</sup>

Figure 5.4 shows the layout and the plated areas of the wafer. Since the electroplating started on a structured seed, all the parts to be electroplated had to be electrically connected. The structured seed layer had a significantly higher resistance and affected the local plating height. Finally, higher height variations occurred, compared to a wafer with a plating seed that covered the entire surface.

Due to the high Pt track resistance of the plating base, areas at the edge of the wafer, in proximity to the terminal plating contacts reached a higher current density than areas at the centre of the wafer. As a compensation, the electroplating process was started at current densities between  $0.1 \text{ A dm}^{-2}$  to  $0.3 \text{ A dm}^{-2}$ . At such low current densities, a first Cu layer was formed to initially decrease the resistance of the seed. After plating up to a thickness of approximately  $2 \mu\text{m}$ , it was possible to increase the current density to accelerate the plating speed.

The Cuprostar LP-1 electrolyte was heated to a temperature of  $30^\circ\text{C}$ . Sufficient bath movement was an essential requirement and the magnetic stirrer was adjusted to a low rotational speed between 80 rpm to 90 rpm. Higher electrolyte temperatures of up to  $40^\circ\text{C}$  allowed for higher current densities, but led to visible bending of the substrate, due to thermal expansion. The structured feed tracks which surrounded each chip are illustrated in Figure 5.4(a). No Cu was deposited onto the RTD and dicing marks, since these Pt metallised areas had no electrical connection, as shown in Figure 5.4(b).

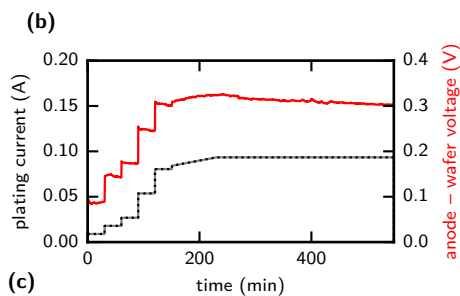
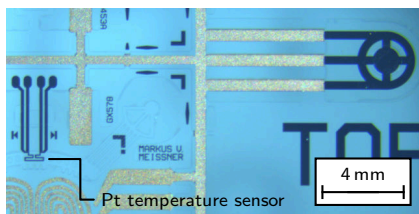
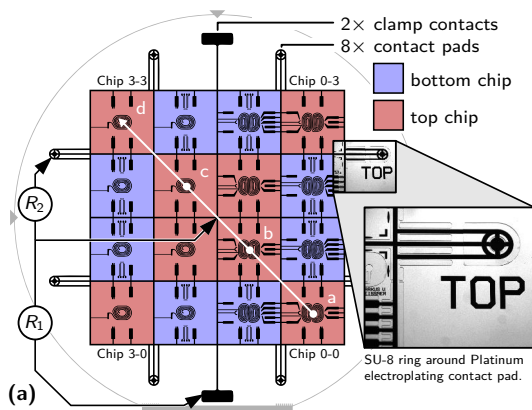


**Figure 5.4:** Electroplating of the 1<sup>st</sup> Gradient coil layer. (a) The Pt metallisation is illustrated in black. The electrical resistance  $R_1$  measured between the clamp contact and the centre was  $107.6\ \Omega$ .  $78.24\ \Omega$  was the resistance between one contact pad and the centre ( $R_2$ ). The lateral tracks of the Pt grid at the edge of each chip measure a resistance of  $34.02\ \Omega$ . (b) The electrically connected coil structures were exclusively electroplated with Cu. (c) Electroplating sequence for plating the 1<sup>st</sup> coil layer for the top gradient coil. This sequence was used with the custom designed PMMA holder as shown in Figure A.3 on page 204.

In the layout, two different contacting methods were tested, to build up the current path through the electroplating bath:

**Clamp based contacting method.** One of the two opposing large pads which were patterned at the edge of the wafer were connected by alligator clips. The substrates were then rotated during the deposition, in order to improve the homogeneity of the plated Cu height. The connected pad was not immersed into the plating bath and no copper deposition occurred on the respective pad. To enhance the conductance of each contact pad, right at the very beginning of the plating, it was necessary to rotate the wafer after a initial Cu layer was formed.

The voltage drop was recorded, as shown in Figure 5.5. Figure 5.5(a) indicates a reduction of the anode to wafer voltage since the resistance of the Pt seed layer continuously reduced as more Cu was deposited. After to the first plating sequence, the contact resistance between at the clamp was reduced further, resulting in a lower voltage drop (Figure 5.5(b)). To reach the target Cu thickness of 100  $\mu\text{m}$  another two plating sequences were carried out at moderate current densities (Figure 5.5(c), Figure 5.5(d)). The total plating time was 9 h 39 min.

**8-pin contacting method.** (G 3.2) To provide a more homogeneous current distribution to the Pt grid, additional contacts positions were established. Eight additional contact pads were added around the edge of the wafer, as shown in Figure 5.4(a) and Figure 5.4(b). Around the Pt pads, 4 mm wide SU-8 rings were patterned within the previous lithography step (G 2.10). O-rings were placed between the SU-8 3050 rings and the custom designed wafer holder in Figure A.3 on page 204 to protect the connecting spring contacts and Pt pads from being exposed to the Cu electrolyte. The o-rings were made of fluoroelastomer (FKM) with an inner diameter of 1.5 mm an width of 1 mm (Alwin Höfert KG, Ammersbek, Germany). The wafer holder was manufactured out of two laser-cut PMMA plates with a thickness of 5 mm and 4 mm. Grooves were milled (monoFab SRM-20,

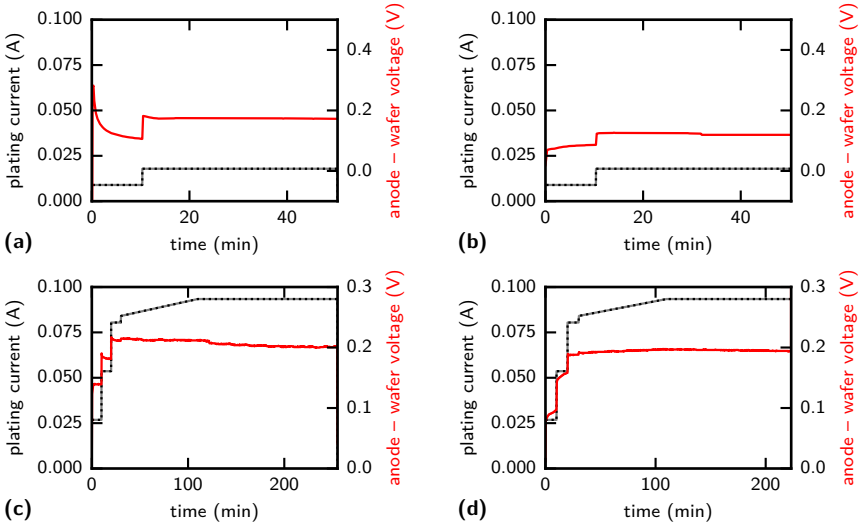


**Figure 5.5:** Electroplating sequences by contacting the wafer with a single clamp. **(a)** The first plating step to deposit an initial layer of  $2\ \mu\text{m}$  Cu. **(b)** Plating of another  $2\ \mu\text{m}$  thick layer with the wafer connected to the opposing clamp. The opposing clamp was already covered with Cu. **(c)** and **(d)** Further electroplating to the desired height.

Roland DGA Corporation) into one PMMA plate to place the gold-coated spring contacts (FK-480, Fixtest Prüfmittelbau GmbH) and cable connections. With the spring contacts in place, the two plates were glued together using polyurethane (PUR) two-component adhesive (technicoll<sup>®</sup> 9430-1, Ruderer Klebetechnik GmbH). During the electroplating, the transparent PUR adhesive turned marginally brown, but remained stable and did not dissolve within the acidic electrolyte. Also bonding of the two PMMA plates using a methyl methacrylate (MMA) reactive adhesive is possible but was not carried out due to the very short curing time (5 min to 10 min).

There was no need to rotate the wafer when mounting it into the PMMA wafer holder since the electrical contacts were distributed around the

substrate and current supply was symmetrically. The electro-deposition could be carried out with a single sequence with a total plating time of 9 h and 7 min as shown in Figure 5.4(c).

Both contacting methods were compared by recording surface profiles as shown in Figure 5.6. Since various different coil designs were implemented on the same wafer, only the surface profiles of coils with an equal effective plating area allow for a comparison. For the clamp based contacting method, a mean height difference of  $14.1\ \mu\text{m}$  was achieved for the z-gradient coils (c) vs. (d) (Figure 5.6). The mean height difference for the 8-pin contacting method showed a lower variation of  $3.8\ \mu\text{m}$  (comparing the z-gradient coils (c) vs. (d)). Another important advantage of the 8-pin holder is the possibility to carry out the entire electroplating by a single sequence, without user intervention. Regardless of the contacting methods, additional height variations resulted from the Pt track width and SU-8 height. Nevertheless, it was possible to investigate different coil designs in the same layout.

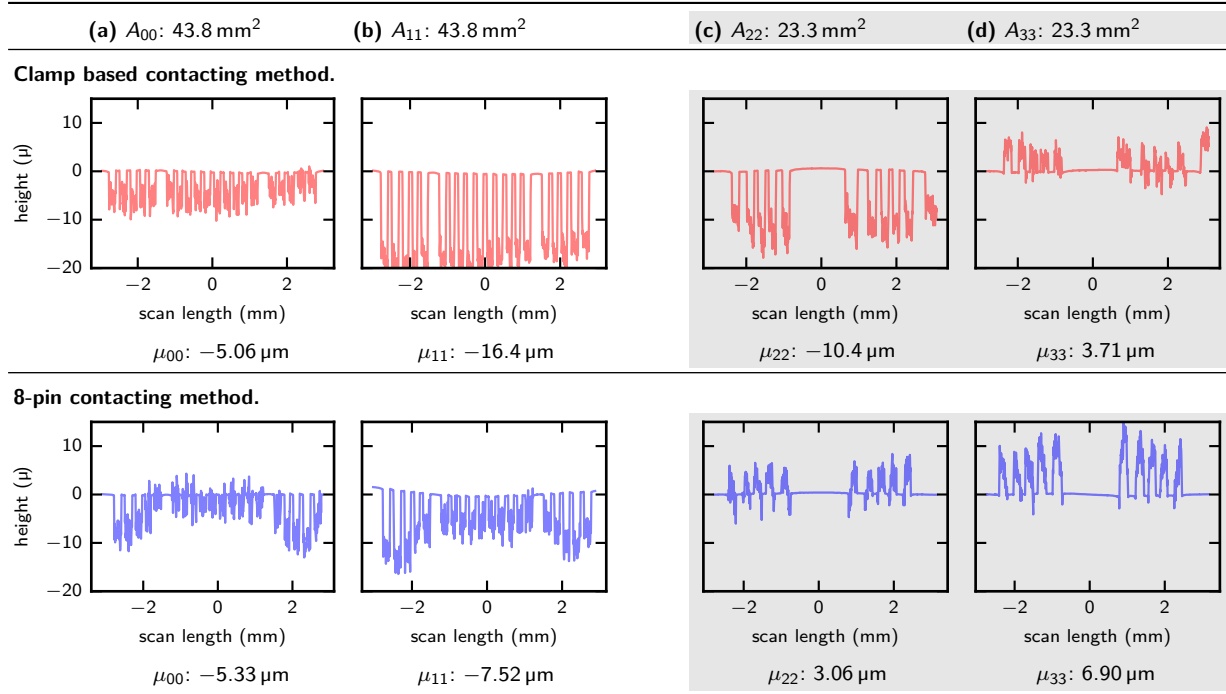


**Figure 5.6:** Profiles of the electroplating for the TOPCOOL design with the wafer connected by a single clamp or by the PMMA wafer holder with 8 spring contacts pins. The height level of the profilometry (Tencor P11, KLA-Tencor) was with respect to the SU-8 plating mould. The positions of the recorded profiles (a-d) are shown in Figure 5.4(a). Scan position (a),(b) and in gray (c),(d) had similar plating areas.

### 5.3 Fluidic cooling channels and first encapsulation

Before supplemental coil layers could be added, an electrical insulating permanent resist had to be applied.<sup>[187]</sup> This encapsulation was then performed by hot-roll lamination for both the TOPCOOL and MIDCOOL designs using a 50 µm thick ADEX DFR.

Prior to the resist application, the substrates were wet chemically cleaned. Copper sulfate residues from the electroplating and an oxide film on the Cu tracks were reduced in 10 % H<sub>2</sub>SO<sub>4</sub>. To minimise a reformation of an oxide layer, the wafers were instantly subjected to QDR, were spin-dried and vacuum dried in an oven. To promote the DFR adhesion, plasma activation was necessary.

Exclusively for the MIDCOOL design, a 100 µm thick DFR sheet was applied by vacuum lamination to structure the cooling channels (G 4.2, page 205). Vacuum lamination had the potential of applying the dry film bubble-free, much similar as described in Section 2.1. The DFR was bonded by the use of a hot-embossing tool under a vacuum pressure of  $2 \cdot 10^{-3}$  mbar with the top and bottom chuck heated up to 58 °C.<sup>[187]</sup> The hold time was 5 min and the bonding force was set to the minimum value of approximately 60 N. As a result of the bonding force and temperature, the initial height of the 100 µm thick DFR decreased by about 10 µm to 15 µm. Hot-roll lamination was also tested and the application of the SUEX caused no shrinkage of the resist film. The vacuum lamination was nevertheless the preferred method since no resist adhesion problems due to trapped air occurred. After performing the lithography, the PEB at 70 °C in an oven, wet development, drying and plasma activation, the MIDCOOL substrate was ready for the lamination of the encapsulating ADEX layer.

It was necessary to apply the ADEX layer by hot-roll lamination, since it was subjected to cover and to seal the fluidic channels. Tests with 10 µm to 20 µm ADEX laminates resulted in more defects during the lamination or after the

resist got cross-linked. Also, pieces of laminate from a 10  $\mu\text{m}$  ADEX were still adhered to the PET film.

Only a 50  $\mu\text{m}$  thick laminate fulfilled the necessary film stability. The resist cross-linking and development was similar as for the SUEX laminate. Sufficient cross-linking was necessary to form a temperature stable basis for the PVD in the next process step. The encapsulation produced an excellent planar surface for both, the MIDCOOL variant in Figure 5.7(a) and also the TOPCOOL design in Figure 5.7(b). Cu over-plating for the TOPCOOL design had to be limited to 5  $\mu\text{m}$

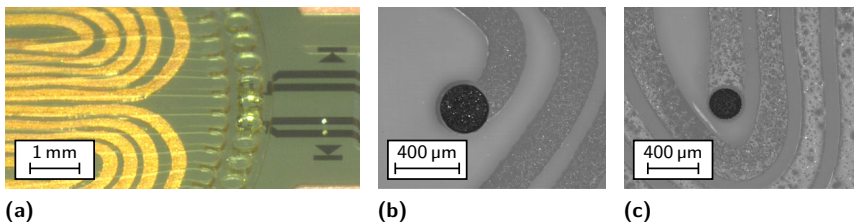


**Figure 5.7:** (a) encapsulation of the MIDCOOL design with integrate fluidic cooling channels. On the right is the Pt temperature detector. (b) TOPCOOL (chip position (3-3), z-grad) without trapped air pockets above the Cu tracks. (c) TOPCOOL encapsulation (chip position (1-1), triax, x-gradient) by hot-roll lamination with air inclusions above the Cu tracks.

to 10  $\mu\text{m}$  in order to prevent trapped air above the SU-8 mould. Depending on the height of the previously Cu plated tracks, air inclusions got visible. However, slight over-plating was much more acceptable than a Cu height which did not reach the level of the first SU-8 layer, see Figure 5.7(c).

## 5.4 VIA top-up by copper electroplating

To interconnect the coil structures to another overlying coil layer, vertical interconnects were established by Cu electroplating.<sup>[187]</sup> From the previous processing step (Figure 5.7(b)), VIA (vertical interconnect access) holes were

structured into the resist, which were topped-up to compensate for the height difference of the encapsulation layer(s).

The TOPCOOL design required to fill the VIAs by 50  $\mu\text{m}$ . Because of clearance constraints within the mask design, different VIA sizes had to be used. For the tri-axial gradient, VIAs with a diameter of  $\varnothing$  210  $\mu\text{m}$  were implemented. For the z-gradient, there was enough space to define larger VIAs of  $\varnothing$  310  $\mu\text{m}$ .

Figure 5.8 illustrates the plating height variations. The depth of the VIA plating was investigated by profilometry. Persisted height differences from the 1<sup>st</sup> electroplating step were propagated to the VIA height. VIAs with a diameter of 210  $\mu\text{m}$  showed slower plating than the  $\varnothing$  310  $\mu\text{m}$  ones. One potential way to compensate for the height variation would be entire over-plating of the VIAs, followed by mechanical post processing, to post-level to the ADEX surface. Farrington *et al* [138] reported a technique to achieve an accurate planar surface finish of multi-layer SU-8 structures by mechanical lapping. High-speed micro milling would be another solution, which would allow to trim the specific regions. To reduce processing complexity and mechanical stress on the SU-8 structures, mechanical post processing was omitted.

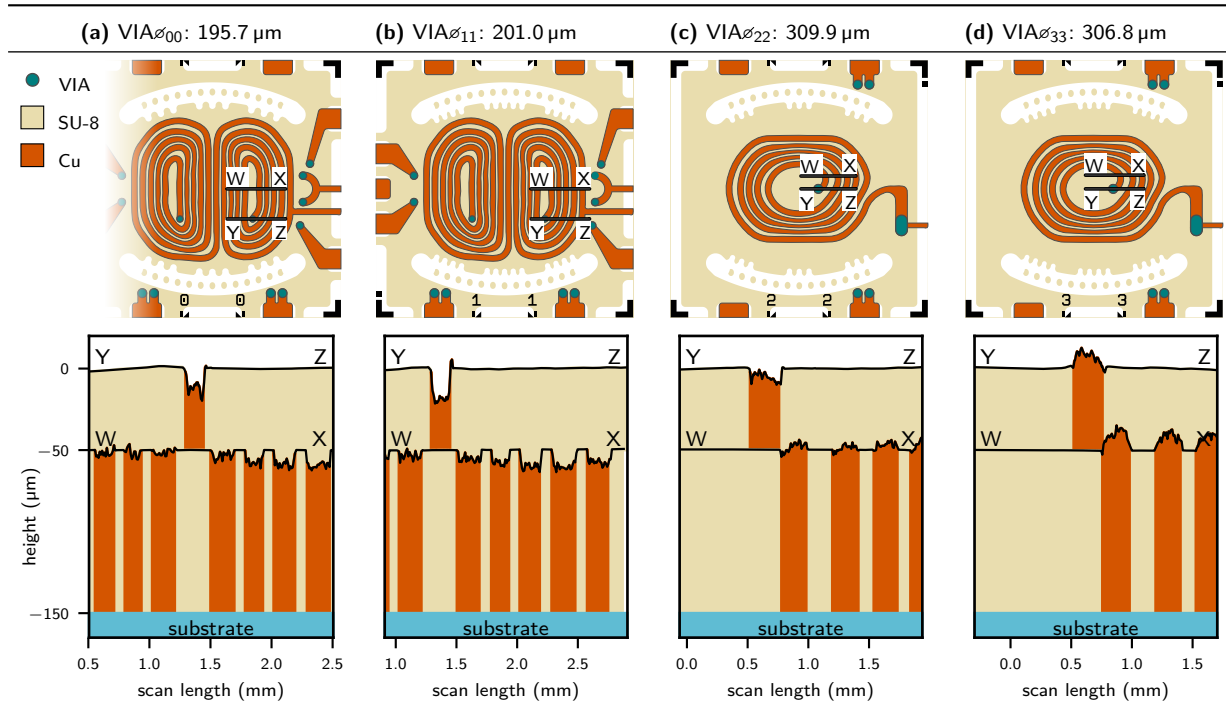
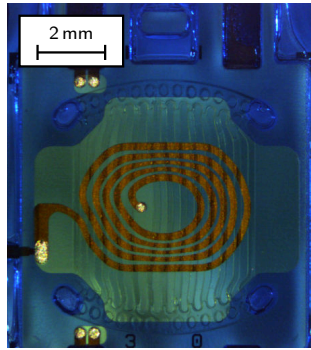


**Figure 5.8:** Profiles acquired for the first coil layer (W-X) and the VIAs (Y-Z) for the TOPCOOL design. The results from the profiometry were combined in the illustration. The coloured areas for the Cu and SU-8/ADEX were extracted from the mask layout.

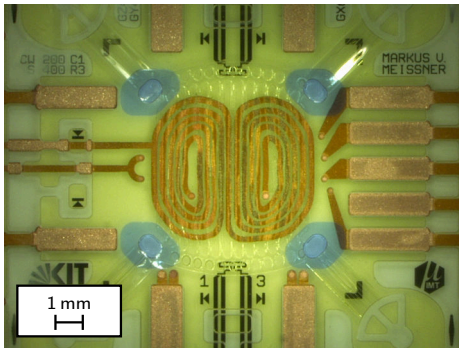
A temporal encapsulation layer for the MIDCOOL design was required to seal the fluidic network to prevent the copper electrolyte from entering the channels above the coil. The ORDYL<sup>®</sup> FP 450 was applied by hot-roll lamination on top of the ADEX and was then structured by lithography for keeping the VIA holes uncovered. The coil areas were also spared out, in order to avoid possible resist residues. The permanent/non-permanent resist combination of ADEX and ORDYL<sup>®</sup> FP 450 maintained adequate adhesion and did tightly seal the fluidic ports, and even oxygen-plasma activation at a vacuum pressure of 0.5 mbar was possible. Figure 5.9 shows the momentary sealing by the use of a single non-permanent ORDYL<sup>®</sup> FP 450 layer, in order to suppress further electroplating of the first coil layer. The pictures were taken after the VIA electroplating.

A first attempt was to protect the entire wafer, except keeping windows for the gradient coil and interconnects (Figure 5.9(a)). It was more difficult to strip the ORDYL<sup>®</sup> FP 450 since it also covered the chip edges, especially the edges of the SU-8/ADEX layer. As illustrated in Figure 5.9(b) and Figure 5.9(c), a resist seal above the primary fluidic openings was entirely sufficient. Thus, also the large contact pads for external chip connection got plated. However, the added copper on the contact pads also improved the heat dissipation within the application.

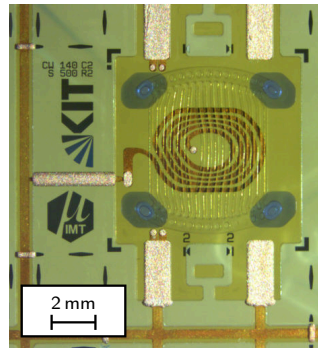
For the MIDCOOL layout, it was not possible to top-up the 130  $\mu\text{m}$  to 150  $\mu\text{m}$  high VIA holes in a comparable precision as performed for the TOPCOOL design. VIAs with a  $\varnothing$  210  $\mu\text{m}$  showed insufficient filling and height differences of  $-55.0 \mu\text{m}$ ,  $-77.9 \mu\text{m}$ ,  $-67.36 \mu\text{m}$  and  $-60.06 \mu\text{m}$  were measured, whereas the  $\varnothing$  310  $\mu\text{m}$  ones were filled-up to the top. In a redesign, all VIAs were unified to a diameter of 310  $\mu\text{m}$ , which further compensated for the plating height variations. Because of clearance issues between the VIA and nearby gradient coils, larger VIAs could only be implemented in the MIDCOOL design, since the trenches between the coil tracks were wider.



(a)



(b)



(c)

**Figure 5.9:** (a) shows the full encapsulation, including the large connecting pads around the chip. (b) and (c) show the ORDYL<sup>®</sup> FP 450 encapsulation of the four fluidic ports for the BOTTOMCHIP/TOpchIP.

Eventually, incomplete VIA filling was offset by the following PVD process as described in the next section.

## 5.5 Formation of the second coil layer

In this processing step, another seed layer was applied on top of the ADEX plateaus. The second seed layer required sufficient adhesion towards the ADEX, had to be electrically connected to allow for a galvanic deposition, and had to remain permanently below the second coil. <sup>[187]</sup>

After the previous VIA electroplating step, extensive surface cleaning was therefore mandatory to remove  $\text{CuSO}_4$  residues and oxides. The wafers were dipped for around 3 min into 20 % sulfuric acid (G 6.9). A minor quantity of 30 %  $\text{H}_2\text{O}_2$  was added to the sulfuric acid to slightly etch the metallised Cu.  $\text{O}_2$  plasma cleaning at 80 W for approximately 10 min was performed, to remove surface contamination above the ADEX layer. The  $\text{O}_2$  activation may also be skipped if the PVD machine would support surface cleaning, for instance by an Ar plasma, right before the metallisation (e.g. 100 W for 30 s). Moisture and trapped DIW in the fluidic channels evaporated during vacuum processing.

The seed layer combinations Cr/Au and also Cr/Cu were tested. In principle, a Cr/Cu seed was easier to remove than the noble Au. However, within our clean room environment, the Cu deposition was not permitted, since Cu diffuses strongly into other materials such as Si. Instead, an externally available machine was taken under consideration, that exclusively allowed for a deposition of a Cr/Cu seed layer. Since the machine was also used for the deposition on poly(dimethylsiloxane) (PDMS), adhesion problems occurred on the wafer's surface because of contaminations within the vacuum chamber. During seed layer stripping, the coil structures lost adhesion (see Figure 5.11(b)), thus no further attempts were carried out for the Cr/Cu combination and it was focused on the Cr/Au system (G 6.12). The wafer alignment marks were masked before the vapour deposition using polytetrafluoroethylene (PTFE) tape. Vacuum metal evaporation and RF magnetron sputtering were evaluated to form the electroplating seed:

**Vacuum metal evaporation.** PVD by vacuum evaporation caused less heat-up and consequently less damage to the ADEX coated plateaus. Since the height difference to the previous applied Cu was too large, it was not possible to build-up an electrical connection to supply the plating current. The electrical resistance between the first Cu layer and the top surface was larger than a few  $M\Omega$ . The rate of Cr and Au deposition was in the range of  $2.5 \text{ \AA/s}$  to  $10 \text{ \AA/s}$ .

**RF magnetron sputtering.** Sputter deposition facilitated the deposition of the sidewalls, and also within the VIAs holes. The deposition in the VIA trenches was significantly improved by the ionised Ar plasma atmosphere. However, the atom bombardment when depositing the Au layer onto the Cr adhesion layer resulted in a composition of both elements, producing an alloy or compound coating. When it came to seed layer stripping, such physically mixed, inter-metallic-layers required to alternate between the wet etching solutions, in order to remove the seed entirely.<sup>[206]</sup> Sputter depositions with a duration of more than 1 min to 2 min resulted in post-curing of the SU-8 structures, and caused added resist stress and substrate bending.

For the TOPCOOL chip design, the vacuum evaporation of a Cr/Au layer established a sufficient electrical connection towards the ADEX plateau. Actually, the electrical connection with the chip plateaus was formed with the large pads at the chip edges.

For the MIDCOOL design, vacuum metal evaporation did not result in a low ohmic connection throughout the VIAs. However, the sputter deposition succeeded by depositing a 15 nm Cr layer (2 steps of 90 s at 200 W, with a waiting time of 10 min in between) followed by a 100 nm Au layer deposition (4 steps of 75 s at 300 W, with waiting times of 10 min). After the sputtering, the substrates showed visual bending, but the measured resistance between the plateaus and the substrate was in an acceptable range. The DC resistance was between  $2.3 \Omega$  to  $3.0 \Omega$  across the entire wafer, as measured for all the individual chips.

Regardless of the achieved connection, substrate bending due to the thermal effects from the sputtering was unacceptable and a different method was attempted. Conventional vacuum evaporation was performed, and after an electron microscope sputtering machine was used, which caused less substrate heat-up. Since the already vapour deposited Au layer was inert toward oxidation, there were no concerns to move the wafers from one machine into another. The additional Au layer was deposited by an EMITECH K550 (Quorum Technologies Ltd.) sputtering machine which was operated at a pressure of approximately  $1 \cdot 10^{-2}$  mbar and a current of 35 mA for 4 min. The final electrical resistance was  $10 \Omega$  to  $30 \Omega$ , measured between the Au deposited plateaus and the Cu pads at the wafer base. No added substrate bending was induced.

Without any waiting time, a non-permanent electroplating mould was applied.<sup>[187]</sup> To obtain an electroplating mould with a height of at least  $95 \mu\text{m}$ , a dual layer of ORDYL<sup>®</sup> FP 450 was laminated (G 7.1). The dry film was successfully applied by lamination at a hot-roll temperature of  $80^\circ\text{C}$  to  $90^\circ\text{C}$ . In general, a reduced lamination temperature caused less thermal penetration to the underlying resist stack and consequently lowered the risk of substrate bending. The substrates were exposed after a wait time of 15 min. The experimentally determined exposure dose for cross-linking the ORDYL<sup>®</sup> FP 450 was  $900 \text{ mJ cm}^{-2}$  to  $1050 \text{ mJ cm}^{-2}$ .

Wet development was performed in a mega-sonic bath. When compared to the development in an ultra-sonic bath, it was less likely to cause de-lamination of structures that were smaller than  $80 \mu\text{m}$  in width. To examine the reproducibility, wafers were developed individually in a petri-dish using 250 mL of developer. For each wafer, the mild alkaline developer ( $0.8\% \text{ Na}_2\text{CO}_3$ ) was freshly prepared. A suitable development time was in the range of 8 min to 9.5 min, while a longer development of 14 min led to resist de-lamination.

In order to achieve a metallisation higher than  $100 \mu\text{m}$ , the lamination of a triple layer of ORDYL<sup>®</sup> FP 450 was attempted. Such a thick layered mould would be particularly useful to compensate for possible over-plating of the VIA

holes or to reduce the electrical resistance by stepping up the Cu height even further.<sup>[187]</sup> Adequate results were not achieved and the structuring of the triple laminate failed due to resist adhesion problems. This happened due to the light absorption within the resist at the respective wavelength of 365 nm, as previously shown in Figure 2.7(a) on page 49. Even though an extensive resist undercut was resolved, with an exposure dose of  $1500 \text{ mJ cm}^{-2}$ . However for the triple laminate, a development time of 15 min was necessary. Despite of performing a plasma activation before the electroplating, electrolyte wetting problems arised in experiments with the triple laminate.

The electroplating using a dual-layer ORDYL<sup>®</sup> FP 450 mould was performed to a height of  $70 \mu\text{m}$ , while rotating the substrates within the middle of the plating time (clamp based contacting).<sup>[187]</sup> Figure 5.10 illustrates the ORDYL<sup>®</sup> FP 450 electroplating mould during microscope inspection after starting the electroplating.

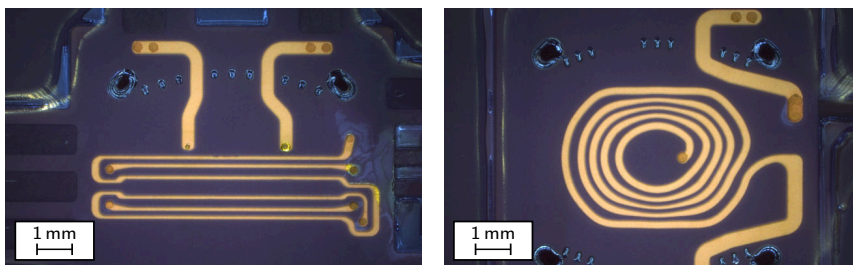


**Figure 5.10:** The ORDYL<sup>®</sup> FP 450 electroplating mould for the tri-axial gradient (*left*) and for the uni-axial z-gradient (*right*).

The ORDYL<sup>®</sup> FP 450 mould was stripped in a strong alkaline solution, which was heated up to  $40 \text{ }^\circ\text{C}$ . As illustrated in Figure 5.11(a), the resist did not solve in the 4% to 10% KOH or NaOH solution, but swelled like a jellyfish. After 18 min to 20 min, the plating mould detached from the surface and could be tied off manually, in one piece. The residue-free removal of the ORDYL<sup>®</sup> FP 450 was facilitated by keeping the plating height below  $80 \mu\text{m}$ .

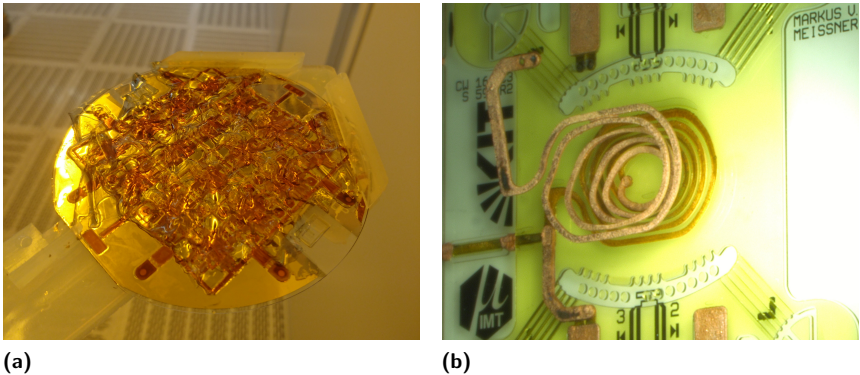


**Figure 5.11:** (a) swelling of the polymer when immersed in the NaOH or KOH remover. (b) the coil structure detached because contaminants caused inadequate seed layer adhesion on the ADEX DFR.

In contrast to the standard wet etching solutions that are commonly used in MEMS technology,<sup>[207]</sup> special, resist-stable and selective etching solutions were used for the removal of the plating base.

The two Au etches were evaluated in here:

**Umicore Gold-Stripper.** The Umicore Gold-Stripper 645 (Umicore GmbH) is a potassium cyanide (KCN) based Au stripper which was evaluated to etch the Au from the Cr/Au plating seed. Cyanide is extremely toxic and is even in small quantities fatal to humans. As described in the product data sheet, it strips Au and Cu at comparable rates of  $0.5 \mu\text{m min}^{-1}$  to  $0.7 \mu\text{m min}^{-1}$  at room temperature. However, the complete removal of the 100 nm thick Au seed layer, even within the  $80 \mu\text{m}$  trenches of the coil took 5 min to 10 min. About  $15 \mu\text{m}$  of the electroplated Cu was also etched away. The Cr layer did not corrode.

**TFAC gold etchant.** Besides the Umicore gold etching solution, the TFAC gold etchant (Transene Company Inc.) for intermetallic substrates was successfully employed. The TFAC is more comparable to the selective Au

etching solution that was invented in [208]. Metal etching with the TFAC was performed with the wafers positioned in a vertical direction. TFAC showed clear selectivity against Cu and did not corrode the Cr adhesion layer. During TFAC etching, a porous, zinc-coloured layer formed on top of the copper structures.<sup>[187]</sup> The etching of a vacuum evaporated seed was nearly twice as fast as for a sputtered seed. While immersing the substrate with a sputter-deposited seed into the TFAC gold etchant for 10 min to 15 min, the Cr layer became first visible at the edges of the wafer. After 30 min to 35 min, the Au was still present between the coil winding and also at the etches of the chips. The Au was visually removed after 45 min to 50 min with the solution heated up to a temperature of 40 °C. The TFAC gold etchant was the preferred etching solution as it only marginally degraded the electroplated Cu patterns at the edges.

A conventional Cr3 etch<sup>[207]</sup> did strip the Cu before the Cr was actually etched. The Cr adhesion layer was etched separately by the commercial Cr-ETCH-200 etchant, that offered an etch rate between 12 nm min<sup>-1</sup> to 15 nm min<sup>-1</sup>. The Cr-ETCH-200 is a selective alkaline etchant based on potassium permanganate (KMnO<sub>4</sub>) and tribasic sodium phosphate (Na<sub>3</sub>PO<sub>4</sub>), much similar as the Cr etch prepared by Cho *et al.*<sup>[209]</sup> For testing purposes, a Cu coated sample (Figure 2.13(a) on page 61) was immersed into the Cr-ETCH-200 etch for more than 48 h and no weight loss was found.

After the Cr etching process, manganese dioxide (MnO<sub>2</sub>) residues remained on the wafers, especially within the fluidic channels. Those MnO<sub>2</sub> residues could not be removed by water. By rinsing the wafers in 10 % oxalic acid (C<sub>2</sub>H<sub>2</sub>O<sub>4</sub>), solid MnO<sub>2</sub> residues were reduced to Mn<sup>2+</sup>.<sup>[210]</sup>

Since a compound layer of Au and Cr atoms was formed between the two deposited layers, it was necessary to alternate between the Cr-ETCH-200 (NB Technologies GmbH) and the TFAC. By repeating the etching and cleaning sequence,

5 min, TFAC → DIW rinse → 5 min, Cr-ETCH-200 →  
5 min, oxalic acid rinse → DIW rinse

for several times, the evaporated seed as well as the sputtered seed were removed successfully.<sup>[187]</sup>

## 5.6 Encapsulation of the second coil layer

SU-8 and epoxy DFRs have been used extensively to perform photo-defined, wafer-level packaging of MEMS. Cross-linking by controlled underexposure of wet applied SU-8 is one way to define hermetical sensor packages to form a lid encapsulation.<sup>[211]</sup> A different group utilised a substrate bonding machine, where the standard SU-8 process was refined to be carried out within a vacuum chamber to perform wafer-level packaging.<sup>[212]</sup> Packaging using DFR lamination simplified processing while reducing thickness variations of the permanently applied resist layer.<sup>[213]</sup> Comparable packaging concepts were also applied to define microfluidic chips.<sup>[214]</sup>

In here, a wafer-level DFR bonding process was developed to encapsulate the second coil layer.<sup>[187]</sup> Before the DFR application, the copper structures were cleaned by dipping the wafers for 1 min to 2 min in 20 % H<sub>2</sub>SO<sub>4</sub>. QDR, nitrogen drying and subsequent dehydration within a vacuum oven at 55 °C at a pressure below 100 mbar were carried out. Much similar as described in Section 5.3 on page 125, a 100 µm thick SUEX laminate was applied by vacuum lamination. The objective in this manufacturing step was to completely enclose the Cu coil structures. However, there were open fluidic ports and channels which should not to be blocked.

As illustrated in Figure 5.12, the DFR was pressed against the bare gradient coil structures. Within the Figure, a TOPCOOL design was considered but the process can be applied analogously to the MIDCOOL design. In general, as less as possible of the DFR should enter the liquid cooling network.

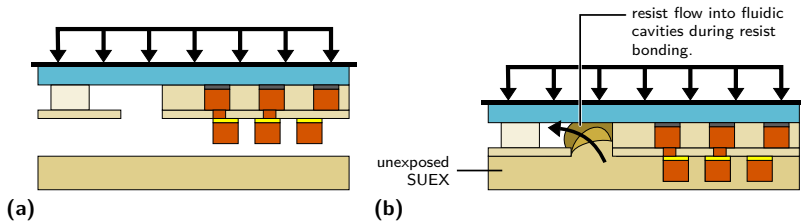


**Figure 5.12:** Illustration of the embossing process to attach the SUEX towards the Cu gradient coil conductors. **(a)** initial state before contact, when loading the wafer it into the substrate bonder. **(b)** bonding at elevated temperatures transported the DFR further into the fluidic cavities.

The tool pressure of the substrate bonder (SB6 Wafer Bonder 1<sup>st</sup> gen., SUSS MicroTec) could not be reduced below 60 N. Precise temperature control during vacuum bonding turned out to be the key process parameter. Therefore, the chuck temperature was adjusted to control the viscosity of the unexposed SUEX.

A number of DFR bond experiments were performed and the chuck temperature was lowered from 58 °C down to 48 °C to 46 °C. For both the TOPCOOL and MIDCOOL designs, the effective surface area of the underlying ADEX plateaus was 21 cm<sup>2</sup> to 23 cm<sup>2</sup> and the area of the plated Cu was 1.7 cm<sup>2</sup>. At a chuck temperature of 58 °C, the SUEX propagated into the main fluidic channels, as shown in Figure 5.13(a). When lowering the temperature down to 48 °C to 52 °C, the menisci of the SUEX got visible as shown in Figure 5.13(b).

Bonding at a chuck temperature of 46 °C did not cause much of the SUEX to flow inside the channels, but the coil structures were embraced completely (see Figure 5.13(b)). In general, more resist propagated into larger openings and therefore, the lithographic masks were adjusted to address this problem. Also chips at the edge of the wafer showed slightly more SUEX inflow, which was somehow related to substrate bending.

If the bond-chuck temperature was further reduced from 45 °C to 44 °C, the gradient coils were still sufficiently encapsulated without entrapped air gaps.

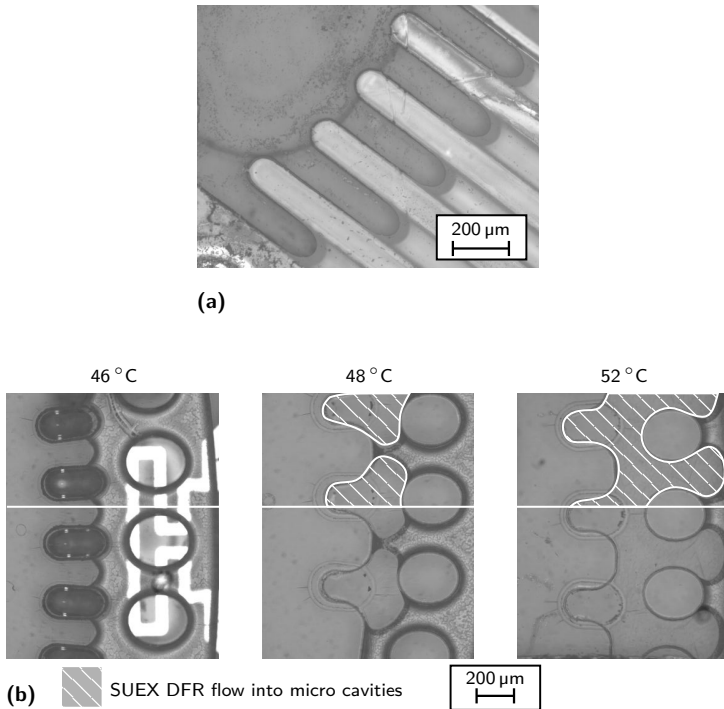


**Figure 5.13:** Inflow of SUEX dry film resist into the resist structures at different chuck temperatures.

Newton's rings were one indicator of incomplete bonding between the ADEX and SUEX layers. In that case, the resist could still be brought into sufficient contact by an additional post lamination step by the use of the hot-roll lamination equipment.

Figure 5.14(a) shows the machine's process cycle, which was carried out for both of the cooling concepts. After resist bonding, lithography was conducted, which followed the standard SUEX development and curing steps. Figure 5.14(b) shows the profile and the shrinkage of the SUEX DFR height. The height of the Cu plating was about 64 μm.

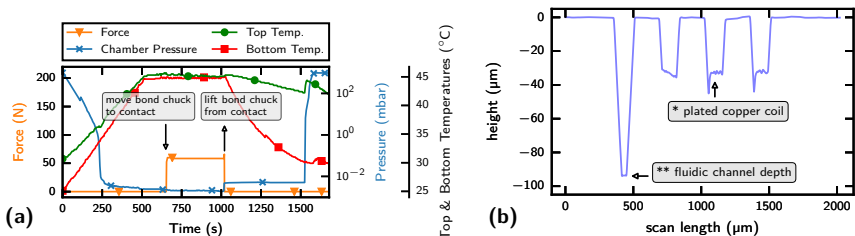


**Figure 5.14:** (a) vacuum lamination process (G 10.2). The cool-down of the top-chuck was slower, since it was not actively cooled. (b) measured profile of a TOPCOOL design, displaying the depth of the cooling network and respectively the height of the plated gradient coil.

Within the TOPCOOL design, the height of the fluidic channels was too low to ensure for a sufficient capacity of the cooling channels. The bonded SUEx layer was then topped up with another ADEX film by hot-roll lamination, which extended the channel height by 50  $\mu\text{m}$  (see G 10.3). After photo lithography, the PEB and wet development were carried for both the bonded SUEx and the laminated ADEX in a single step. To top-seal the fluidic channels, an additional 50  $\mu\text{m}$  ADEX film had to be laminated and exposed on the TOPCOOL design.

A final 50  $\mu\text{m}$  ADEX film was applied to resolve alignment structures (G 11.2). The chip regained a perfectly planar encapsulation plateau, which was imperative for the flip-chip alignment and for placing the Tx/Rx coil.

## 5.7 Back-end processing

After finishing the front-end processing, the wafers were subjected to dicing, which was performed in two steps. Since different chip sizes were integrated on the substrate, the larger BOTTOMCHIPS were diced first, and were individually pulled-off from the dicing tape as shown in Figure 5.15. With the BOTTOMCHIPS removed, the pre-cut wafer was diced again to tailor the TOPCHIPS. Since the substrates were removed from the chuck to release the BOTTOMCHIPS, the

re-clamping into the saw resulted in a cut offset of less than 100  $\mu\text{m}$ , however only for the TOPCHIPS. This dicing offset did not impact the flip-chip assembly, as the chips were aligned with respect to the SU-8 alignment structures and not by the glass edges of the chip.

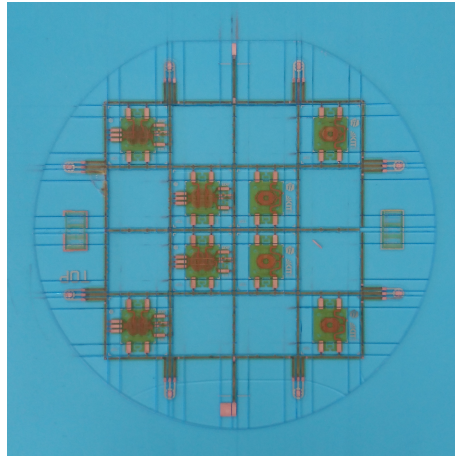


**Figure 5.15:** The diced 4" wafer with the BOTTOMCHIPS removed.

To mount and electrically connect to the chips, a custom designed printed circuit board (PCB) with a milled insert was purchased.<sup>[187]</sup> The pads on the chip and the traces on the PCB were on the same height level when inserting the chip into the milled pocket. A few droplets of EPO-TEK<sup>®</sup> 353ND epoxy were dispensed onto the PCB before inserting the BOTTOMCHIP. The EPO-TEK<sup>®</sup> 353ND adhesive had a low viscosity and entirely spread between the glass chip and the PCB. The glue was cured at 80 °C for 1 h in an oven to fixate the gradient chip.

A semiautomatic aluminium wire bonder was used to interconnect the two RTDs with the PCB. To establish a low-impedance connection of the gradient coils to the PCB, blank copper leads in combination with a low temperature solder alloy ( $\text{Bi}_{57}\text{Sn}_{42}\text{Ag}_1$ , Stannol GmbH, Velbert) were used. The purchased

solder alloy did not contain any soldering flux, which had to be dispensed separately to the pads. It was possible to solder the Cu pads of the chip at a temperature of 150 °C, which did not alter the surrounding SU-8.<sup>[187]</sup> A picture of the z-gradient coil that was attached to the carrier PCB is shown in Figure 7.11 on page 177.

As illustrated in the explosion view in Figure 4.1(b) on page 84, the chip spacers were manufactured out of a glass wafer, in a much similar way as described by Spengler *et al.*<sup>[56]</sup> Dicing and alignment marks for the flip-chip alignment were previously structured on the glass wafer by a Cr lift-off process. In addition, it was tested to structure fluidic feedthroughs by laser drilling.<sup>[215]</sup> Therefore an ultrashort pulse laser, that operated at a wavelength of 1030 nm was employed (Tangerine Amplitude Systems, France, 400 fs pulse length, 8.2 W, 200 kHz, scan speed 200 mm s<sup>-1</sup>). With this laser, it was possible to ablate circular shaped fluidic ports by rastering a hatch pattern. The manufacturing of the laser drilled flip-chip spacers showed feasibility, hence they were not applied, as the gradient was not actively cooled within the NMR experiment.

In addition, spacers without the laser-drilled fluidic feedthroughs were fabricated, to seal the fluidic ports for single chip thermal testing, as further performed in Section 6.3 on page 147. Glass spacers were dipped into a thin film of EPO-TEK<sup>®</sup>353ND and were positioned towards the alignment structures.

## 6 Characterisation

In this chapter, the layer structure, electrical performance and thermal properties of the fabricated micro-gradient coils are discussed. The electrical characterisation was mainly concerned with the uni-axial  $z$ -gradient, as it was further investigated by NMR methods as described in Chapter 7.

### 6.1 Physical characteristics

Figure 6.1 shows the diced cross-section of a TOPCOOL  $z$ -gradient chip. The copper tracks in the first electroplated layer (e.g.  $\mathbf{G}_{z2}$ , see also Figure 4.2 on page 87) rendered a high aspect-ratio, that was achieved by the BS lithography into the SU-8 mould. The copper electroplating showed slight overplating, that was compensated by the laminated ADEX layer. The second coil layer (e.g.  $\mathbf{G}_{z1}$ ) formed a tapered cross-section with an angle  $\theta$  of around  $20^\circ$ . This was caused by the limited aspect ratio of the non-permanent ORDYL<sup>®</sup> FP 450 and also by the seed layer etching of the Au and the Cr.

The vacuum encapsulation of the SUEX layer was carried out at a chuck temperature of  $52^\circ\text{C}$ . As a result, the embossed SUEX closed up with the plating height of the second coil layer. In contrast to the theoretical design process, it was therefore decided to apply another  $50\ \mu\text{m}$  ADEX resist layer to extend the channel height for the liquid cooling. The resulting surface of the final ADEX layer showed no irregularities and reached a perfect planarity. Therefore, the top surface of the chip qualified for the flip-chip assembly.

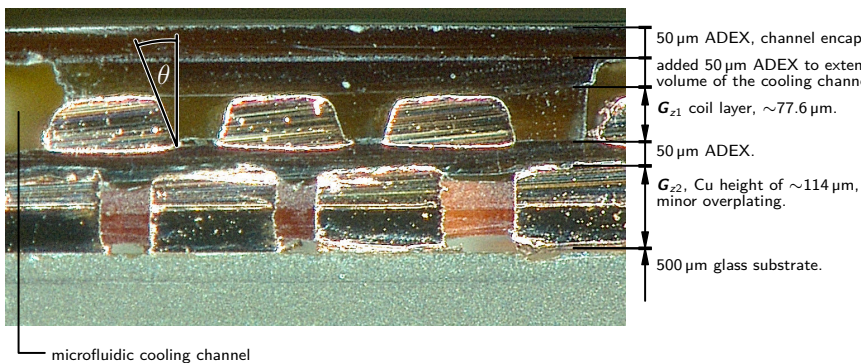


**Figure 6.1:** Profile of the layer structure by dicing through a TOPCOOL z-gradient chip.

## 6.2 Electrical characteristics

The equivalent circuit of a gradient coil can be considered as a resistance  $R_G$  and in series to it an inductance  $L_G$ .<sup>[187]</sup> A gradient coil that is driven by an ideal amplifier results in an exponential rise of the coil current, that generates the magnetic field. The time constant for such an  $RL$  circuit is then given by  $\tau = L_G/R_G$ , to reach 63.2% of the final current. Capacitive effects can be neglected since the amplifiers slew-rate in a NMR experiment is generally in the range of 4  $\mu\text{s}$  to 6  $\mu\text{s}$ .<sup>[70]</sup>

The electrical parameters of four z-gradient TOPCHIPS were recorded using an impedance analyser. The four chips were picked from the same fabrication batch. 2 cm long wires were soldered to the chips for electrical contact with the clamps of the measuring device. However, the connecting wires supplemented additional resistance and inductance to the measurement result. Four-terminal sensing was performed and the result is plotted in Figure 6.2.

For the BOTTOMCHIPS, probing was easier by clamping directly to the large pads on the chip. The values of the impedance in Table 6.1 were recorded at 1 kHz. When driving the assembled gradient with an ideal amplifier, the time

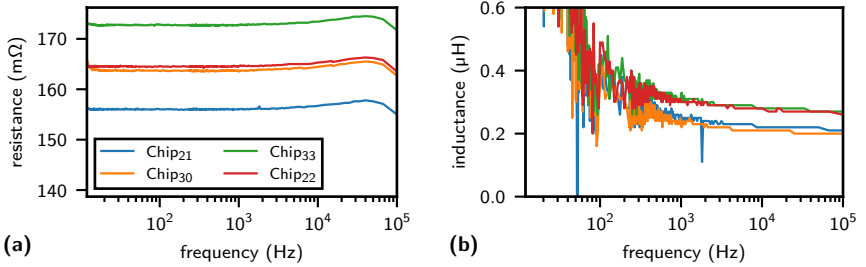


**Figure 6.2:** Electrical measurement of four z-gradient TOPCHIPS using a digital LCR-meter (LCR-821, Good Will Instrument Co., Ltd).

to settle the current to 99.3% ( $5\tau$ ) after a step response would be  $0.45\ \mu s$ . The measured inductance was significantly lower compared to the commercial counterparts, listed in the introduction in Table 1.2 on page 25. For instance, the tri-axial gradient by Shtirberg *et al*<sup>[81]</sup> offered a comparable high gradient efficiency but measured a five times higher inductance.

TOPCHIP		BOTTOMCHIP		assembled z-gradient	
$R_{TOPCHIP}$	$L_{TOPCHIP}$	$R_{BOTTOMCHIP}$	$L_{BOTTOMCHIP}$	$R_{z-Grad}$	$L_{z-Grad}$
134.5 $m\Omega$	0.14 $\mu H$	133.9 $m\Omega$	0.13 $\mu H$	262.8 $m\Omega$	0.34 $\mu H$

**Table 6.1:** Electrical parameters of the assembled z-gradient coil as used in the NMR measurement, see Figure 7.11(b) on page 177. (Table reproduced from [187])

Scattering parameters of the assembled z-gradient coil were acquired using a network analyser (NWA). The electrical impedance was extracted as shown in Figure 6.3. Within the NMR experiment, the frequency of interest is the *Larmor frequency*, that was in this project at 500.12 MHz. The self resonance of the gradient must not be in the same range as the RF pickup coil. Since the Tx/Rx coil was placed within the centre of the gradient, coupling between the two gradient loops and the Tx/Rx pickup coil had to be attenuated to retain maximum RF signal strength. In case of inductive coupling, a fraction of the RF energy would get lost within the gradient loop.

The backside of the glass substrate of the RF coil was metallised to a thickness of around  $12\ \mu\text{m}$  to shield the interaction with the gradient. The metallisation thickness was  $12\ \mu\text{m}$  and was chosen to be several times the skin depth. At frequencies of around 500 MHz, the skin conductive depth of Cu is around  $3\ \mu\text{m}$ . The copper shield added additional load capacitance to the gradient coil, which caused the self resonance to drop from 189 MHz to 65 MHz. [187]

A metallised RF shield also has the added effect of attenuating the reception of the  $^1\text{H}$  signal from the gradient's coolant. The metal shield would cause the RF waves from the Tx/Rx coil to reflect back to the sample. However, such a shield metallisation may also heat-up during the RF excitation and as a consequence it would also result in additional sample heating. RF heating effects on the sample were not investigated in this context, but structuring of the RF shield would be one way to limit thermal effects. [216] Figure 6.3 illustrates the z-gradient frequency characteristic for the assembled flip-chip, including the matched RF coil without the shield, and with the copper shield below the Tx/Rx coil loop.

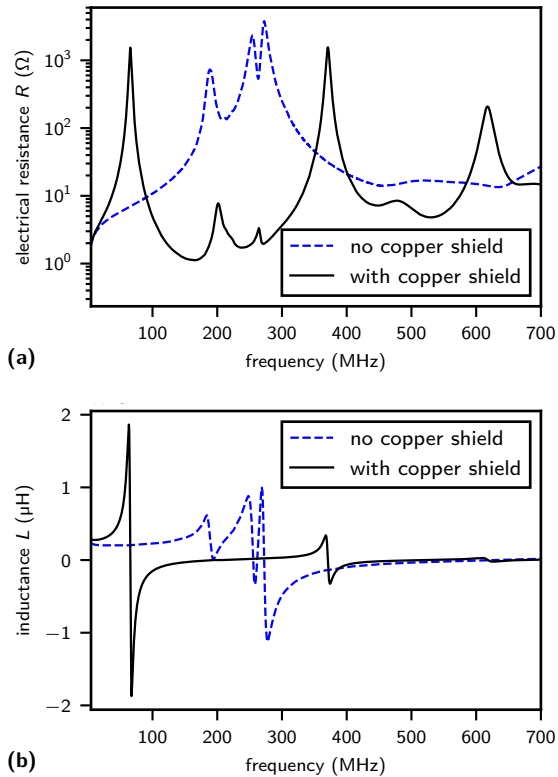


**Figure 6.3:** Electrical impedance analysis, extracted from the scattering parameter, acquired by a vector network analyzer (VNA) (Agilent Technologies, E5071B). The measurement refers to the chip assembly shown in Figure 7.11(a) on page 177.

## 6.3 Thermal characterisation

In the following, the thermal investigations are described for the BOTTOMCHIPS. When high currents are applied to the gradient coil, the near surroundings will heat-up by *Joule heating* and will penetrate the sample region. Temperature variations also affect the NMR measurement and lead to de-tuning of the RF

resonance coil.<sup>[25]</sup> In the following, the thermal dissipation was measured for constant currents and also for pulsed current loads, however both measurements gave comparable results, since only the subjected electrical power over time was relevant.

Only the BOTTOMCHIPS contained the Pt temperature sensors and fluidic supply channels and therefore making them suitable such an evaluation. Temperature readout from the Pt RTDs was done by four-terminal sensing. Four-terminal sensing eliminated the voltage drop over the connecting tracks. The surface temperature of the chip was captured by an infrared (IR) camera PI-160 (Optris GmbH, Berlin).

With respect to the Pt RTDs, the raw data of the recorded IR images were post processed by a two point correction procedure to adjust for gain and offset.<sup>[217]</sup> The current leads of the RTD were supplied by a constant current source. A custom PCB based on the LT1880 OP-AMP (Linear Technology, see datasheet's application note) was build up to deliver an exact current of 1.00 mA. Readout of the voltage drop over the resistors was performed directly without amplification or buffering using an ADC (ADS1112, Texas Instruments). The ADC offered differential inputs and the internal programmable gain amplifier (PGA) of the ADS1112 allowed to adjust for the voltage range of the RTDs and consequently required no additional amplifiers.

The RTDs were in direct contact with the in- and out-flowing de-ionised water (DIW) coolant. For the on-chip RTDs ( $R_{\vartheta_{in}}$  and  $R_{\vartheta_{out}}$ ), the electric current was supplied by separate sources. A test measurement was performed to define the temperature coefficient of resistance (TCR)  $\alpha_0$  of the RTD, that was calculated by,

$$\alpha_0 = \frac{1}{R_0} \left[ \frac{\delta R}{\delta T} \right]_{T=T_0}. \quad (6.1)$$

A value of  $(2.60 \pm 0.04) \cdot 10^{-3} \text{ K}^{-1}$  for the  $\alpha_0$  was obtained by measuring four RTDs over a range between 23 °C to 50 °C. The calibration was performed

with a thermocouple connected to a multimeter. With the available oven, no temperatures above 50 °C could be applied. For temperatures above 50 °C no calibration measurements for the RTD was performed.

In comparison to a conventional Pt100 sensor with  $\alpha_{\text{Pt}} = 3.92 \cdot 10^{-3} \text{ K}^{-1}$ , the obtained temperature coefficient of the RTDs was smaller. Generally, the compound layer between the WTi and Pt due to re-sputtering and predominantly contamination within the vacuum chamber from the other targets affected  $\alpha_0$ .<sup>[187]</sup> Besides, variations from the lithography that rendered the RTD pattern affected the TCR.<sup>[218]</sup> The RTD measurement resulted in drift of  $\pm 0.1 \text{ }^\circ\text{C}$  while measuring for a couple of minutes ( $\mu = 24.54 \text{ }^\circ\text{C}$ ,  $\sigma = 0.08 \text{ }^\circ\text{C}$ ).

The first experiments observed the current carrying capacity without liquid cooling. Figure 6.4 shows selected thermographic images from the tri-axial and uni-axial gradient coils. The isolation between the tri-axial coils was higher than few  $\text{M}\Omega$ . The z-gradient from this measurement was from a different fabrication batch as previously performed in the electrical evaluation and had a lower copper thickness.

The hot-spot temperatures with respect to the constantly applied currents are illustrated in Figure 6.5(a). All measurements were taken after a settling time of 5 min, while the electrical energy supplied continued to be uniform. Under steady-state conditions, an equilibrium state arises, in which the thermal dissipation equals the applied electrical power. Thermal heat-up  $T$  in dependence of the electrical current  $i$  can be described by the quadratic relationship,  $T_{(i)} = a \cdot i^2 + c$ .

The quadratic coefficient  $a$  can be considered as a benchmark to evaluate the coil performance and cooling. The constant  $c$  represents the lab or initial temperature. With the aid of the `optimize.curve_fit` function from the `scipy` module<sup>[189]</sup>, the coefficients for the quadratic best-fit were computed, that are summarised in Table 6.2 on page 161.

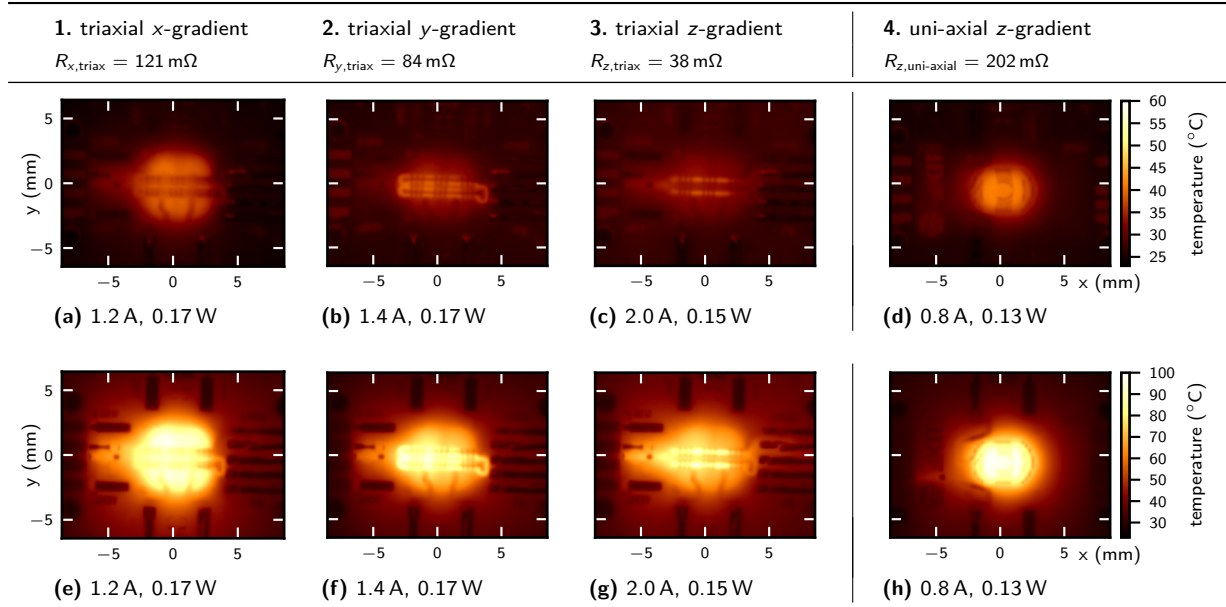


**Figure 6.4:** Thermographic images of the BOTTOMCHIPS by a constant current. Measured power includes the added resistance from the solder connections to the PCB. The resistance values were acquired by four-terminal sensing. Triaxial gradient coil: 1. plating height of 1<sup>st</sup> layer  $\approx 100 \mu\text{m}$ ; 2.,3. plating height of 2<sup>nd</sup> layer  $\approx 70 \mu\text{m}$  to  $80 \mu\text{m}$ , conductor width  $100 \mu\text{m}$  to  $120 \mu\text{m}$ ; 4. uni-axial z-gradient coil: plating height of 1<sup>st</sup> layer  $\approx 100 \mu\text{m}$ , 2<sup>nd</sup> layer  $\approx 45 \mu\text{m}$  to  $55 \mu\text{m}$ .

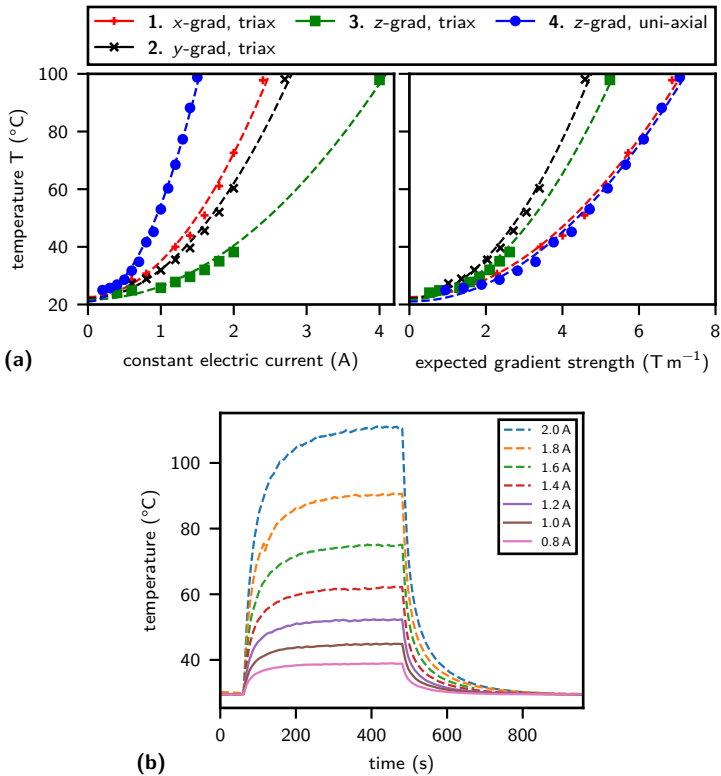


**Figure 6.5:** (a) the heat-up for different gradient coils as shown in Figure 6.4 with respect to the current (*left*) and to the expected gradient strength (*right*). (b) the thermal step response after switching to a selection of currents.

Figure 6.5(b) illustrates the time resolved joule heating of the z-gradient with the temperature measured at one RTD. The measurement was performed under different lab conditions compared to Figure 6.5(a). The current on-time in Figure 6.5(b) was set to capture the quasi-stationary state.

### 6.3.1 Thermal characteristics of the Topcool design

Active liquid cooling allowed to drive the gradient coils at higher current loads. Figure 6.6 shows the thermal behaviour with and without active liquid cooling. A PMMA holder was designed and attached to the chip's fluidic interconnects.

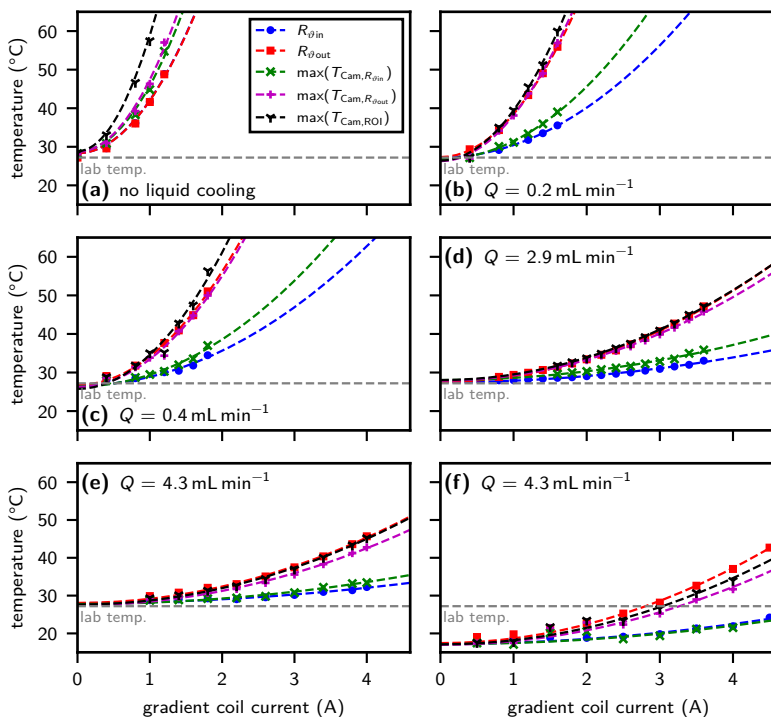


**Figure 6.6:** Heat-up of the z-gradient coil for a TOPCOOL design. (a) the gradient coil was operated without active liquid cooling. Hence, the graphs of  $R_{\phi in}$  and  $R_{\phi out}$  overlay within the plot. In (b) – (e) the flow-rate  $Q$  of the coolant was varied. (f) the temperature of the coolant was below the lab temperature. (Figure adapted from [187])

The holder is further illustrated for the MIDCOOL tri-axial gradient chip in Figure 6.9(a) on page 158. A peristaltic pump was used to deliver the DIW

coolant. The coolant that went through the chip was delivered back to the reservoir, to maintain a closed loop.

In the experiment in Figure 6.6(f), ice buckets were added to adjust the temperature of the reservoir to around 4 °C. Still, the coolant heated up through the tubing and measured a temperature of 18 °C at the input at the RTD  $R_{\theta in}$ . Within the application as a MR gradient coil, the supply current will be pulsed for around 1 ms to 10 ms and possibly at a higher amplitude compared to the steady-state current in Figure 6.6.

An adjustable current source was constructed, to rapidly pulse the electric load (see Figure 6.7(c)). The pulse current source was designed to meet the requirements for using it in an NMR pulsed gradient experiment. The circuit Figure 6.7(a) was based on an OPA549 OP-AMP (Texas Instruments) and operated as a voltage-controlled current source, in a much similar way as presented by Arango *et al* [219]. Arango used a push-pull configuration that required a single 12 V supply rail and on the other hand, required two OP-AMPs to drive the current in a bipolar direction.

In here, the circuit was based on a single OP-AMP and consequently required a bipolar power supply of  $\pm 15$  V to deliver an output current of up to 10 A for a maximum resistive load  $R_{Grad}$  of 0.8  $\Omega$ . [187] The switching power supplies generated a 120 mV peak-peak noise, measured at the internal switching regulator frequency of 40 kHz. A low-pass LC filter (9 mH and 10 mF) was added to the output of the switching power supplies to suppress the noise. The LC filter had a cut-off frequency of approximately 16.7 Hz. The results was a noise suppression of approximately -135 dB which corresponded to a residual noise of 0.178  $\mu$ V peak-peak. Further low frequency noise was suppressed within the OP-AMP.

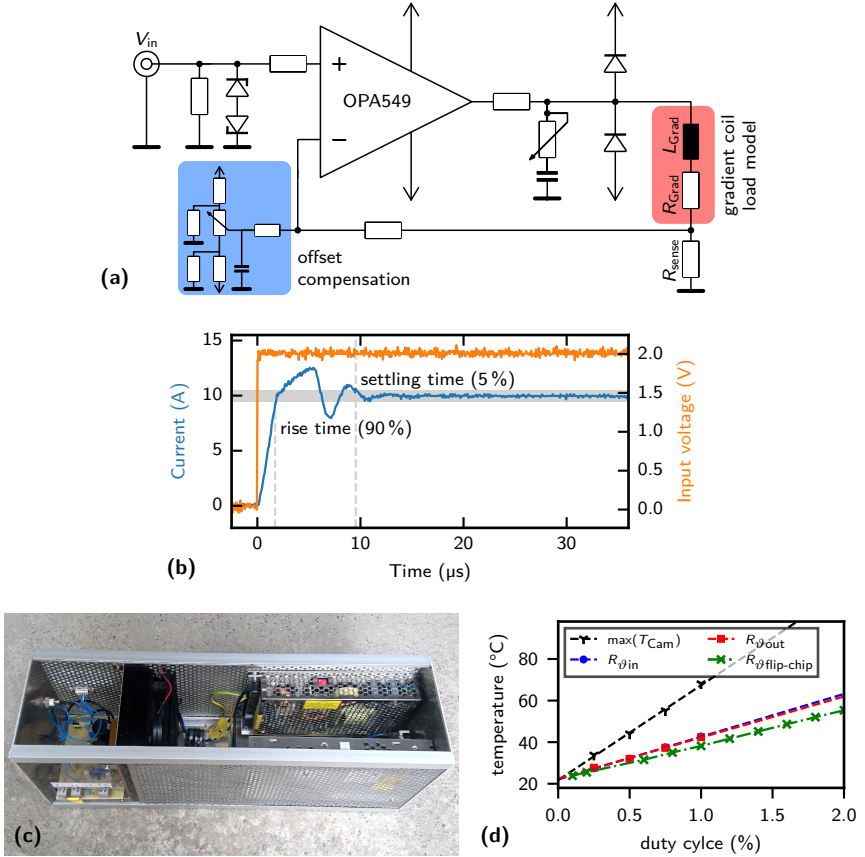
An adjustable RC-snubber network allowed to trim the overshoot to an acceptable value without continuously creating an infinite oscillation, in order to

keep the rise time short. The measured overshoot was 24 %, the rise time to 90 % was  $1.72\ \mu\text{s}$  and the settling time to 5 % was  $9.54\ \mu\text{s}$ .<sup>[187]</sup>

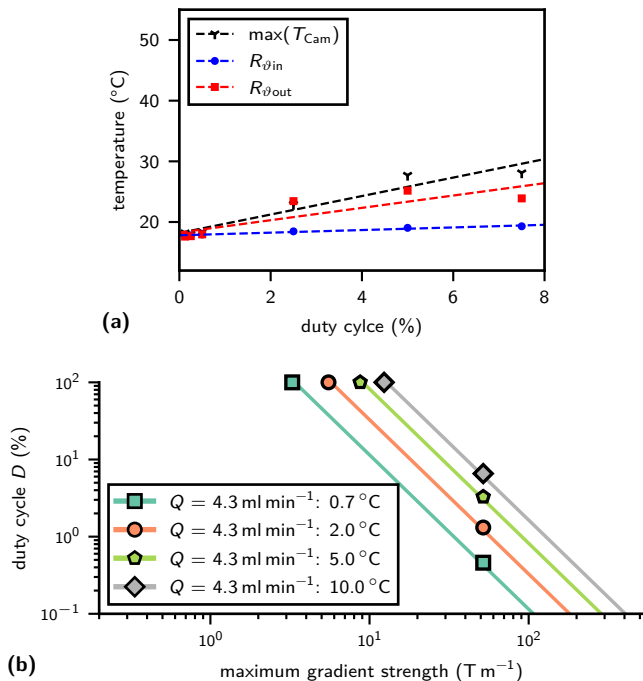
The circuit presented here had the disadvantage of having the  $R_{\text{Grad}}$  not connected to a fixed potential.<sup>[220]</sup> As shown in the schematic, the  $R_{\text{sense}}$  was connected to ground which kept the  $R_{\text{Grad}}$  floating. Galvanic isolation of the power supply is one possible solution, but would also add additional complexity of the entire circuit, especially when using multiple pulsed current sources within a tri-axial gradient setup.

Figure 6.7(d) shows the heat up from a pulse current experiment for a z-gradient without active liquid cooling. A period time  $T$  of 400 ms was selected to closely match with the repetition time  $TR$  of previously performed MRM experiments.<sup>[54,221]</sup> If the current was switched on for the entire echo time  $TE$  of typically 5 ms, the corresponding duty-cycle was about 1.3 %. The duty cycle  $D$  is defined as the squared ratio of the root-mean-square current  $I_{\text{RMS}}$  by the peak current  $I_p$ , given by  $D = (I_{\text{RMS}}/I_p)^2$ .<sup>[187]</sup>

Figure 6.8(a) shows the thermal characteristic with attached liquid cooling. The achievable gradient strength in relation to the duty cycle is shown in Figure 6.8(b). The figure was created using the data of Figure 6.6 and Figure 6.8(a). The gradient strength for a temperature rise of approximately  $2\ ^\circ\text{C}$  was comparable to the gradient strength of the tri-axial gradient from Weiger *et al.*<sup>[82]</sup>



**Figure 6.7:** (a) schematics of the pulse current source. (b) step response of the pulse amplifier, captured with a Tektronix MSO4104 Oscilloscope. The overshoot resulted from the delay within the feedback loop. (c) the assembled current sink of size 44 cm  $\times$  13 cm  $\times$  17 cm with the two switching power supplies. (d) the result of the pulsed-current experiment without active liquid cooling. (Figure adapted from [187])



**Figure 6.8:** (a) pulse current testing of the TOPCOOL z-gradient chip with liquid cooling at a flow-rate of  $4.3 \text{ mL min}^{-1}$ . The peak current was  $10 \text{ A}$  and the period time was  $400 \text{ ms}$ . (b) the de-rating curve with respect to the achievable gradient strength for different maximum surface temperatures. (Figure adapted from [187])

### 6.3.2 Thermal characteristics of the Midcool design

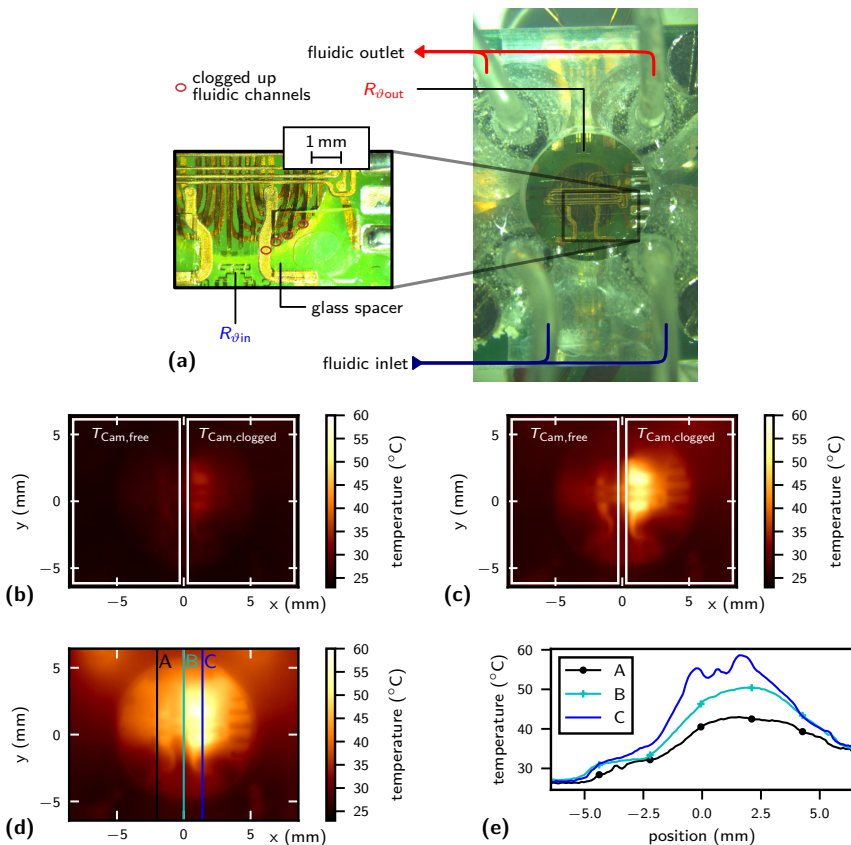
In the following, the MIDCOOL chip design on the basis of a tri-axial gradient is discussed. Some processing limitations during the fabrication were encountered. The coil layer that was first applied on the substrate was cooled more efficiently, since the coolant flowed in direct contact above the coil. Only the  $x$ -gradient coil was analysed, since the  $y$ - and  $z$ -gradient degraded during the Cr/Au etching process and had a final thickness below of  $40\ \mu\text{m}$ .

For the coolant delivery, the peristaltic pump from the previous experiment had to be exchanged by another one, and consequently the flow-rates were different. Cleansing of the fluidic channels during processing was not sufficiently emphasised. Due to insufficient rinsing after stripping the Cr/Au seed layer, residues from etching blocked some of the cooling channels which affected the cooling efficiency on the right side of the coil.

Figure 6.9(a) shows the setup of the fluidic delivery system attached to the PCB mounted chip. A glass slide was glued onto the chip to seal the flip-chip fluidic feedthroughs. The pair of the fluidic supply ports ensured a better reliability and avoided trapped air bubbles. On the left side of the thermal images, the channels were free and allowed for acceptable cooling. The temperature difference between the two areas was in the range of  $15\ ^\circ\text{C}$  to  $20\ ^\circ\text{C}$  at a moderate flow rate as shown in Figure 6.9(d).

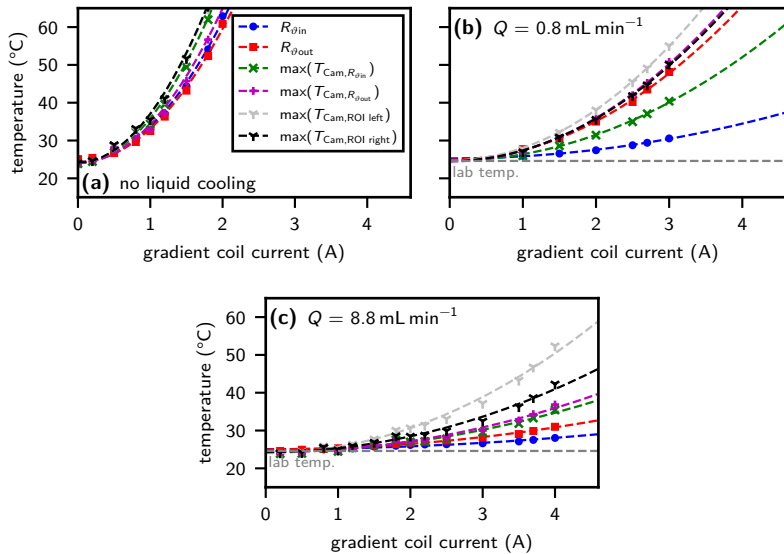
Figure 6.10 shows the hot-spot temperatures at the different regions in comparison to the measurement at the RTDs. Despite the calibration of the thermal imaging camera, a major difference in temperature between the SU-8 surface captured by the IR camera and the RTDs was observed. This difference was particularly noticeable at a lower flow rate of  $0.8\ \text{mL min}^{-1}$ . The DIW somehow cooled the RTDs while the SU-8 covering surface stayed undeterred by the liquid cooling.

Figure 6.11(a) and Figure 6.11(b) show the pulse experiment for the spacious  $x$ -gradient coil. In addition, the Anderson  $z$ -gradient was tested. However, it



**Figure 6.9:** (a) the PMMA fluidic delivery holder the MIDCOOL tri-axial gradient. The channels on the right in the scaled view were clogged by residues from metal etching. (b) thermal imaging of the  $x$ -gradient coil with an applied current of 2.5 A, at a power of (1.33 W) and a flow rate of  $8.8 \text{ mL min}^{-1}$ . (c) thermal imaging with an applied current of 4 A (3.3 W). (d) at flow rate  $0.8 \text{ mL min}^{-1}$ . (e) extracted thermal profiles along the flow directing.

got damaged at duty cycle above 1.2%, due to local defects in the electroplated tracks. With the utilised thermal camera, the heat-up of the  $z$ -gradient coil at the given pulse rate could not be analysed at a high precision.



**Figure 6.10:** Hotspot temperatures for the MIDCOOL x-gradient. (a) without liquid cooling, (b) and (c) with active liquid cooling for different flow rates.

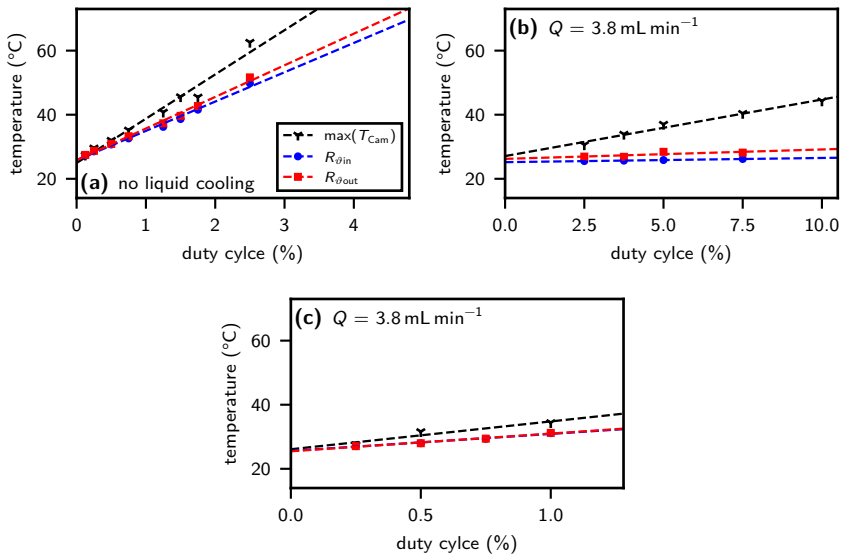


**Figure 6.11:** (a), (b) pulsed testing of the  $x$ -gradient at a peak current  $I_P$  of 10 A. (c) pulsed current testing of the Anderson  $z$ -gradient.

				$MAX(T_{Cam})$ $a (^{\circ}C A^{-2})$ $c (^{\circ}C)$						
Figure 6.5(a)	1. x-grad, triax	-	-	-	-	12.5	22.6	-	-	no liquid cooling
Figure 6.5(a)	2. y-grad, triax	-	-	-	-	10.0	22.1	-	-	no liquid cooling
Figure 6.5(a)	3. z-grad, triax	-	-	-	-	4.7	21.7	-	-	no liquid cooling
Figure 6.5(a)	4. z-grad, uni-axial	-	-	-	-	33.5	21.0	-	-	no liquid cooling

		Temp. $T_{\vartheta in}$ at RTD $a (^{\circ}C A^{-2})$ $c (^{\circ}C)$		Temp. $T_{\vartheta out}$ at RTD $a (^{\circ}C A^{-2})$ $c (^{\circ}C)$		$MAX(T_{Cam})$ $a (^{\circ}C A^{-2})$ $c (^{\circ}C)$		flow rate $Q$ (mL min <sup>-1</sup> )		
Figure 6.6(a)		13.7	28.4	13.6	28.3	30.0	28.9	-	-	no liquid cooling
Figure 6.6(b)		3.2	27.2	11.1	27.3	13.0	26.4	-	-	0.2
Figure 6.6(c)		2.3	26.6	7.3	26.8	8.8	25.8	-	-	0.4
Figure 6.6(d)		0.4	27.5	1.5	27.6	1.5	28.1	-	-	2.9
Figure 6.6(e)		0.3	28.0	1.1	28.1	1.1	27.6	-	-	4.3
Figure 6.6(f)		0.3	17.2	1.2	17.4	1.1	17.1	-	-	4.3

		Temp. $T_{\vartheta in}$ at RTD $a (^{\circ}C A^{-2})$ $c (^{\circ}C)$		Temp. $T_{\vartheta out}$ at RTD $a (^{\circ}C A^{-2})$ $c (^{\circ}C)$		$MAX(T_{Cam,free})$ $a (^{\circ}C A^{-2})$ $c (^{\circ}C)$		$MAX(T_{Cam,clogged})$ $a (^{\circ}C A^{-2})$ $c (^{\circ}C)$		flow rate $Q$ (mL min <sup>-1</sup> )
Figure 6.10(a)		9.3	24.3	8.8	24.3	12.9	24.2	12.7	24.1	no liquid cooling
Figure 6.10(b)		0.6	25.3	2.5	24.9	2.8	24.6	3.4	24.7	0.8
Figure 6.10(c)		0.2	25.1	0.4	25.0	1.0	24.3	1.6	24.0	8.8

				$MAX(T_{Cam})$ $a (^{\circ}C A^{-2})$ $c (^{\circ}C)$						
LTCC Ag, non-embossed [222]	-	-	-	-	-	59.0	21.0	-	-	-
LTCC Ag, embossed [222]	-	-	-	-	-	13.5	21.0	-	-	-

**Table 6.2:** Summary of the fitting curve parameters as performed in the experiments in this chapter. The table was extended with a comparative example from the literature, where the heat-up of a coil structured into a low temperature cofired ceramics (LTCC) substrate was analysed. [222]



## 7 NMR experiments

This chapter discusses the NMR and MRI experiments performed with the ink-jet printed micro coil<sup>[127]</sup> and the extraction of 1D profiles using the micro fabricated z-gradient.<sup>[187]</sup>

To conduct the imaging or spectroscopy experiments using the manufactured field coils, they had to be integrated into the NMR spectrometer as illustrated in Figure 7.1.<sup>[223]</sup> The high field NMR experiments were carried out inside a superconducting magnet, which was constantly kept below 4.2 K by using cryogenic liquids. The spatial homogeneity of the main magnetic field  $B_0$  must be fulfilled over the detection region and requires to be stable over time. Linear and higher order field variations are adjusted by the so called shim coils, that compensate for linear and higher order field errors, in order to maintain a field homogeneity better than  $10^{-9}$ .

The relevant component is the probe-head, which comprises the NMR detector and keeps it rigidly in position, within the iso-centre of the magnet. In the most basic scenario, the detector is an RF Tx/Rx coil, which is connected to a tuning and matching network to readjust for the coil resonance. More sophisticated probe-heads contain additional components e.g., for spinning the sample or sample manipulation and may contain extra RF coils and gradient coils or supplemental electric circuits for multi-nuclei detection.<sup>[29,224]</sup>

In this work, the utilised magnet possessed a main magnetic field strength  $B_0$  of 11.7 T (Avance III, wide-bore, Bruker GmbH, Germany) which corresponded to a centre frequency of 500.13 MHz. The commercial Micro5 probe-head (Bruker GmbH, Germany) served as the platform to firmly integrate the miniaturised

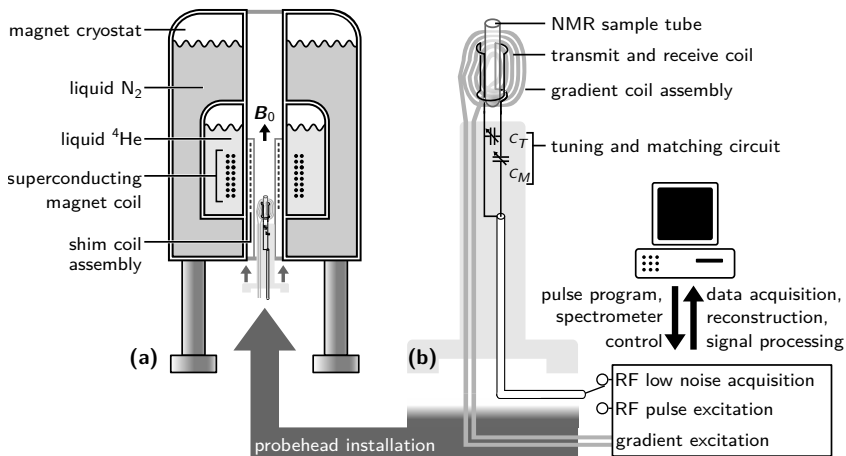


**Figure 7.1:** Fundamental components of the NMR spectrometer. **(a)** sectional view of a superconducting magnet. **(b)** principle components of an NMR probe-head. Electrical periphery and signal processing. (Figure inspired by [4, 6])

NMR detectors within the magnet. Throughout the probe-head, the custom designed coil inserts and gradient holders were connected to the amplifiers and signal converters of the spectrometer to process the NMR signal.

## 7.1 MRI experiments with the printed micro coil

In a first study, the printed RF micro coil was subjected to MRI experiments while using the commercial Micro5 gradient system for spatial encoding.<sup>[127]</sup> The mask-less fabricated planar micro coil<sup>[182]</sup> from Section 3.2 was composed out of non-magnetic materials and possessed a magnetic susceptibility close to that of water.<sup>[160]</sup> Accordingly, such a coil can be operated within high magnetic fields without degrading the magnetic field homogeneity, which is an important prerequisite for MRI.<sup>[127]</sup>

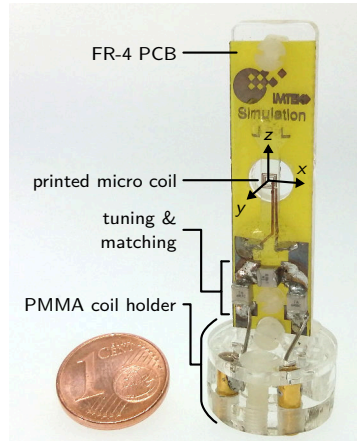


**Figure 7.2:** Magnetic resonance coil insert with the printed micro coil attached.  
(Figure reproduced from [127])

The constructed probe-holder with the attached coil slide is shown in Figure 7.2. To meet the resonance condition at 500.13 MHz for  $^1\text{H}$  spin excitation and reception, impedance transforming capacitors for frequency tuning and matching were soldered close the coil to form the resonance circuit. Therefore, non-magnetic capacitors (CHB HiQ, Temex Ceramics, France) were soldered onto the 0.5 mm FR-4 PCB. The insert was composed out of laser-cut PMMA parts.<sup>[127]</sup>

With the Micro5 magnetic field gradient system (Bruker GmbH, Germany) it was possible to achieve a gradient strength of up to  $2 \text{ T m}^{-1}$  when using 40 A pulse amplifiers. Prior to this work, Meier *et al*.<sup>[54]</sup> reported an isotropic spatial resolution of  $10 \mu\text{m}$  using the subjected gradient system.

The interior of a spring onion was imaged by taking slices in the coronal x, z-plane. A gradient echo pulse sequence was used for the acquisition, that uses the imaging concept as described in Figure 1.3 on page 13. The saggital y-position of the acquired slice was  $\approx 200 \mu\text{m}$  above the coil's surface. The spring onion was wrapped and attached by a layer of Parafilm M (Pechiney

Plastic Packaging, USA) towards the coil to protect the sample from drying out during the long measurement time. The excellent micro imaging performance of the coil is illustrated in the two images in Figure 7.3 that were captured with an in-plane resolution of  $20\ \mu\text{m}$  and  $10\ \mu\text{m}$  respectively. [127]

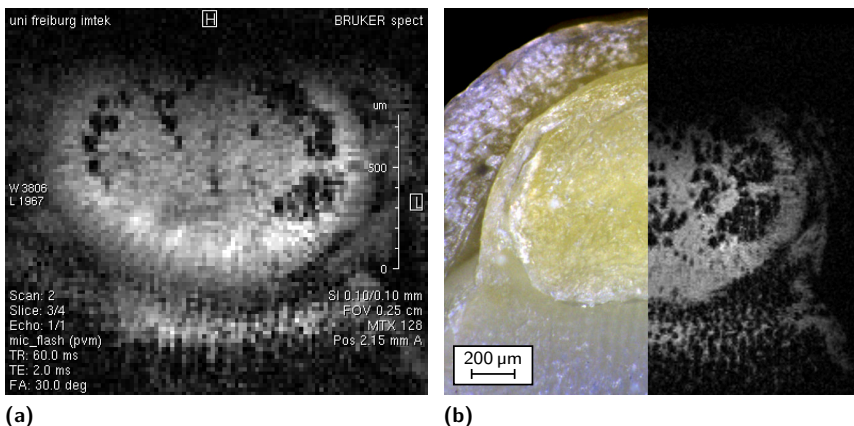


**Figure 7.3:** (a) Rapidly acquired MRM image from a slice of a spring onion in an acquisition time  $T_A$  of 4 min 5 s using 32 averages with a slice thickness of  $100\ \mu\text{m}$  and an in-plane resolution of  $20\ \mu\text{m}$ . The  $^1\text{H}$  image was captured using micFLASH sequence at a flip angle of  $30^\circ$ . Figure (b) shows a comparison of an optical microscope image and a high resolution MR image. The MR image was acquired with an in-plane resolution of  $10\ \mu\text{m} \times 10\ \mu\text{m}$  and a slice thickness of  $40\ \mu\text{m}$  in 9 h and 6 min ( $T_A$ ). Each acquisition was repeated every 500 ms ( $T_R$ ) while recording 256 averages. (Figure reproduced from [127])

According to the coil's geometry, the FOV spanned a rectangular region of  $1.5\ \text{mm} \times 1.5\ \text{mm}$  laterally in the  $x, z$ -plane. The FOV in  $y$ -direction, measured less than  $1\ \text{mm}$ , while the sensitivity decreased when imaging further apart from the coil's surface.

The SNR was calculated for both scans (Figure 7.3(a) SNR of 16.1, Figure 7.3(b) SNR of 14.8) from a signal-intense region divided by the mean noise taken from an image-free region. [127] The respective spin density of the high resolution scan was 10 times less and, hence, exhibited a lower signal intensity. This resulted in

a lower SNR, which was compensated by capturing more image averages. The SNR could be improved by recording more image averages, since the NMR signal accumulates linearly, whereas the statistically distributed noise level only accumulates with the squared number of image averages  $\sqrt{N}$ .<sup>[39,223]</sup>

In a second imaging experiment, the structure of a sesame grain was observed.<sup>[225]</sup> Furthermore, a comparative study of MRM and X-ray computed tomography (X-ray CT) on such an oil-seed grain was performed. With X-ray

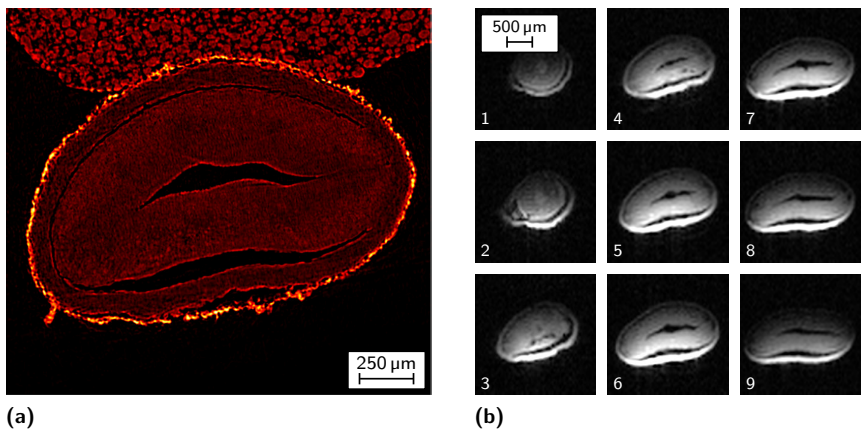


**Figure 7.4:** (a) Sesame seed grain X-ray CT conducted on a Bruker Skyscan 1172 system. The grain was attached using modelling wax. (b) The MR images were acquired with an isotropic resolution of  $40 \mu\text{m}^3$  in 23 h and 30 min ( $T_A$ ) (micFLASH sequence, flip angle  $30^\circ$ ). Each acquisition was repeated every 400 ms ( $T_R$ ). The echo time ( $T_E$ ) was  $970 \mu\text{s}$ . (Figure adapted from [225])

CT, resolutions in the range of about  $1 \mu\text{m}$  or even slightly below can be realised on standard laboratory setups. At the same time, however, the contrast information in the X-ray images is quite rudimentary when it comes to the organic constituents of the seeds.

Figure 7.4 shows selected imaging slices with the data obtained from the same sesame seed grain. The slice from the X-ray CT scan used 40 keV unfiltered X-ray radiation and an isotropic voxel resolution of  $2.30 \mu\text{m}$  was achieved.

The most dominating contrast feature in the image was the silica-rich husk. This structure was not observed in the MRM experiments. There, the most dominating signal came from the outer layer of the grain. The outer layer wrapped around the inner part of the seed, which essentially consisted of the two cotyledons with a gap in between. Image slices were captured in the coronal  $x,y$ -plane, as indicated in Figure 7.2. The gaps between the outer seed tissue and the cotyledons and in between the two cotyledons were reproduced in the MRI as well as in the X-ray CT image.

Such a combined imaging approach is especially interesting for imaging small, *hard* biological specimens such as seeds. With the considerably shrunk gap in

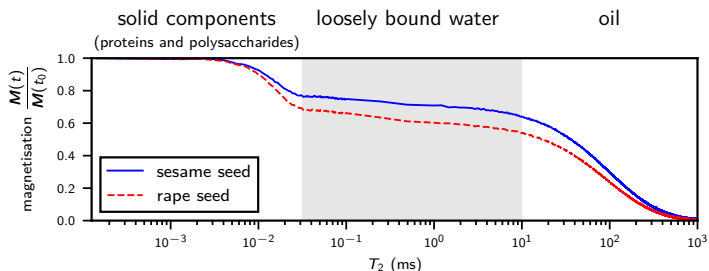


**Figure 7.5:** Transverse magnetization decay curves recorded at 20 MHz in a Bruker minispec mq20 using an SE-Carr-Purcell-Meiboom-Gill (CPMG) sequence. The magnetic resonance relaxometry (MRR) experiment was performed in collaboration with Nikolaus Nestle (BASF, Ludwigshafen).

resolution between the two techniques, correlating features found by the two imaging techniques on the same grain comes into the reach of feasibility.<sup>[225]</sup> On the other hand, MRR (see Figure 7.5) and MRM fit better to detect this specific information. Due to the availability of both, the relaxation time and the chemical shift as specific contrast moieties to discern oil and water, NMR techniques are more suitable to study the local composition of the seed, like the oil and water distribution.<sup>[225]</sup>

## 7.2 Evaluation of the uni-axial z-gradient

Studying the micro gradient performance by MR techniques required to integrate an RF detection coil.<sup>[187]</sup> The printed micro coil, used in the previous imaging experiments was based on a 500  $\mu\text{m}$  thick glass substrate, and due to its substrate thickness, it did not qualify for embedding it into the confined micro gradient. As a more simplified alternative, a single layered RF coil was fabricated, based on a similar structuring approach. Since the presented design of the coil reminded of a paper clip, it is referred to as the PAPERCLIP coil.

The here performed gradient evaluation was conducted for the uni-axial z-gradient since the Tx/Rx coil was less tedious to be integrated, when compared to a tri-axial gradient assembly. A tri-axial gradient assembly would require considerably more solder connections, with the consequence of a higher probability of failure.

### 7.2.1 PAPERCLIP micro coil

The focus on the design and fabrication of the PAPERCLIP micro coil was to notably minimise the processing complexity, with the objective of carrying out a basic, single-pulse NMR experiment. The design concept of the PAPERCLIP micro coil was previously described in Section 4.4 on page 107. The introduced manufacturing process required only single electroplated copper layer, since the two diced bi-plates were further flip-chip assembled and connected by soldering and required no copper bridges or multi-layer VIAs.<sup>[187]</sup>

Figure 7.6 illustrates the frequency-tuned PAPERCLIP coil, which was attached to a probe holder in a much similar way as performed for the ink-jet printed microcoil in Section 7.1. By the large pads and the use of low-temperature solder, it was possible to interconnect the coil bi-plates, even when there was limited access during the gradient flip-chip assembly.

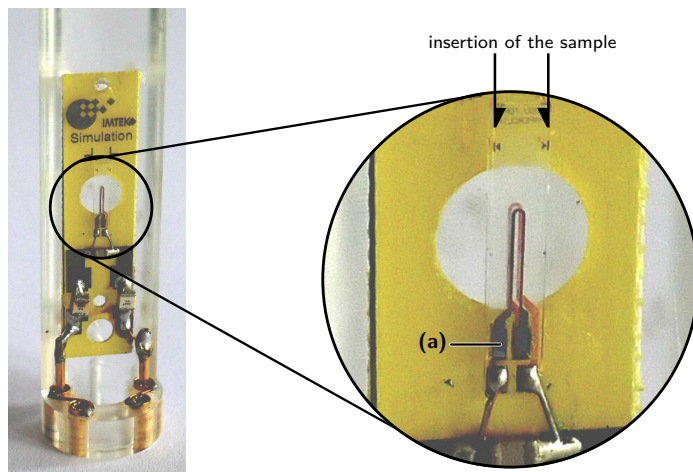


**Figure 7.6:** The PAPERCLIP micro coil attached onto a Micro5 compatible holder. The two glass slides were held in place by a solder connection (a).

The PAPERCLIP coil was also characterised using the Micro5 hardware, in a much similar way as for the printed micro coil. The return loss ( $S_{11}$ ) was measured using a NWA, which resulted in a dip of  $-37.8$  dB at the respective resonance frequency.<sup>[187]</sup>

First, the coil's  $B_1$  field uniformity was examined by a nutation experiment as shown in Figure 7.7(a).<sup>[226]</sup> With a fixed pulse power (PP), the pulse length (PL) was varied to identify the required PL for a  $90^\circ$  flip-angle. In this experiment, a rectangular glass capillary was used as the sample container (Product 5012, sample space depth  $100\ \mu\text{m}$ , width  $2\ \text{mm}$ , glass thickness  $100\ \mu\text{m}$  and capillary length  $5\ \text{cm}$ , VitroCom, USA). The capillary was filled with a  $0.5\ \text{M}$  nicotinamide  $\text{D}_2\text{O}$  solution, and the sample area spanned over the entire RF sensitive region of the micro coil.

Due to the  $B_1$  inhomogeneities, it was not possible to detect a  $180^\circ$  pulse. Fugariu *et al*.<sup>[227]</sup> made a similar observation, during the analysis of a variety of planar micro coils, while performing the nutation experiment.

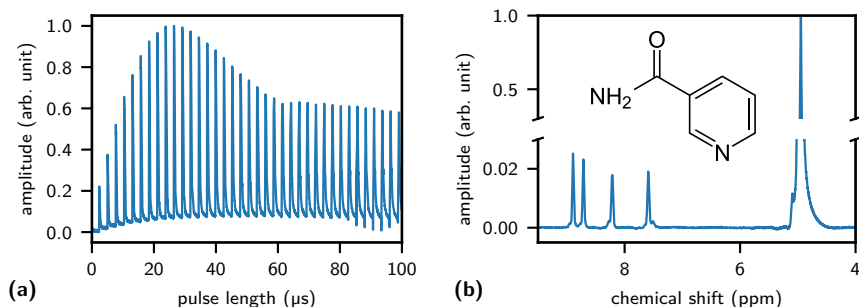


**Figure 7.7:** (a) nutation spectra of the PAPERCLIP micro coil. The  $90^\circ$  pulse was found at a PL of  $27.75 \mu\text{s}$  and the PP was  $0.23 \text{ W}$ . (b)  $^1\text{H}$  spectrum of  $0.5 \text{ M}$  nicotinamide ( $\text{C}_6\text{H}_6\text{N}_2\text{O}$ ) in  $\text{D}_2\text{O}$  (deuterium oxide), with an acquisition time of  $81.92 \text{ s}$  and the number of scans was  $100$ .

Furthermore, the PAPERCLIP micro coil was subjected to single pulse experiments with a flip-angle below  $90^\circ$ . Based on the parameter estimation from the nutation experiment, an NMR spectrum of nicotinamide was recorded, as shown in Figure 7.7(b). The applied PP was  $0.23 \text{ W}$  and the PL was  $20 \mu\text{s}$ , which corresponded to a flip-angle of approximately  $65^\circ$ . Peaks were detected at  $\delta^1\text{H} = 8.82 \text{ ppm}$ ,  $8.64 \text{ ppm}$ ,  $8.14 \text{ ppm}$ ,  $7.52 \text{ ppm}$  and  $4.87 \text{ ppm}$ .<sup>[187]</sup> The dominant peak at  $4.87 \text{ ppm}$  resulted from the residual  $\text{H}_2\text{O}$  and hydrogen-deuterium oxide (HDO) in the  $\text{D}_2\text{O}$  bottle. This peak had a FWHM of  $9.84 \text{ Hz}$  after moderate shimming. The FID raw data was post-processed using the *nmrglue* python module.<sup>[228]</sup>

A MRI experiment with a commercial field gradient was carried out to study the spatial intensity of the coil. Figure 7.8(a) illustrates the reconstructed FLASH image from the capillary tube that was filled with DIW. The slice thickness was chosen wider than the actual thickness of the capillary tube, in order to collect the signal over the entire tube. When using such a micro coil within the uni-axial miniaturised gradient, the expected profile would be much similar to the extracted profile in Figure 7.8(b), that summed up the voxel intensities over  $y$ .

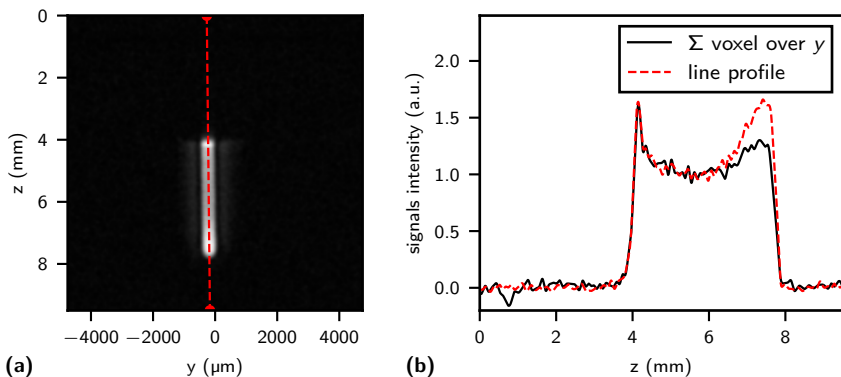


**Figure 7.8:** (a) MRI image to investigate the sensitive area of the PAPERCLIP micro coil. The scan time was 38 s and the slice thickness was 3.1 mm. (b) the profile extracted from the MRI image.

The line profile in Figure 7.8(b) presents an increase of the signal intensity, at the edges and especially where the coil windings changed the direction, at a  $z$ -position of around 7.8 mm. One possible way to suppress these signal-intense regions would be a copper sheet to attenuate the signal.<sup>[229]</sup> Such an additional metallisation<sup>[221]</sup> for implementing a signal shield is possible, but was omitted. The discontinuity of the intensity also restricted an inversion recovery experiment, that would require a  $180^\circ$  excitation pulse. A selective excitation of the more homogeneous centre region by the use of the field gradient could be investigated.

## 7.2.2 Micro engineered phantom

In previous research, grid phantoms with water filled, geometrically predefined sections were used to study the gradient field homogeneity.<sup>[230]</sup> For a microscopic investigation, Jasiński *et al*<sup>[42]</sup> used a bunch of capillaries, positioned side by side to build up a test phantom.

In here, a micro phantom was cleanroom fabricated to investigate the field of the z-gradient. The custom-designed phantom had a compatible size as the rectangular capillary tube from the previous study, but included photo-defined alternating structures. To illustrate the NMR active regions, one fabricated sample insert was filled with blue ink as shown in Figure 7.9(a). The fabrication of the phantom was based on a substrate bonding process of ORDYL<sup>®</sup> SY, in a much similar way as previously performed by Spengler *et al.*<sup>[56,183]</sup>

In this work, micro fluidic channels were patterned between the two bonded glass substrates ( $2 \times \text{D 263}^{\text{®}}$  T, SCHOTT Malaysia, see also Table 4.3 on page 105). The alternating parallel channels were structured to a width of  $80 \mu\text{m}$  and the ORDYL<sup>®</sup> SY 390 between the channels formed a width of  $120 \mu\text{m}$ . The structuring resolution was at the resist's resolution limit. To render triangular shaped channels, the utilised ORDYL<sup>®</sup> SY 390 DFR was exposed from the backside through the glass substrate. In principle, improved adhesion of the glass–ORDYL<sup>®</sup> SY interface was achieved by the aforementioned backside lithography, since the incident light got first absorbed at the respective glass–ORDYL<sup>®</sup> SY interface.<sup>[187]</sup>

Spengler<sup>[183]</sup> employed soda-lime glass substrates that offered an improved adhesion towards the ORDYL<sup>®</sup> SY, when compared to the utilised  $\text{D 263}^{\text{®}}$  T borosilicate float glass. However, equivalent soda-lime substrate were not available in the required thickness of  $100 \mu\text{m}$ .

The MR image in Figure 7.9(c) of the channel's cross-section rendered triangular shaped peaks, that were achieved by the tapered channels, which resulted from the backside lithography. The image reconstruction was based on a python module to read in Bruker MRI files.<sup>[231]</sup> The software was adjusted in terms of fast Fourier transform (FFT) shifting and  $k$ -space ordering. The imaged slice in Figure 7.9(c) was positioned to the centre of the coil. A SNR of 19.3 was calculated for the average signal intensities, extracted from the highlighted areas in Figure 7.9(c).<sup>[187]</sup>

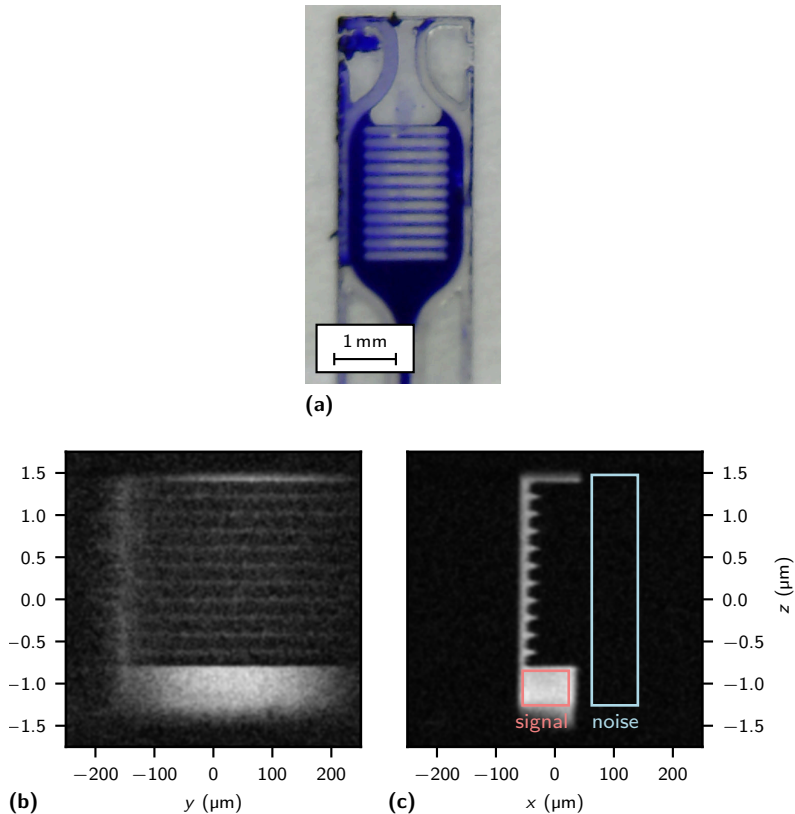


**Figure 7.9:** (a) the ink-filled insert, that measured a thickness of  $288\ \mu\text{m}$  for the stack of D 263<sup>®</sup> T, ORDYL<sup>®</sup> SY 390 and D 263<sup>®</sup> T. (b), (c)  $^1\text{H}$  micFLASH images from the custom designed phantom filled with DIW using the Bruker Micro5 gradient. The matrix size was  $128 \times 128$ . The anisotropic in-plane resolution was  $27.3\ \mu\text{m} \times 3.9\ \mu\text{m}$ , the slice thickness was  $0.25\ \text{mm}$ , the echo time  $T_E$  was  $4.98\ \text{ms}$ , the number of scans was 500 and the scan time  $T_A$  was  $1\ \text{h}\ 46\ \text{min}$ . (Figure reproduced from [187])

For both the MRI images, the z-profiles were generated as shown in Figure 7.10. The maximum peak-to-peak variation was  $\pm 9.9\ \mu\text{m}$ , which corresponded roughly to the accuracy of the utilised lithographic foil mask.

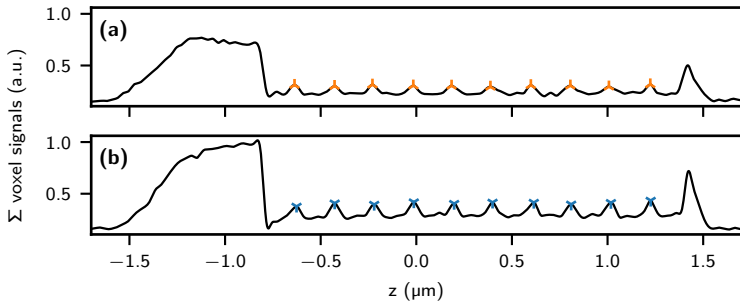


**Figure 7.10:** Extracted z-profiles from the MRI images. Figure 7.9(b) is shown in (a) and Figure 7.9(c) is shown in (b).

These imaging experiments gave sufficient insight about the cross-section of the test phantom and allowed to proceed with a 1D NMR imaging sequence to evaluate the micro gradient.

### 7.2.3 1D-imaging using the miniaturised uni-axial z-gradient

Figure 7.11(a) shows the opened, micro gradient flip-chip during the assembly. The BOTTOMCHIP attached to the carrier PCB. Four glass spacers with a size of  $2.6\text{ mm} \times 7.4\text{ mm} \times 500\text{ }\mu\text{m}$  were glued to the BOTTOMCHIP and TOPCHIP with the EPO-TEK<sup>®</sup>353ND (Epoxy Technology Inc.) two-component adhesive. The alignment structures, that were applied in the last processing step facilitated the accurate positioning. In addition, Cr deposited alignment markings on the glass spacers allowed for the flip-chip positioning under the microscope.

In the next step, the PAPERCLIP coil bi-plates were manually aligned and glued to each gradient half-chip. The diced Tx/Rx coil had a final thickness of  $277\text{ }\mu\text{m}$ . In contrast to Table 4.3 on page 105, the coil loops on the glass slides were embedded into two layers of ORDYL<sup>®</sup> SY 330. The tuning capacitor was directly soldered to the Cu pads on PAPERCLIP coil (0805 2.7 pF, SRT-MICROCERAMIQUE, Vendome, France). The  $500\text{ }\mu\text{m}$  thick glass spacer maintained the required gap for placing the coil and sample insert in between the gradient bi-plates.<sup>[187]</sup>

In Figure 7.11(a), below the Cu coil loop, one can see the Cr adhesion layer of the Cr/Au electroplating seed. Below the Cr/Au layer, a  $12\text{ }\mu\text{m}$  thick RF shield was electroplated, which attenuated the coupling to the gradient coil (see also Section 6.2 on page 146). The shield was structured on the rear of each glass slide and was not connected to ground.

The RF shield was also added to suppress any  $^1\text{H}$  signal from the DIW from the gradient's cooling network. However, in order to reduce the complexity of the probe setup, active liquid cooling was not performed. In comparison to the previous PAPERCLIP coil evaluation in Figure 7.7(a), different RF pulse parameters were retrieved for the shielded Tx/Rx coil and the adjustments to the gradient flip-chip spacing.

To sustain thermal stability without active liquid cooling, very low currents were applied to the gradient coil, such that the rise in temperature of gradient

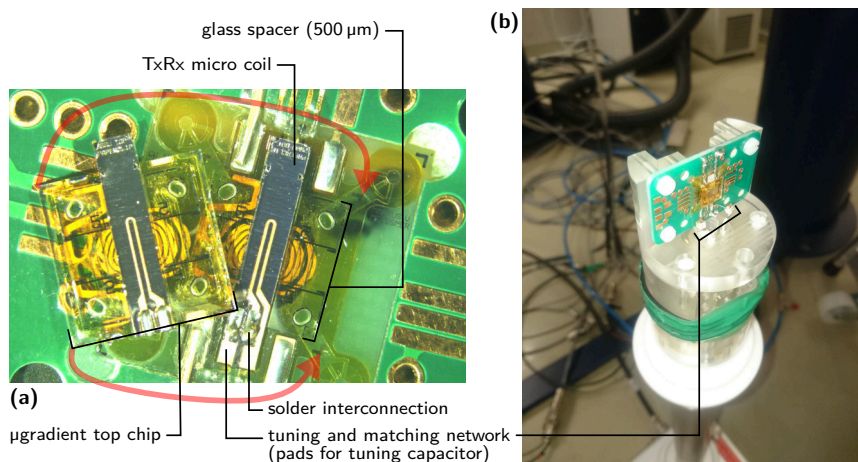


**Figure 7.11:** (a) the two z-gradient coil biplanes with the micro Tx/Rx and glass-spacers attached. (b) the custom designed NMR probe with the micro gradient assembly. The PMMA holder was attached to the Bruker Micro5 probe base. (Figure adapted from [187])

coils and the sample region could be neglected. For driving the micro gradient, the single-channel GAP amplifier (Bruker GmbH, Germany) was used, as it was directly available without requiring fundamental hardware modifications to the spectrometer. The amplifier permitted a maximum current of 10 A, with a rise and fall time smaller than  $10\ \mu\text{s}$  (to 90%).<sup>[187]</sup> The integrated DAC had a 16-bit resolution, which corresponded to approximately  $\pm 0.31\ \text{mA}$ .

A power resistor of  $1\ \Omega$  was added to the current path, in series to the gradient, to inhibit damage to the amplifier through overheating while pulsing the low-ohmic gradient coil.<sup>[187]</sup> The self-constructed current source as shown in Figure 6.7(a) on page 155 was not employed, since the spectrometer did not provide the suitable interfaces to allow a straightforward integration.

First, the protocol to acquire the 1D profile along the z-direction is described. The pulse sequence was implemented using the spectrometer's control software

TOPSPIN™ (Bruker GmbH, Germany). In here, the standard *zg* pulse program was extended with a gradient pulse. The pulse sequence was inspired by Mansfield<sup>[232]</sup> by applying the z-gradient during signal readout. As illustrated in the pulse sequence diagram in Figure 7.12(a), the NMR signal was recorded in the presence of the applied linear gradient  $G_z$ .

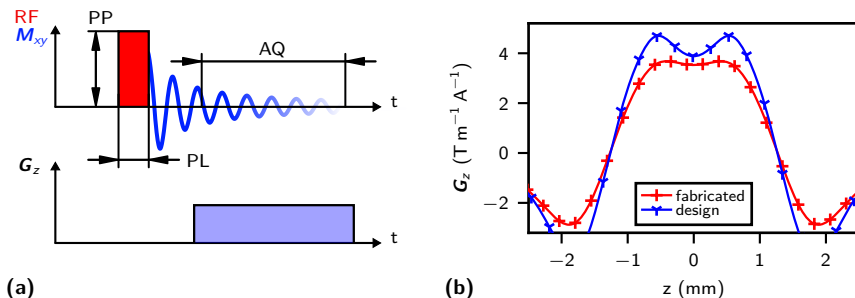


**Figure 7.12:** (a) the pulse sequence for capturing the 1D profile. (b) the calculated gradient slope in the centre of the gradient coil. (Figure adapted from [187])

A pre-phasing gradient pulse as performed by Topgaard *et al*<sup>[233]</sup> was omitted, and the phase correction was rather applied as part of the signal post-processing.<sup>[187]</sup> The signal was obtained directly from the FID without generating an echo. After computing the FFT of the time-domain FID signal, the spin isochromats (as a function of frequencies) mapped to the position of the DIW filled channels, and revealed the projected cross-section of the phantom.

FID post-processing was performed using the `numpy`<sup>[189,234]</sup> and the `nmrglue`<sup>[228]</sup> python toolkit. In the post-processing cycle, the FFT and manual zero-order and first-order phase correction were performed. Any baseline correction was omitted. The frequency spectrum was smoothed to de-noise the signal.

As outlined in the previous section in Figure 7.10(a), the channel structures rendered sharp peaks in the MRI experiment and also in the recorded NMR spectrum. Within the relevant frequency range, peaks in the NMR

spectrum with a selected height threshold were extracted using the module `nmrglue.analysis.peakpick`. The local gradient strength  $\mathbf{G}$  between the neighbouring peaks was calculated by,

$$\mathbf{G}_{P_{n+1},n} = \frac{\omega'_{P_{n+1}} - \omega'_{P_n}}{\gamma_{1H} \cdot (P_{n+1} - P_n)}, \quad (7.1)$$

where  $\omega$  is the angular frequency of precession,  $\gamma_{1H}$  is the gyromagnetic ratio, and  $P$  is the  $z$  position of the detected channel peak. For plotting the gradient linearity, the lithographically defined channels of the phantom were considered to have an equidistant spacing to each other. From the layout data, a fixed value of 200  $\mu\text{m}$  was considered as the channel-to-channel spacing ( $P_{n+1} - P_n$ ), which was used to determine the gradient linearity of each segment.<sup>[187]</sup>

To examine the linearity and strength, the micro  $z$ -gradient was compared to the approved Micro5 gradient, to test the pulse sequence and post-processing. The relevant acquisition parameters and the measured gradient linearity are summarised in Table 7.1.

**Reference 1D imaging:** First, two 1D profiles from the Micro5 gradient were captured as shown in Figure 7.13. The temperature of the Micro5's liquid cooling system was reduced to 10 °C which caused minor condensation but allowed for a longer measurement duration. The filled sample insert could not be sealed but the outer cooling slowed down the evaporation of the DIW within the sample phantom. The mapping of the Micro5 gradient in Figure 7.13(a) confirmed the advertised gradient efficiency of 0.05  $\text{T m}^{-1} \text{A}^{-1}$ .<sup>[187]</sup> The homogeneity of the gradient is generally improved with the gradient coils located further apart from the specimen. Since the commercial Micro5 was constructed to provide a FOV of approximately 1  $\text{cm}^3$ , the achieved gradient linearity was considerably better for the confined test phantom.

The Micro5 gradient centre for both of the measurements in Figure 7.13 appeared at different positions since the coil insertion and mechanical tuning and matching caused a displacement of the Tx/Rx coil insert in the z-direction. The profiles in Figure 7.13 were centred between the peaks P3 and P4.

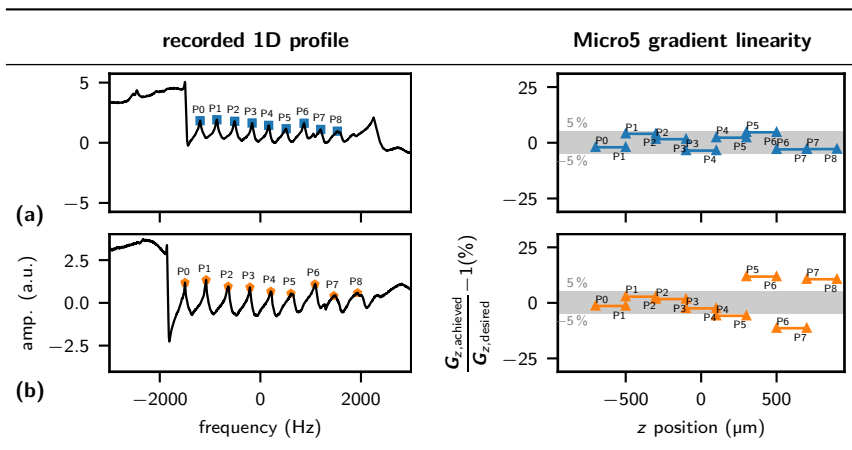


**Figure 7.13:** Reference measurement using the Micro5 gradient coil. A fresh sample insert was used for each recorded profile. (Figure adapted from [187])

**Micro z-gradient 1D imaging:** For mapping the micro-gradient, several profiles with different gradient currents were recorded to detect irregularities in the gradient field (see Figure 7.14).<sup>[187]</sup> In the beginning, the initial amplifier setting was tuned to closely match the gradient strength of the Micro5 experiment from Figure 7.13(a). The experiments in Figure 7.14(a) and Figure 7.14(b) demonstrated clear readability of the peaks. Since the Tx/Rx coil was rigidly attached to the gradient coil, the gradient centre frequency did not change in position with respect to the FOV of the receive coil.

To analyse the loss in gradient strength which was caused by thicker glass spacers, a Biot-Savart calculation was performed. The 500  $\mu\text{m}$

thicker spacers added 200  $\mu\text{m}$  additional spacing to the gradient bi-plate separation. The calculated field of the gradient in the centre region is shown in Figure 7.12(b), which illustrates a drop in the resulting gradient strength to  $3.2 \text{ T m}^{-1} \text{ A}^{-1}$  and a reduced FOV in z-direction. Occasionally, some channels did not fill with the DIW, were blocked or showed patterning imperfections from the fabrication (Figure 7.14(c), Figure 7.14(d)).

The centre frequency of the micro gradient was determined by the  $^1\text{H}$  spectrum without gradient coils switched off. By knowing the frequency, it is also feasible to estimate the accuracy for positioning the phantom insert. A maximum offset of 28  $\mu\text{m}$  for the manual positioning of the insert was extracted from the 1D profiles.

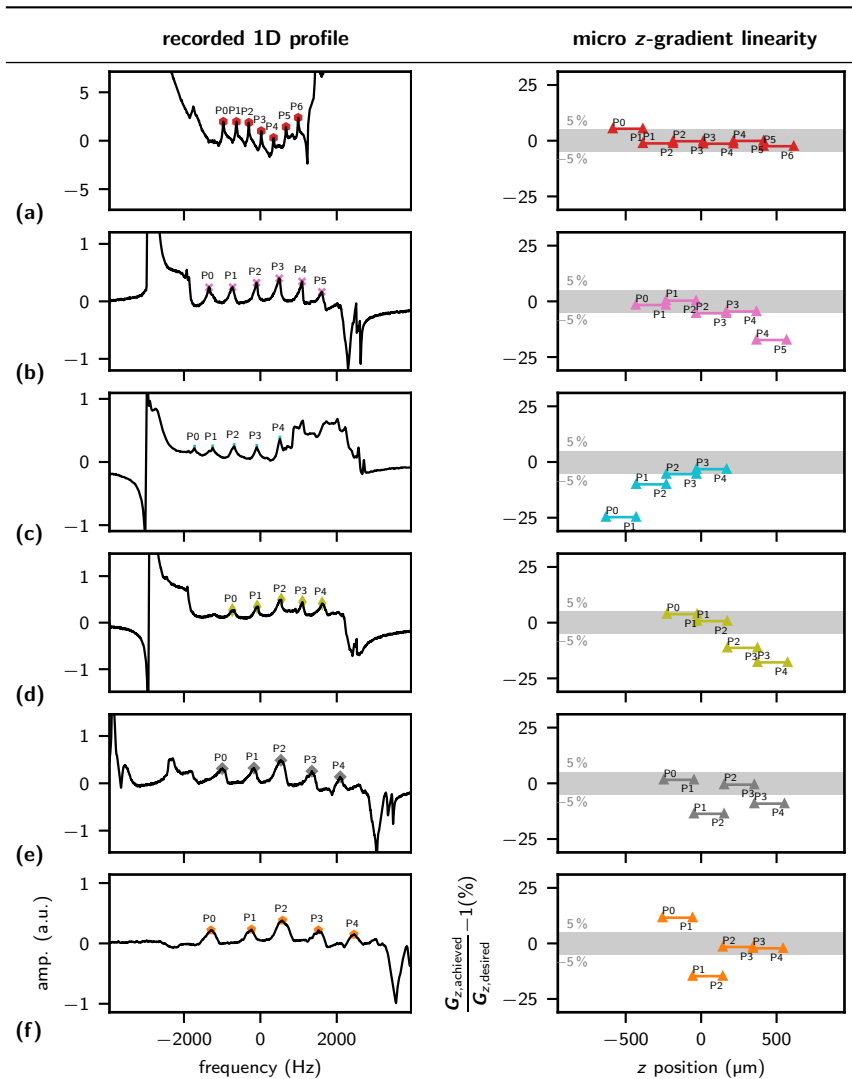


**Figure 7.14:** Recording of micro gradient line profiles. For each recorded profile, a fresh sample insert was used. (Figure adapted from [187])

Besides the linearity of the gradient itself, the measurement accuracy for the peak position was also affected by the FID resolution. According to the *Nyquist-Shannon* sampling theorem, an extra long acquisition time (AQ) is required to minimise the error caused by the FID resolution. The FID resolution was calculated from the reciprocal of the AQ and also affected the measurement of the gradient strength. To get maximum resolution out of the NMR experiment, the AQ must be as long as possible, which is calculated from the number of point digitised (TD) and the sweep-width (SW),  $AQ = TD \cdot (2 SW)^{-1}$ . The error related to FID resolution was added to Table 7.1.

Through the above described experiment, the magnetic field accuracy of a micro-gradient was analysed for the first time by mapping the field with precisely manufactured micro-structures. A gradient efficiency of  $3.15 \text{ T m}^{-1} \text{ A}^{-1}$  was extracted from the peaks P0–P6 as shown in Figure 7.14(a).<sup>[187]</sup> This gradient efficiency was applied as the desired  $\mathbf{G}_{\text{desired}}$  to the *right* side of all plots in Figure 7.14.

The other experiments in Figure 7.14 (Figure 7.14(b) – (f)) were recorded with longer measurement times and showed somehow incomplete filling of the channels. In fact, the RF power from the spin excitation got absorbed by the copper shield around the coil and converted into heat, which also heated up the sample insert. The mean  $\mathbf{G}_z$  in Table 7.1 also contained channels that had incorrect physical dimensions due to the liquid state.

The modular assembly facilitated the replacement of the Tx/Rx microcoil by a different coil design.<sup>[57,235]</sup> With the performed 1D profiling it was not possible to address the magnetic field uniformity in the *x*- and *y*-direction. To determine such parasitic field variations in the respective axial directions, specially fabricated sample inserts should be considered. Other resist materials or an alternative structuring method to define the sample insert could provide an improved peak resolution during 1D profiling.

Experiment	AQ (s)	FID resolution (Hz)	error FID resolution ( $\pm\%$ )	number of scans	gradient current $I_{G_z}$ (A)	mean $G_z$ ( $T m^{-1}$ )	mean lin. error (%)	std (%)	max lin. error (%)	min lin. error (%)
<b>Micro5 gradient:</b>										
Figure 7.13(a)	0.133	7.5	2.3	200	0.816	0.040	3.0	1.0	4.7	1.6
Figure 7.13(b)	0.133	7.5	2.0	300	1.020	0.050	6.0	4.3	11.8	1.4
<b>micro z-gradient:</b>										
Figure 7.14(a)	0.167	6.0	1.9	100	0.012	0.038	1.8	1.8	5.4	0.1
Figure 7.14(b)	0.250	4.0	0.8	100	0.023	0.069	5.8	6.0	17.3	0.3
Figure 7.14(c)	0.250	4.0	0.8	80	0.023	0.066	10.9	8.4	24.7	3.2
Figure 7.14(d)	0.250	4.0	0.8	80	0.023	0.069	8.4	6.7	17.8	0.7
Figure 7.14(e)	0.250	4.0	0.6	200	0.031	0.091	6.2	5.4	13.7	0.6
Figure 7.14(f)	0.250	4.0	0.5	200	0.036	0.110	7.5	5.7	14.7	1.6

**Table 7.1:** The parameters of the pulse sequence in Figure 7.12(a) used to perform the experiments in Figure 7.13 and Figure 7.14. For all the measurements, the RF pulse power (PP) was 0.1 W and the pulse length (PL) was 38  $\mu$ s.

## 8 Conclusion and outlook

This thesis reports on novel micro gradient designs which were microfabricated, characterised and tested in nuclear magnetic resonance (NMR) experiments. The strong magnetic field gradients were generated by bringing the gradient coils physically closer to the sample.<sup>[236]</sup>

The fundamental objective was to **explore new field gradient approaches and the related fabrication methods to create a micro-integrated field gradient on a confined footprint**. This work demonstrates the next a level of integration and miniaturisation in magnetic resonance imaging (MRI) by combining a microfabricated gradient system with a compact transmit and receive (Tx/Rx) coil on a microchip. Optimisations were carried out in the design process and by recombining MEMS processes and materials in a unique new way to reach a high level of integration. A multi-layer, topology-optimised gradient coil was presented, which exceeded the complexity and manufacturing time of conventional micro-engineered NMR pickup coils.

This research aimed to identify whether **a miniaturised gradient system can produce a particularly strong field variation without causing excessive heat-up towards the sample region**. Due to the high integration density and the very close physical distance to the sample, the thermal stability from the gradient became a significant concern. Therefore, a gradient coil design was introduced for implementing insertable bi-planar gradient coils to exhibit minimum power dissipation. An active cooling system maintained the thermal stability of the gradient coil with integrated temperature monitoring by adding resistance temperature detectors (RTDs) to the chip.

Thus, the question arises if **the linearity of the gradient can be verified even at the microscopic dimensions**. The dense construction made it increasingly difficult to analyse the gradient's generated field accurately. A method was developed to determine the gradient linearity by employing a micro-machined phantom insert. The field gradient was subjected to a one-dimensional (1D) NMR imaging experiment. From the custom-designed phantom, line profiles were recorded to address the linearity of the gradient coil.

The development and the optimisations were carried out in diverse fields, and the systematic approach is discussed in the following:

**Process evaluation.** The first part of this thesis was dedicated to identifying the materials and their properties for gradient coil fabrication. SU-8 and SU-8 based dry film resists (DFRs) were advantageous for multi-layer applications since they achieved high-resolution patterning and remained stable without material loss or shrinkage during thermal load. However, the significant weight loss of the ORDYL<sup>®</sup> SY material during thermal load and the physical vapour deposition (PVD) incompatibility did not qualify the resist to be used for the gradient assembly. Poor solvent stability was another concern of the ORDYL<sup>®</sup> SY, and the product degraded quickly in standard solvents like acetone or trichloromethane, which are often used in NMR experiments. Alternative materials could replace the ORDYL<sup>®</sup> SY, which can be used similarly within a substrate bonding process and could be applied without photolithography, for example, by screen printing.

A silver nano-particle ink-jet printing process was introduced, which essentially brought up the manufacturing processes for the miniaturised gradient chip. For a sufficient structuring resolution, it was important to control the silver ink wetting behaviour. A method was demonstrated to adjust the hydrophilic contact angle on the SU-8 and ORDYL<sup>®</sup> SY surfaces by plasma treatment in combination with thermal annealing, to adjust for the printing quality.<sup>[127]</sup>

Optically transparent photoresists and substrates allowed to define an electroplating mould by the back-side (BS) lithography, where the ink-jet printed silver tracks were used as the lithographic mask. In addition, the direct application of the silver seed layer by the printing process reduced the material consumption to a minimum. Furthermore, the ink-jet printing process offered a unique way to apply electroplated conductive microstructures even on the acrylic-based ORDYL<sup>®</sup> SY resist. The aspect ratio and minimum feature size of the ORDYL<sup>®</sup> SY showed excellent compatibility concerning the achievable jetting resolution.<sup>[127]</sup> Much comparable to the conventional printed circuit board (PCB) manufacturing methods, highly conductive metal structures were implemented on a confined footprint. A rectangular radio frequency (RF) micro coil was fabricated using the newly derived ink-jet printing process, and the coil was successfully employed in a magnetic resonance microscopy (MRM) experiment.

Thus, high-resolution ink-jet printing was restricted to rectangular structuring, since the utilised printer deposited the ink droplets line-by-line on a raster grid. An alternative, path-based droplet jetting technique could have opened up a broader range of applications, including curved patterning.<sup>[127]</sup> However, another concern of the ink-jet printing was nozzle blocking, induced by the accumulation of silver ink nanoparticles. Consequently, the BS lithography process was successfully transferred to PVD based lift-off structuring, which was used to apply the micro gradient coil patterns.

**Micro electroplating.** A custom-designed plating bath further refined the copper electroplating process. The presented deposition process made it possible to structure the miniaturised gradient coils without requiring subsequent post-processing and consequently conserved material and processing effort. Application-specific wafer holders were developed, which

perfectly integrated with the pre-structured seed layer any the SU-8 plating mould.

Furthermore, a current source was developed, which not only allowed for parallel deposition within one bath but also the reproducibility of the entire process was improved. The programmable current source for the electroplating of 4" substrates offered a stable output current and allowed a vast flexibility in the specification of the plating parameters, including monitoring of the plating process. The developed circuit also served as the basis for its further development towards a pulse current source, which was presented in close collaboration with Nassar *et al.* [121]

**Gradient coil design.** A topologically optimised micro gradient design was presented that provided an elevated gradient strength while minimising the power dissipation (in collaboration with While *et al.* [103]). To optimise the power dissipation with respect to the achievable gradient efficiency in  $\text{T m}^{-1} \text{A}^{-1}$ , tracks of variable width were used to lower the electrical resistivity. A method was presented to interconnect the stream-function contours to define practically realisable coil windings. The design generation was intensively automated by a b-spline based interconnection of the nested stream-contours, to generate a fabrication-ready coil layout. The chip design allowed for an orthogonal orientation, and likewise in a parallel orientation with respect to the direction of the main magnetic field  $\mathbf{B}_0$ . Thus, the design allowed for a modular integration of application-specific bi-planar Tx/Rx coils.

A uni-axial z-gradient design was presented, which was composed of two bi-layers. The coil design allowed the construction of a closed coil loop, to compensation for the distortion of the coil interconnects. However, two gradient bi-layers achieve improved field homogeneity compared to single-layer implementation. [86] Two design iterations were required to improve the manufacturability, and it was necessary to stretch the target field to a larger sample area.

Besides, a tri-axial gradient coil design was considered where the  $x$ -gradient was based on a single bi-layer. The  $x$ -gradient coil was a trade-off between easier fabricability and in consequence, a higher induced field error. The classical Anderson<sup>[77]</sup> shim coil design was refined, and it was possible to implement the  $y$ - and  $z$ -gradient on the same bi-layer to conserve space. The  $y$ - and  $z$ -gradient coils were based on straight conductors, and the presented approach represents a further decrease of coil layers compared to Seeber's tri-axial field gradient.<sup>[50]</sup> The  $y$ -gradient implementation is typically used to produce a gradient in the transversal direction and is still technologically relevant.<sup>[83]</sup> The design of the tri-axial gradient would allow for placement into a permanent *Halbach magnet*, considering its limited space in the  $z$ -dimension.<sup>[32]</sup> Since the tri-axial gradient had an equal number of copper layers compared to the uni-axial  $z$ -gradient, it was possible to test and incorporate both designs on the same wafer.

**Gradient coil fabrication.** With the manufacturing process introduced here, it was possible to accommodate the design freedom for the *genuine-minimum-power* gradient coils and to move them into fabrication. Due to the demanding multi-layer precision and the high requirements on the current carrying capacity, the manufacturing process significantly exceeded the fabrication complexity of previously developed microfabricated NMR detection coils.

In addition, the lift-off process of the Pt seed layer enabled the structuring of the RTDs in physical distance to the gradient coils to allow on-chip temperature monitoring. Using of the Pt seed layer as an alignment reference, misalignment errors did not propagate throughout the layer stack.

The BS exposure also achieved enhanced adhesion of the initial SU-8 layer. Using vacuum lamination instead of hot-roll lamination for applying the SU-8 dry film resist improved the process reliability.

It is worth rethinking the use of the Cr/Au seed layer system for depositing the second coil layer. By replacing it with a Cr/Cu or Ti/Cu seed layer combination, the use of less hazardous chemicals and cyanide-free stripping would become feasible.

From the perspective of a more simplified fabrication, the TOPCOOL cooling method with the channel routing above the chip should be preferred. However, the TOPCOOL design added an additional separation between the gradient coil and the sample, which resulted in a reduced gradient strength. The MIDCOOL cooling between the coil layers would require a refined cleaning and rinsing procedure to avoid channel blocking, caused by the seed layer stripping. Indeed, a combination of both, the TOPCOOL and the MIDCOOL would be desirable to advance the cooling performance.

One way to reduce chip footprint would be to use a through glass VIA (TGV) technology to establish the gradient coil's electrical connection.<sup>[237]</sup> With TGVs, the fluidic and the electrical interconnects could be moved to the rear side of the chip. Both, the TOPCHIP and the BOTTOMCHIP could be based on the same layout, and the chip dimensions would essentially reduce to the size of the TOPCHIP, with a chip side length smaller than 9 mm. Another approach could be an inverse layer stack of the gradient design, with the glass substrate oriented towards the imaging region. Consequently, the processing should then be based on very thin glass substrates to achieve the required gradient strength.

The process presented here required a manufacturing time of around 70 h. In a future design iteration, adaptive manufacturing techniques should be investigated to reduce the processing effort further.

**Assembly concept.** The flip-chip structure was subdivided into three modules, the gradient bi-plates, the receiving coil and the glass spacers, which separate the bi-planar gradient in a well-defined way. The presented approach achieved a high level of miniaturisation. However, the substrates

of previously developed microcoils<sup>[54,61,183]</sup> were too thick (1 mm to 2 mm) and did not qualify for combining them with the uni-axial micro gradient. Also, the support structures for aligning the coils were oversized. Most suitable for a possible integration was Spengler's *Helmholtz* coil, which had a total thickness of at least 1 mm to 1.5 mm. The coils also missed a copper shield to attenuate the coupling of the RF coil with the gradient.

Consequently, a Tx/Rx coil on a considerably thin glass substrate was developed here, benefiting from the BS lithography process. The dielectric constant of the MEMpax<sup>®</sup> was smaller than for the D263<sup>®</sup> T ECO substrate, and the MEMpax<sup>®</sup> was chosen explicitly to moderate the capacitive effects of the Cu shield. With the insights obtained in the assembly process, a combined spacer and coil construction should be pursued. Fine-tuning of the layout and the thickness of the Tx/Rx coil must become the subject of further investigation.

An even smaller format of the solder pads on the BOTTOMCHIP would also allow for a more space-saving package. But, the large solder pads ensured the stability of the electrical connections and remained without defects even at high current loads.

**Thermal management.** The heat-up of the microfabricated gradient was evaluated in multiple experiments. The active, liquid cooling system improved the thermal stability, and no leakage was detected at the applied moderate flow rates. For an applied constant current of 4 A, the uni-axial z-gradient half-chip can generate a gradient strength of  $12.8 \text{ T m}^{-1}$ , causing Joule heating up to 18 K above ambient within the sample region-of-interest (ROI). However, the maximum flow rate of the coolant was limited by the available peristaltic pump, and there would be still potential by using a pump at a higher flow rate.<sup>[187]</sup>

The routing and direction of the cooling channels cause a temperature gradient across the chip. A fractal-like liquid cooling network, as described by Pence *et al.*,<sup>[238]</sup> would distribute the cooling more evenly across the chip, by reducing thermal hot-spots near the centre. In addition, injecting the coolant through the glass substrate in the middle of the chip would improve the thermal stability in proximity to the sample.

Considering the thermal characteristics, it is of particular interest to compare the performance of the glass chip with a low temperature cofired ceramics (LTCC) substrate. In the standard LTCC process, the embedded conductors show a much higher resulting resistance than the electroplated, pure Cu conductors here. LTCC substrates suffer from a high sheet resistance with a final, fired track thickness of a few  $\mu\text{m}$ . Perrone *et al.*<sup>[222]</sup> improved the LTCC track thickness by embossing a mould into the ceramic to extend the conductor thickness (the thermal properties were added to Table 6.2 on page 161). Comparing Perrone's experiment with the liquid-cooled gradient would require a thermodynamic model. However, the description of the effects with a simple model is limited. Many influencing factors such as the thermoconductive energy transport, thermal radiation and even no direct relationship between the injected current and the liquid cooling performance do not allow to come up with a simple model. The use of ceramic materials<sup>[239]</sup> to optimise the heat transfer would remain subject to further optimisation.<sup>[187]</sup> Other research reported enhanced heat flux reduction by using a sapphire substrate, which would still allow for the introduced BS lithography.<sup>[240]</sup>

**Micro coil evaluation.** The ink-jet printed microcoil and the PAPERCLIP microcoil were subjected to NMR experiments using a high-field 11.7 T magnet.<sup>[127]</sup> In terms of the resulting imaging resolution, the ink-jet printed coil performed comparably to microcoils fabricated with other technologies,<sup>[61]</sup> but the mask-less fabrication process would allow for a faster redesign.

For the purpose of investigating the micro gradient linearity, the PAPERCLIP coil was designed to possess a sensitive region that extends over the homogeneous region of the uni-axial z-gradient. In combination with a commercial gradient system, the RF field was investigated in a gradient-echo MRI experiment, to investigate the  $B_1$  field along the z-direction. Knowledge about the field distribution was an essential prerequisite for measuring the gradient field since it affected the imaging intensity across the recorded line profile. However, there would be potential other coil designs with a higher field homogeneity,<sup>[57]</sup> which are also capable of imaging an elongated region and would allow for a more uniform flip-angle across the sample than the PAPERCLIP coil.

**Gradient coil evaluation.** There are different methods to evaluate the field distribution of a gradient coil. Commercially available Hall probes were one solution but were too large to map the confined ROI.<sup>[92]</sup> However, NMR was the foremost accurate technology within reach. NMR imaging requires a suitable RF coil, and the aforementioned PAPERCLIP coil was extensively tested before it was integrated into the gradient assembly. NMR diffusion experiments are one way to evaluate the gradient linearity, but such measurements are also very temperature-dependent, since RF heating of the sample became another influencing factor. Also, for a diffusion measurement, the sample space must be restricted to the linear imaging region of the gradient field.

An NMR experiment was set up, and 1D profiling was chosen as it allows for calibrating the gradient. The imaged structures of a micro-engineered phantom were independent with respect to liquid diffusion. In contrast, a diffusion experiment is unaffected by the patterning accuracy of the test phantom and would be affected, at most, by the edge geometry of the test phantom. Due to the low resistivity and inductance of the z-gradient coil, the current load was reduced, and also the gradient operation without amplifier pre-emphasis became feasible. The benefit

of the low inductance z-gradient is that the low inductance of  $0.34\ \mu\text{H}$  allows for rapid switching at a high slew-rate.<sup>[187]</sup> Looking at the uni-axial gradient efficiency of  $3.15\ \text{T m}^{-1}\ \text{A}^{-1}$ , the presented chip can be compared with the macroscopic, hand-wound circular gradient coils by Zhang *et al*.<sup>[25]</sup> or Bowtell *et al*.<sup>[94]</sup>. Due to the compact chip design, a profiled length of  $1.2\ \text{mm}$  was achieved,<sup>[187]</sup> whereas Bowtell *et al*.<sup>[94]</sup> captured a profile of  $4.5\ \text{mm}$ .

Testing of the presented tri-axial gradient system becomes the subject of ongoing work and would require the integration of a suitable Tx/Rx coil. However, the theoretically achievable gradient efficiency can be compared with the electron spin resonance (ESR) gradient system by Shtirberg *et al*.<sup>[81]</sup> or Weiger *et al*.<sup>[82]</sup>

# A Process description

## A.1 Gradient chip fabrication

Processing started on 500  $\mu\text{m}$  thick, 4" Borofloat 33 (Schott Glass Malaysia) substrate. The lithography steps show the snippets of the layout and the displayed size corresponds to 16 mm  $\times$  16 mm. The diced chip size would finally measure 14.6 mm  $\times$  14.6 mm for the BOTTOMCHIP and 8.8 mm  $\times$  8.8 mm for the TOPCHIP.

G 1: Platinum seed layer		$\Sigma$ Machine Time (MT): 316 min	
G 1.1:	Cleaning standard I.	MT:	7 min
	temperature:	70	$^{\circ}\text{C}$
	time:	7	min
	type:	Caro acid ( $\text{H}_2\text{SO}_4 + \text{H}_2\text{O}_2$ ) + QDR	
No wait time after QDR.			
G 1.2:	Spin rinse dry	Semitool	MT: 5 min
	angular velocity:	2000	rpm
Include nitrogen flush. No wait time after spin rinse dry.			
G 1.3:	Dehydration bake	oven	MT: 30 min
	temperature:	200	$^{\circ}\text{C}$
Let borosilicate wafers cool down to room temperature after dehydration.			

## A Process description

---

<b>G 1.4:</b>	<b>Oxygen plasma</b>	TePla, Technics Plasma GmbH	MT:	7 min
	oxygen flow:		500	sccm
	power:		200	W
	time:		4	min

To oxidize the surface of the borosilicate substrate.

<b>G 1.5:</b>	<b>HMDS</b>	hotplate	MT:	2 min
	temperature:		120	°C

<b>G 1.6:</b>	<b>Spin coating</b>	std. spin coater	MT:	2 min
	dispense:	statically	2	mL
	ramp plateau:	30 s	3000	rpm
	resist:	ma-N 1440		
	thickness:		4	µm

The thicker ma-N 1440 resin compared to the ma-N 1420 did result in a cleaner and also faster lift-off.

<b>G 1.7:</b>	<b>Pre-bake</b>	hotplate with pins	MT:	2 min
	temperature:		100	°C
	time:		180	s

<b>G 1.8:</b>	<b>Lithography</b>	MA6, SÜSS Micro Tec	MT:	2 min
	alignment:	flat		
	contact mode:	soft		
	exposure dose:	at 365 nm	850	$\text{mJ cm}^{-2}$
	mask type:	film mask		
	mask layout:			

Extend lithography dose by factor 1.5 to compensate the absorption of the polymer mask (already included in the exposure dose value) ( $95 \text{ s at } 9 \text{ mW cm}^{-2}$ ).

<b>G 1.9:</b>	<b>Development</b>	megasonic bath	MT:	4 min
	developer:	ma-D 533s		
	frequency:		1	MHz
	power:		800	W
	time:		155	s

Gently rinse and shower wafers with DIW.

<b>G 1.10:</b>	<b>Spin rinse dry</b>	Semitoool	MT:	5 min
	angular velocity:		2000	rpm

Include nitrogen flush. No wait time after spin rinse dry.

<b>G 1.11:</b>	<b>PVD</b>	Leybold UNIVEX 500	MT:	180 min
	layer 01 height:	WTi: 1 min 30 s at 100 W	9	nm
	layer 02 height:	Pt: 1 min 42 s at 300 W	80	nm
	pressure:		$1.9 \cdot 10^{-7}$	mbar

Magnetron sputtering. WTi growth rate at 100 W:  $6 \text{ nm min}^{-1}$ , Pt growth rate at 300 W:  $47 \text{ nm min}^{-1}$ , Ar flow rate  $26 \text{ mL/min}$

<b>G 1.12:</b>	<b>Lift-off</b>	ultrasonic bath	MT: 70 min
	power:		100 – 200 W
	stripper:	acetone or DMSO or mr-Rem 700	
	time:	3 × different baths:	45 + 2 × 10 min

First lift-off bath without ultrasonic. After, rinse in DIW, acetone and IPA. Perform QDR and spin dry. For a non clean lift-off release, repeat lift-off using mr-Rem 700 (Micro Resist Technology GmbH, Berlin), QDR, IPA, followed by dry-cleaning using oxygen plasma at 200 W, 10 min.

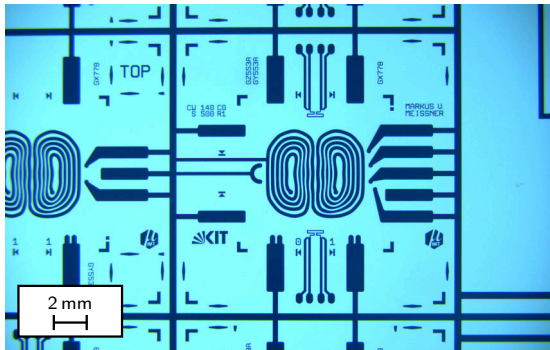


**Figure A.1:** The picture shows the structured platinum seed layer after lift-off. The x-gradient coil is displayed in the centre of the die. Added seed tracks maintain an electrical connection for the electroplating and additionally for connecting the gradient coils on the next layer.

<b>G 2:</b>	<b>1<sup>st</sup> electroplating mould</b>	$\Sigma$ Machine Time (MT): 660 min
-------------	--	-------------------------------------

<b>G 2.1:</b>	<b>Cleaning standard III.</b>	ultrasonic bath	MT: 12 min
	time acetone:		5 min
	time isopropyl alcohol:		5 min
	type:	acetone + isopropyl alcohol + QDR	

Gently rinse and shower wafers with DIW.

<b>G 2.2:</b>	<b>Spin rinse dry</b>	Semitoool	MT:	5 min
	angular velocity:		2000	rpm
Include nitrogen flush. No wait time after spin rinse dry.				
<b>G 2.3:</b>	<b>Oxygen plasma</b>	TePla, Technics Plasma GmbH	MT:	13 min
	oxygen flow:		500	sccm
	power:		80	W
	time:		10	min
<b>G 2.4:</b>	<b>Dehydration bake</b>	oven	MT:	45 min
	temperature:		200	°C
<b>G 2.5:</b>	<b>Spin coating (optional)</b>	std. spin coater	MT:	1 min
	dispense:	statically	1.6	mL
	primer:	Ti-Prime		
	ramp acceleration:		100	rpm s <sup>-1</sup>
	ramp plateau:	30 s	2500	rpm
<b>G 2.6:</b>	<b>Bake (optional)</b>	hotplate with vacuum chuck	MT:	5 min
	temperature:		130	°C
	time:		120	s
Allow the wafers to cool to below 60 °C before proceeding with the next step.				
<b>G 2.7:</b>	<b>Spin coating</b>	std. spin coater	MT:	4 min
	dispense:	statically	4.5	mL
	ramp 01 acceleration:		100	rpm s <sup>-1</sup>
	ramp 01 plateau:	10 s	500	rpm
	ramp 02 acceleration:		300	rpm s <sup>-1</sup>
	ramp 02 plateau:	35 s	1250	rpm
	resist:	SU-8 3050		
thickness:		100	µm	

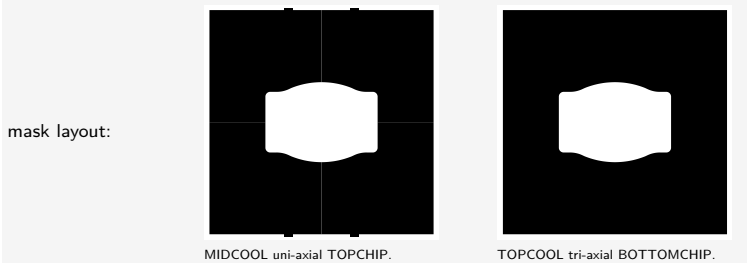
## A Process description

---

<b>G 2.8:</b>	<b>Soft bake</b>	hotplate		MT: 240 min
	temperature 01:	45 min	95 °C	
	temperature 02:	45 min	95 °C	

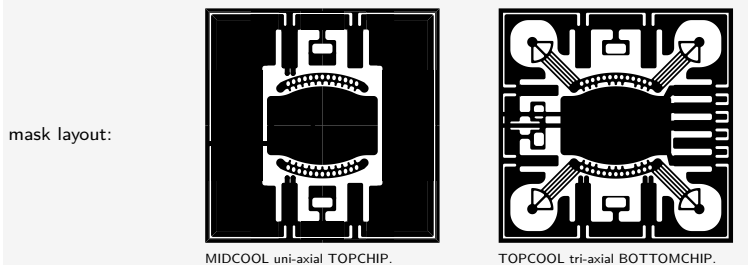
Temperature 01: ramp with wafer covered by petri dish. Let wafers cool down to room temperature on the hot-plate after soft bake.

<b>G 2.9:</b>	<b>Lithography</b>	MA6, SÜSS Micro Tec		MT: 5 min
	alignment:	mark, BS		
	contact mode:	soft		
	exposure dose:	at 365 nm	550 mJ cm <sup>-2</sup>	
	mask type:	film mask		
	side to exposure:	BS		



Since the wafer chuck pulled vacuum for the fixation and due to the uneven SU-8 surface at the edges, the wafer was additionally fixed with tape. The lithography dose was extended by a factor of 1.5 to compensate the absorption of the polymer mask (already included in the exposure dose value). 61 s at 9 mW cm<sup>-2</sup>. In addition, an anti-reflective foil was used to protect against imprints from the wafer chuck. It was important to expose the backside before exposing the topside, since the SU-8 got deformed at the edges, during the WEC when the wafer was loaded into the mask-aligner.

<b>G 2.10:</b>	<b>Lithography</b>	MA6, SÜSS Micro Tec	MT:	5 min
	alignment:	mark, BS		
	contact mode:	soft		
	exposure dose:	at 365 nm	740	mJ cm <sup>-2</sup>
	mask type:	film mask		
	substrate-side to expose:	FS		



The lithography dose was extended by a factor of 1.5 to compensate the absorption of the polymer mask (already included in the exposure dose value). 82 s at 9 mW cm<sup>-2</sup>.

<b>G 2.11:</b>	<b>PEB</b>	oven	MT:	300 min
	temperature:		75	°C
	time:		1	h

Ramp temperature to 65 °C by approximately 2 °C min<sup>-1</sup> to 5 °C min<sup>-1</sup>. Let wafers cool down to room temperature.

<b>G 2.12:</b>	<b>Development</b>	ultrasonic bath	MT:	25 min
	developer:	PGMEA		
	power:		50	W
	time:		20	min

A white film indicated under-development and required to repeat the development process. Finally, re-develop with fresh developer in a separate petri dish (PGMEA). Rinse in IPA after development. Gently rinse and shower wafers with DIW. Dry wafers using a nitrogen gun.

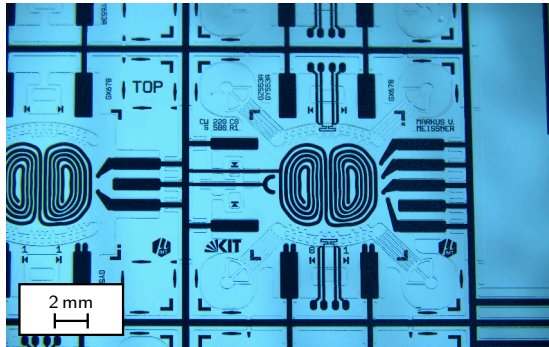


**Figure A.2:** The structured SU-8 3050 plating mould with the platinum seed below.

Distance from the centre:	-24 mm	-8 mm	8 mm	24 mm	mean	std.
Wafer 1:	95.6 $\mu\text{m}$	97.4 $\mu\text{m}$	98.9 $\mu\text{m}$	97.4 $\mu\text{m}$	97.3 $\mu\text{m}$	1.2 $\mu\text{m}$
Wafer 2:	97.7 $\mu\text{m}$	95.9 $\mu\text{m}$	98.6 $\mu\text{m}$	98.6 $\mu\text{m}$	97.7 $\mu\text{m}$	1.1 $\mu\text{m}$
Wafer 3:	103.0 $\mu\text{m}$	97.7 $\mu\text{m}$	97.2 $\mu\text{m}$	104.7 $\mu\text{m}$	100.6 $\mu\text{m}$	3.3 $\mu\text{m}$
Wafer 4:	102.4 $\mu\text{m}$	103.0 $\mu\text{m}$	103.2 $\mu\text{m}$	103.5 $\mu\text{m}$	103.0 $\mu\text{m}$	0.4 $\mu\text{m}$

**Table A.1:** Profilometry of the electroplating mould height for a batch of 4 wafers.

<b>G 3:</b> 1 <sup>st</sup> gradient layer electroplating		$\Sigma$ Machine Time (MT): 510 min	
<b>G 3.1:</b>	<b>Oxygen plasma</b>	TePla, Technics Plasma GmbH	MT: 10 min
	oxygen flow:	500	sccm
	power:	50	W
	time:	5	min

<b>G 3.2:</b>	<b>Electroplating</b>	copper electroplating bath	MT:	500 min
	current:		9.05 – 183	mA
	electrolyte:	Cuprostar® LP1		
	plating area, MIDCOOL:		9.05	cm <sup>2</sup>
	plating area, TOPCOOL:		9.14	cm <sup>2</sup>
	target height:		100	µm

Rinse in DIW after the electroplating. The electroplating parameters apply to the entire wafer, containing 8 uni-axial and 8 tri-axial chips.

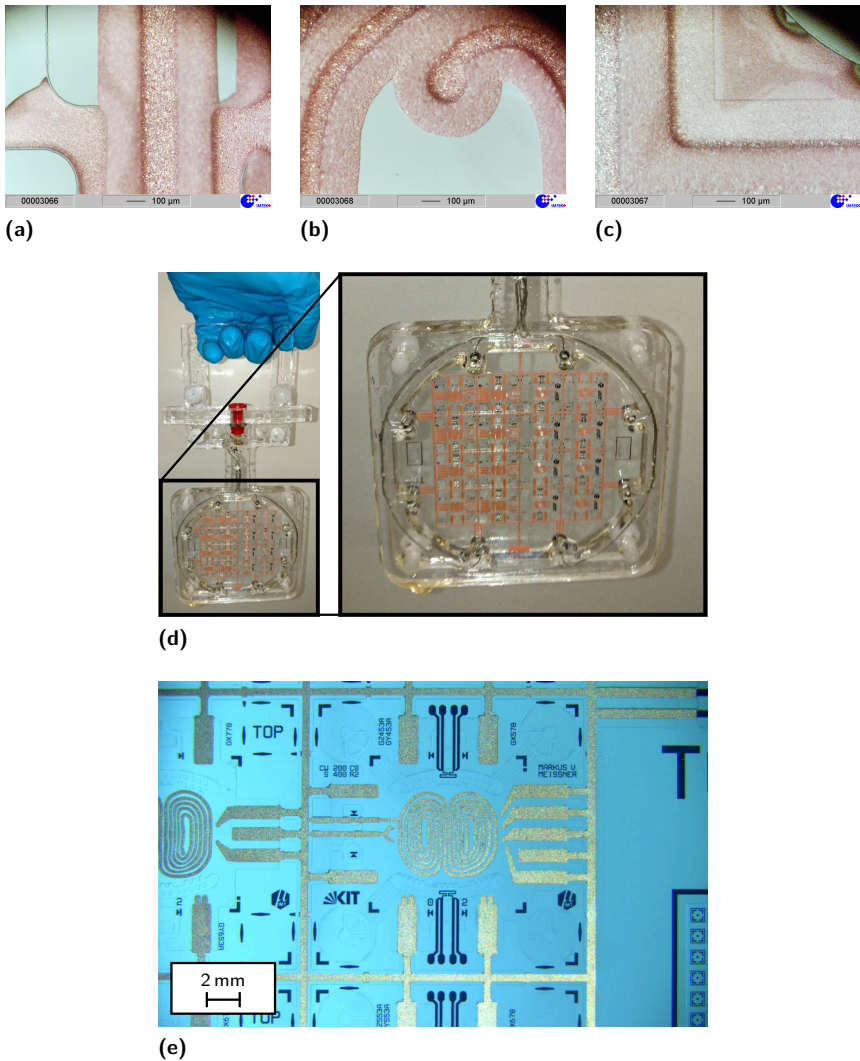


**Figure A.3:** (a),(b),(c) with a plasma power greater than 150 W to 200 W, the platinum seed got immobilised and re-sputtered onto the SU-8 plating mould, which consequently got covered with Cu during the electroplating. (d) the poly(methyl methacrylate) (PMMA) electroplating holder with the wafer inserted, after the 1<sup>st</sup> electroplating step. (e) the electroplated x-gradient coil layer.

---

**G 4: Fluidic channels (only MIDCOOL)** Σ Machine Time (MT): 378 min


---

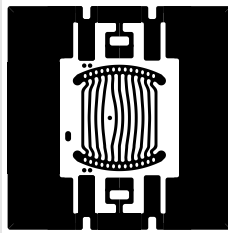
<b>G 4.1:</b>	<b>Oxygen plasma</b>	TePla, Technics Plasma GmbH	MT:	8 min
	oxygen flow:	500	sccm	
	power:	80	W	
	time:	5	min	

<b>G 4.2:</b>	<b>Vacuum lamination</b>	SB6, SÜSS Micro Tec or EVG 540	MT:	40 min
	bonding force:	60	N	
	chamber pressure:	< 10	mbar	
	hold time:	10	min	
	material:	SUEX TDFS D100		
	temperature:	58	°C	

Process steps: 1. heat up substrate. 2. release dry-film from separation. 3. apply pressure. 4. release bond chuck to pressure. 5. release bond chuck. 6. cool down substrates.

<b>G 4.3:</b>	<b>Lithography</b>	MA6, SÜSS Micro Tec	MT:	5 min
	alignment mode:	mark, BS		
	contact mode:	soft		
	exposure dose:	900	mJ cm <sup>-2</sup>	
	mask type:	film mask		

mask layout:



MIDCOOL uni-axial TOPCHIP.

The lithography dose was extended by a factor of 1.5 to compensate the absorption of the polymer mask (already included in the exposure dose value). (100 s at 9 mW cm<sup>-2</sup>).

## A Process description

---

<b>G 4.4:</b>	<b>PEB</b>	oven	MT: 300 min
	temperature:	70	°C
	Ramp temperature to 70 °C by approximately 2 °C min <sup>-1</sup> to 5 °C min <sup>-1</sup> .		
<b>G 4.5:</b>	<b>Development</b>	ultrasonic bath	MT: 20 min
	developer:	PGMEA	
	power:	100	W
	Rinse in IPA after development.		
<b>G 4.6:</b>	<b>Spin rinse dry</b>	Semitool	MT: 5 min
	angular velocity:	2000	rpm

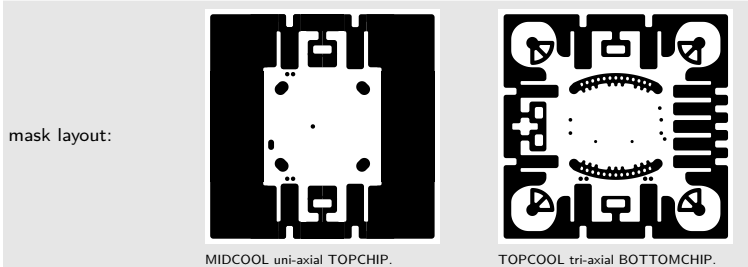
---

### **G 5: Encapsulation** Σ Machine Time (MT): 343 min

---

<b>G 5.1:</b>	<b>Oxygen plasma</b>	TePla, Technics Plasma GmbH	MT: 8 min
	oxygen flow:	500	sccm
	power:	80	W
	time:	5	min
<b>G 5.2:</b>	<b>Hot-roll lamination</b>	Polamat UVL 600, Polatek	MT: 5 min
	material:	ADEX TDFS A50	
	pressure:	1	bar
	speed:	0.3	m min <sup>-1</sup>
	temperature:	68	°C

<b>G 5.3:</b>	<b>Lithography</b>	MA6, SÜSS Micro Tec	MT:	10 min
	alignment mode:	mark, BS		
	contact mode:	soft		
	exposure dose:		700	$\text{mJ cm}^{-2}$
	mask type:	film mask		



Extend lithography dose by factor 1.5 to compensate absorption by the polymer mask. (77 s at  $9 \text{ mW cm}^{-2}$ ).

<b>G 5.4:</b>	<b>PEB</b>	oven	MT:	300 min
	temperature:		70	$^{\circ}\text{C}$

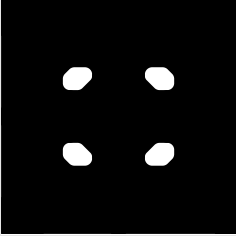
Heat oven with substrates inside.

<b>G 5.5:</b>	<b>Development</b>	ultrasonic bath	MT:	15 min
	developer:	PGMEA		
	power:		100	W
	time:		15	min

Rinse in IPA after development.

<b>G 5.6:</b>	<b>Spin rinse dry</b>	Semitool	MT:	5 min
	angular velocity:		2000	rpm

Include nitrogen flush. No wait time after spin rinse dry.

<b>G 6:</b>		<b>VIA electroplating &amp; PVD</b>		$\Sigma$ Machine Time (MT): 596 min	
<b>G 6.1:</b>	<b>Oxygen plasma (only MIDCOOL)</b>	TePla, Technics Plasma GmbH		MT:	8 min
	oxygen flow:	500	sccm		
	power:	80	W		
	time:	5	min		
<b>G 6.2:</b>	<b>Hot-roll lamination (only MIDCOOL)</b>	Polamat UVL 600, Polatek		MT:	5 min
	material:	ORDYL <sup>®</sup> FP 450			
	pressure:	2	bar		
	speed:	0.2	m min <sup>-1</sup>		
	temperature:	80 – 90 °C			
The post-lamination hold time was 20 min.					
<b>G 6.3:</b>	<b>Lithography (only MIDCOOL)</b>	MA6, SÜSS Micro Tec		MT:	10 min
	alignment mode:	mark, BS			
	contact mode:	soft			
	exposure dose:	500	mJ cm <sup>-2</sup>		
	mask type:	film mask			
mask layout:					
MIDCOOL uni-axial TOPCHIP.					

The lithography dose was extended by a factor of 1.5 to compensate the absorption of the polymer mask (already included in the exposure dose value). The exposure time was 100s.

<b>G 6.4:</b>	<b>Development (only MIDCOOL)</b>	megasonic bath	MT:	10 min
	developer:	$\text{Na}_2\text{CO}_3 + \text{H}_2\text{O}$	0.8 – 1.3 %	
	frequency:		1 MHz	
	power:		800 W	
	time:		$2 \times 4$ min	

Gently rinse and shower wafers with DIW.

<b>G 6.5:</b>	<b>Spin rinse dry (only MIDCOOL)</b>	Semitoool	MT:	5 min
	angular velocity:		800 rpm	

Include nitrogen flush. No wait time after spin rinse dry.

<b>G 6.6:</b>	<b>Oxygen plasma</b>	TePla, Technics Plasma GmbH	MT:	5 min
	oxygen flow:		500 sccm	
	power:		80 W	
	time:		2 min	

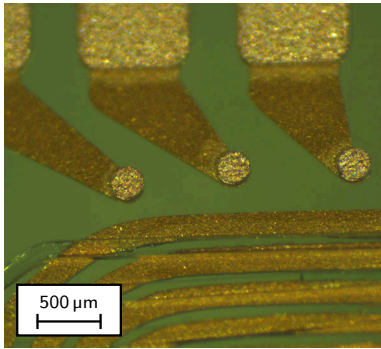
<b>G 6.7:</b>	<b>Electroplating</b>	copper electroplating bath	MT:	330 min
	current, MIDCOOL:		12 – 69 mA	
	current, TOPCOOL:		23 – 47 mA	
	electrolyte:	Cuprostar® LP1		
	plating area, MIDCOOL:		4.56 cm <sup>2</sup>	
	plating area, TOPCOOL:		4.68 cm <sup>2</sup>	
	target height, MIDCOOL:		130 μm	
	target height, TOPCOOL:		50 μm	

Rinse in DIW after the electroplating. The electroplating parameters apply to the entire wafer, containing 8 uni-axial and 8 tri-axial chips.

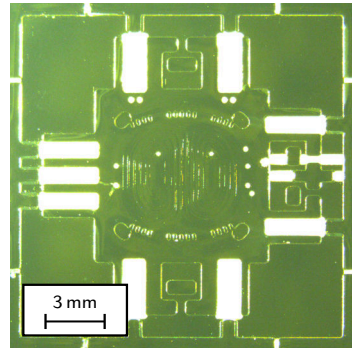
## A Process description

---

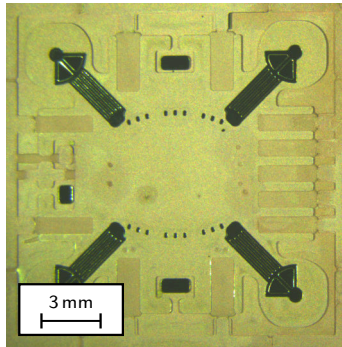
<b>G 6.8:</b>	<b>Strip</b>	<b>ORDYL® FP</b>			
	<b>450</b>		petri dish on hotplate		MT: 20 min
	<b>(only Midcool)</b>				
	stripper:	NaOH + H <sub>2</sub> O		4 %	
	temperature:			40 °C	
	time:			10 – 15 min	
Gently shower and rinse substrates with DIW after stripping.					
<b>G 6.9:</b>	<b>Remove</b>		beaker		MT: 10 min
	<b>Cu-plating residues</b>				
	type:	20 % H <sub>2</sub> SO <sub>4</sub>			
Add 30 % H <sub>2</sub> O <sub>2</sub> to slightly etch the Cu surface. Afterwards, perform QDR.					
<b>G 6.10:</b>	<b>Spin rinse dry</b>		Semitool		MT: 5 min
	angular velocity:			800 rpm	
Include nitrogen flush. No wait time after spin rinse dry.					
<b>G 6.11:</b>	<b>Oxygen plasma</b>		TePla, Technics Plasma GmbH		MT: 8 min
	oxygen flow:			500 sccm	
	power:			50 W	
	pressure:			120 mbar	
	time:			5 min	
No wait time after oxygen plasma.					
<b>G 6.12:</b>	<b>PVD</b>		vacuum coating, Mini-Coater, TecTra		MT: 180 min
	layer 01:	Cr: 0.3 nm s <sup>-1</sup>		5 – 10 nm	
	layer 02:	Au: 0.8 nm s <sup>-1</sup>		80 – 100 nm	
	pressure:			5 – 7 · 10 <sup>-6</sup> mbar	



(a)



(b)



(c)

**Figure A.4:** (a) the topped up VIAs after the electroplating process for the MIDCOOL chip design. (b) the applied Au seed layer by vacuum evaporation onto a TOPCHIP. (c) testing of Cu electroplating onto the Au seed layer. This test was carried out to evaluate, whether a  $\mu$ layer of Cu improves the adhesion on the ORDYL<sup>®</sup> FP 450. However, the ORDYL<sup>®</sup> FP 450 adhesion did not become any better. In addition, this test also highlights the interconnected regions from the seed layer.

## A Process description

**G 7:**      **2<sup>nd</sup> electroplating mould**       $\Sigma$  Machine Time (MT): 35 min

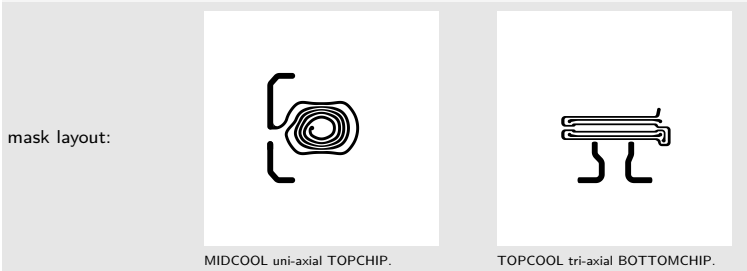
**G 7.1:**      **Hot-roll lamination**      Polamat UVL 600, Polatek      MT:      10 min

material:	ORDYL <sup>®</sup> FP 450		
pressure:	2	bar	
speed:	0.2	m min <sup>-1</sup>	
temperature:	80 – 90 °C		

Remove the PET protection foil of the 1<sup>st</sup> ORDYL<sup>®</sup> FP 450 layer. The lamination step was repeated, to form a double DFR layer. The PET foil of the 2<sup>nd</sup> layer was removed after the lithography. The post lamination hold time was around 20 min.

**G 7.2:**      **Lithography**      MA6, SÜSS Micro Tec      MT:      5 min

alignment mode:	mark, BS		
contact mode:	soft		
exposure dose:	900	mJ cm <sup>-2</sup>	
mask type:	film mask		



The lithography dose was extended by a factor of 1.5 to compensate the absorption of the polymer mask (already included in the exposure dose value).

**G 7.3:**      **Development**      ultrasonic bath      MT:      15 min

developer:	Na <sub>2</sub> CO <sub>3</sub> + H <sub>2</sub> O	0.8 – 1.3	%
power:		100	W
time:		15	min

Gently rinse and shower wafers with DIW.

**G 7.4:**      **Spin rinse dry**      Semitool      MT:      5 min

angular velocity:	800	rpm
-------------------	-----	-----

Angular velocity was reduced and the nitrogen purge was skipped to protect the delicate plating mould.

---

**G 8: 2<sup>nd</sup> gradient layer electroplating** Σ Machine Time (MT): 138 min


---

<b>G 8.1:</b>	<b>Oxygen plasma</b>	TePla, Technics Plasma GmbH	MT:	8 min
	oxygen flow:		500	sccm
	power:		50	W
	time:		5	min

<b>G 8.2:</b>	<b>Electroplating</b>	copper electroplating bath	MT:	130 min
	current:		12 – 38	mA
	electrolyte:	Cuprostar® LP1		
	plating area, MIDCOOL:		1.9	cm <sup>2</sup>
	plating area, TOPCOOL:		2.0	cm <sup>2</sup>
	target height:		70 – 80	µm

Rinse in DIW after the electroplating. The electroplating parameters apply to the entire wafer, containing 8 uni-axial and 8 tri-axial chips.

---

**G 9: Photoresist & seed stripping** Σ Machine Time (MT): 100 min


---

<b>G 9.1:</b>	<b>Strip ORDYL® FP 450</b>	petri dish on hotplate	MT:	25 min
	stripper:	NaOH + H <sub>2</sub> O	4	%
	temperature:		40	°C
	time:		18 – 20	min

Gently shower and rinse substrates with DIW after stripping.

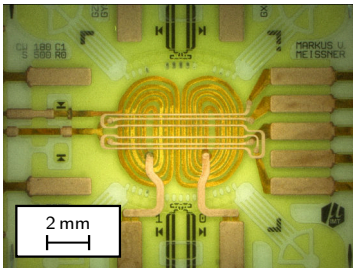
<b>G 9.2:</b>	<b>Au seed stripping</b>	petri dish	MT:	50 min
	etchant:	TFAC, Transene Company Inc.		
	temperature:		40	°C
	time:		45 – 50	min

Gently shower and rinse substrates with DIW after Au etching.

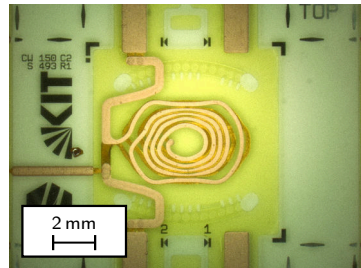
## A Process description

---

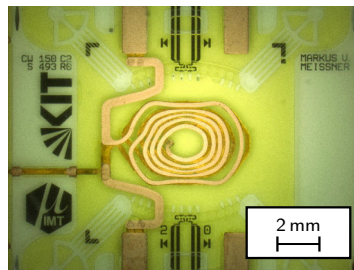
<b>G 9.3:</b>	<b>Cr seed stripping</b>	petri dish	MT: 20 min
	etchant:	Cr-ETCH-200, NB Technologies GmbH	
	Etch rate is approximately $12 \text{ nm min}^{-1}$ to $15 \text{ nm min}^{-1}$ . <sup>[241]</sup> Gently shower and rinse substrates with DIW after stripping. No wait time after Cr stripping.		
<b>G 9.4:</b>	<b>Spin rinse dry</b>	Semitooll	MT: 5 min
	angular velocity:	2000	rpm



(a)



(b)



(c)

**Figure A.5:** The second coil layer of a TOPCOOL gradient batch. (a) the BOTTOMCHIP of a tri-axial gradient design. (b) the TOPCHIP of a uni-axial z-gradient. (c) BOTTOMCHIP of the uni-axial z-gradient.

---

**G 10: DFR hot-embossing** Σ Machine Time (MT): 700 min


---

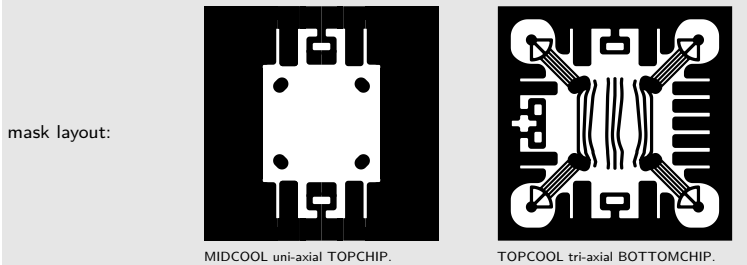
<b>G 10.1:</b>	<b>Oxygen Plasma</b>	TePla, Technics Plasma GmbH	MT:	10 min
	oxygen flow:		500	sccm
	power:		60	W
	time:		10	min

<b>G 10.2:</b>	<b>DFR hot-embossing</b>	SB6, SÜSS Micro Tec or EVG 540	MT:	30 min
	bonding force:		60	N
	chamber pressure:		1	mbar
	hold time:		10	min
	material:	SUEX TDFS D100		
	temperature:		46 – 50	°C

Process steps: 1. heat up substrate. 2. release dry-film from separation. 3. apply pressure. 4. release bond chuck to pressure. 5. release bond chuck. 6. cool down substrates.

<b>G 10.3:</b>	<b>Hot roll lamination (only TOPCOOL)</b>	Polamat UVL 600, Polatek	MT:	5 min
	material:	ADEX TDFS A50		
	pressure:		1	bar
	speed:		0.3	m min <sup>-1</sup>
	temperature:		68	°C

<b>G 10.4:</b>	<b>Lithography</b>	MA6, SÜSS Micro Tec	MT:	5 min
	alignment:	mark, BS		
	contact mode:	soft		
	exposure dose:	900	$\text{mJ cm}^{-2}$	
	mask type:	film mask		



The lithography dose was extended by a factor of 1.5 to compensate the absorption of the polymer mask (already included in the exposure dose value).

<b>G 10.5:</b>	<b>PEB</b>	oven	MT:	300 min
	temperature:	60	$^{\circ}\text{C}$	
	time:	5	h	

Ramp temperature to  $60^{\circ}\text{C}$  by approximately  $2^{\circ}\text{C min}^{-1}$  to  $5^{\circ}\text{C min}^{-1}$ .

<b>G 10.6:</b>	<b>Development</b>	ultrasonic bath	MT:	25 min
	developer:	PGMEA		
	time:	20	min	

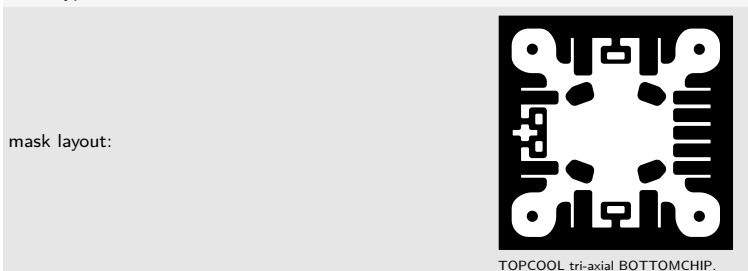
Rinse in IPA after development. A white film indicated that the substrate had been under-developed which required to repeat the development process.

<b>G 10.7:</b>	<b>Spin rinse dry</b>	Semitool	MT:	5 min
	angular velocity:	2000	rpm	

<b>G 10.8:</b>	<b>Oxygen plasma</b>	TePla, Technics Plasma GmbH	MT:	10 min
	oxygen flow:	500	sccm	
	power:	60	W	
	time:	10	min	

<b>G 10.9:</b>	<b>Hot roll lamination</b> (only TOPCOOL)	Polamat UVL 600, Polatek	MT:	5 min
	material:	ADEX TDFS A50		
	pressure:	1	bar	
	speed:	0.3	$\text{m min}^{-1}$	
	temperature:	68	$^{\circ}\text{C}$	

<b>G 10.10:</b>	<b>Lithography</b> (only TOPCOOL)	MA6, SÜSS Micro Tec	MT:	5 min
	alignment:	mark, BS		
	contact mode:	soft		
	exposure dose:	at 365 nm	700	$\text{mJ cm}^{-2}$
	mask type:	film mask		



The lithography dose was extended by a factor of 1.5 to compensate the absorption of the polymer mask (already included in the exposure dose value).

<b>G 10.11:</b>	<b>PEB (only TOPCOOL)</b> oven		MT:	300 min
	temperature:	60	$^{\circ}\text{C}$	
	time:	5	h	

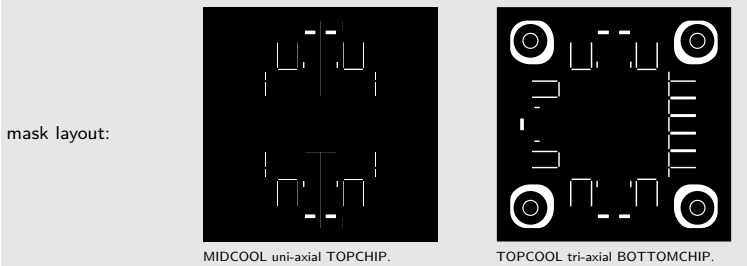
Ramp temperature to  $60^{\circ}\text{C}$  by approximately  $2^{\circ}\text{C min}^{-1}$  to  $5^{\circ}\text{C min}^{-1}$ .

**G 11: Coil alignment structures** Σ Machine Time (MT): 345 min

<b>G 11.1:</b>	<b>Oxygen plasma (only MIDCOOL)</b>	TePla, Technics Plasma GmbH	MT: 10 min
	oxygen flow:	500	sccm
	power:	50	W
	time:	5	min

<b>G 11.2:</b>	<b>Hot roll lamination</b>	Polamat UVL 600, Polatek	MT: 5 min
	material:	ADEX TDFS A50	
	pressure:	1	bar
	speed:	0.3	m min <sup>-1</sup>
	temperature:	68	°C

<b>G 11.3:</b>	<b>Lithography</b>	MA6, SÜSS Micro Tec	MT: 10 min
	alignment mode:	mark	
	contact mode:	soft	
	exposure dose:	490	mJ cm <sup>-2</sup>
	mask type:	film mask	



The lithography dose was extended by a factor of 1.5 to compensate the absorption of the polymer mask (already included in the exposure dose value).

<b>G 11.4:</b>	<b>PEB</b>	oven	MT: 300 min
	temperature:	60	°C
	time:	5	h

Pre-heat oven with substrates inside.

<b>G 11.5:</b>	<b>Development</b>	ultrasonic bath	MT:	15 min
	developer:	PGMEA		
	power:		100	W
	time:		15	min

Rinse in IPA after development.

<b>G 11.6:</b>	<b>Spin rinse dry</b>	Semitoool	MT:	5 min
	angular velocity:		2000	rpm

## A.2 Tx/Rx micro coil fabrication

Processing of the Tx/Rx coil started on a 200  $\mu\text{m}$  thick, 4" MEMpax<sup>®</sup> (Schott Glass Malaysia) substrate.

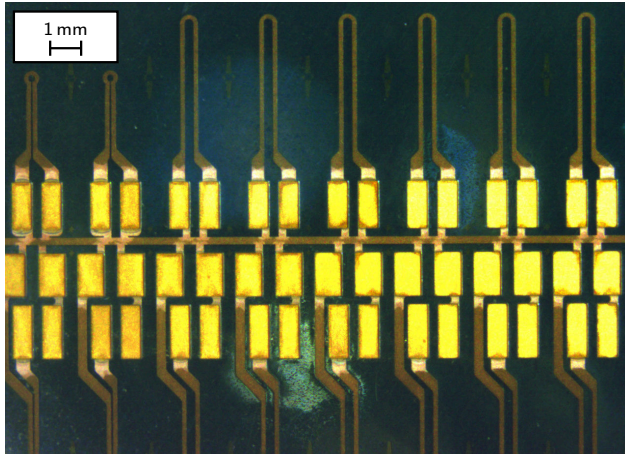


**Figure A.6:** Illustration of different Tx/Rx micro coil designs, implemented on a single wafer. The coil to coil separation was 2.37 mm. For improved solderability, the pads for interconnections were additionally Au electroplated.

<b>C 1: Seed Layer</b>		$\Sigma$ Machine Time (MT): 236 min	
<b>C 1.1:</b>	<b>Oxygen plasma</b>	TePla, Technics Plasma GmbH	MT: 13 min
	oxygen flow:	500	sccm
	power:	100	W
	time:	10	min
	To oxidise the surface of the glass substrate.		
<b>C 1.2:</b>	<b>HMDS</b>	hotplate	MT: 2 min
	temperature:	120	$^{\circ}\text{C}$



## A Process description

---

<b>C 1.8:</b>	<b>Lift-off</b>	beaker, ultrasonic bath	MT:	30 min
	power:		20 – 50 W	
	stripper:	acetone or DMSO or mr-Rem 700		
	time:	3 × different baths:	10 + 2 × 10 min	

First lift-off bath without ultrasonic. Rinse in IPA, DIW, after QDR.

---

### C 2: Electroplating Mould

Σ Machine Time (MT): 35 min

---

<b>C 2.1:</b>	<b>Oxygen plasma</b>	TePla, Technics Plasma GmbH	MT:	13 min
	oxygen flow:		500 sccm	
	power:		80 W	
	time:		10 min	

<b>C 2.2:</b>	<b>Hot-roll lamination</b>	MyJoy-9, GMP, office laminator	MT:	5 min
	material:	ORDYL® SY 330		
	temperature selection:		3–4	

Do not remove top foil after lamination.

<b>C 2.3:</b>	<b>PLB (optional)</b>	hotplate with vacuum chuck	MT:	2 min
	temperature:		80 °C	
	time:		120 s	

To flatten the surface if ripples after lamination occurred.

<b>C 2.4:</b>	<b>Lithography</b>	MA6, SÜSS Micro Tec	MT:	5 min
	contact mode:	soft		
	exposure dose:	at 365 nm	115 mJ cm <sup>-2</sup>	
	mask type:	maskless		
	side to exposure:	BS		

Use an anti-reflection foil below the ORDYL® SY covered substrate.

<b>C 2.5:</b>	<b>PEB</b>	vacuum hotplate with pins	MT:	2 min
	temperature:		85	°C
	time:		2	min

Remove top foil after the PEB.

<b>C 2.6:</b>	<b>Development</b>	ultrasonic bath	MT:	8 min
	developer:	ORDYL <sup>®</sup> SY developer		
	power:		100	%
	time bath 01:		3	min
	time bath 02:		3	min

Rinse for 2 min in IPA after development. Gently rinse and shower wafers with DIW. Dry by nitrogen stream. No wait time after development.

---

<b>C 3:</b>	<b>Electroplating of the Tx/Rx Micro Coil</b>	$\Sigma$ Machine Time (MT): 188 min
-------------	---	-------------------------------------

---

<b>C 3.1:</b>	<b>Oxygen plasma</b>	TePla, Technics Plasma GmbH	MT:	8 min
	oxygen flow:		500	sccm
	power:		50	W
	time:		5	min

<b>C 3.2:</b>	<b>Electroplating</b>	copper electroplating bath	MT:	180 min
	electrolyte:	Cuprostar <sup>®</sup> LP1		
	plating height:		30	$\mu\text{m}$

Dip substrate in 20 % H<sub>2</sub>SO<sub>4</sub>. Gently rinse and shower wafers with DIW. Dry by nitrogen stream. No wait time after electroplating.

---

<b>C 4:</b>	<b>Encapsulation and interconnect openings</b>	$\Sigma$ Machine Time (MT): 54 min
-------------	--	------------------------------------

---

<b>C 4.1:</b>	<b>Oxygen plasma</b>	TePla, Technics Plasma GmbH	MT:	13 min
	oxygen flow:		500	sccm
	power:		80	W
	time:		10	min

## A Process description

---

<b>C 4.2:</b>	<b>Hot-roll lamination</b>	MyJoy-9, GMP, office laminator	MT:	5 min
	material:	ORDYL® SY 330		
	temperature switch:		3–4	

In the case of substantial thickness variations of the electroplated layer, a more time consuming vacuum lamination process can yield in a superior encapsulation of the plated copper structures.

<b>C 4.3:</b>	<b>PLB (optional)</b>	hotplate with vacuum chuck	MT:	2 min
	temperature:		80	°C
	time:		120	s

To flatten the surface, if ripples after lamination occurred.

<b>C 4.4:</b>	<b>Lithography</b>	MA6, SÜSS Micro Tec	MT:	5 min
	alignment:	mark		
	contact mode:	soft		
	exposure dose:	at 365 nm	115	mJ cm <sup>-2</sup>
	mask type:	film mask		
	mask layout:	 PAPERCLIP coil, for the uni-axial gradient	 Butterfly coil, for the tri-axial gradient	

<b>C 4.5:</b>	<b>PEB</b>	vacuum hotplate with pins	MT:	4 min
	temperature:		85	°C
	time:		2	min

<b>C 4.6:</b>	<b>Development</b>	ultrasonic bath	MT:	25 min
	developer:	ORDYL® SY developer		
	power:		100	%
	time bath 01:		3	min
	time bath 02:		3	min

Rinse for 2 min in IPA after development. Gently rinse and shower wafers with DIW. Dry by nitrogen stream. No wait time after development.

<b>C 5:</b>	<b>Backside metalisation</b>		$\Sigma$ Machine Time (MT): 373 min
<b>C 5.1:</b>	<b>Oxygen Plasma</b>	TePla, Technics Plasma GmbH	MT: 13 min
	oxygen flow:	500	sccm
	power:	80	W
	time:	10	min
	Depending on the surface condition, additional chemical cleaning steps may be necessary to guarantee sufficient adhesion for the PVD deposited layers.		
<b>C 5.2:</b>	<b>PVD</b>	vacuum coating, Mini-Coater, TecTra	MT: 180 min
	layer 01:	Cr: $0.3 \text{ nm s}^{-1}$	5 – 10 nm
	layer 02:	Au: $0.8 \text{ nm s}^{-1}$	80 – 100 nm
	pressure:		$5 - 7 \cdot 10^{-6}$ mbar
<b>C 5.3:</b>	<b>Hot-roll lamination</b>	Polamat UVL 600, Polatek	MT: 5 min
	material:	ORDYL <sup>®</sup> FP 450	
	pressure:	2	bar
	speed:	0.2	$\text{m min}^{-1}$
	temperature:	80 – 90	$^{\circ}\text{C}$
	The post-lamination hold time was 20 min.		
<b>C 5.4:</b>	<b>Lithography</b>	MA6, SÜSS Micro Tec	MT: 5 min
	alignment:	mark	
	contact mode:	soft	
	exposure dose:	at 365 nm	450 $\text{mJ cm}^{-2}$
	mask type:	film mask	
	side to exposure:	BS	
	mask layout:	 PAPERCLIP coil, for the uni-axial gradient	 Butterfly coil, for the tri-axial gradient

## A Process description

---

<b>C 5.5:</b>	<b>Development</b>	megasonic bath	MT:	10 min
	developer:	$\text{Na}_2\text{CO}_3 + \text{H}_2\text{O}$	0.8 – 1.3 %	
	frequency:		1	MHz
	power:		800	W
	time:		$2 \times 4$	min

Gently rinse and shower wafers with DIW.

<b>C 5.6:</b>	<b>Electroplating</b>	copper electroplating bath	MT:	120 min
	electrolyte:	Cuprostar® LP1		
	plating height:		12 – 20	$\mu\text{m}$

Dip substrate in 20 %  $\text{H}_2\text{SO}_4$ . Gently rinse and shower wafers with DIW. Dry by nitrogen stream. No wait time after electroplating.

<b>C 5.7:</b>	<b>Strip</b>	<b>ORDYL® FP</b>	petri dish on hotplate	MT:	20 min
	<b>450</b>				
	stripper:	$\text{NaOH} + \text{H}_2\text{O}$	4	%	
	temperature:		40	$^\circ\text{C}$	
	time:		10 – 15	min	

Gently shower and rinse substrates with DIW after stripping.

<b>C 5.8:</b>	<b>Cr seed stripping</b>	petri dish	MT:	20 min
	etchant:	Cr-ETCH-200, NB Technologies GmbH		

Etch rate is approximately  $12 \text{ nm min}^{-1}$  to  $15 \text{ nm min}^{-1}$ .<sup>[241]</sup> Gently shower and rinse substrates with DIW after stripping. No wait time after Cr stripping.

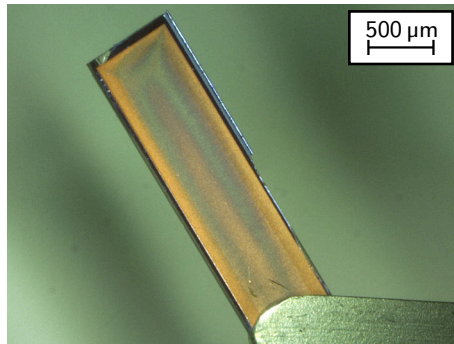


**Figure A.7:** The metallised rear of the micro coil with some remaining dicing burr. This side of the chip was glued to the gradient coil.



# Bibliography

- [1] Edwin D. Becker. A brief history of nuclear magnetic resonance. *Anal. Chem.*, 1993. ISSN 0003-2700. doi: 10.1021/ac00054a716.
- [2] Kurt Wüthrich. NMR-Untersuchungen von Struktur und Funktion biologischer Makromoleküle (Nobel-Vortrag). *Angew. Chemie*, 2003. ISSN 00448249. doi: 10.1002/ange.200300595.
- [3] Eiichi Fukushima and Stephen B. W. Roeder. *Experimental Pulse NMR: A Nuts and Bolts Approach*. CRC Press, Boca Raton, USA, 1993. ISBN 978-02-0162-726-8.
- [4] Malcolm H. Levitt. *Spin Dynamics: Basics of Nuclear Magnetic Resonance*. John Wiley & Sons Ltd, Chichester, England, 2008. ISBN 978-0-470-51117-6.
- [5] James Keeler. *Understanding NMR Spectroscopy*. John Wiley & Sons Ltd, Chichester, England, 2005. ISBN 978-0-470-01787-6.
- [6] Jianming Jin. *Electromagnetic Analysis and Design in Magnetic Resonance Imaging*. CRC Press, Boca Raton, USA, 1998. ISBN 978-08-4939-693-9.
- [7] Matt A. Bernstein, Kevin F. King, and Xiaohong Joe Zhou. *Handbook of MRI Pulse Sequences*. Elsevier Academic Press, Burlington, MA, USA, 2004. ISBN 978-00-8053-312-4.
- [8] Sarah L. Codd and Joseph D. Seymour. *Magnetic Resonance Microscopy*. Wiley-VCH GmbH, Weinheim, Germany, 2009. ISBN 978-35-2732-008-0.
- [9] Thomas Vaughan and John Griffiths. *RF Coils for MRI*. John Wiley & Sons Ltd, Chichester, England, 2012. ISBN 978-1-118-59045-4.
- [10] Michael E. Lacey, Raju Subramanian, Dean L. Olson, Andrew G. Webb, and Jonathan V. Sweedler. High-Resolution NMR Spectroscopy of Sample Volumes from 1 nL to 10  $\mu$ L. *Chem. Rev.*, 1999. ISSN 0009-2665. doi: 10.1021/cr980140f.
- [11] Paul Glover and Sir Peter Mansfield. Limits to magnetic resonance microscopy. *Reports Prog. Phys.*, 2002. ISSN 0034-4885. doi: 10.1088/0034-4885/65/10/203.

- [12] W. Gerlach and O. Stern. Der experimentelle Nachweis des magnetischen Moments des Silberatoms. *Zeitschrift für Phys.*, 1922. ISSN 1434-6001. doi: 10.1007/BF01329580.
- [13] Felix Bloch. The Principle of Nuclear Induction. *Science*, 1953. ISSN 0036-8075. doi: 10.1126/science.118.3068.425.
- [14] Vikram S. Bajaj, Jeffrey Paulsen, Elad Harel, and Alexander Pines. Zooming in on microscopic flow by remotely detected MRI. *Science*, 2010. ISSN 1095-9203. doi: 10.1126/science.1192313.
- [15] P.T. Callaghan and C.D. Eccles. Diffusion-limited resolution in nuclear magnetic resonance microscopy. *J. Magn. Reson.*, 1988. ISSN 00222364. doi: 10.1016/0022-2364(88)90151-5.
- [16] P.T. Callaghan, A. Coy, L.C. Forde, and C.J. Rofe. Diffusive relaxation and edge enhancement in NMR microscopy. *J. Magn. Reson. A*, 1993. ISSN 10641858. doi: 10.1006/jmra.1993.1057.
- [17] Einstein Albert. Über die von der molekularkinetischen Theorie der Wärme geforderte Bewegung von in ruhenden Flüssigkeiten suspendierten Teilchen. *Ann. Phys.*, 1905. ISSN 00033804. doi: 10.1002/andp.19053220806.
- [18] Daniel M. Patterson, Anwar R. Padhani, and David J. Collins. Technology Insight: water diffusion MRI — a potential new biomarker of response to cancer therapy. *Nat. Clin. Pract. Oncol.*, 2008. ISSN 1743-4254. doi: 10.1038/ncponc1073.
- [19] E. L. Hahn. Spin Echoes. *Phys. Rev.*, 1950. ISSN 0031-899X. doi: 10.1103/PhysRev.80.580.
- [20] H. Y. Carr and E. M. Purcell. Effects of Diffusion on Free Precession in Nuclear Magnetic Resonance Experiments. *Phys. Rev.*, 1954. ISSN 0031-899X. doi: 10.1103/PhysRev.94.630.
- [21] H. C. Torrey. Bloch Equations with Diffusion Terms. *Phys. Rev.*, 1956. ISSN 0031-899X. doi: 10.1103/PhysRev.104.563.
- [22] E. O. Stejskal and J. E. Tanner. Spin Diffusion Measurements: Spin Echoes in the Presence of a Time-Dependent Field Gradient. *J. Chem. Phys.*, 1965. ISSN 0021-9606. doi: 10.1063/1.1695690.
- [23] Nikolaus Nestle and Achim Gädke. Diffusionseffekte in der Magnetresonanztomographie - Eine kleine Übersicht bekannter und weniger bekannter Effekte. *Chemie Ing. Tech.*, 2013. ISSN 0009286X. doi: 10.1002/cite.201300062.

- [24] Timothy D. W. Claridge. Diffusion NMR spectroscopy. In *Tetrahedron Org. Chem. Ser.*, volume 27, pages 303–334. Elsevier, 2009. ISBN 9780080546285. doi: 10.1016/S1460-1567(08)10009-5.
- [25] Wurong Zhang and D. G. Cory. Pulsed Gradient NMR Probes for Solid State Studies. *J. Magn. Reson.*, 1998. ISSN 10907807. doi: 10.1006/jmre.1998.1408.
- [26] Peter Mansfield. Snapshot Magnetic Resonance Imaging (Nobel Lecture). *Angew. Chemie Int. Ed.*, 2004. ISSN 1433-7851. doi: 10.1002/anie.200460078.
- [27] Paul C. Lauterbur. All Science Is Interdisciplinary – From Magnetic Moments to Molecules to Men (Nobel Lecture). *Angew. Chemie Int. Ed.*, 2005. ISSN 1433-7851. doi: 10.1002/anie.200462400.
- [28] John D. Biglands, Aleksandra Radjenovic, and John P. Ridgway. Cardiovascular magnetic resonance physics for clinicians: Part II. *J. Cardiovasc. Magn. Reson.*, 2012. ISSN 10976647. doi: 10.1186/1532-429X-14-66.
- [29] Zhehong Gan, Ivan Hung, Xiaoling Wang, Joana Paulino, Gang Wu, Ilya M. Litvak, Peter L. Gor'kov, William W. Brey, Pietro Lendi, Jeffrey L. Schiano, Mark D. Bird, Iain R. Dixon, Jack Toth, Gregory S. Boebinger, and Timothy A. Cross. NMR spectroscopy up to 35.2 T using a series-connected hybrid magnet. *J. Magn. Reson.*, 2017. ISSN 10907807. doi: 10.1016/j.jmr.2017.08.007.
- [30] Thomas F. Budinger and Mark D. Bird. MRI and MRS of the human brain at magnetic fields of 14 T to 20 T: Technical feasibility, safety, and neuroscience horizons. *Neuroimage*, 2018. ISSN 10959572. doi: 10.1016/j.neuroimage.2017.01.067.
- [31] Xiaoping Hu and David G. Norris. Advances in high-field magnetic resonance imaging. *Annu. Rev. Biomed. Eng.*, 2004. ISSN 1523-9829. doi: 10.1146/annurev.bioeng.6.040803.140017.
- [32] Giorgio Moresi and Richard Magin. Miniature permanent magnet for table-top NMR. *Concepts Magn. Reson. Part B Magn. Reson. Eng.*, 2003. ISSN 10437347. doi: 10.1002/cmr.b.10082.
- [33] Hakho Lee, Eric Sun, Donhee Ham, and Ralph Weissleder. Chip-NMR biosensor for detection and molecular analysis of cells. *Nat. Med.*, 2008. ISSN 1546-170X. doi: 10.1038/nm.1711.
- [34] David Issadore, Changwook Min, Monty Liong, Jaehoon Chung, Ralph Weissleder, and Hakho Lee. Miniature magnetic resonance system for point-of-care diagnostics. *Lab Chip*, 2011. ISSN 1473-0189. doi: 10.1039/c1lc20177h.

- [35] Sergey S. Zalesskiy, Ernesto Danieli, Bernhard Blümich, and Valentine P. Ananikov. Miniaturization of NMR systems: desktop spectrometers, microcoil spectroscopy, and "NMR on a chip" for chemistry, biochemistry, and industry. *Chem. Rev.*, 2014. ISSN 1520-6890. doi: 10.1021/cr400063g.
- [36] Jan G. Korvink, Vlad Badilita, Dario Mager, Oliver Gruschke, Nils Spengler, Shyam Sundar Adhikari Parenky, Ulrike Wallrabe, and Markus Meissner. Innovative coil fabrication techniques for miniaturized magnetic resonance detectors. In *Micro and Nanoscale NMR*, pages 109–113. Wiley-VCH, Weinheim, 2018. ISBN 978-3-527-34056-9.
- [37] Hans Wolfgang Spiess. NMR spectroscopy: pushing the limits of sensitivity. *Angew. Chem. Int. Ed. Engl.*, 2008. ISSN 1521-3773. doi: 10.1002/anie.200704428.
- [38] Luisa Ciobanu, Andrew G. Webb, and Charles H. Pennington. Magnetic resonance imaging of biological cells. *Prog. Nucl. Magn. Reson. Spectrosc.*, 2003. ISSN 00796565. doi: 10.1016/S0079-6565(03)00004-9.
- [39] D.I Hoult and R.E Richards. The signal-to-noise ratio of the nuclear magnetic resonance experiment. *J. Magn. Reson.*, 1976. ISSN 00222364. doi: 10.1016/0022-2364(76)90233-X.
- [40] Andrew G. Webb. Radiofrequency microcoils in magnetic resonance. *Prog. Nucl. Magn. Reson. Spectrosc.*, 1997. ISSN 00796565. doi: 10.1016/S0079-6565(97)00004-6.
- [41] J. E. Stocker, T. L. Peck, A. G. Webb, M. Feng, and R. L. Magin. Nanoliter volume, high-resolution NMR microspectroscopy using a 60-micron planar microcoil. *IEEE Trans. Biomed. Eng.*, 1997. ISSN 0018-9294. doi: 10.1109/10.641340.
- [42] Krzysztof Jasiński, Anna Młynarczyk, Peter Latta, Vyacheslav Volotovskyy, Władysław P Węglarz, and Bogusław Tomanek. A volume microstrip RF coil for MRI microscopy. *Magn. Reson. Imaging*, 2012. ISSN 0730725X. doi: 10.1016/j.mri.2011.07.010.
- [43] Antoine Dupré, Ka Meng Lei, Pui In Mak, Rui P. Martins, and Weng Kung Peng. Micro- and nanofabrication NMR technologies for point-of-care medical applications – A review. *Microelectron. Eng.*, 2019. ISSN 01679317. doi: 10.1016/j.mee.2019.02.005.
- [44] Vlad Badilita, Robert Ch. Meier, Nils Spengler, Ulrike Wallrabe, Marcel Utz, and Jan G. Korvink. Microscale nuclear magnetic resonance: a tool for soft matter research. *Soft Matter*, 2012. ISSN 1744-683X. doi: 10.1039/c2sm26065d.

- 
- [45] L. Ciobanu and C. H. Pennington. 3D micron-scale MRI of single biological cells. *Solid State Nucl. Magn. Reson.*, 2004. ISSN 0926-2040. doi: 10.1016/j.ssnmr.2003.03.008.
- [46] M. Mohmmadzadeh, N. Baxan, V. Badilita, K. Kratt, H. Weber, J. G. Korvink, U. Wallrabe, J. Hennig, and D von Elverfeldt. Characterization of a 3D MEMS fabricated micro-solenoid at 9.4T. *J. Magn. Reson.*, 2011. ISSN 10907807. doi: 10.1016/j.jmr.2010.09.021.
- [47] Vlad Badilita, K. Kratt, N. Baxan, J. Anders, D. Elverfeldt, G. Boero, J. Hennig, J. G. Korvink, and U. Wallrabe. 3D solenoidal microcoil arrays with CMOS integrated amplifiers for parallel MR imaging and spectroscopy. In *2011 IEEE 24th Int. Conf. Micro Electro Mech. Syst.*, pages 809–812. 2011. ISBN 978-1-4244-9632-7. doi: 10.1109/MEMSYS.2011.5734548.
- [48] Andrew G. Webb. Microcoils. In *RF Coils MRI*, page 225. John Wiley & Sons Ltd, Chichester, England, 2012. ISBN 978-1-118-59045-4.
- [49] James B. Aguayo, Stephen J. Blackband, Joseph Schoeniger, Mark A. Mattingly, and Markus Hintermann. Nuclear magnetic resonance imaging of a single cell. *Nature*, 1986. ISSN 0028-0836. doi: 10.1038/322190a0.
- [50] D. A. Seeber, J. H. Hoftiezer, W. B. Daniel, M. A. Rutgers, and C. H. Pennington. Triaxial magnetic field gradient system for microcoil magnetic resonance imaging. *Rev. Sci. Instrum.*, 2000. ISSN 00346748. doi: 10.1063/1.1313800.
- [51] L. Ciobanu, D. A. Seeber, and C. H. Pennington. 3D MR microscopy with resolution 3.7  $\mu\text{m}$  by 3.3  $\mu\text{m}$  by 3.3  $\mu\text{m}$ . *J. Magn. Reson.*, 2002. ISSN 10907807. doi: 10.1016/S1090-7807(02)00071-X.
- [52] Dean L. Olson, Timothy L. Peck, Andrew G. Webb, Richard L. Magin, and Jonathan V. Sweedler. High-Resolution Microcoil 1 H-NMR for Mass-Limited, Nanoliter-Volume Samples. *Science*, 1995. ISSN 0036-8075. doi: 10.1126/science.270.5244.1967.
- [53] K. Kratt, V. Badilita, T. Burger, J. G. Korvink, and U. Wallrabe. A fully MEMS-compatible process for 3D high aspect ratio micro coils obtained with an automatic wire bonder. *J. Micromechanics Microengineering*, 2010. ISSN 0960-1317. doi: 10.1088/0960-1317/20/1/015021.
- [54] Robert Ch. Meier, Jens Höfflin, Vlad Badilita, Ulrike Wallrabe, and Jan G. Korvink. Microfluidic integration of wirebonded microcoils for on-chip applications in nuclear magnetic resonance. *J. Micromechanics Microengineering*, 2014. ISSN 0960-1317. doi: 10.1088/0960-1317/24/4/045021.

- [55] Erin E. McDonnell, Songl Han, Christian Hilty, Kimberly L. Pierce, and Alexander Pines. NMR analysis on microfluidic devices by remote detection. *Anal. Chem.*, 2005. ISSN 0003-2700. doi: 10.1021/ac051320+.
- [56] Nils Spengler, Jens Höfflin, Ali Moazen-zadeh, Dario Mager, Neil MacKinnon, Vlad Badilita, Ulrike Wallrabe, and Jan G. Korvink. Heteronuclear Micro-Helmholtz Coil Facilitates  $\mu\text{m}$ -Range Spatial and Sub-Hz Spectral Resolution NMR of nL-Volume Samples on Customisable Microfluidic Chips. *PLoS One*, 2016. ISSN 1932-6203. doi: 10.1371/journal.pone.0146384.
- [57] N. Wang, M. V. Meissner, N. MacKinnon, V. Luchnikov, D. Mager, and J. G. Korvink. Fast prototyping of microtubes with embedded sensing elements made possible with an inkjet printing and rolling process. *J. Micromechanics Microengineering*, 2018. ISSN 0960-1317. doi: 10.1088/1361-6439/aa7a61.
- [58] T. L. Peck, R. L. Magin, J. Kruse, and M. Feng. NMR microspectroscopy using 100  $\mu\text{m}$  planar RF coils fabricated on gallium arsenide substrates. *IEEE Trans. Biomed. Eng.*, 1994. ISSN 00189294. doi: 10.1109/10.301740.
- [59] Raluca M. Fratila, M. Victoria Gomez, Stanislav Sýkora, and Aldrik H. Velders. Multinuclear nanoliter one-dimensional and two-dimensional NMR spectroscopy with a single non-resonant microcoil. *Nat. Commun.*, 2014. ISSN 2041-1723. doi: 10.1038/ncomms4025.
- [60] Jan Watzlaw, Stefan Glöggler, Bernhard Blümich, Wilfried Mokwa, and Uwe Schnakenberg. Stacked planar micro coils for single-sided NMR applications. *J. Magn. Reson.*, 2013. ISSN 1096-0856. doi: 10.1016/j.jmr.2013.02.013.
- [61] C. Massin, G. Boero, F. Vincent, J. Abenhaim, P. A. Besse, and R. S. Popovic. High-Q factor RF planar microcoils for micro-scale NMR spectroscopy. *Sensors Actuators A Phys.*, 2002. ISSN 09244247. doi: 10.1016/S0924-4247(01)00847-0.
- [62] Stefan Leidich, Marco Braun, Thomas Gessner, and Thomas Riemer. Silicon cylinder spiral coil for nuclear magnetic resonance spectroscopy of nanoliter samples. *Concepts Magn. Reson. Part B Magn. Reson. Eng.*, 2009. ISSN 15525031. doi: 10.1002/cmr.b.20131.
- [63] Jens Anders, Paul SanGiorgio, and Giovanni Boero. A fully integrated IQ-receiver for NMR microscopy. *J. Magn. Reson.*, 2011. ISSN 10907807. doi: 10.1016/j.jmr.2010.12.005.

- 
- [64] M. Alfonsetti, V. Clementi, S. Iotti, G. Placidi, R. Lodi, B. Barbiroli, A. Sotgiu, and M. Alecci. Versatile coil design and positioning of transverse-field RF surface coils for clinical 1.5-T MRI applications. *MAGMA*, 2005. ISSN 0968-5243. doi: 10.1007/s10334-004-0090-4.
- [65] Ka-Meng Lei, Pui-In Mak, Man-Kay Law, and Rui P. Martins. A  $\mu$ NMR CMOS Transceiver using a Butterfly-Coil Input for Integration with a Digital Microfluidic Device Inside a Portable Magnet. *IEEE J. Solid-State Circuits*, 2016. ISSN 0018-9200. doi: 10.1109/JSSC.2016.2579158.
- [66] Jens Anders, Giuseppe Chiamonte, Paul SanGiorgio, and Giovanni Boero. A single-chip array of NMR receivers. *J. Magn. Reson.*, 2009. ISSN 10907807. doi: 10.1016/j.jmr.2009.09.019.
- [67] Oliver G. Gruschke, Nicoleta Baxan, Lars Clad, Kai Kratt, Dominik von Elverfeldt, Andreas Peter, Jürgen Hennig, Vlad Badilita, Ulrike Wallrabe, and Jan G. Korvink. Lab on a chip phased-array MR multi-platform analysis system. *Lab Chip*, 2012. ISSN 1473-0197. doi: 10.1039/C2LC20585H.
- [68] J. M. Tyszka, S. E. Fraser, and R. E. Jacobs. Magnetic resonance microscopy: recent advances and applications. *Curr. Opin. Biotechnol.*, 2005. ISSN 09581669. doi: 10.1016/j.copbio.2004.11.004.
- [69] R. W. Bowtell. Resolution of cellular structures by NMR microscopy at 11.7 T. *Philos. Trans. R. Soc. London. Ser. A Phys. Eng. Sci.*, 1990. ISSN 0962-8428. doi: 10.1098/rsta.1990.0173.
- [70] F. David Doty. MRI Gradient Coil Optimization. In *Spat. Resolv. Magn. Reson.*, pages 647–674. Wiley-VCH Verlag GmbH, Weinheim, Germany, 1998. ISBN 9783527611843. doi: 10.1002/9783527611843.ch60.
- [71] P.T. While, L.K. Forbes, and Stuart Crozier. 3-D Gradient Coil Design - Initial Theoretical Framework. *IEEE Trans. Biomed. Eng.*, 2009. ISSN 0018-9294. doi: 10.1109/TBME.2009.2013199.
- [72] C. B. Ahn and Z. H. Cho. Analysis of eddy currents in nuclear magnetic resonance imaging. *Magn. Reson. Med.*, 1991. ISSN 07403194. doi: 10.1002/mrm.1910170119.
- [73] P. Mansfield and B. Chapman. Active magnetic screening of coils for static and time-dependent magnetic field generation in NMR imaging. *J. Phys. E.*, 1986. ISSN 0022-3735. doi: 10.1088/0022-3735/19/7/008.

- [74] Sir Peter Mansfield, Barry L. W. Chapman, Robert Turner, and Roger M. Bowley. US Patent 4978920. Magnetic field screens. 1990.
- [75] K. Yoda. Analytical design method of self-shielded planar coils. *J. Appl. Phys.*, 1990. ISSN 00218979. doi: 10.1063/1.344953.
- [76] B. L. W. Chapman. Shielded gradients. And the general solution to the near field problem of electromagnet design. *Magma Magn. Reson. Mater. Physics, Biol. Med.*, 1999. ISSN 1352-8661. doi: 10.1007/BF02594613.
- [77] Weston A. Anderson. Electrical current shims for correcting magnetic fields. *Rev. Sci. Instrum.*, 1961. ISSN 00346748. doi: 10.1063/1.1717338.
- [78] I. Zupancic. Current shims for high-resolution nuclear magnetic resonance on the problem of correcting magnetic field inhomogeneities. *J. Sci. Instrum.*, 1962. ISSN 0950-7671. doi: 10.1088/0950-7671/39/12/331.
- [79] R. S. Parker, I. Zupancic, and J. Pirs. Coil system to produce orthogonal, linear magnetic field gradients. *J. Phys. E.*, 1973. ISSN 0022-3735. doi: 10.1088/0022-3735/6/9/028.
- [80] David C. Alsop and Thomas J. Connick. Optimization of torque-balanced asymmetric head gradient coils. *Magn. Reson. Med.*, 1996. ISSN 07403194. doi: 10.1002/mrm.1910350614.
- [81] Lazar Shtirberg, Ygal Twig, Ekaterina Dikarov, Revital Halevy, Michael Levit, and Aharon Blank. High-sensitivity Q-band electron spin resonance imaging system with submicron resolution. *Rev. Sci. Instrum.*, 2011. ISSN 00346748. doi: 10.1063/1.3581226.
- [82] Markus Weiger, Daniel Schmidig, Schimun Denoth, Charles Massin, Franck Vincent, Michael Schenkel, and Michael Fey. NMR microscopy with isotropic resolution of 3.0  $\mu\text{m}$  using dedicated hardware and optimized methods. *Concepts Magn. Reson. Part B Magn. Reson. Eng.*, 2008. ISSN 15525031. doi: 10.1002/cmr.b.20112.
- [83] Dai Tsuchiya and Tetsuji Dohi. A compact magnetic resonance imaging system integrated micro RF and gradient coils for small sample measurement. In *2018 IEEE Micro Electro Mech. Syst.*, volume 2018-Janua, pages 426–429. 2018. ISBN 978-1-5386-4782-0. doi: 10.1109/MEMSYS.2018.8346579.
- [84] Micro5, Bruker BioSpin MRI GmbH, Ettlingen, Germany. *Datasheet*, accessed on 2020-04-05.

- 
- [85] MRI Catalog Small, Doty Scientific Inc., Columbia, USA. *Product Cat.*, accessed on 2019-06-21.
- [86] Andrey V. Demyanenko, Lin Zhao, Yun Kee, Shuyi Nie, Scott E. Fraser, and J. Michael Tyszka. A uniplanar three-axis gradient set for in vivo magnetic resonance microscopy. *J. Magn. Reson.*, 2009. ISSN 10907807. doi: 10.1016/j.jmr.2009.05.014.
- [87] Steven M. Wright, David G. Brown, Jay R. Porter, David C. Spence, Emilio Esparza, David C. Cole, and F. Russell Huson. A desktop magnetic resonance imaging system. *Magn. Reson. Mater. Physics, Biol. Med.*, 2002. ISSN 13528661. doi: 10.1016/S1352-8661(01)00147-8.
- [88] John C. Price and Chris Jonkman. US Patent 8729898B2. Shim coils and shimming miniaturized nuclear magnetic resonance magnets. 2014.
- [89] I. Frollo. Parallel plane gradient system for NMR experiments. *Rev. Sci. Instrum.*, 1989. ISSN 00346748. doi: 10.1063/1.1140542.
- [90] Stephen J. Dodd and Chien Ho. Short Planar Gradient Coils for MR Microscopy Using Concentric Return Paths. *J. Magn. Reson.*, 2002. ISSN 10907807. doi: 10.1006/jmre.2002.2532.
- [91] A. G. Goloshevsky, J. H. Walton, M. V. Shutov, J. S. Ropp, S. D. Collins, and M. J. McCarthy. Integration of biaxial planar gradient coils and an RF microcoil for NMR flow imaging. *Meas. Sci. Technol.*, 2005. ISSN 0957-0233. doi: 10.1088/0957-0233/16/2/024.
- [92] Dennis Ellersiek, Georg Dura, Wilfried Mokwa, Uwe Schnakenberg, Silke Harms, Federico Casanova, and Bernhard Blumich. Micro Structured Planar Gradient Coils for Low Field Magnetic Resonance Imaging. *2007 IEEE Sensors*, 2007. doi: 10.1109/ICSENS.2007.4388546.
- [93] R. Sahebjavaher, B. Stoeber, and K. Walus. Microfabricated multi-turn gradient coils for microscale flow imaging. In *TRANSDUCERS 2009 Int. Solid-State Sensors, Actuators Microsystems Conf.*, pages 1570–1573. 2009. ISBN 978-1-4244-4190-7. doi: 10.1109/SENSOR.2009.5285787.
- [94] R. Bowtell and P. Robyr. Multilayer Gradient Coil Design. *J. Magn. Reson.*, 1998. ISSN 10907807. doi: 10.1006/jmre.1998.1369.

- [95] A. C. Wright, H. Bataille, H. H. Ong, S. L. Wehrli, H. K. Song, and F. W. Wehrli. Construction and calibration of a 50 T/m z-gradient coil for quantitative diffusion microimaging. *J. Magn. Reson.*, 2007. ISSN 10907807. doi: 10.1016/j.jmr.2007.01.011.
- [96] Marcel J. E. Golay. Field homogenizing coils for nuclear spin resonance instrumentation. *Rev. Sci. Instrum.*, 1958. ISSN 00346748. doi: 10.1063/1.1716184.
- [97] Aharon Blank, Curt R. Dunnam, Peter P. Borbat, and Jack H. Freed. High resolution electron spin resonance microscopy. *J. Magn. Reson.*, 2003. ISSN 10907807. doi: 10.1016/S1090-7807(03)00254-4.
- [98] Aharon Blank, Ekaterina Suhovoy, Revital Halevy, Lazar Shtirberg, and Wolfgang Harneit. ESR imaging in solid phase down to sub-micron resolution: methodology and applications. *Phys. Chem. Chem. Phys.*, 2009. ISSN 1463-9076. doi: 10.1039/b905943a.
- [99] R. Turner and R. M. Bowley. Passive screening of switched magnetic field gradients. *J. Phys. E.*, 1986. ISSN 0022-3735. doi: 10.1088/0022-3735/19/10/023.
- [100] R. Turner. Gradient coil design: a review of methods. *Magn. Reson. Imaging*, 1993. ISSN 0730725X. doi: 10.1016/0730-725X(93)90209-V.
- [101] R. Turner. Minimum inductance coils. *J. Phys. E.*, 1988. ISSN 00223735. doi: 10.1088/0022-3735/21/10/008.
- [102] Peter T. While, Larry K. Forbes, and Stuart Crozier. Designing gradient coils with reduced hot spot temperatures. *J. Magn. Reson.*, 2010. ISSN 10907807. doi: 10.1016/j.jmr.2009.12.004.
- [103] Peter T. While, Markus V. Meissner, and Jan G. Korvink. Insertable biplanar gradient coils for magnetic resonance microscopy: theoretical minimization of power dissipation for different fabrication methods. *Biomed. Phys. Eng. Express*, 2018. ISSN 2057-1976. doi: 10.1088/2057-1976/aab5db.
- [104] Rostislav A. Lemdiasov and Reinhold Ludwig. A stream function method for gradient coil design. *Concepts Magn. Reson. Part B Magn. Reson. Eng.*, 2005. ISSN 1552-5031. doi: 10.1002/cmr.b.20040.
- [105] Michael Poole and Richard Bowtell. Novel gradient coils designed using a boundary element method. *Concepts Magn. Reson. Part B Magn. Reson. Eng.*, 2007. ISSN 15525031. doi: 10.1002/cmr.b.20091.

- 
- [106] Juergen Hennig, Anna Masako Welz, Gerrit Schultz, Jan Korvink, Zhenyu Liu, Oliver Speck, and Maxim Zaitsev. Parallel imaging in non-bijective, curvilinear magnetic field gradients: a concept study. *MAGMA*, 2008. ISSN 0968-5243. doi: 10.1007/s10334-008-0105-7.
- [107] Daniel Gallichan, Chris Cocosco, Andrew Dewdney, Gerrit Schultz, Anna Welz, Jürgen Hennig, and Maxim Zaitsev. Simultaneously driven linear and nonlinear spatial encoding fields in MRI. *Magn. Reson. Med.*, 2011. ISSN 1522-2594. doi: 10.1002/mrm.22672.
- [108] Sebastian Littin, Daniel Gallichan, Anna Masako Welz, Feng Jia, Andrew Dewdney, Hans Weber, Gerrit Schultz, Jürgen Hennig, and Maxim Zaitsev. Monoplanar gradient system for imaging with nonlinear gradients. *Magn. Reson. Mater. Physics, Biol. Med.*, 2015. ISSN 0968-5243. doi: 10.1007/s10334-015-0481-8.
- [109] Bernhard Gleich and Jürgen Weizenecker. Tomographic imaging using the nonlinear response of magnetic particles. *Nature*, 2005. ISSN 0028-0836. doi: 10.1038/nature03808.
- [110] Tobias Knopp, Marlitt Erbe, Timo F. Sattel, Sven Biederer, and Thorsten M. Buzug. Generation of a static magnetic field-free line using two Maxwell coil pairs. *Appl. Phys. Lett.*, 2010. ISSN 0003-6951. doi: 10.1063/1.3486118.
- [111] Jean-Baptiste Mathieu and Sylvain Martel. Magnetic Steering of Iron Oxide Microparticles Using Propulsion Gradient Coils in MRI. In *2006 Int. Conf. IEEE Eng. Med. Biol. Soc.*, volume 1, pages 472–475. 2006. ISBN 1-4244-0032-5. doi: 10.1109/IEMBS.2006.259818.
- [112] Seungmun Jeon, Gunhee Jang, Hyunchul Choi, and Sukho Park. Magnetic Navigation System With Gradient and Uniform Saddle Coils for the Wireless Manipulation of Micro-Robots in Human Blood Vessels. *IEEE Trans. Magn.*, 2010. ISSN 0018-9464. doi: 10.1109/TMAG.2010.2040144.
- [113] Markus V. Meissner, Erwin Fuhrer, Sebastian Z. Kiss, Herbert B. Ryan, Neil MacKinnon, Peter T. While, and Jan G. Korvink. Low Expense General Operation probe. In *55th Exp. Nucl. Magn. Reson. Conf. (ENC), Pacific Grove, CA, USA*. 2014.
- [114] R. Turner. A target field approach to optimal coil design. *J. Phys. D. Appl. Phys.*, 1986. ISSN 0022-3727. doi: 10.1088/0022-3727/19/8/001.
- [115] The *c. elegans* Sequencing Consortium. Genome Sequence of the Nematode *C. elegans*: A Platform for Investigating Biology. *Science*, 1998. ISSN 00368075. doi: 10.1126/science.282.5396.2012.

- [116] E. W. Becker, W. Ehrfeld, P. Hagmann, A. Maner, and D. Münchmeyer. Fabrication of microstructures with high aspect ratios and great structural heights by synchrotron radiation lithography, galvanofforming, and plastic moulding (LIGA process). *Microelectron. Eng.*, 1986. ISSN 01679317. doi: 10.1016/0167-9317(86)90004-3.
- [117] Jan Korvink and Oliver Paul. *MEMS: A Practical Guide of Design, Analysis, and Applications*. Springer-Verlag GmbH & Co. KG, Heidelberg, Germany, 2006. ISBN 3-540-21117-9.
- [118] Zheng Cui. *Nanofabrication*. Springer US, Boston, MA, 2008. ISBN 978-0-387-75576-2. doi: 10.1007/978-0-387-75577-9.
- [119] T. H. J. van Osch, J. Perelaer, A. W. M. de Laat, and U. S. Schubert. Inkjet Printing of Narrow Conductive Tracks on Untreated Polymeric Substrates. *Adv. Mater.*, 2008. ISSN 09359648. doi: 10.1002/adma.200701876.
- [120] Henning Meier, Ute Löffelmann, Dario Mager, Patrick J. Smith, and Jan G. Korvink. Inkjet printed, conductive, 25  $\mu\text{m}$  wide silver tracks on unstructured polyimide. *Phys. status solidi*, 2009. ISSN 18626300. doi: 10.1002/pssa.200925088.
- [121] Omar Nassar, Markus V. Meissner, Sagar Wadhwa, Jan G. Korvink, and Dario Mager. Load sensitive stable current source for complex precision pulsed electroplating. *Rev. Sci. Instrum.*, 2019. ISSN 0034-6748. doi: 10.1063/1.5113790.
- [122] Rabih Zaouk, Benjamin Y. Park, and Marc J. Madou. Introduction to Microfabrication Techniques. In *Microfluid. Tech.*, volume 321, pages 5–16. Humana Press, New Jersey, 2004. doi: 10.1385/1-59259-997-4:3.
- [123] Nancy C. LaBianca and Jeffrey D. Gelorme. High-aspect-ratio resist for thick-film applications. In *SPIE's 1995 Symp. Microlithogr.*, pages 846–852. 1995. doi: 10.1117/12.210413.
- [124] Markus Deubel, Georg Von Freymann, Martin Wegener, Suresh Pereira, Kurt Busch, and Costas M. Soukoulis. Direct laser writing of three-dimensional photonic-crystal templates for telecommunications. *Nat. Mater.*, 2004. ISSN 03778401. doi: 10.1016/j.nature.2007.04.010.
- [125] Wen Dai, Kun Lian, and Wanjun Wang. A quantitative study on the adhesion property of cured SU-8 on various metallic surfaces. *Microsyst. Technol.*, 2005. ISSN 09467076. doi: 10.1007/s00542-005-0587-4.

- 
- [126] Amritha Rammohan, Prabhat K. Dwivedi, Rodrigo Martinez-duarte, Hari Katepalli, Marc J. Madou, and Ashutosh Sharma. One-step maskless grayscale lithography for the fabrication of 3-dimensional structures in SU-8. *Sensors Actuators B. Chem.*, 2011. ISSN 0925-4005. doi: 10.1016/j.snb.2010.10.021.
- [127] M. V. Meissner, N. Spengler, D. Mager, N. Wang, S. Z. Kiss, J. Höfflin, P. T. While, and J. G. Korvink. Ink-jet printing technology enables self-aligned mould patterning for electroplating in a single step. *J. Micromechanics Microengineering*, 2015. ISSN 0960-1317. doi: 10.1088/0960-1317/25/6/065015.
- [128] Paul M. Dentinger, Miles W. Clift, and Steven H. Goods. Removal of SU-8 photoresist for thick film applications. *Microelectron. Eng.*, 2002. ISSN 01679317. doi: 10.1016/S0167-9317(02)00490-2.
- [129] M. Despont, H. Lorenz, N. Fahrni, J. Brugger, P. Renaud, and P. Vettiger. High-aspect-ratio, ultrathick, negative-tone near-uv photoresist for MEMS applications. In *Proc. IEEE Tenth Annu. Int. Work. Micro Electro Mech. Syst. An Investig. Micro Struct. Sensors, Actuators, Mach. Robot.*, pages 518–522. 1997. ISBN 0-7803-3744-1. doi: 10.1109/MEMSYS.1997.581916.
- [130] H. Lorenz, M. Laudon, and P. Renaud. Mechanical characterization of a new high-aspect-ratio near UV-photoresist. *Microelectron. Eng.*, 1998. ISSN 01679317. doi: 10.1016/S0167-9317(98)00086-0.
- [131] Bo Li. Low-stress ultra-thick SU-8 UV photolithography process for MEMS. *J. Micro/Nanolithography, MEMS, MOEMS*, 2005. ISSN 1932-5150. doi: 10.1117/1.2117108.
- [132] D. W. Johnson, A. Jeffries, D. W. Minsek, and R. J. Hurditch. Improving the Process Capability of SU-8. Part II. *J. Photopolym. Sci. Technol.*, 2001. ISSN 0914-9244. doi: 10.2494/photopolymer.14.689.
- [133] Rodrigo Martinez-Duarte and Marc Madou. SU-8 Photolithography and Its Impact on Microfluidics. In *Microfluid. Nanofluidics Handb.*, volume 21, pages 245–282. CRC Press, 2016. doi: 10.1201/b11188-12.
- [134] Santeri Tuomikoski and Sami Franssila. Free-standing SU-8 microfluidic chips by adhesive bonding and release etching. *Sensors Actuators A Phys.*, 2005. ISSN 09244247. doi: 10.1016/j.sna.2005.01.012.

- [135] M. Agirregabiria, F. J. Blanco, J. Berganzo, M. T. Arroyo, A. Fullaondo, K. Mayora, and J. M. Ruano-López. Fabrication of SU-8 multilayer microstructures based on successive CMOS compatible adhesive bonding and releasing steps. *Lab Chip*, 2005. ISSN 1473-0197. doi: 10.1039/b500519a.
- [136] Nils Schuergers, Tchern Lenn, Ronald Kampmann, Markus V Meissner, Tiago Esteves, Maja Temerinac-Ott, Jan G Korvink, Alan R Lowe, Conrad W Mullineaux, and Annegret Wilde. Cyanobacteria use micro-optics to sense light direction. *eLife*, 2016. ISSN 2050-084X. doi: 10.7554/eLife.12620.
- [137] Ferdinand Walther, Polina Davydovskaya, Stefan Zürcher, Michael Kaiser, Helmut Herberg, Alexander M Gigler, and Robert W Stark. Stability of the hydrophilic behavior of oxygen plasma activated SU-8. *J. Micromechanics Microengineering*, 2007. ISSN 0960-1317. doi: 10.1088/0960-1317/17/3/015.
- [138] Novak E. S. Farrington and Stavros Iezekiel. Accurate layer thickness control and planarization for multilayer SU-8 structures. *J. Micro/Nanolithography, MEMS, MOEMS*, 2011. ISSN 1932-5150. doi: 10.1117/1.3563599.
- [139] George Gal. EP0671024B1. European Patent Office. Method for fabricating microlenses. 1992.
- [140] Don Johnson, Anja Voigt, Gisela Ahrens, and Wen Dai. Thick epoxy resist sheets for MEMS manufacturing and packaging. In *2010 IEEE 23rd Int. Conf. Micro Electro Mech. Syst.*, pages 412–415. 2010. ISBN 978-1-4244-5761-8. doi: 10.1109/MEMSYS.2010.5442479.
- [141] Donald W. Johnson, Jost Goettert, Varshni Singh, and Dawit Yemane. SUEX process optimization for ultra-thick high-aspect ratio LIGA imaging. volume 7972, 2011. ISBN 9780819485311. doi: 10.1117/12.882872.
- [142] Robert Ch. Meier, Vlad Badilita, Jens Brunne, Ulrike Wallrabe, and Jan G. Korvink. Complex three-dimensional high aspect ratio microfluidic network manufactured in combined PerMX dry-resist and SU-8 technology. *Biomicrofluidics*, 2011. ISSN 19321058. doi: 10.1063/1.3613668.
- [143] DuPont™ PerMX™ Series, DuPont Electronic Technologies, 14 T.W. Alexander Drive, Research Triangle Park, NC, USA. *Datasheet*, accessed on 2013-05-22.
- [144] A. Voigt, M. Heinrich, K. Hauck, R. Mientus, G. Gruetzner, M. Töpfer, and O. Ehrmann. A single layer negative tone lift-off photo resist for patterning a magnetron sputtered Ti/Pt/Au contact system and for solder bumps. *Microelectron. Eng.*, 2005. ISSN 01679317. doi: 10.1016/j.mee.2004.12.064.

- 
- [145] Daniel Rodriguez Ponce, Karen Lozano, Thomas Eubanks, Ahmad Harb, Domingo Ferrer, Yuankun Lin, Daniel Rodriguez Ponce, Karen Lozano, Thomas Eubanks, Ahmad Harb, Domingo Ferrer, and Yuankun Lin. Thermophysical analysis of SU8-modified microstructures created by visible light lithography. *J. Polym. Sci. Part B Polym. Phys.*, 2010. ISSN 08876266. doi: 10.1002/polb.21842.
- [146] Ru Feng and Richard J. Farris. Influence of processing conditions on the thermal and mechanical properties of SU8 negative photoresist coatings. *J. Micromechanics Microengineering*, 2003. ISSN 0960-1317. doi: 10.1088/0960-1317/13/1/312.
- [147] P. Vulto, N. Glade, L. Altomare, J. Bablet, L. Del Tin, G. Medoro, I. Chartier, N. Maresi, M. Tartagni, and R. Guerrieri. Microfluidic channel fabrication in dry film resist for production and prototyping of hybrid chips. *Lab Chip*, 2005. ISSN 1473-0197. doi: 10.1039/b411885e.
- [148] Philipp Muller, Nils Spengler, Hans Zappe, and Wolfgang Monch. An Optofluidic Concept for a Tunable Micro-iris. *J. Microelectromechanical Syst.*, 2010. ISSN 1057-7157. doi: 10.1109/JMEMS.2010.2079917.
- [149] Paul Vulto, Till Huesgen, Björn Albrecht, and G. A. Urban. A full-wafer fabrication process for glass microfluidic chips with integrated electroplated electrodes by direct bonding of dry film resist. *J. Micromechanics Microengineering*, 2009. ISSN 0960-1317. doi: 10.1088/0960-1317/19/7/077001.
- [150] P. Vulto, G. Igel, and G. A. Urban. Full Wafer Fabrication Process for Microfluidic Glass Chips with Electroplated Electrodes. In *TRANSDUCERS 2007 - Int. Solid-State Sensors, Actuators Microsystems Conf.*, pages 117–120. 2007. ISBN 1-4244-0841-5. doi: 10.1109/SENSOR.2007.4300085.
- [151] Till Huesgen, Gabriel Lenk, Björn Albrecht, Paul Vulto, Thomas Lemke, and Peter Woias. Optimization and characterization of wafer-level adhesive bonding with patterned dry-film photoresist for 3D MEMS integration. *Sensors Actuators A Phys.*, 2010. ISSN 09244247. doi: 10.1016/j.sna.2010.06.008.
- [152] Debjani Paul, Laure Saias, Jean-Cedric Pedinotti, Max Chabert, Sebastien Magnifico, Antoine Pallandre, Bertrand De Lambert, Claude Houdayer, Bernard Brugg, Jean-Michel Peyrin, and Jean-Louis Viovy. A "dry and wet hybrid" lithography technique for multilevel replication templates: Applications to microfluidic neuron culture and two-phase global mixing. *Biomicrofluidics*, 2011. ISSN 1932-1058. doi: 10.1063/1.3569946.

- [153] Anja Voigt, Gisela Ahrens, Marina Heinrich, Andrew Thompson, and Gabi Gruetzner. Improved adhesion of novolac and epoxy based resists by cationic organic materials on critical substrates for high volume patterning applications. In Thomas I. Wallow and Christoph K. Hohle, editors, *Adv. Patterning Mater. Process. XXXI*, volume 9051, 2014. ISBN 9780819499745. doi: 10.1117/12.2046258.
- [154] Anya Voigt, Gabi Gruetzner, E. Sauer, S. Helm, T. Harder, Simone Fehlberg, and Juergen Bendig. Series of AZ-compatible negative photoresists. In Robert D. Allen, editor, *Proc. SPIE*, volume 2438, 1995. ISBN 0819417866. doi: 10.1117/12.210420.
- [155] M. Agarwal, R. A. Gunasekaran, P. Coane, and K. Varahramyan. Scum-free patterning of SU-8 resist for electroforming applications. *J. Micromechanics Microengineering*, 2005. ISSN 09601317. doi: 10.1088/0960-1317/15/1/020.
- [156] F. Greiner, S. Quednau, F. Dassinger, R. Sarwar, H. F. Schlaak, M. Guttmann, and P. Meyer. Fabrication techniques for multiscale 3D-MEMS with vertical metal micro- and nanowire integration. *J. Micromechanics Microengineering*, 2013. ISSN 0960-1317. doi: 10.1088/0960-1317/23/2/025018.
- [157] Matthias Staab, Felix Greiner, Michael Schlosser, and Helmut F. Schlaak. Applications of Novel High-Aspect-Ratio Ultrathick UV Photoresist for Microelectroplating. *J. Microelectromechanical Syst.*, 2011. ISSN 1057-7157. doi: 10.1109/JMEMS.2011.2159098.
- [158] K. Kalkandjiev, L. Riegger, D. Kosse, M. Welsche, L. Gutzweiler, R. Zengerle, and P. Koltay. Microfluidics in silicon/polymer technology as a cost-efficient alternative to silicon/glass. *J. Micromechanics Microengineering*, 2011. ISSN 0960-1317. doi: 10.1088/0960-1317/21/2/025008.
- [159] Patrick Abgrall, Christine Lattes, Véronique Conédéra, Xavier Dollat, Stéphane Colin, and Anne Marie Gué. A novel fabrication method of flexible and monolithic 3D microfluidic structures using lamination of SU-8 films. *J. Micromechanics Microengineering*, 2006. ISSN 0960-1317. doi: 10.1088/0960-1317/16/1/016.
- [160] Matthias Wapler, Jochen Leupold, Iulius Dragonu, Dominik von Elverfeld, Maxim Zaitsev, and Ulrike Wallrabe. Magnetic properties of materials for MR engineering, micro-MR and beyond. *J. Magn. Reson.*, 2014. ISSN 1096-0856. doi: 10.1016/j.jmr.2014.02.005.

- 
- [161] Yoshihiro Kawahara, Steve Hodges, Benjamin S. Cook, Cheng Zhang, and Gregory D. Abowd. Instant inkjet circuits. In *Proc. 2013 ACM Int. Jt. Conf. Pervasive ubiquitous Comput.*, UbiComp '13, pages 363–372, 2013. ACM. ISBN 9781450317702. doi: 10.1145/2493432.2493486.
- [162] Milan Paunovic, Mordechai Schlesinger, and Dexter D. Snyder. Fundamental Considerations. In *Mod. Electroplat.*, pages 1–32. John Wiley Sons, Inc., Hoboken, NJ, USA, 2011. doi: 10.1002/9780470602638.ch1.
- [163] Christopher D. Meyer, Sarah S. Bedair, Brian C. Morgan, and David P. Arnold. High-Inductance-Density, Air-Core, Power Inductors, and Transformers Designed for Operation at 100–500 MHz. *IEEE Trans. Magn.*, 2010. ISSN 0018-9464. doi: 10.1109/TMAG.2010.2045742.
- [164] Jack W. Dini and Dexter D. Snyder. Electrodeposition of Copper. In *Mod. Electroplat.*, number January 2002, pages 33–78. John Wiley & Sons, Inc., Hoboken, NJ, USA, 2011. doi: 10.1002/9780470602638.ch2.
- [165] M. R. H. Hill and G. T. Rogers. Polyethylene glycol in copper electrodeposition onto a rotating disk electrode. *J. Electroanal. Chem. Interfacial Electrochem.*, 1978. ISSN 00220728. doi: 10.1016/S0022-0728(78)80365-9.
- [166] Kurt R. Hebert, Saikat Adhikari, and Jerrod E. Houser. Chemical Mechanism of Suppression of Copper Electrodeposition by Poly(ethylene glycol). *J. Electrochem. Soc.*, 2005. ISSN 00134651. doi: 10.1149/1.1882112.
- [167] A. Vicenzo and P. L. Cavallotti. Copper electrodeposition from a pH 3 sulfate electrolyte. *J. Appl. Electrochem.*, 2002. doi: 10.1023/A:1020191111298.
- [168] Thomas Allmendinger. Theorie und Praxis der Hullzelle. In *Galvanotechnik*, volume 10, pages 2237–2251. Eugen G. Leuze Verlag, Bad Saulgau, Germany, 2010.
- [169] Cuprostar<sup>®</sup> LP-1 Mattabscheidender saurer Kupferelektrolyt, Enthone GmbH, Langenfeld, Germany. *Verfahrensanleitung*, 2003, accessed on 2013-03-05.
- [170] DIN Deutsches Institut für Normung e.V., Berlin, Germany. DIN EN ISO 3819, (ISO/DIS 3819:2013) – Laboratory glassware 2013.
- [171] Ouk S. Lee and Oh K. Kwon. An experimental study on crack healing of various glassy polymers. *KSME J.*, 1987. ISSN 1011-8861. doi: 10.1007/BF02953380.

- [172] Pedro Bertemes-Filho, Alexandre Felipe, and Volney C. Vincence. High Accurate Howland Current Source: Output Constraints Analysis. *Circuits Syst.*, 2013. ISSN 2153-1285. doi: 10.4236/cs.2013.47059.
- [173] LT1990,  $\pm 250$  V Input Range  $G = 1, 10$ , Micropower, Difference Amplifier, Rev.B, Analog Devices, Wilmington, MA, USA. *Datasheet*, 2004, accessed on 2018-10-22.
- [174] Ulrich Tietze, Christoph Schenk, Ch. Schenk, and Eberhard Gamm. Electronic circuits: Handbook for design and application. page 884. Springer-Verlag GmbH & Co. KG, Heidelberg, Germany, 2008. ISBN 978-35-4000-429-5.
- [175] DAC8568, 16-Bit, Octal-Channel, Ultra-Low Glitch, Voltage Output Digital-to-Analog Converter with 2.5 V, 2 ppm/ $^{\circ}$ C Internal Reference, Texas Instruments, Dallas, Texas, USA. *Datasheet*, 2009, accessed on 2018-12-22.
- [176] Derek Molloy. *Exploring BeagleBone: Tools and Techniques for Building with Embedded Linux*. John Wiley & Sons Inc., Indianapolis, USA, 2019. ISBN 1119533163.
- [177] Bokeh Development Team. Bokeh: Python library for interactive visualization, <https://docs.bokeh.org/>, accessed on 2016-12-22.
- [178] ADS1112, 16-Bit Analog-to-Digital Converter with Input Multiplexer and Onboard Reference, Texas Instruments, Dallas, Texas, USA. *Datasheet*, 2004, accessed on 2018-12-22.
- [179] Markus V. Meissner, Robert Ch. Meier, Peter T. While, Ali Moazenzadeh, and Jan G. Korvink. Micro Magnetic Resonance  $x,y$ -Gradient System for Microscopic Samples. In *Proc. Intl. Soc. Mag. Reson. Med. (ISMRM 21)*, Salt Lake City, Utah, USA, volume 21, 2013.
- [180] Markus V. Meissner, Robert Ch. Meier, Nils Spengler, Peter T. While, and Jan G. Korvink. Micro-integrated Biaxial Gradient System for Magnetic Resonance Microscopy. In *54th Exp. Nucl. Magn. Reson. Conf. (ENC)*, Pacific Grove, CA, USA. 2013.
- [181] Markus Meissner, Nils Spengler, Sebastian Kiss, Neil MacKinnon, Peter While, and Jan Korvink. Maskless, low cost fabrication of NMR field coils. In *Proc. Euromar 2014 Conf. Zürich, Switz.*, 2014.
- [182] Markus V. Meissner, Nils Spengler, Dario Mager, Jens Höfflin, Peter T. While, and Jan G. Korvink. Ink-jet printing enables maskless electroplating mould patterning for rapid MRI coil fabrication. In *Proc. Intl. Soc. Mag. Reson. Med. (ISMRM 23)*, Toronto, Canada, volume 23, 2015.

- 
- [183] N. Spengler, A. Moazenzadeh, R. Ch. Meier, V. Badilita, J. G. Korvink, and U. Wallrabe. Micro-fabricated Helmholtz coil featuring disposable microfluidic sample inserts for applications in nuclear magnetic resonance. *J. Micromechanics Microengineering*, 2014. ISSN 0960-1317. doi: 10.1088/0960-1317/24/3/034004.
- [184] A. C. Fischer, J. G. Korvink, N. Roxhed, G. Stemme, U. Wallrabe, and F. Niklaus. Unconventional applications of wire bonding create opportunities for microsystem integration. *J. Micromechanics Microengineering*, 2013. ISSN 0960-1317. doi: 10.1088/0960-1317/23/8/083001.
- [185] A. L. Robinson, D. A. Antoniadis, and E. W. Maby. Fabrication of fully self-aligned joint-gate CMOS structures. *Electron Devices, IEEE Trans.*, 1985. ISSN 0018-9383. doi: 10.1109/T-ED.1985.22087.
- [186] D. A. Frickey. Conversions between S, Z, Y, H, ABCD, and T parameters which are valid for complex source and load impedances. *IEEE Trans. Microw. Theory Tech.*, 1994. ISSN 00189480. doi: 10.1109/22.275248.
- [187] M. V. Meissner, P. T. While, D. Mager, and J. G. Korvink. Microscale nuclear magnetic resonance gradient chip. *J. Micromechanics Microengineering*, 2023. ISSN 0960-1317. doi: 10.1088/1361-6439/ac9e4a.
- [188] Ann K. Corsi, Bruce Wightman, and Martin Chalfie. A Transparent Window into Biology: A Primer on *Caenorhabditis elegans*. *Genetics*, 2015. ISSN 0016-6731. doi: 10.1534/genetics.115.176099.
- [189] Travis E. Oliphant. Python for Scientific Computing. *Comput. Sci. Eng.*, 2007. ISSN 1521-9615. doi: 10.1109/MCSE.2007.58.
- [190] Herbert Ryan, Alison Smith, and Marcel Utz. Structural shimming for high-resolution nuclear magnetic resonance spectroscopy in lab-on-a-chip devices. *Lab Chip*, 2014. ISSN 1473-0189. doi: 10.1039/c3lc51431e.
- [191] L. K. Forbes and S. Crozier. Novel Target-Field Method for Designing Shielded Biplanar Shim and Gradient Coils. *IEEE Trans. Magn.*, 2004. ISSN 0018-9464. doi: 10.1109/TMAG.2004.828934.
- [192] Peter T. While, Jan G. Korvink, N. Jon Shah, and Michael S. Poole. Theoretical design of gradient coils with minimum power dissipation: accounting for the discretization of current density into coil windings. *J. Magn. Reson.*, 2013. ISSN 1096-0856. doi: 10.1016/j.jmr.2013.07.017.

- [193] Chia-Jung Chang, Chung-Shi Yang, Li-Hua Lan, Pen-Cheng Wang, and Fan-Gang Tseng. Fabrication of a SU-8-based polymer-enclosed channel with a penetrating UV/ozone-modified interior surface for electrokinetic separation of proteins. *J. Micromechanics Microengineering*, 2010. ISSN 0960-1317. doi: 10.1088/0960-1317/20/11/115031.
- [194] Christopher Bettinger, Jeffrey T. Borenstein, and Sarah L. Tao. *Microfluidic Cell Culture Systems*. Elsevier, 2013. ISBN 9781437734591. doi: 10.1016/C2010-0-65919-0.
- [195] P. Dierckx. Algorithms for smoothing data with periodic and parametric splines. *Comput. Graph. Image Process.*, 1982. ISSN 0146664X. doi: 10.1016/0146-664X(82)90043-0.
- [196] S. Langlois, M. Desvignes, J. M. Constans, and M. Revenu. MRI geometric distortion: a simple approach to correcting the effects of non-linear gradient fields. *J. Magn. Reson. Imaging*, 1999. ISSN 1053-1807. doi: 10.1002/(sici)1522-2586(199906)9:6<821::aid-jmri9>3.0.co;2-2.
- [197] Erhard Wendlandt. DE Patent 000019738626C2. Mikrodurchfluss- und Kulturküvette. 1997.
- [198] Nils Spengler. *Modular  $\mu$ NMR Probe*. Doctoral thesis, Freiburg, Germany, 2015, <https://freidok.uni-freiburg.de/data/159664>.
- [199] R. Kamberger, A. Moazenzadeh, J. G. Korvink, and O. G. Gruschke. Hollow microcoils made possible with external support structures manufactured with a two-solvent process. *J. Micromechanics Microengineering*, 2016. ISSN 13616439. doi: 10.1088/0960-1317/26/6/065002.
- [200] Kosuke Murashige and Tetsuji Dohi. The micro saddle coil with switchable sensitivity for Magnetic Resonance Imaging. In *2015 28th IEEE Int. Conf. Micro Electro Mech. Syst.*, volume 2015-Febru, pages 674–677. 2015. ISBN 978-1-4799-7955-4. doi: 10.1109/MEMSYS.2015.7051047.
- [201] Zhiyong Li, Patricia Beck, Douglas A. A. Ohlberg, Duncan R. Stewart, and R. Stanley Williams. Surface properties of platinum thin films as a function of plasma treatment conditions. *Surf. Sci.*, 2003. ISSN 00396028. doi: 10.1016/S0039-6028(03)00015-3.
- [202] SU-8 3000 Permanent Epoxy Negative Photoresist, Kayaku Advanced Materials Inc., Westborough, MA, USA. *Datasheet*, accessed on 2014-01-03.

- [203] Hun Lee, Kangsun Lee, Byungwook Ahn, Jing Xu, Linfeng Xu, and Kwang W. Oh. A new fabrication process for uniform SU-8 thick photoresist structures by simultaneously removing edge bead and air bubbles. *J. Micromechanics Microengineering*, 2011. ISSN 09601317. doi: 10.1088/0960-1317/21/12/125006.
- [204] Zhong-geng Ling and Kun Lian. Improved patterning quality of SU-8 microstructures by optimizing the exposure parameters IK1usUInul. *Proc. SPIE*, 2000. ISSN 0277786X. doi: 10.1117/12.388266.
- [205] Won-Jong Kang, Erik Rabe, Stefan Kopetz, and Andreas Neyer. Novel exposure methods based on reflection and refraction effects in the field of SU-8 lithography. *J. Micromechanics Microengineering*, 2006. ISSN 0960-1317. doi: 10.1088/0960-1317/16/4/020.
- [206] Donald M. Mattox. Physical Sputtering and Sputter Deposition (Sputtering). In *Handb. Phys. Vap. Depos. Process.*, pages 237–286. Elsevier, 2010. ISBN 978-0-81-552037-5. doi: 10.1016/B978-0-8155-2037-5.00007-1.
- [207] K. R. Williams, Kishan Gupta, and Matthew Wasilik. Etch rates for micromachining processing-part II. *J. Microelectromechanical Syst.*, 2003. ISSN 1057-7157. doi: 10.1109/JMEMS.2003.820936.
- [208] Grunwald John J. US Patent 3242090. Compositions for and methods of removing gold deposits by chemical action. 1966.
- [209] S. H. Cho, S. H. Kim, J. G. Lee, and N.-E. Lee. Micro-scale metallization of high aspect-ratio Cu and Au lines on flexible polyimide substrate by electroplating using SU-8 photoresist mask. *Microelectron. Eng.*, 2005. ISSN 01679317. doi: 10.1016/j.mee.2004.09.007.
- [210] S. Krongelb, L. T. Romankiw, and J. A. Tornello. Electrochemical process for advanced package fabrication. *IBM J. Res. Dev.*, 1998. ISSN 0018-8646. doi: 10.1147/rd.425.0575.
- [211] I. Zine-El-Abidine and M. Okoniewski. A Low-Temperature SU-8 Based Wafer-Level Hermetic Packaging for MEMS Devices. *IEEE Trans. Adv. Packag.*, 2009. ISSN 1521-3323. doi: 10.1109/TADVP.2008.2006757.
- [212] Gonzalo Murillo, Zachary J. Davis, Stephan Keller, Gabriel Abadal, Jordi Agusti, Alberto Cagliani, Nadine Noeth, Anja Boisen, and Nuria Barniol. Novel SU-8 based vacuum wafer-level packaging for MEMS devices. *Microelectron. Eng.*, 2010. ISSN 01679317. doi: 10.1016/j.mee.2009.12.048.

- [213] Janggil Kim, Seonho Seok, Preeti Sharma, Nathalie Rolland, and Paul-alain Rolland. Low Loss Zero-Level Packaging for High Frequency RF Applications by Using PerMX dry film Photoresist. In *Microw. Conf. (EuMC), 2011 41st Eur.*, number October, 2011. ISBN 978-2-87487-022-4. doi: 10.23919/EuMC.2011.6101892.
- [214] Santeri Tuomikoski and Sami Franssila. Free-standing SU-8 microfluidic chips by adhesive bonding and release etching. *Sensors Actuators A*, 2005. doi: 10.1016/j.sna.2005.01.012.
- [215] Lars Brusberg, Marco Queisser, Clemens Gentsch, Henning Schröder, and Klaus-Dieter Lang. Advances in CO<sub>2</sub>-Laser Drilling of Glass Substrates. *Phys. Procedia*, 2012. ISSN 18753892. doi: 10.1016/j.phpro.2012.10.072.
- [216] Chin H. Wu, Christopher V. Grant, Gabriel A. Cook, Sang Ho Park, and Stanley J. Opella. A strip-shield improves the efficiency of a solenoid coil in probes for high-field solid-state NMR of lossy biological samples. *J. Magn. Reson.*, 2009. ISSN 10907807. doi: 10.1016/j.jmr.2009.06.004.
- [217] H. Budzier and G. Gerlach. Calibration of uncooled thermal infrared cameras. *J. Sensors Sens. Syst.*, 2015. ISSN 2194-878X. doi: 10.5194/jsss-4-187-2015.
- [218] Jikwang Kim, Jongsung Kim, Younghwa Shin, and Youngsoo Yoon. A study on the fabrication of an RTD (resistance temperature detector) by using Pt thin film. *Korean J. Chem. Eng.*, 2001. ISSN 0256-1115. doi: 10.1007/BF02707199.
- [219] Nick Arango, Jason P. Stockmann, Thomas Witzel, Lawrence Wald, and Jacob White. Open-source, low-cost, flexible, current feedback-controlled driver circuit for local B0 shim coils and other applications. In *Proc. Intl. Soc. Mag. Reson. Med. 24*, 2016, [https://www.ismrm.org/16/program\\_files/043.htm](https://www.ismrm.org/16/program_files/043.htm).
- [220] Ulrich Tietze, Christoph Schenk, Ch. Schenk, and Eberhard Gamm. *Electronic Circuits: Handbook for Design and Application*. Springer-Verlag GmbH & Co. KG, Heidelberg, Germany, 2008. ISBN 978-35-4000-429-5.
- [221] Nils Spengler, Peter T. While, Markus V. Meissner, Ulrike Wallrabe, and Jan G. Korvink. Magnetic Lenz lenses improve the limit-of-detection in nuclear magnetic resonance. *PLoS One*, 2017. ISSN 1932-6203. doi: 10.1371/journal.pone.0182779.
- [222] R. Perrone, H. Bartsch de Torres, M. Hoffmann, M. Mach, and J. Müller. Miniaturized Embossed Low Resistance Fine Line Coils in LTCC. *J. Microelectron. Electron. Packag.*, 2009. ISSN 1551-4897. doi: 10.4071/1551-4897-6.1.42.

- [223] Malcolm H. Levitt. Part 2: The NMR Experiment. In *Spin Dyn. Basics Nucl. Magn. Reson.*, pages 86–89. John Wiley & Sons Ltd, Chichester, England, 2008. ISBN 978-0-470-51117-6.
- [224] Joël Mispelter, Mihaela Lupu, and André Briguet. *NMR Probeheads for Biophysical and Biomedical Experiments*. Imperial College Press, 2015. ISBN 978-1-84816-662-2. doi: 10.1142/p759.
- [225] Markus V. Meissner, Nikolaus Nestle, Nils Spengler, Dario Mager, Worgull Mathias, and Jan G. Korvink. Comparative study of  $\mu$ -MRI and X-ray  $\mu$ -CT on an oilseed grain. In *Int. Conf. Magn. Reson. Microsc. Tech. Univ. Munich, Ger.*, 2015.
- [226] K. Ehrmann, M. Gersbach, P. Pascoal, F. Vincent, C. Massin, D. Stamou, P.-A. Besse, H. Vogel, and R. S. Popovic. Sample patterning on NMR surface microcoils. *J. Magn. Reson.*, 2006. ISSN 10907807. doi: 10.1016/j.jmr.2005.08.018.
- [227] I. Fugariu, R. Soong, D. Lane, M. Fey, W. Maas, F. Vincent, A. Beck, D. Schmidig, B. Treanor, and A. J. Simpson. Towards single egg toxicity screening using microcoil NMR. *Analyst*, 2017. ISSN 0003-2654. doi: 10.1039/C7AN01339F.
- [228] Jonathan J. Helmus and Christopher P. Jaroniec. Nmrglue: an open source Python package for the analysis of multidimensional NMR data. *J. Biomol. NMR*, 2013. ISSN 0925-2738. doi: 10.1007/s10858-013-9718-x.
- [229] Nikolay V. Orlov and Valentine P. Ananikov. NMR analysis of chiral alcohols and amines: development of an environmentally benign “in tube” procedure with high efficiency and improved detection limit. *Green Chem.*, 2011. ISSN 1463-9262. doi: 10.1039/c1gc15191f.
- [230] Z. H. Cho and J. H. Yi. A novel type of surface gradient coil. *J. Magn. Reson.*, 1991. ISSN 00222364. doi: 10.1016/0022-2364(91)90133-E.
- [231] Jörg Döpfert. brukerMRI <https://github.com/jdoepfert/brukerMRI>, git-commit: e70f90d95275035546cb54ec09e2f560848d9122.
- [232] P. Mansfield. Imaging by nuclear magnetic resonance. *J. Phys. E.*, 1988. ISSN 0022-3735. doi: 10.1088/0022-3735/21/1/002.
- [233] D. Topgaard, R. W. Martin, D. Sakellariou, C. A. Meriles, and A. Pines. “Shim pulses” for NMR spectroscopy and imaging. *Proc. Natl. Acad. Sci.*, 2004. ISSN 0027-8424. doi: 10.1073/pnas.0408296102.

- [234] John D. Hunter. Matplotlib: A 2D Graphics Environment. *Comput. Sci. Eng.*, 2007. ISSN 1521-9615. doi: 10.1109/MCSE.2007.55.
- [235] Laurel O. Sillerud, Andrew F. McDowell, Natalie L. Adolphi, Rita E. Serda, David P. Adams, Michael J. Vasile, and Todd M. Alam.  $^1\text{H}$  NMR Detection of superparamagnetic nanoparticles at 1T using a microcoil and novel tuning circuit. *J. Magn. Reson.*, 2006. ISSN 1090-7807. doi: 10.1016/j.jmr.2006.04.005.
- [236] Markus Meissner, Peter While, Nils Spengler, Dario Mager, and Jan Korvink. Micro-integrated Gradient System for Magnetic Resonance Microscopy. In *Proc. Euromar 2018, Nantes, France*, 2018.
- [237] Aric B. Shorey and Rachel Lu. Progress and application of through glass via (TGV) technology. In *2016 Pan Pacific Microelectron. Symp. (Pan Pacific)*, pages 1–6. 2016. ISBN 978-0-9888-8739-8. doi: 10.1109/PanPacific.2016.7428424.
- [238] Deborah Pence. Reduced pumping power and wall temperature in microchannel heat sinks with fractal-like branching channel networks. *Microscale Thermophys. Eng.*, 2003. ISSN 1089-3954. doi: 10.1080/10893950290098359.
- [239] A. J. Blodgett and D. R. Barbour. Thermal Conduction Module: A High-Performance Multilayer Ceramic Package. *IBM J. Res. Dev.*, 1982. ISSN 0018-8646. doi: 10.1147/rd.261.0030.
- [240] E. Baker. Liquid immersion cooling of small electronic devices. *Microelectron. Reliab.*, 1973. ISSN 00262714. doi: 10.1016/0026-2714(73)90462-9.
- [241] Cr-etch-200, Chromätzmittel zur Strukturierung für Halbleiter- und Mikrosystemtechnik, NB-Technologies GmbH, Bremen, Germany. *Datasheet*, accessed on 2016-02-21.

# Acronyms

*c. elegans*    *caenorhabditis elegans*

**1D**            one-dimensional

**2D**            two-dimensional

**3D**            three-dimensional

**ABS**           acrylonitrile butadiene styrene

**ADC**           analog-to-digital converter

**AFM**           atomic/scanning force microscope

**AQ**            acquisition time

**BBB**           BeagleBoneBlack

**BJT**           bipolar junction transistor

**BS**            back-side

**BW**            band-width

**CMOS**        complementary metal oxide semiconductor

**CPMG**        Carr-Purcell-Meiboom-Gill

**CTE**           coefficient of thermal expansion

<b>DAC</b>	digital-to-analog converter
<b>DC</b>	direct current
<b>DFR</b>	dry film resist
<b>DIW</b>	de-ionised water
<b>DMSO</b>	dimethyl sulfoxide
<b>DRIE</b>	deep reactive-ion etching
<b>DSC</b>	differential scanning calorimetry
<b>EBR</b>	edge bead removal
<b>ESR</b>	electron spin resonance
<b>FDM</b>	fused deposition modeling
<b>FFT</b>	fast $\mathcal{F}$ ourier transform
<b>FID</b>	free induction decay
<b>FKM</b>	fluoroelastomer
<b>FLASH</b>	fast low angle shot
<b>FOV</b>	field-of-view
<b>FS</b>	front-side
<b>FWHM</b>	full width at half maximum
<b>GRE</b>	gradient echo

<b>HDO</b>	hydrogen-deuterium oxide
<b>HMDS</b>	hexamethyldisilazane
<b>I<sup>2</sup>C</b>	Inter-Integrated Circuit
<b>ID</b>	inner diameter
<b>IPA</b>	isopropyl alcohol
<b>IR</b>	infrared
<b>LIGA</b>	lithography, electroplating, and moulding <i>German acronym for: Lithographie Galvanoformung, Abformung</i>
<b>LNA</b>	low-noise amplifier
<b>LTCC</b>	low temperature cofired ceramics
<b>MEMS</b>	micro electro mechanical systems
<b>MMA</b>	methyl methacrylate
<b>MR</b>	magnetic resonance
<b>MRI</b>	magnetic resonance imaging
<b>MRM</b>	magnetic resonance microscopy
<b>MRR</b>	magnetic resonance relaxometry
<b>NMP</b>	N-Methyl-2-pyrrolidone
<b>NMR</b>	nuclear magnetic resonance
<b>NWA</b>	network analyser

<b>OP-AMP</b>	operational amplifier
<b>PCB</b>	printed circuit board
<b>PDMS</b>	poly(dimethylsiloxane)
<b>PEB</b>	post exposure bake
<b>PEG</b>	polyethylene glycol
<b>PET</b>	polyethylene terephthalate
<b>PFG</b>	pulsed field gradient
<b>PGA</b>	programmable gain amplifier
<b>PGMEA</b>	propylene glycol methyl ether acetate, 1-methoxy-2-propanol acetate
<b>PL</b>	pulse length
<b>PLB</b>	post lamination bake
<b>PMMA</b>	poly(methyl methacrylate)
<b>PP</b>	pulse power
<b>PTFE</b>	polytetrafluoroethylene
<b>PUR</b>	polyurethane
<b>PVD</b>	physical vapour deposition
<b>QDR</b>	quick-dump-rinsing
<b>RF</b>	radio frequency
<b>RMS</b>	root-mean-square
<b>ROI</b>	region-of-interest

<b>RTD</b>	resistance temperature detector
<b>SE</b>	spin-echo
<b>SEM</b>	scanning electron microscope
<b>SI</b>	slice thickness
<b>SNR</b>	signal-to-noise ratio
<b>SPI</b>	serial peripheral interface
<b>SW</b>	sweep-width
<b>TCR</b>	temperature coefficient of resistance
<b>TD</b>	number of point digitised
<b>TE</b>	echo time
<b>TG</b>	thermogravimetry
<b>TGV</b>	through glass VIA
<b>TMS</b>	tetramethylsilane
<b>Tx/Rx</b>	transmit and receive
<b>UV</b>	ultra-violet
<b>VIA</b>	vertical interconnect access
<b>VNA</b>	vector network analyzer
<b>WB</b>	wire-bond

**WEC**      wedge error compensation

**X-ray CT**      X-ray computed tomography

# List of publications

## Peer-reviewed journals

- **M.V. Meissner**, P.T. While, D. Mager, J.G. Korvink.  
**Microscale nuclear magnetic resonance gradient chip.**  
Journal of Micromechanics and Microengineering. (2023).  
<https://doi.org/10.1088/1361-6439/ac9e4a>
- O. Nassar, **M.V. Meissner**, S. Wadhwa, J.G. Korvink, D. Mager.  
**Load sensitive stable current source for complex precision pulsed electroplating.**  
Review of Scientific Instruments. (2019).  
<https://doi.org/10.1063/1.5113790>
- P.T. While, **M.V. Meissner**, J.G. Korvink.  
**Insertable biplanar gradient coils for magnetic resonance microscopy: theoretical minimization of power dissipation for different fabrication methods.**  
Biomedical Physics & Engineering Express. (2018).  
<https://doi.org/10.1088/2057-1976/aab5db>
- N. Spengler, P.T. While, **M.V. Meissner**, U. Wallrabe, J.G. Korvink.  
**Magnetic Lenz lenses improve the limit-of-detection in nuclear magnetic resonance.**  
PLOS ONE. (2017).  
<http://doi.org/10.1371/journal.pone.0182779>
- N. Wang, **M.V. Meissner**, N. MacKinnon, V. Luchnikov, D. Mager, J.G. Korvink.  
**Fast prototyping of microtubes with embedded sensing elements made possible with an inkjet printing and rolling process.**  
Journal of Micromechanics and Microengineering. (2017).  
<https://doi.org/10.1088/1361-6439/aa7a61>

- N. Schuergers, T. Lenn, R. Kampmann, **M.V. Meissner**, T. Esteves, M. Temerinac-Ott, J.G. Korvink, A.R. Lowe, C.W. Mullineaux, A. Wilde.  
**Cyanobacteria use micro-optics to sense light direction.**  
eLife. (2016).  
<http://doi.org/10.7554/eLife.12620>
- S.Z. Kiss, A. Rostas, L. Heidinger, N. Spengler, **M.V. Meissner**, N. MacKinnon, E. Schleicher, S. Weber, J.G. Korvink.  
**A microwave resonator integrated on a polymer microfluidic chip.**  
Journal of Magnetic Resonance. (2016).  
<http://doi.org/10.1016/j.jmr.2016.07.008>
- **M.V. Meissner**, N. Spengler, D. Mager, N. Wang, S.Z. Kiss, J. Höfflin, P.T. While, J.G. Korvink.  
**Ink-jet printing technology enables self-aligned mould patterning for electroplating in a single step.**  
Journal of Micromechanics and Microengineering. (2015).  
<http://doi.org/10.1088/0960-1317/25/6/065015>

## Book chapter

- J.G. Korvink, V. Badilita, D. Mager, O. Gruschke, N. Spengler, S.S. Adhikari Parenky, U. Wallrabe, **M.V. Meissner**.  
**Innovative coil fabrication techniques for miniaturized magnetic resonance detectors.**  
In Micro and Nanoscale NMR, pages 109–136, Wiley-VCH, Weinheim. (2018).  
ISBN 978-3-527-34056-9

## Conference contributions with oral presentation

- **M.V. Meissner**, P.T. While, N. Spengler, D. Mager, J.G. Korvink.  
**Micro-integrated gradient system for magnetic resonance microscopy.**  
Euromar 2018, Nantes, France. (2018).

- **M.V. Meissner**, N. Spengler, D. Mager, J.G. Korvink.  
**Tintenstrahldruck ermöglicht eine maskenfreie strukturierte Mikrogalvanik zur Herstellung von miniaturisierten Spulen.**  
MikroSystemTechnik Kongress 2015, Karlsruhe, Germany. (2015).
- **M.V. Meissner**, N. Spengler, D. Mager, J. Höfflin, P.T. While, J.G. Korvink.  
**Ink-jet printing enables maskless electroplating mould patterning for rapid MRI coil fabrication.**  
23<sup>rd</sup> Scientific Meeting, International Society for Magnetic Resonance (ISMRM), Toronto, Ontario, Canada. (2015).
- N. Schuergers, T. Esteves, T. Lenn, **M. Meissner**, J.G. Korvink, C.W. Mullineaux, A. Wilde.  
**Cyanobacteria use micro-optics to sense light direction.**  
15<sup>th</sup> International Symposium on Phototrophic Prokaryotes (ISPP), University of Tübingen, Germany. (2015).
- **M.V. Meissner**, R.Ch. Meier, P.T. While, A. Moazenzadeh, J. G. Korvink.  
**Micro Magnetic Resonance x,y-Gradient System for Microscopic Samples.**  
21<sup>st</sup> Scientific Meeting, International Society for Magnetic Resonance (ISMRM), Salt Lake City, UTAH, USA. (2013).

## Conference contributions with poster presentation

- **M.V. Meissner**, N. Nestle, N. Spengler, D. Mager, M. Worgull, J.G. Korvink.  
**Comparative study of  $\mu$ -MRI and X-ray  $\mu$ -CT on an oilseed grain.**  
13<sup>th</sup> International Conference on Magnetic Resonance Microscopy, Technical University of Munich, Germany. (2015).
- **M.V. Meissner**, N. Spengler, D. Mager, S.Z. Kiss, P.T. While, J.G. Korvink.  
**Single step mold and metal patterning for electro-deposition enables rapid and low-cost fabrication of MR field coils.**  
56<sup>th</sup> Experimental Nuclear Magnetic Resonance Conference (ENC), Pacific Grove, CA, USA. (2015).

- S.Z. Kiss, **M.V. Meissner**, N. Spengler, J.G. Korvink.  
**A disposable fluidic insert with integrated microwave resonator for Ku-band applications.**  
56<sup>th</sup> Experimental Nuclear Magnetic Resonance Conference (ENC),  
Pacific Grove, CA, USA. (2015).
- **M.V. Meissner**, N. Spengler, D. Mager, S.Z. Kiss, J. Höfflin, N. MacKinnon, P.T. While, J.G. Korvink.  
**Single step mould and metal patterning for electro-deposition enables rapid and low-cost fabrication of NMR field coils.**  
NMRPM, Quantitative NMR Methods for Reaction and Process Monitoring,  
University of Kaiserslautern, Germany. (2015).
- **M.V. Meissner**, N. Spengler, S.Z. Kiss, N. MacKinnon, P.T. While, J.G. Korvink.  
**Maskless, low cost fabrication of NMR field coils.**  
Euromar 2014, Zürich, Switzerland. (2014).
- P.T. While, **M.V. Meissner**, J.G. Korvink.  
**Biplanar gradient coil design with minimum power dissipation for MRM studies.**  
Euromar 2014, Zürich, Switzerland. (2014).
- P.T. While, **M.V. Meissner**, J.G. Korvink.  
**Designing biplanar gradient coils with minimum power dissipation for NMR microscopy.**  
22<sup>nd</sup> Scientific Meeting, International Society for Magnetic Resonance (ISMRM),  
Milan, Italy. (2014).
- **M.V. Meissner**, E. Fuhrer, S.Z. Kiss,  
H.B. Ryan, N. MacKinnon, P.T. While, J.G. Korvink.  
**Low Expense General Operation probe.**  
55<sup>th</sup> Experimental Nuclear Magnetic Resonance Conference (ENC),  
Boston, MA, USA. (2014).
- S.Z. Kiss, **M.V. Meissner**, R.C. Meier, N. Spengler, N. MacKinnon, J.G. Korvink.  
**Does the NMR coil-type influence the performance of microwave resonators?**  
55<sup>th</sup> Experimental Nuclear Magnetic Resonance Conference (ENC),  
Boston, MA, USA. (2014).

- **M.V. Meissner**, R.Ch. Meier, P.T. While, J.G. Korvink.  
**Micro-integrated Gradient System for Magnetic Resonance Microscopy.**  
10<sup>th</sup> MicRO Alliance Meeting, Kyoto University, Japan. (2013).
- **M.V. Meissner**, R.Ch. Meier, N. Spengler, P.T. While, J. G. Korvink.  
**Micro-integrated Biaxial Gradient System for Magnetic Resonance Microscopy.**  
54<sup>th</sup> Experimental Nuclear Magnetic Resonance Conference (ENC),  
Pacific Grove, CA, USA. (2013).
- R.Ch. Meier, V. Badilita, E. Fischer, **M. Meissner**,  
D. v. Elverfeldt, J. Hennig, U. Wallrabe, J. G. Korvink.  
**Microfluidic magnetic resonance chip with integrated solenoidal microcoil  
for disposable use in a modular probe.**  
microTAS, Okinawa, Japan. (2012).
- R.Ch. Meier, V. Badilita, E. Fischer, **M. Meissner**,  
D. v. Elverfeldt, J. Hennig, U. Wallrabe, J. G. Korvink.  
**A modular microcoil device realized with conductive interconnect stripes.**  
Euromar 2012, Dublin, Ireland. (2012).



# Acknowledgement

It is with great appreciation and gratitude that I would like to take this opportunity to acknowledge the people who have played a significant role in my academic path. Their support, guidance, and encouragement have been invaluable in helping me to achieve my academic goals.

I thank Professor Jan G. Korvink for providing me with a unique and enriching research opportunity in your esteemed research group. I am grateful for giving me the freedom in my approach and for giving me the opportunity to collaborate with different research groups across disciplines. Your brilliant and unconventional ideas opened up new perspectives on the research topic. I am very grateful to you for allocating the necessary funds, such as those from the ERC, which enabled our team to conduct experiments using excellent research and measurement equipment, including the ultra-high-field wide-bore magnet. Your proactive guidance in writing publications and the possibility to present my scientific contributions at numerous international conferences was instrumental in improving the quality of my work.

I thank Professor Jürgen Hennig for taking over the second opinion for my work. Your unparalleled expertise in the field of magnetic resonance imaging and your deep understanding of the subject matter have been instrumental in shaping the quality and direction of my research. Furthermore, I would like to express my gratitude to your staff at the Department of Radiology for their cooperation and good relationship. Additionally, your exceptional talks at the International Society for Magnetic Resonance in Medicine (ISMRM) were both enlightening and informative, providing me with valuable insights and new perspectives.

I would like to express my deepest gratitude to my esteemed colleague and group leader, Dario Mager, for your support, mentorship, and hands-on approach

throughout my academic journey. Your solution-oriented mindset and your willingness to tackle challenges head-on have been a source of inspiration and motivation for me. I am grateful for your continuous dedication to student laboratory courses, your appreciative attitude towards our team's achievements, and your unwavering support for our social life within the Low-Cost MEMS group. Your passion for embracing new challenges and your heroic deeds have earned you the nickname "*Super Dario*", and that for good reason. Your positive and supportive character has made a significant impact on my academic and personal growth, and I am honoured to have worked alongside you.

I thank Professor Peter T. While, who I met at the beginning of my research career at the IMTEK in Freiburg. Your interdisciplinary expertise and internationally acclaimed experience in modeling and method development have contributed immensely to our discussions and collaborations. I am impressed by your precise and thoughtful approach, as well as your unique and enriching perspectives. I would also like to express gratitude to the *Alexander von Humboldt Foundation* for giving Peter the opportunity to relocate from Tasmania and to develop an intensive collaboration in Freiburg. I am deeply thankful that we had the opportunity to attend various international conferences together. Thank you for the enriching and enjoyable time we shared.

Kay Steffen, I want to say how much I appreciate your spontaneous and uncomplicated support. Thank you! During my student courses, I had the opportunity to visit your electroplating lab, and since then, it became my desire to conduct experiments there. Thanks to your kindness, my wish came true, and you granted access to your laboratory in Freiburg in a very desperate situation when I needed to perform essential experiments. Especially after the relocation of our research group from IMTEK to KIT, you provided me with the necessary lab-space to conduct my electroplating experiments. Without it, it would not have been possible to implement the gradient coils. It was a great time to collaborate with such a kind and supportive colleague like you.

I am also very thankful to Nikolaus Nestle from BASF in Ludwigshafen for sharing your expertise in diffusion NMR and your interest in miniaturised NMR detectors and gradient fields. Our first encounter was at the ENC conference

in California, where we discovered that we were actually working in so close proximity. I would like to express my sincere appreciation for our enthusiastic collaboration on the experiments involving the sesame grain, that we conducted using the developed micro integrated NMR detectors.

I am deeply grateful to Professor Ulrike Wallrabe for your constructive feedback and guidance during my time at the IMTEK. I would like to express my appreciation for organising the Black Forest Symposia. These Symposia provided an exceptional platform for interdisciplinary exchange and inspired me to think beyond the boundaries of my own research.

I would like to express my profound gratitude to Professor Annegret Wilde. Your participation in my *cyanobacteria* lithography experiments inside the cleanroom was truly remarkable and a highlight of my academic journey. Moreover, I am honoured that the experiment was appreciated by reviewer 3#, as written in the open access review letter: "*Also, the experiment described in Figure 3D and 3E was very cool.*" (see <https://doi.org/10.7554/eLife.12620.012>).<sup>[136]</sup>

The team of the IMTEK Cleanroom Service Centre, especially Michael Reichel and Nico Lehmann for your trouble-free help and for the perfectly maintained machines one could completely rely on. From the KIT, Achim Voigt deserves my sincere appreciation for being an important discussion partner, and for providing valuable insights that helped me tremendously. Your technical expertise was pivotal in building up the pulse current source.

Working within the Low-Cost MEMS group has been a brilliant experience. I want to extend my heartfelt gratitude to Omar Nassar. Even though we only worked together for a brief period at KIT, we were able to collaborate effectively and publish the current sink for micro electroplating. I am also grateful to Nan Wang for our collaborative work on the unconventional methods of creating new micro MR pickup coils. Patrick Bollgrün deserves special recognition for your remarkable composure and calmness, especially when working with the inkjet material printer inside the glovebox. Sarai Torres' fantastic ideas and impressive creativity have been invaluable to the group. I am particularly grateful to Nils Spengler for sharing your expertise on wafer sawing and your special tricks on the ORDYL laminate. Furthermore, I want to express my gratitude to you for

being a reliable commuting partner during our bike rides through the *Hardtwald* to the KIT campus north.

I thank my classmate Varun Arya for your amazing curry cuisine and Taimur Aftab for fruitful discussions and the possibility of using the high-frequency measuring instruments at Professor Reindl's chair. Jens Höfflin for the road trip along the two NMR conferences in California and Utah, as well as the eventful and memorable time in China. Christoph Trautwein for the winter bike packing tour to Spain. This tour was before the chair moved to the KIT, for practising whether daily commuting by the ICE train from Freiburg with a folding bike through the *Hardtwald* to the campus north is feasible. My brother Felix as an important discussion partner and for your interest in my research activities as well as your support at the EuroMAR in Zürich, where your flat turned into a hotel beyond comparison.

Thanks should also go to the Inkscape, Blender, Gimp and L<sup>A</sup>T<sub>E</sub>X contributors who impacted my thesis by creating high-quality software tools. Their dedication enabled me to produce high-quality figures, 3D models, and typesetting. The Kicad developers deserve my gratitude for creating a professional PCB design tool that was employed throughout this thesis. Their commitment to open-source software has greatly contributed to the advancement of scientific research and innovation. My special thanks are extended to Mathias Köfferlein for maintaining and supporting his free GDS editor Klayout, and there was no other tool that could match its functionality.

If I have unintentionally missed to mention someone in my acknowledgement, please forgive me as it was not intentional, and please know that your contribution is highly appreciated.

Finally, I wish to express my gratitude to my family, and particularly to my mother Anita, for their unwavering social and financial support, as well as their constant encouragement. Their belief in my abilities has been a constant source of motivation and inspiration, allowing me to wholeheartedly devote myself to a highly engaging research topic. I cannot overstate the impact their support had on my success, and for that, I am truly grateful.

